Integrative Analysis of Dynamic Allostery and Hydration Networks in p38α Map Kinase using Nuclear Magnetic Resonance and Molecular Dynamics Simulations

DISSERTATION

For the achievement of the academic degree of the

Dr in Natural Sciences

(Dr.rer.nat)

Submitted to

Department of Chemistry and Chemical Biology

TU DORTMUND UNIVERSITY

by

Suchandra Roy Acharyya

from

Kolkata, India

Acknowledgement

I started my journey of PhD as an excited kid, with my entire life packed into two suitcases, travelling across oceans to a foreign land, without a single familiar place or a single familiar face. Amidst all the unknown that lay ahead, my excited heart was ready to embrace the adventure that awaited me. Almost four years have passed since that day, and the kid has now grown into an adult. In between lies a journey filled with struggles, adversities, love from strangers and family, some successes and some failures, countless memories, and so many people to be grateful for.

My first thanks would go to my project supervisor, Prof. Dr. Rasmus Linser, for making this entire journey smooth and enjoyable. Thank you for allowing me to work independently and foster my own thoughts and ideas, while also guiding me whenever I needed support. I learned so many new things, and that was only possible because of the belief you had in me. I truly loved the work I did, and it turned out exactly the way I had hoped it would. Thank you as well for being such a kind and generous person, because I have always believed that kindness is one of the most difficult attributes to possess.

My second thanks would go to Dr. Rafael Bernardi, not only my second reviewer, but also my co-supervisor, who was kind enough to host me during my three-month internship in the USA and continued to guide me even afterwards. Thank you for giving me the confidence I so deeply needed during that time, helping me feel capable as a researcher. Thank you also for making me fall in love with MD simulations and the mechanistic biological questions they can address.

I started my PhD without any prior knowledge of NMR or protein chemistry, and I would therefore like to extend my gratitude to my entire working group who have helped me overcome all the obstacles and to keep on learning and growing. I am especially thankful to Dr. Suresh Kumar Vasa for always helping me with the spectrometers, and to Dr. Anya Aucharova for being my biggest support system in the lab, for boosting my confidence in protein biochemistry, and for being one of my very first friends here. I would also like to thank all my current colleagues: Dr. Alexander Klein, Dr. Dmitry Blokhin, Dr. Florian Lindemann, Dorothea Dierks, Tye Gonzalez, and Dr. Or Lusky, as well as my past colleagues: Dr. Benedikt Soeldner, Dr. Laura Kukuk, Dr. Ekaterina Burakova, Dr. Himanshu Singh, Dr. Sara Medina Gomez, Dr. Julia Kotschy, and Dr. Elnaz Banijamali, for always helping me whenever I needed support. My gratitude extends to Christa from the MPI, who has been like a mother to many of us. From the moment I arrived in Germany, she helped me with almost every problem: moving, settling in, and finding my way

through a new system. I am deeply grateful for her kindness, patience, and constant support. I would thank Christine Wehbrink, Vanessa Slota, and Antje Peukert for all the administration related help. I would also like to mention Dr. Diego Gomes from Auburn, whom I still continue to annoy whenever I cannot access the cluster or my workstation in the USA.

I never imagined I would end up finding such an incredible support system here in Germany. For that, I am deeply grateful to my friends-Parijat, Debarshee, Sayan, Prakash, Antara Di, Kaustav Da, Anushka, Somarghya, and Agradeep,for being the most amazing band of friends one could ever hope for. I honestly don't know what I would do without you all. Thank you for keeping me mentally sane, grounded, and happy. I wish I could carry each one of you in my pocket, wherever I go. You are my family now. I would also like to thank Ahalya and Akash Da for being the first sense of familiarity I had at the beginning of this journey. I will always be grateful. I am eternally thankful for my "do Anmol ratan," Bedadeep and Vishal, who I've lovingly kept on their toes with my endless ability to test their patience. No matter which continent we are in, I will always find my way back to them; if only to annoy them a little. A special thank you to my best friend Dipanwita, who has been my safest harbour for the past ten years, and to my childhood friends Aaratrika, Ushasi, and Naheli, who are always just one call away.

I would like to mention my soulmate, my little sister, my tiny guiding light, whose existence makes me breathe a little easier every single day. Thank you, Momzi, for everything you are, for being my little human diary, for holding my feelings when I have no words left for them. When life falls apart, I somehow manage to gather myself from the broken pieces only because of you.

Everything I am today, I owe to my Amma, Ma, and Baba. You have shaped me into who I am, supported, guided, and stood by me through every phase of becoming. Without your relentless love and unwavering support, I would not have found my footing in this world. Thank you for holding me when I fall, and for teaching me how to stand again each time.

And lastly, but never the least, I want to thank my partner and companion, Shailendra. You have been my constant through the years, my sharpest critic when I needed to grow, and my loudest cheerleader when I doubted myself. You've pushed me beyond the boundaries I thought I could never cross, and you've held my hand through every pitfall along the way. Thank you for believing in me even when I struggled to believe in myself. Life feels gentler, fuller, and infinitely better with you in it. Thank you for always pulling me back from the darkness and reminding me that I am never alone.

I am grateful to all of you.

Publications

1. **Roy Acharyya, S**., Weisner, J., Bernardi, R. C*. & Linser, R*. Mapping of dynamic allostery within p38 alpha kinase via network analyses and NMR spectroscopy. *Manuscript revision submitted in Nature Communications (Manuscript ID : N-COMMS-26-016585) preprint : https://doi.org/10.21203/rs.3.rs 8958159/v1*

2. **Roy Acharyya, S.,** Vasa, S. K., Gasper, R., Bernardi, R. C. & Linser, R. Coupling DFG-loop-dependent allostery and water dynamics : the two key players in the game of p38α regulation. *Manuscript in preparation.*

3. Kosel, B., Bigler, K., Buchmuller, B. C., **Roy Acharyya, S**., Linser, R. & Summerer, D. (2024) Evolved readers of 5-carboxylcytosine CpG dyads reveal a high versatility of the methyl-CpG-binding domain for recognition of noncanonical epigenetic marks. Angewandte Chemie, 136(17), e202318837.https://doi.org/10.1002/ange.202318837

Conferences & Workshops

Oral Presentations

1. Dynamic Allostery of p38α Kinase Tag De Chemie (02/ 2026, Dortmund)
2. Bio-NMR Network NRW (09/ 2025, Düsseldorf)
3. RESOLV Klausurtagung (03/ 2025, Klosterpforte)

Poster Presentations

1. Solvent-Driven Allostery of p38α Kinase, Tag De Chemie (02/ 2026, Dortmund)
2. The Future of NMR in Biology (11/ 2025, Berlin)
3. RESOLV Autumn Workshop (11/ 2025, Bochum)
4. Allosteric Dynamics of p38α Kinase IMPRS-LM Student Symposium (04/ 2025, Dortmund)
5. Bio-NMR Network NRW (09/ 2024, Essen)
6. RESOLV Klausurtagung (03/ 2024, Klosterpforte)
7. Dynamic Network Analysis of p38α Kinase EUROMAR 2024 (07/ 2024, Bilbao)
8. Les Houches–Telluride Workshop (06/ 2024, Chamonix)
9. Bio-NMR Network NRW (09/ 2023, RWTH Aachen)
10. IMPRS-LM Student Symposium 2023 (05/ 2023, Dortmund)
11. NMR Symposium & Workshop 2023 (05/ 2023, ISTA)

List of Acronyms

Abbreviation	Full form
MAP kinase	Mitogen-Activated Protein Kinase
NMR	Nuclear Magnetic Resonance
DFG	Aspartate–Phenylalanine–Glycine motif
MD	Molecular Dynamics
MBD	MAP Kinase Binding Domain / Molecular Binding Domain *(depends on your thesis context; define carefully)*
PBC	Periodic Boundary Conditions
NVT	Constant Number of particles, Volume, and Temperature ensemble
NVE	Constant Number of particles, Volume, and Energy ensemble
NPT	Constant Number of particles, Pressure, and Temperature ensemble
RMSD	Root Mean Square Deviation
RMSF	Root Mean Square Fluctuation
SASA	Solvent Accessible Surface Area
RDF	Radial Distribution Function
CSA	Chemical Shift Anisotropy
INEPT	Insensitive Nuclei Enhanced by Polarization Transfer
HSQC	Heteronuclear Single Quantum Coherence
NOE	Nuclear Overhauser Effect
CPMG	Carr–Purcell–Meiboom–Gill

Abbreviation	Full form
PCR	Polymerase Chain Reaction
IPTG	Isopropyl β-D-1-thiogalactopyranoside
PDGFR	Platelet-Derived Growth Factor Receptor
VEGFR	Vascular Endothelial Growth Factor Receptor
BOG	β-Octyl Glucoside / n-Octyl-β-D-glucopyranoside
NAMD	Nanoscale Molecular Dynamics
CHARMM	Chemistry at HARvard Macromolecular Mechanics
PKA	Protein Kinase A
EGFR	Epidermal Growth Factor Receptor
WT	Wild Type
HTRF	Homogeneous Time-Resolved Fluorescence
FRET	Förster Resonance Energy Transfer
ATF2	Activating Transcription Factor 2
GST	Glutathione S-Transferase
TROSY	Transverse Relaxation-Optimized Spectroscopy
CSP	Chemical Shift Perturbation
JAWS	Just Add Waters
NOESY	Nuclear Overhauser Effect Spectroscopy
HDX	Hydrogen–Deuterium Exchange
CLEANEX-PM	CLEAN chemical EXchange by Phase-Modulated spin-lock
VMD	Visual Molecular Dynamics

Abstract

Protein kinases are major therapeutic targets, but the high conservation of their ATP-binding sites limits the development of selective inhibitors. This has increased interest in kinase conformational ensembles and long-range allosteric communication as alternative routes for selective modulation. Here, p38α MAP kinase was used as a model system to investigate how dynamic communication across the kinase domain regulates structure, stability, hydration, and ligand response. Large-scale molecular dynamics simulations combined with dynamical network analysis identified key residues that mediate communication between the N- and C-lobes and connect functional regions including the activation loop, hinge, lipid-binding domain, and cryptic allosteric pocket. These predictions were experimentally tested using NMR spectroscopy, biochemical activity assays, and selected p38α mutants in the presence and absence of an active-site inhibitor.

A second part of the study focused on Asp168, the conserved aspartate of the DFG motif, which is essential for catalytic activity and activation-loop organisation. Mutation of this residue induced long-range effects beyond the active site, altering thermal stability, residue-level flexibility, cross-lobe correlations, ligand behaviour, and hydration networks in distal pockets. In particular, D168A reorganised water-associated signals around the activation loop and lipid pocket, obtained through experimental solution and solid-state NMR and bolstered by molecular dynamics simulations, demonstrating that perturbation of a catalytic DFG residue can reshape both protein dynamics and solvent organisation across the kinase domain. Together, these results provide atomistic insight into how local perturbations propagate through p38α to regulate allosteric communication. This integrated computational and experimental structural-biology framework to understand the dynamic allostery functioning within the kinase may guide the rational design of selective allosteric kinase modulators that exploit dynamic and hydration-mediated regulatory networks rather than conserved active-site features alone.

Zusammenfassung

Proteinkinasen sind wichtige therapeutische Zielstrukturen, aber die hohe Konservierung ihrer ATP-Bindungsstellen schränkt die Entwicklung selektiver Inhibitoren ein. Dies hat das Interesse an Kinase-Konformationsensembles und langreichweitiger allosterischer Kommunikation als alternative Wege für eine selektive Modulation erhöht. Hier wurde die p38α-MAP-Kinase als Modellsystem verwendet, um zu untersuchen, wie dynamische Kommunikation innerhalb der Kinasedomäne Struktur, Stabilität, Hydratation und Ligandenantwort reguliert. Großskalige Molekulardynamik-Simulationen, kombiniert mit dynamischer Netzwerkanalyse, identifizierten zentrale Residuen, die die Kommunikation zwischen dem N- und C-Lobus vermitteln und funktionelle Regionen verbinden, darunter die Aktivierungsschleife, die Hinge-Region, die Lipidbindungsdomäne und eine kryptische allosterische Tasche. Diese Vorhersagen wurden experimentell mittels NMR-Spektroskopie, biochemischer Aktivitätsassays und ausgewählter p38α-Mutanten in An- und Abwesenheit eines aktiven-Zentrum-Inhibitors getestet.

Ein zweiter Teil der Studie konzentrierte sich auf Asp168, das konservierte Aspartat des DFG-Motivs, das essenziell für die katalytische Aktivität und die Organisation der Aktivierungsschleife ist. Die Mutation dieses Residues induzierte langreichweitige Effekte über das aktive Zentrum hinaus und veränderte die thermische Stabilität, residuenspezifische Flexibilität, lobusübergreifende Korrelationen, das Ligandenverhalten und Hydratationsnetzwerke in distalen Taschen. Insbesondere reorganisierte D168A wasserassoziierte Signale um die Aktivierungsschleife und die Lipidtasche, die durch experimentelle Lösungs- und Festkörper-NMR erhalten und durch Molekulardynamik-Simulationen gestützt wurden. Dies zeigt, dass die Störung eines katalytischen DFG-Residues sowohl die Proteindynamik als auch die Lösungsmittelorganisation über die Kinasedomäne hinweg umgestalten kann.

Zusammen liefern diese Ergebnisse atomistische Einblicke darin, wie lokale Störungen durch p38α propagieren, um allosterische Kommunikation zu regulieren. Dieser integrierte rechnergestützte und experimentelle strukturbiologische Rahmen zum Verständnis der dynamischen Allosterie innerhalb der Kinase könnte die rationale Entwicklung selektiver allosterischer Kinase-Modulatoren unterstützen, die dynamische und hydratationsvermittelte regulatorische Netzwerke ausnutzen, anstatt ausschließlich auf konservierte aktive-Zentrum-Merkmale abzuzielen.

Contents

Acknowledgement……..….3

Publications……5

Conferences & workshops……..6

List of Acronyms ……...7

Abstract……..9

Zusammenfassung……10

Contents ..……11

1.**Introduction**……13

1.1 Proteins: Structure, Function and Dynamics……...14

1.2 Dynamic Allostery……16

1.3 Structural-biology Strategies for Unravelling Dynamic Allostery……18

1.4 Recombinant Protein Production……...45

1.5 p38α MAP kinase: biological relevance, inhibition, and structural basis of regulation…… 47

2. **Research Gap**…… 52

3. **Mapping the dynamic allostery of p38α kinase**……...54

3.1 Introduction……55

3.2 Dynamic Network Analysis of p38α……58

3.3 Change in network properties on perturbation……67

3.4 Validating the dynamic network ensemble……...71

3.5 Pathway level changes on network perturbation in apo and holo p38α……73

3.6 Change in biological activity on the absence of network residues…….80

3.7 Chemical shift perturbations on network element mutations……....83

3.8 Modulation of protein dynamics in the absence of network elements studied

through NMR relaxation……90
3.9 Conclusion……....104
3.10 Discussion……105
4. **DFG-loop-dependent allostery extends to water dynamics in p38α**……111
4.1 Introduction……112
4.2 Differences in thermal stability on DFG-loop mutation……117
4.3 Water residence times between different pocket changes upon mutation..126
4.4 DFG mutation reshapes water organization around the different pockets.130
4.5 DFG mutation rewires the solvent exchange capacities……134
4.6 H/D Exchange in Solution NMR……137
4.7 H/D Exchange in Solid state NMR……..143
4.8 Conclusion……150
4.9 Discussion……151
5. **Outlook**……153
6. **Methodology**……154
6.1 Molecular Dynamics Simulation……155
6.2 Dynamical Network Analysis……157
6.3 Sample Preparation……158
6.4 Protein Crystallisation……160
6.5 X-ray diffraction measurements……161
6.6 HTRF Analysis……..161
6.7 nano DSF analysis……162
6.8 Solution State NMR……...163
6.9 H/D exchange with Solid state NMR……165
7. **References**……166
8. **List of Figures**……...186
9. **List of Tables**……195
10. **Appendix**……196

1. Introduction

This section presents the conceptual and methodological framework of the study. It covers protein dynamics, dynamic allostery, the main structural-biology techniques used in this work, molecular dynamics simulations, NMR spectroscopy, X-ray crystallography, recombinant protein production and the biological relevance of p38α kinase.

1.1 Proteins: Structure, Function and Dynamics

Proteins are biopolymers composed of amino acids and perform a wide range of essential biological functions. They serve as structural components, enzymes, signaling molecules, transporters, receptors, and regulators of cellular processes, including programmed cell death[1]. Depending on their amino acid sequence, proteins fold into specific three-dimensional structures that determine their stability, interactions, and function. Protein structure is commonly described at four hierarchical levels of increasing complexity: primary, secondary, tertiary, and quaternary structure.

The primary structure (**Fig. 1.1**) refers to the linear sequence of amino acids in a polypeptide chain and provides the basis for all higher levels of protein organization[2]. The secondary structure (**Fig. 1.1**) describes the local spatial arrangement of the polypeptide backbone, excluding the side chains. The major secondary structural elements are α-helices, β-sheets, and loops. These structures are defined by the backbone dihedral angles φ and ψ, as well as by characteristic hydrogen-bonding patterns. An α-helix is formed when the protein backbone adopts a right-handed helical conformation with 3.6 residues per turn, stabilized by hydrogen bonds between the carbonyl group of residues *i* and the amide group of residues *i+4*. A β-sheet consists of at least two β-strands in an extended conformation, with hydrogen bonds formed between adjacent strands. Loops and turns are less regular structural elements that connect helices and β-sheets and often contribute to functional flexibility.

The tertiary structure (**Fig. 1.1**) refers to the overall three-dimensional arrangement of all atoms within a single polypeptide chain, including the precise spatial organization of secondary structural elements and functional groups[3]. Tertiary structure can be described in terms of domains, folds, and motifs. Domains are compact, semi-independent structural units that often correspond to specific functions. Folds describe characteristic three-dimensional arrangements of secondary structure elements, whereas motifs are recurring structural patterns that often contribute to biological function.

The quaternary structure (Fig. 1.1) describes the spatial arrangement and interaction of multiple polypeptide subunits within a protein complex. This level of organization is often closely linked to protein function and allosteric regulation as established in early research[4]. Allostery refers to the ability of a protein to adopt different functional states that exist in dynamic equilibrium and can be shifted by ligand binding or other regulatory events. In multimeric proteins, this may involve distinct conformations of individual subunits assembling into different higher-order states, thereby modulating the activity and properties of the overall complex[5]. With more investigation of this phenomena, modern reviews explicitly note that allosteric effects also occur in monomeric proteins, and that quaternary structural change is not a requirement for allostery.

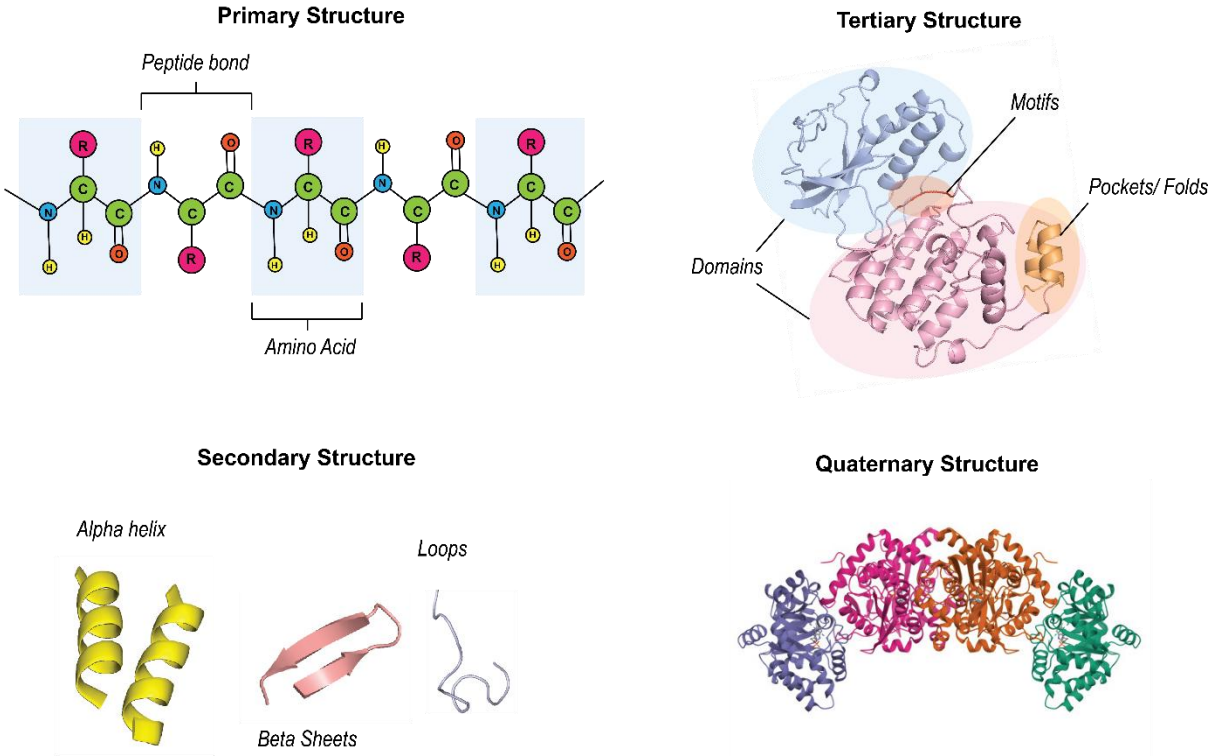

Fig. 1.1: Illustrating some examples of hierarchical levels of protein structure, including the primary, secondary, tertiary, and quaternary levels.

1.2 Dynamic Allostery

Allostery describes the phenomenon by which a perturbation at one site is sensed at another, spatially distinct site. This communication may arise from substantial structural rearrangements or, even in the absence of major conformational change[6], from interdependent dynamic features distributed throughout the protein[6, 7]. The latter mechanism, commonly termed dynamic allostery, involves the redistribution of correlated motions across the protein. Ligand binding may reshape the frequencies and amplitudes of thermally driven macromolecular fluctuations[8], whereas distal mutations can influence function through "hinge-shift" mechanisms that preserve the core architecture and may facilitate evolutionary diversification of protein function[9].

The conceptual development of allostery has progressed from discrete state-transition models to an ensemble-based framework. Classical allostery was first formalized in the Monod–Wyman–Changeux (MWC) model as a concerted structural transition between discrete functional states[7], in which ligand binding shifts the equilibrium between these states. This framework was later expanded by the Koshland–Némethy–Filmer (KNF) model, which proposed that, rather than occurring through a fully concerted switch, ligand binding can induce local conformational changes sequentially across subunits[10]. As the understanding of protein dynamics advanced, Cooper and Dryden explicitly introduced the concept of "dynamic allostery,"(**Fig. 1.2**) proposing that allosteric coupling can arise even in the absence of a change in the mean structure, through alterations in the frequencies and amplitudes of thermal fluctuations[8]. This marked a major conceptual shift in the field, moving away from the idea that one structure corresponds to one function and toward an energy landscape view in which function emerges from redistribution among conformational substates[11].

In this context, NMR has become a key experimental tool for probing molecular motions and conformational exchange, firmly establishing dynamics as a central component of allosteric regulation[12]. These developments gave rise to the view that all dynamic proteins may, in principle, possess allosteric potential[13], and that allostery itself can occur through multiple mechanistic forms rather than a single universal pathway[14].

The modern perspective therefore recognizes that structure, dynamics, entropy, and population shifts all contribute to allosteric regulation, with their relative importance

depending on the system under investigation[15]. Current research increasingly seeks to detect, quantify, and exploit these features through integrative, mechanism-driven approaches aimed at resolving genuine allosteric pathways and identifying druggable sites.

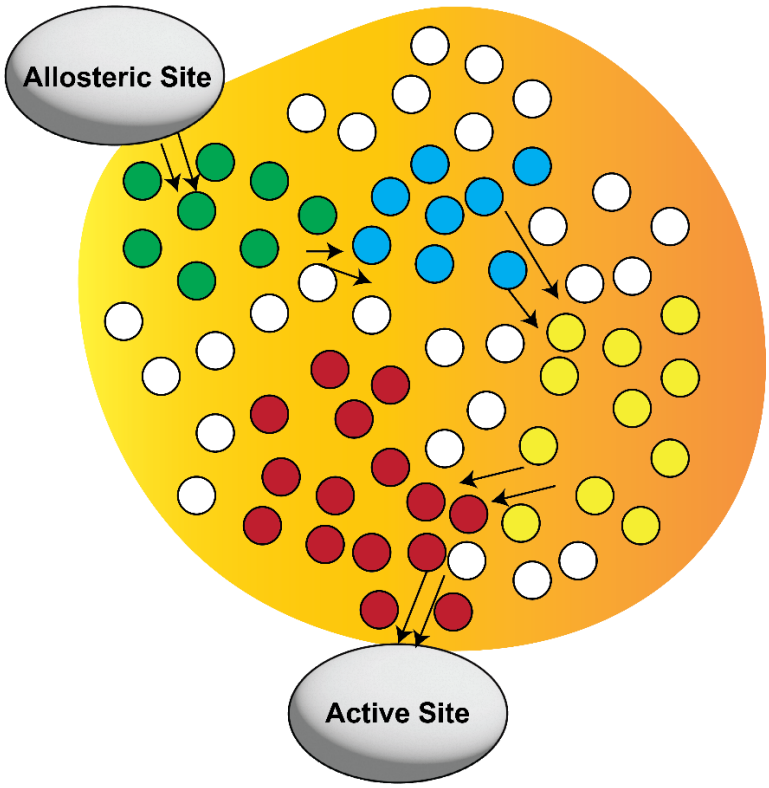

Fig.1.2 Entropy- or dynamics-driven allostery model. Distinct residue communities that move coherently as semi-rigid bodies are highlighted in different colors, while intermediate residues that cannot be assigned to a specific community are represented as white circles. Information flux passes through dynamic motions of the semi rigid bodies from the allosteric to the active site.

1.3 Structural-Biology Strategies for Unravelling Dynamic Allostery

As discussed earlier, dynamic allostery is inherently difficult to capture because its functional basis often lies in shifts in conformational populations, fluctuations, and transient states rather than in large, easily visible structural rearrangements. To characterise it, a suite of complementary structural-biology techniques is required. High-resolution methods such as X-ray crystallography and cryo-EM define the structural framework, whereas Nuclear Magnetic Resonance (NMR) spectroscopy and Molecular Dynamics (MD) simulations are particularly valuable for probing protein dynamics. NMR enables the experimental characterization of residue-specific motions, conformational exchange, and population redistribution in solution, thereby revealing transient states that are central to allosteric signaling. In parallel, MD simulations provide an atomistic and time-resolved description of protein dynamics, allowing the identification of correlated fluctuations, transient contacts, and long-range communication networks. When used together, NMR and MD offer a powerful and complementary strategy for understanding how protein motions encode allosteric regulation.

1.3.1 Computational Methods to assess Dynamic Allostery

Molecular Modelling

Molecular modelling comprises a range of computational methods used to represent, construct, visualize, and analyse molecular systems at atomic resolution. These approaches enable the investigation of the structural organisation, physicochemical properties, and interaction patterns of biomolecules in cases where experimental methods alone may not provide a complete picture[16]. In structural-biology and biochemistry, molecular modelling is widely applied to study proteins, nucleic acids, ligands, ions, and solvent molecules, and to examine how their spatial arrangement influences molecular recognition, stability, and function.

A key strength of molecular modelling lies in its ability to generate structural hypotheses for complex biological systems. Depending on the question being addressed, modelling can be used to predict missing structural regions, construct protein variants, position ligands or ions within binding sites, analyse intermolecular contacts, estimate energetic favourability, and compare alternative conformational or interaction states. These methods therefore provide a practical framework for interpreting structure-function relationships and for identifying mechanistic features that may be difficult to resolve directly from experiment[17, 18].

An example of the application of molecular modelling in biomolecular research is provided by the study of evolved readers of 5-carboxylcytosine-containing CpG dyads based on the methyl-CpG-binding domain (MBD) of MeCP2[19]. In this work, molecular modelling was used alongside directed evolution and binding experiments to explain how a conserved DNA-binding scaffold could be reprogrammed to recognize noncanonical epigenetic marks with high selectivity. Rather than analysing conformational changes over time, the modelling served to examine how specific amino acid substitutions altered the geometry and chemical character of the protein–DNA interface at atomic resolution.

The study showed that selective recognition of caC-containing CpG dyads could be understood through changes in the interaction network between mutant MBD residues and modified cytosines. Modelling of the KLTR and GMRN mutants via CHARMM Gui[20] suggested that conserved guanine recognition by arginine residues was maintained, while newly introduced residues established favourable contacts with the 5-carboxyl groups of caC. In particular, mutations such as S134R in KLTR and Y123R/S134N in GMRN created new electrostatic interactions that were absent in the wild-type binding mode, while simultaneously disrupting the canonical hydrophobic environment used for methylcytosine recognition (**Fig. 1.3**). In this way, molecular modelling helped explain how a protein scaffold could abandon its native recognition strategy and adopt an alternative binding mode tailored to a chemically distinct DNA modification.

This example highlights the broader value of molecular modelling as a tool for interpreting structure-function relationships. By enabling the visualization and analysis of residue-level contacts, steric complementarity, and electrostatic interactions, molecular modelling provides mechanistic insight into molecular recognition that cannot be obtained from sequence or affinity data alone. It is therefore particularly useful for understanding how mutations, ligands, or chemical modifications reshape binding interfaces and alter biomolecular specificity.

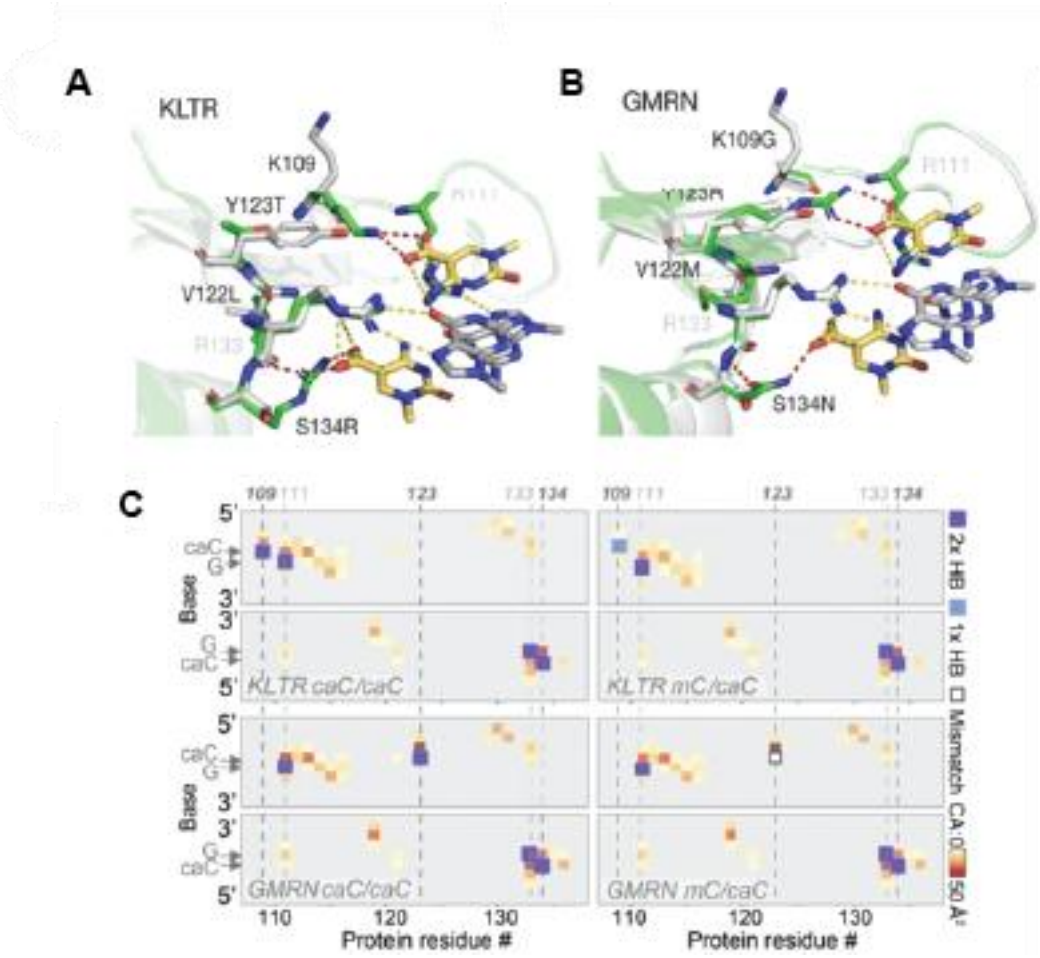

Fig. 1.3. **A, B**) Models of KLTR (**A**) and GMRN (**B**) interacting with caC/caC/dyad. Mutants in green, superimposed MeCP2 wt (pdb 3c2i) in white. Retained, canonical interactions found in both wt and mutant in yellow, new interactions uniquely occurring in mutants in red. **C**) Contact arrays for KLTR and GMRN with caC/caC and mC/caC. Note canonical, wt-like interactions of R111/133 with Gs (numbered in white), and new interactions of mutant-specific residues (numbered in black). Favorable interactions to C 5-substituents marked with green arrow–GMRN cannot interact with mC 5-methyl (red arrow), explaining its high selectivity for caC/caC. Interaction color code on the right (HB=hydrogen bond; CA: contact area).

Basics of Molecular Dynamics Simulations

While molecular modelling help us to visualise biological components and their interactions, superficially, molecular dynamics simulations delve into the dynamics of a protein, and can provide time-dependent motions of individual atoms or molecules. Thus, they can be used to investigate the properties of a model system,

often more conveniently than experiments on the real system[21]. The origin of this method dates back to the 1950s[22], with the simulation of gaseous molecules[22, 23], after which it rapidly evolved into protein simulations[24]. With the advent of computational resources and power, the field has progressed rapidly to visualise molecular motions. Such simulations are capable of describing a broad spectrum of biomolecular processes, including conformational transitions, ligand binding, and protein folding, with atomistic resolution on the femtosecond timescale[25] and thus have become a suitable tool to complement exhaustive experimental techniques deciphering protein dynamics and allostery along with drug optimisation and design, structure determination and protein-protein interactions[26, 27, 28, 29].

To understand molecular dynamics (MD), it is essential to begin with Newton's laws of motion[25]. The atoms that constitute a biomolecule are in continuous motion, and the resulting dynamics play a fundamental role in molecular function. In an MD simulation, the forces acting on the atoms are calculated using a molecular mechanics model known as a force field, which is typically parameterized using quantum mechanical calculations together with selected experimental data. By repeatedly evaluating these forces over time, the simulation generates a trajectory that can be viewed as a three-dimensional movie of the system, describing its atomic configuration throughout the simulated time interval[30]. Common biomolecular force fields include GROMOS[31, 32], OPLS-AA[33], CHARMM[34, 35, 36], and AMBER[37, 38, 39], all of which describe the potential energy of a protein as a function of its atomic coordinates. The energy terms in these force fields are generally divided into bonded and nonbonded contributions. Bonded terms account for bond stretching, angle bending, and dihedral rotation, whereas nonbonded terms describe electrostatic interactions, van der Waals dispersion, including attractive dispersion and an empirical short-range repulsive component. Accordingly, the total potential energy can be expressed as the sum of bonded and nonbonded contributions, together with any additional force-field-specific terms[30]. Here, E_{bonded} represents the bonded contribution, and $E_{nonbonded}$ the nonbonded contribution[40].

$$E_{total} = \underbrace{\sum_{bonds} K_r(r - r_{eq})^2 + \sum_{angle} K_\theta(\theta - \theta_{eq})^2 + \sum_{dihedrals} \frac{V_\pi}{2}[1 + cos(n\emptyset - \gamma)]}_{E_{bonded}} + \underbrace{\sum_{i=j}[\frac{A_{ij}}{R_{ij}^{12}} - \frac{B_{ij}}{R_{ij}^{6}} + \frac{q_i q_j}{cR_{ij}}]}_{E_{nonbonded}} \quad \text{[eq.1]}$$

The bonded and nonbonded Lennard-Jones parameters of the above-mentioned force fields must be optimised according to the system needs to make it reproducible for a large set of experimental target data.

Along with the refined use of force fields, the properties of a system are also dependent on the simulation methodology and solvent systems.

Most biomolecular molecular dynamics (MD) simulations are performed in explicit solvent under periodic boundary conditions (PBC), which provide a practical representation of a bulk-like environment while reducing edge effects[40]. In this setup, the simulation box is replicated in all spatial directions, and the system interacts with the nearest periodic images of itself. PBC are therefore a boundary treatment and do not, by themselves, impose a particular thermodynamic ensemble[41].

Ewald summation has effectively addressed the challenge of treating long-range electrostatic interactions in molecular dynamics simulations[42]. By assuming an infinitely periodic system, interactions beyond the real-space cutoff are computed using the Ewald formalism in reciprocal space rather than through direct Coulombic evaluation. Neutralizing counterions are typically introduced to remove excess net charge, although Ewald methods may also be used for non-neutral systems by assuming a uniform neutralizing background. In most biomolecular simulations, Particle Mesh Ewald (PME) is the method of choice for electrostatic interactions beyond a cutoff of about 10 Å[43, 44, 45], and long-range dispersion corrections are commonly applied to account for Lennard–Jones interactions outside the cutoff range[46, 47, 48].

In unmodified classical MD, Newton's equations of motion generate trajectories in the microcanonical (NVE) ensemble, where the number of particles, volume, and total energy are conserved[49]. When an explicit solvent representation becomes computationally too demanding, alternative approaches such as implicit solvent models or stochastic boundary methods may be used, although these involve additional approximations[30]. In the present work, all simulations were carried out in explicit solvent with periodic boundary conditions.

To reproduce experimentally relevant conditions, MD simulations are often performed in ensembles other than NVE. In the canonical (NVT) ensemble, a thermostat is used to maintain the temperature at its target value on average while keeping the number of particles and the volume fixed. In the isothermal–isobaric (NPT) ensemble, both a thermostat and a barostat are applied so that the temperature and pressure remain controlled on average, while the box volume is allowed to fluctuate[50]. Classical examples include the Nosé[51] and Nosé–Hoover[52]

thermostats for canonical sampling, the Berendsen[50] weak-coupling approach for temperature and pressure control, the extended-system barostats[53, 54], or the Langevin piston in which frictional and random forces are added to mimic coupling to an external heat bath[55] for pressure regulation. Because Berendsen coupling does not generate a rigorously correct ensemble, it is commonly viewed as more suitable for equilibration than for final production sampling, whereas methods such as Nosé–Hoover or stochastic velocity rescaling for temperature control and Parrinello–Rahman for pressure control are widely preferred for production simulations[50, 51, 52, 53, 54].

Biomolecular simulations depend on numerical integration algorithms to solve Newton's equations of motion in a stepwise manner. In this work, the Verlet and velocity-Verlet algorithms were used to propagate atomic positions and velocities at timesteps typically ranging from 1 to 2 fs, allowing accurate sampling of molecular motion[56]. In addition, constraint algorithms such as SHAKE[57] and LINCS[58] were employed to fix high-frequency covalent bond vibrations, especially those involving hydrogen atoms. This reduces the need to explicitly model the fastest bond-stretching motions and permits the use of larger timesteps, thereby enhancing computational efficiency and numerical stability.

The development of GPUs and dedicated computational hardware has markedly advanced the field of biomolecular simulations. As a result, simulations extending from the microsecond to millisecond timescale are now feasible in practice, allowing the exploration of larger biomolecular systems and the generation of multiple replicas for improved statistical reliability[59, 60, 61].

Structural & Dynamical Metrics from Molecular Dynamics Simulations

RMSD or root mean square deviation measures the overall structural deviation of the protein relative to a reference structure over time[62]. A stable RMSD evolution plot indicates that the protein has reached a structurally consistent state. **RMSF** measures the average positional fluctuation of each atom or residue around its mean position within a selected, equilibrated portion of the trajectory [63]. In proteins for our study, it is calculated using Cα regions to determine flexible and rigid regions of the proteins.

$$RMSD(t) = \sqrt{\frac{1}{N}\sum_{i=1}^{N} |r_i(t) - r_i^{ref}|^2}$$

[eq. 2]

$$RMSF(i) = \sqrt{\frac{1}{T}\sum_{t=1}^{T} ||r_i(t) - \langle r_i \rangle||^2}$$

[eq.3]

Where N is the number of selected atoms, T is the number of trajectory frames, $r_i(t)$ is the position of atom i at time t, r_i^{ref} is its position of reference structure, and $\langle r_i \rangle$ is its average position over the trajectory.

An example of the calculation and interpretation of basic metrics from a molecular dynamics (MD) trajectory is shown in **Fig. 1.4**. In this case, the analyses were performed on the β-subunit of the αββα multi-enzyme complex tryptophan synthase from Pyrococcus furiosus, with the aim of examining how different solvent constituents and ions influence protein dynamics and allosteric behaviour. In particular, the study compared sodium- and cesium-containing systems, as cesium substitutes sodium ions at a site in TrpB located close to the active site. Such analyses provide a first quantitative view of how changes in the ionic environment affect structural stability, flexibility, compactness, and solvent exposure, and therefore offer insight into how solvent composition may modulate enzyme dynamics and allosteric communication.

As discussed earlier, the most commonly used MD descriptors are the root mean square deviation (RMSD), root mean square fluctuation (RMSF), along with radius of gyration (Rg), and solvent-accessible surface area (SASA). In the present example, the cesium-solvated ensemble displays higher RMSD values than its sodium-bound counterpart, indicating that replacement of sodium by cesium leads to a greater deviation from the starting structure (**Fig. 1.4.A**). The allosteric mutant 2B9 also shows enhanced dynamics relative to the sodium-bound wild type, although its deviations remain lower than those observed for the cesium-containing wild-type system. With respect to RMSF, in monomer A, the 2B9 mutant exhibits the largest fluctuations, particularly in the region spanning residues 250–300, followed by the cesium-solvated system, whereas the sodium-bound wild type remains the least flexible (**Fig. 1.4.B**). Monomer B shows a somewhat different pattern, with the N-terminus becoming markedly more dynamic in the cesium-solvated system. Overall,

the cesium-containing wild type exhibits the largest deviations in this chain, suggesting that the influence of cesium is more pronounced in the B monomer. A comparison of mean RMSF values across the systems would further clarify the extent of these differences.

The radius of gyration is another important descriptor, as it reports on the overall compactness of the protein during the simulation (**Fig. 1.4C**). Changes in R_g can indicate structural expansion, contraction, or shifts in the distribution of mass within the protein. When the three ensembles are compared, the cesium-solvated TrpB system shows greater variation in R_g than the other systems, consistent with the increased dynamic behaviour introduced by the altered ionic environment.

SASA complements these measures by quantifying the extent to which the protein surface is exposed to solvent (**Fig. 1.4D**). This metric is particularly useful for assessing changes in protein–solvent interactions and for detecting structural rearrangements that alter surface accessibility. In the present example, the sodium-bound wild type exhibits a solvent-accessible surface area of approximately 310–320 nm^2, and the 2B9 mutant shows a similar range. By contrast, the cesium-bound system displays increased solvent accessibility, suggesting that cesium induces changes in the protein surface that may contribute to the altered dynamics observed in the other analyses.

Together, these basic MD-derived metrics provide a quantitative framework for comparing protein ensembles under different solvent and ionic conditions. While they do not by themselves explain the molecular origin of allostery, they serve as essential first-level descriptors of stability, flexibility, compactness, and solvent interaction, and therefore form the basis for deeper mechanistic analyses of ion-dependent modulation in enzymes.

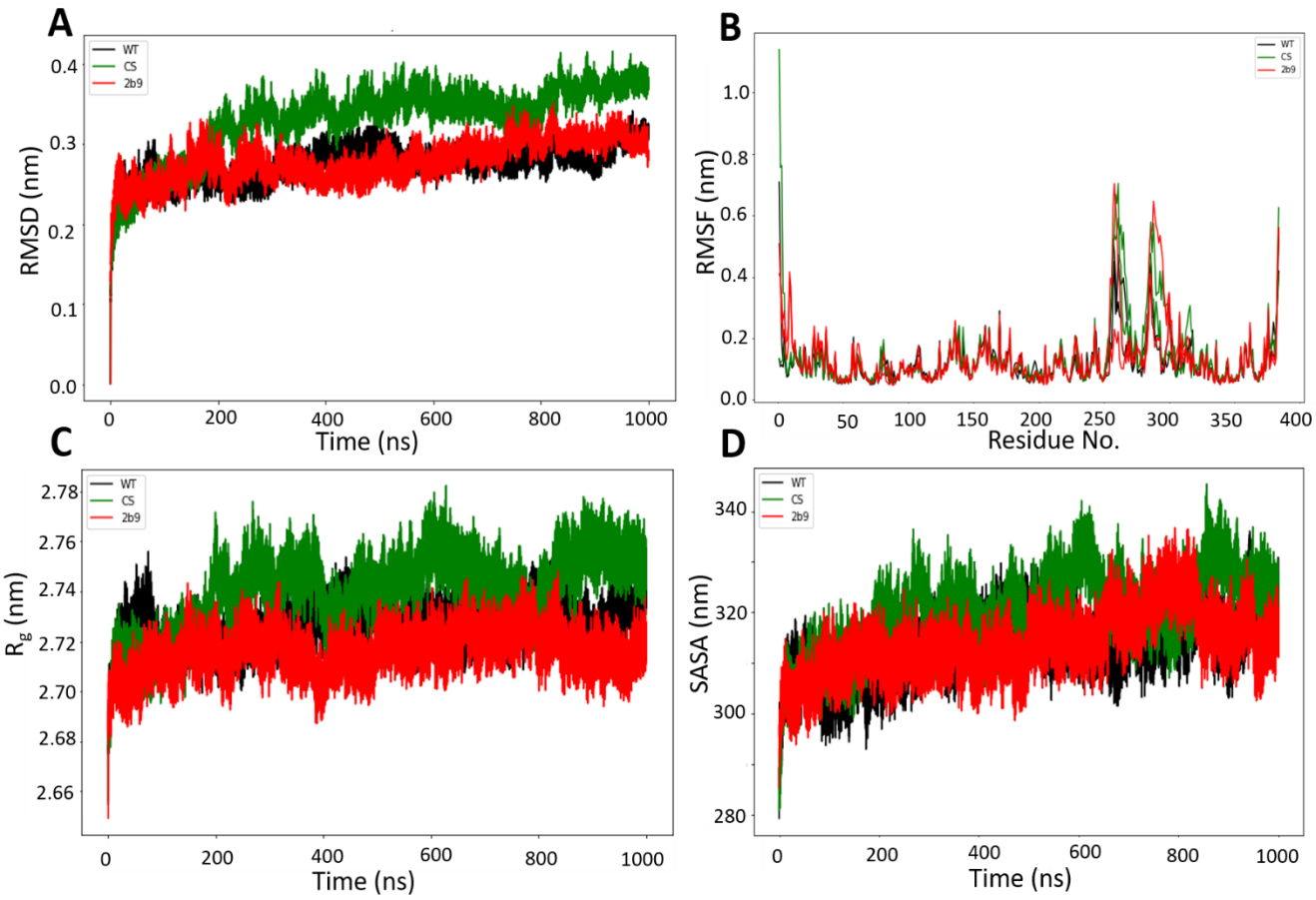

Fig. 1.4 A) Root mean square deviations **B**) Root mean square fluctuations **C**) Radius of gyration **D**) Solvent Accessible Surface Area of the wildtype in Na ions, wildtype in Cs ions and the mutant 2b9 in Na ions.

Radial Distribution Function (RDF) *g(r)* is a statistical mechanical quantity that describes how a particle density varies with distance from a reference particle[64]. RDF is a standard structural descriptor in simulations and is computed by histogramming pair distance over frames under PBC[65].

$$g_{ab}(r) = \frac{1}{N_a \rho_b 4\pi r^2} \langle \sum_{i=1}^{N_a} \sum_{j=1}^{N_b} \delta(|r_i - r_j| - r) \rangle$$

[eq.4]

Where N_a is the number of atoms in group *a*, N_b is the number of atoms in group *b*, and $\rho_b = \frac{N_b}{V}$ is the average number density of group b. The delta function, δ selects atom pairs whose separation falls at the radial distance *r*. This form states that $g_{ab}(r)$ is the probability of finding a particle of type *b* at distance *r* from a particle

of type *a*, relative to an ideal gas at the same density. Our study quantified the local distribution of water oxygen atoms around selected protein sites as pair density, normalised by the corresponding ideal gas density at the same bulk condition.

Generalized Correlation-Based Dynamical Network Analysis

Computational approaches have been widely employed to investigate allostery from several complementary angles, including the prediction of large-scale conformational rearrangements, the identification of residue-level communication pathways, and the mapping of interactions that connect distant functional sites. Earlier strategies often relied on static structural descriptors such as contact maps or topology-based elastic network models to infer putative communication routes. While these methods are useful for defining the structural framework of a protein, they are limited in their ability to capture the time-dependent coupling that underlies dynamic allostery. More recent approaches therefore integrate molecular dynamics (MD) simulations with network theory, allowing allosteric communication to be analysed directly from correlated motions encoded in the trajectory. In this framework, proteins are represented as residue interaction networks, where individual residues are treated as nodes, commonly defined by their Cα atoms, and persistent residue contacts are represented as edges. The dynamical network study showed that residue–residue communication pathways can be extracted from MD-derived correlations and used to describe long-range signal propagation through biomolecules[66, 67, 68, 69, 70, 71].

Within such a network, edges may be assigned on the basis of geometric proximity, interaction energies, or, more informatively for allosteric processes, correlation-based measures derived from the trajectory. Correlation-weighted networks are particularly valuable because allostery is fundamentally a dynamical phenomenon: the functional coupling between distant regions often arises not merely from physical contact, but from concerted fluctuations and information transfer across the protein. In practice, a contact cutoff is first imposed to define persistent interactions, after which the strength of communication between node pairs is weighted using dynamical descriptors such as mutual information or generalized correlation. The resulting graph can then be analysed to identify communities of strongly coupled residues, shortest or suboptimal communication pathways, and highly connected residues that act as allosteric hubs. In the present work, the allosteric topology was constructed using this dynamical network framework, in which residues were connected if they remained within a 4.5 Å cutoff for at least 75% of the trajectory, and the edges were weighted according to mutual-

information-based correlations. This approach is particularly well suited for identifying long-range communication pathways because it combines the structural persistence of residue contacts with the dynamical information required to capture correlated motion across both kinase lobes[69].

The edge distance, *d* between two nodes *i* and *j* were defined as;

$$d_{ij} = -logr_{(MI[i,j])}$$

[eq.5]

where d_{ij} represents the graph distance between residues *i* and *j*, and $r_{MI[i,j]}$ is the mutual-information-derived generalized correlation coefficient between the two residues. This transformation assigns shorter graph distances to strongly correlated residue pairs and longer graph distances to weakly correlated pairs[72]. The generalised-correlation based coefficients are calculated as :

$$r_{MI}[i,j] = (1 - e^{-\frac{2\,I[i,j]}{3}})^{\frac{1}{2}}$$

[eq.6]

where *I[i, j]* is the Shannon mutual information between the positional fluctuations of residues *i* and *j*. The factor 3 accounts for the three Cartesian dimensions of residue motion. Mutual information was estimated using a density-based estimator:

$$I[i,j] = \psi(k) - \frac{1}{k} - \psi(n_i) - \psi(n_j) + \psi(N)$$

[eq.7]

where ψ is the digamma function, k is the number of nearest neighbours used in the estimator, n_i and n_i are the neighbour counts associated with residues *i* and *j*, and N is the total number of sampled conformations or trajectory frames.

The network being constructed can now be analysed in accordance with the graph theory. The path between two nodes, the sink and the source also depend on the number of intermediate nodes lying between them. The two nodes must have an optimal shortest path associated with them if they belong to the same network and the remaining de-routed pathways are referred to as the suboptimal shortest path. The length of a path D_{ij} [eq.8] between distant nodes *i* and *j* is the sum of the edge weights ($W_{k,l}$) between the consecutive nodes *(k,l)* along the path. The shortest distance D_{ij}^{0} between all pairs of nodes in the network is found by using the Floyd–Warshall algorithm[73, 74].

$$D_{ij}^{0} = \sum_{k,l} W_{k.l}$$

[eq.8]

Betweenness centrality is defined as the number of shortest paths between all pairs of nodes that pass through a given node. Also referred to as node centrality, it is one of the most informative metrics for identifying potential hubs of allosteric communication. Nodes with high betweenness occupy strategically important positions within the network, as they mediate communication between otherwise distant regions. In the context of protein residue networks, such nodes often correspond to residues that play key roles in regulating inter-domain communication and long-range signal transmission. Betweenness centrality is calculated as :

$$b_i = \frac{1}{c} \sum_{s,t \epsilon v} \frac{\sigma(s,t|i)}{\sigma(s,t)}$$

[eq.9]

where $\sigma(s,t)$ is the total number of shortest paths between source node s and target node *t*, and $\sigma(s,t|i)$ is the number of those shortest paths that pass-through node *i*. The summation was performed over all distinct source–target node pairs s and t in the node set υ, excluding cases where node *i* itself was the source or target. Here, υ denotes the set of graph nodes, and *C* is a normalization factor.

Another metric employed in our analysis was community detection. Here, communities were identified using the Louvain heuristic method[75], which builds on concepts originally introduced in the Girvan–Newman[76] framework. A complex network is considered to exhibit community structure when its nodes can be partitioned into groups that are more densely connected internally than externally. In other words, interactions within a community are stronger than interactions between different communities. In protein residue networks, such communities often correspond to structurally or functionally coordinated regions and can therefore help identify groups of residues or domains that act together during allosteric communication.

Taken together, these complementary network descriptors provide a powerful framework for resolving the allosteric architecture of a protein. Metrics such as centrality, path analysis, and community structure can reveal how information is transmitted across the molecular network and which regions are most critical for long-range coupling. When integrated with experimental structural-biology

approaches such as NMR spectroscopy and X-ray crystallography, these analyses offer a more robust and mechanistic understanding of protein dynamics and allostery.

1.3.2 Foundational Techniques in NMR Spectroscopy

Nuclear Magnetic Resonance (NMR) is one of the major techniques in structural-biology for investigating molecular structure, molecular recognition, and intermolecular interactions. Unlike methods that primarily provide static structural snapshots, NMR offers the unique advantage of probing biomolecules in solution, thereby allowing the observation of conformational heterogeneity and dynamic behaviour under conditions that more closely resemble the native environment. This makes NMR particularly valuable for studying proteins whose function is closely linked not only to their three-dimensional structure but also to their intrinsic motions across multiple timescales[77, 78, 79].

Since the central objective of this thesis is to elucidate protein dynamics and, consequently, the mechanistic basis of dynamic allostery, NMR serves as the principal experimental technique for characterizing the conformational ensembles populated by the proteins under investigation across various timescales. Through its ability to detect subtle changes in chemical environment, structural flexibility, and exchange between distinct conformational states, NMR provides critical insight into how proteins sample functionally relevant substates rather than existing as a single rigid structure. In this way, it enables a more complete understanding of how dynamic processes contribute to allosteric communication.

Quantum Mechanics of Nuclear Spin Systems

As compared to optical spectroscopic techniques, NMR spectroscopy does not involve transitions driven by visible or ultraviolet light. Instead, it relies on the interaction of nuclear magnetic moments with an applied external magnetic field, B_0. For a nucleus to be observable by NMR, it must possess a non-zero nuclear spin quantum number, I; examples include ^{1}H, ^{13}C, and ^{15}N, all of which have $I = 1/2$. In an external magnetic field, a nucleus with spin I can adopt $2I + 1$ allowed spin states, described by the magnetic quantum number m, which takes values from $-I$ to $+I$ in integer steps. Therefore, for spin-1/2 nuclei, two energy levels are possible,

with m = −1/2 and m = +1/2. The nuclear spin angular momentum is a vector quantity (**Fig. 1.5**), and its magnitude is given by:

$$|\mathbf{I}| = \hbar[I(I+1)]^{1/2}$$

[eq.10]

where *I* is the nuclear spin quantum number and $\hbar$ is the reduced Planck constant. According to quantum mechanics, the magnitude of the total spin angular momentum and one of its Cartesian components can be specified simultaneously. Conventionally, this component is taken along the z-axis, parallel to the external magnetic field B_0, and is given by:

$$I_z = \hbar m$$

[eq.11]

where m is the magnetic quantum number. Nuclei with non-zero spin angular momentum possess a nuclear magnetic moment, μ, which is proportional to the nuclear spin angular momentum:

$$\boldsymbol{\mu} = \gamma \mathbf{I},$$

The z-component of the magnetic moment is therefore:

$$\mu_z = \gamma I_z = \gamma \hbar m$$

[eq.12]

in which the gyromagnetic ratio (γ), is a characteristic constant for a particular nucleus. As discussed earlier, since angular momentum is quantized, the nuclear magnetic moment becomes a quantized property too. The magnitude of γ thus is an important feature as it determines the receptivity of the nucleus in NMR spectroscopy.

NMR-active isotopes of the fundamental constituents of biological systems like hydrogen, carbon, nitrogen and phosphorus exist, which makes it possible to analyse signals from biopolymers via biosynthetic labelling strategies.

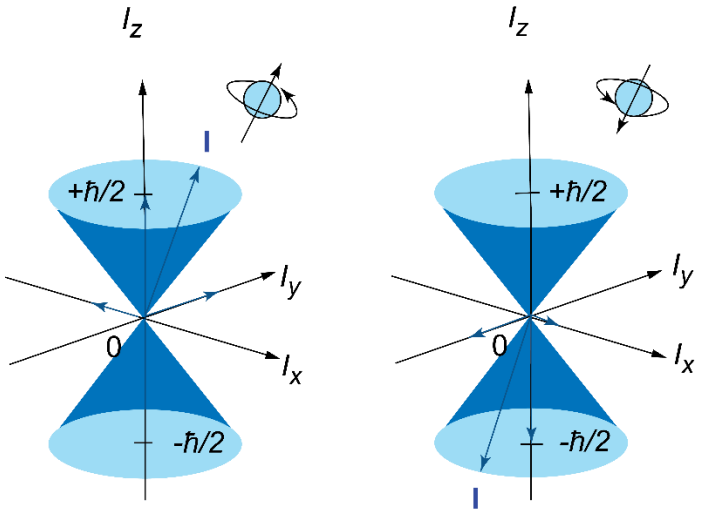

Fig. 1.5. Angular momentum I of the spin -$\frac{1}{2}$ along with its Z-component, rotating about an external magnetic field.

In the absence of any magnetic field, nuclear magnetic moments are randomly oriented and no net magnetization is observed. However, when an external magnetic field is applied, along the laboratory z-axis, the allowed projection of the nuclear magnetic moment becomes quantized. For spin-1/2 nuclei with a positive gyromagnetic ratio, two Zeeman energy levels are formed: the α state, with m = +1/2, is lower in energy and corresponds to the magnetic moment aligned parallel to B_0, whereas the β state, with m = −1/2, is higher in energy and corresponds to the magnetic moment aligned antiparallel to B_0.

The energy of a nuclear magnetic moment in an external magnetic field is given by:

$$E = -\boldsymbol{\mu} \cdot \mathbf{B}$$

[eq.13]

where **μ** is the nuclear magnetic moment vector and **B** is the magnetic field vector. Since, by convention for NMR, the static magnetic field is along the z-axis of the laboratory coordinate systems, the equation reduced to :

$$E_m = -\gamma I_z B_0 = -m\hbar\gamma B_0$$

[eq.14]

in which B_0 is the static magnetic field strength.

Bloch considered a simple, semiclassical vector model, due to the absence of nuances in the classical model, describing the behaviour of a non-interacting -1/2 nuclei in a static magnetic field. In this model, a magnetic moment **μ** in an external magnetic

field **B** experiences a torque, causing it to precess around the field direction. The torque is equal to the time derivative of the spin angular momentum **J**:

$$\frac{d\mathbf{J}(t)}{dt} = \boldsymbol{\mu}(t) \times \mathbf{B}(t)$$

[eq.15]

Since the magnetic moment is related to angular momentum by $\boldsymbol{\mu} = \gamma\mathbf{J}$, the corresponding precessional motion of the bulk magnetization **M**(t) is described by:

$$\frac{d\mathbf{M}(t)}{dt} = \gamma\mathbf{M}(t) \times \mathbf{B}(t)$$

[eq.16]

Due to Zeeman splitting on the spin-half nuclei in an external magnetic field, there would be two levels of energy:

$$E_\alpha = -\frac{1}{2}\hbar\gamma B_0 \;;\; E_\beta = +\frac{1}{2}\hbar\gamma B_0$$

[eq.17]

The energy difference between the two states is computed as :

$$\Delta E = E_\beta - E_\alpha = \hbar\gamma B_0$$

[eq.18]

And using the relationship, $E = \hbar\omega$, we establish the Larmor equation:

$$\omega = \gamma B_0, \nu = \frac{\omega}{2\pi} = \frac{\gamma B_0}{2\pi}$$

[eq.19]

In units s^{-1} and Hertz respectively.

The population differences between the two energy levels are small and can be calculated by Boltzmann relationship:

$$\frac{N_\alpha}{N_\beta} = e^{\frac{-\gamma\hbar B}{kT}} \approx 1 - \frac{\gamma\hbar B}{kT}$$

[eq.20]

Chemical Shift

The actual magnetic field at the nucleus is attenuated or deshielded by the electrons, giving a modified magnetic field, which is ultimately known as chemical shift:

$$B = (1 - \sigma)B_o$$

$$\Delta E = -\hbar\gamma(1 - \sigma)B_0$$

[eq.21]

It is thus evident that different nuclei differ in their local environment and hence the observed resonance frequencies are different. The motions of electrons induced by the external magnetic field give rise to secondary magnetic fields. This chemical shift also depends on the orientation of the molecule with respect to B_0 and can be represented in 3x3 matrix in the principal axis system.

$$\sigma = \begin{bmatrix} \sigma_{xx} & \sigma_{xy} & \sigma_{xz} \\ \sigma_{yx} & \sigma_{yy} & \sigma_{yz} \\ \sigma_{zx} & \sigma_{zy} & \sigma_{zz} \end{bmatrix}$$

[eq.22]

The diagonal represents the isotropic shielding constant, represented as :

$$\sigma_{iso} = \sigma = \frac{1}{3}(\sigma_{xx} + \sigma_{yy} + \sigma_{zz})$$

[eq.23]

With the chemical shift anisotropy (CSA) defined as :

$$\sigma_{CSA} = \Delta\sigma = \frac{1}{2}\Big(\sigma_{zz} - \big(\sigma_{yy} + \sigma_{xx}\big)\Big),$$

[eq.24]

And the asymmetry tensor regarded as :

$$\eta = \frac{3(\sigma_{yy} - \sigma_{xx})}{2\Delta\sigma}$$

[eq.25]

In solution, due to collisions, rapid reorientations within the molecule average the CSA out throughout the experimental timescale.

The unit for chemical shifts is parts per million (ppm) relative to a reference resonance signal; in usual cases tetramethyl silane (TMS) or 2,2-dimethyl-1-2-silapentane-5-sulfonate (DSS) are used. The calculation from the reference can be performed as:

$$\delta = \frac{\omega - \omega_{ref}}{\omega_0} \times 10^6 ppm$$

[eq.26]

Spin Interactions

The dynamics of the spin systems can only be explained by their interactions with each other. In the language of quantum mechanics, evolution of a system is dictated by the Schrodinger equation that involves motion of all the nuclei and the electrons, the Hamiltonian operator ($\hat{H}$), denotes the interactions between them, and the wavefunction ψ(t) encodes the positional, velocity and spin state information.

$$\frac{\partial \psi(t)}{\partial t} = -\frac{i}{\hbar}\hat{H}\,\psi(t)$$

[eq.27]

The Hamiltonian Ĥ is the energy operator of the spin systems. Nuclear spin dynamics is described using the Cartesian spin operators $\hat{I}_x$, $\hat{I}_y$and $\hat{I}_z$, the components of the spin angular momentum along the respective axes. The transverse operators are described as in-phase magnetization, whereas $\hat{I}_z$ describe longitudinal magnetization.The Hamiltonian for a single spin -1/2 nucleus in presence of a strong static magnetic field, describing the Zeeman interaction, is given by:

$$\hat{H}_z = -\gamma B_0 \hat{I}_z$$

[eq.28]

Along with $\hat{H}_z$ the chemical shift Hamiltonian $\hat{H}_{CS}$, magnetic susceptibility and RF fields, define the spin field interactions. The spin-spin interactions include J-coupling and dipolar coupling. All these interactions, the spin-spin and spin-field, are described by their respective Hamiltonian, and the complete NMR Hamiltonian is as follows:

$$\hat{H} = \hat{H}_z + \hat{H}_{CS} + \hat{H}_J + \hat{H}_{DD}$$

[eq.29]

J-coupling or scalar coupling, a fundamental spin-spin interaction, originates from the indirect bond communication between two nuclear spins, **I** and **S**, propagated through polarization of bonding electrons. In the presence of the external magnetic field B_0, a nuclear magnetic moment perturbs the surrounding bonding electron density, leading to spin polarization that can be transmitted to neighboring nuclei through covalent bonds. This interaction arises primarily from the Fermi contact mechanism, in which electron spin density at the nucleus mediates coupling between nuclear spins. Scalar, or J, coupling is therefore a through-bond interaction. The J-coupling for two coupled spins is:

$$\hat{H}_J = 2\pi J(\mathbf{I} \cdot \mathbf{S}) = 2\pi J(\hat{I}_x\hat{S}_x + \hat{I}_y\hat{S}_y + \hat{I}_z\hat{S}_z)$$

[eq.30]

Where J is the scalar coupling constant. In the high-field, weak-coupling limit relevant to most solution-state NMR experiments, this expression can be simplified using the secular approximation. In this treatment, only the term that commutes with the dominant Zeeman Hamiltonian is retained, while the transverse terms $\hat{I}_x\hat{S}_x$and $\hat{I}_y\hat{S}_y$ are neglected because they average out under rapid precession about the external magnetic field. The scalar coupling Hamiltonian therefore reduces to:

$$\hat{H}_J^{secular} = 2\pi J\hat{I}_z\hat{S}_z$$

[eq.31]

Although J-coupling depends on molecular orientation, in liquids it is averaged out by molecular tumbling.

The secular form of the scalar coupling Hamiltonian provides the basis for the splitting of NMR resonances into multiplets. In a coupled spin system, the magnetic state of one nucleus influences the local magnetic environment experienced by its coupling partner, leading to a splitting of the resonance into multiple components separated by the coupling constant J. For two weakly coupled spin-$\frac{1}{2}$ nuclei, this interaction gives rise to the familiar doublet structure. More generally, scalar coupling encodes through-bond connectivity and therefore provides important structural information in NMR spectroscopy.

In addition to generating multiplet structure, scalar coupling can be used as a mechanism for controlled magnetization transfer between coupled nuclei. This principle is used in INEPT-based pulse sequences, where appropriately timed delays allow magnetization transfer through J-coupling between two spin species, such as ^{1}H and ^{15}N or ^{1}H and ^{13}C. INEPT-based transfer (**Fig. 1.6**) therefore constitutes a fundamental element of modern biomolecular NMR experiments, particularly in heteronuclear correlation and backbone assignment strategies.

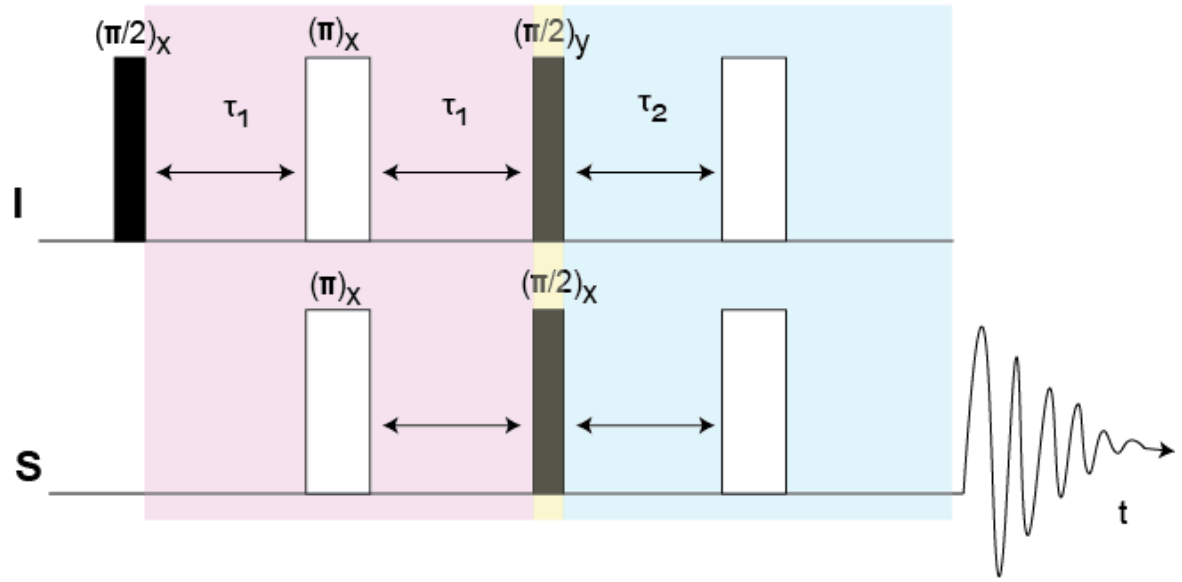

Fig. 1.6. Schematic representation of an INEPT-based magnetization transfer between two scalar-coupled spin species.

Dipolar coupling is an interaction originating from the direct through-space interaction between the nuclear spins I and S, without the involvement of the electron cloud, separated by an internuclear vector **r**. Every nuclear spin generates its own local magnetic field that interferes with the magnetic moment of the nearby nuclei. The dipolar Hamiltonian is expressed as:

$$\widehat{H}_{DD} = -\frac{\mu_0 \hbar \gamma_I \gamma_S}{4\pi r^3}[3(\hat{\mathbf{I}} \cdot \hat{\mathbf{r}})(\hat{\mathbf{S}} \cdot \hat{\mathbf{r}}) - (\hat{\mathbf{I}} \cdot \hat{\mathbf{S}})$$

$$= -\frac{\mu_0 \hbar \gamma_I \gamma_S}{4\pi r^3}\left(\frac{3cos^2\theta - 1}{2}\right)[\widehat{2I_z}\hat{S}_z - (\hat{I}_y\hat{S}_y + \hat{I}_x\hat{S}_x)$$

[eq.32]

where $\mu_0$denotes the magnetic permeability of free space, $\hbar$ the reduced Planck constant, and $\gamma_I$and γ_S the gyromagnetic ratios of the interacting nuclei.

Here, $r = |\,\mathbf{r}\,|$ is the internuclear distance and $\hat{\mathbf{r}} = \mathbf{r}/r$ is the unit vector defining the internuclear axis. The operators $\hat{\mathbf{I}}$ and $\hat{\mathbf{S}}$ denote the spin angular momentum operators of two different nuclei involved in a heteronuclear dipole–dipole interaction. Upon expansion of the dipolar Hamiltonian, the $\hat{I}_z\hat{S}_z$ term constitutes the longitudinal component, whereas the remaining terms containing transverse spin operators form the transverse contribution. Similar to the scalar coupling, transverse terms that oscillate at higher frequencies are removed by secular approximation that transforms the equation into:

$$\widehat{H}_j^{secular} = -\frac{\mu_0 \hbar \gamma_I \gamma_S}{4\pi r^3}\left(\frac{3cos^2\theta - 1}{2}\right)\hat{I}_z\hat{S}_z$$

[eq.33]

Relaxation and Timescales of Molecular Motion

When a system is perturbed from equilibrium, thermodynamics dictates that it will relax back to its equilibrium state over time[80, 81, 82]. In NMR, this principle is reflected in the behavior of nuclear magnetization in an external magnetic field B_0. At equilibrium, the bulk magnetization is aligned predominantly along the z-axis. Application of an RF pulse rotates this magnetization toward the transverse plane, reducing its longitudinal component and creating transverse magnetization. Following the pulse, the transverse magnetization precesses about the static magnetic field while the system relaxes back toward equilibrium. The return of the longitudinal magnetization to its equilibrium value is described as longitudinal relaxation (T_1), whereas the loss of transverse magnetization is described as transverse relaxation (T_2).

Bloch equations defining Relaxation ;

Using Bloch's theory of relaxation, the rate of longitudinal relaxation can be characterized by first-order kinetic process:

$$\frac{dM_z}{dt} = R_1[M_0 - M_z(t)]$$

$$\Rightarrow M_z(t) = M_0 - [M_0 - M_z(0)]e^{-R_1 t},$$

[eq.34]

where R_1 is the longitudinal relaxation rate constant $(R_1 = \frac{1}{T_1})$ First order rate expression is also used to define the transverse relaxation:

$$\frac{dM_x(t)}{dt} = -R_2 M_x(t) \Rightarrow M_x(t) = M_x(0)e^{-R_2 t},$$

$$\frac{dM_y(t)}{dt} = -R_2 M_y(t) \Rightarrow M_y(t) = M_y(0)e^{-R_2 t},$$

[eq.35]

where R_2 is the transverse relaxation rate constant $(R_2 = \frac{1}{T_2})$; $M_x(0)$ and $M_y(0)$ being the values of transverse magnetisation at $t = 0$

Redfield's relaxation theory:

Before 1966, most chemical applications of NMR were carried out using continuous-wave spectrometers, which detected the steady-state transverse magnetization as a function of the applied static magnetic field. The central role of the Bloch equations in NMR theory diminished with the emergence of Fourier transform (FT) NMR, which gradually replaced the continuous-wave approach. In addition, the Bloch equations are phenomenological in nature: they describe relaxation behavior effectively, but do not provide a microscopic explanation or derivation of the underlying relaxation mechanisms.

Redfield postulated a semi-classical theory that the relaxation in the sample originates from the local fluctuations in the magnetic field[83, 84], the strength of which is determined by how the fluctuations correlate in time where the full Hamiltonian system in the laboratory frame is determined as ;

$$\hat{H}(t) = \hat{H}_0(t) + \hat{H}_1(t),$$

[eq.36]

where $\hat{H}_0(t)$ is the deterministic Hamiltonian that consists of a static part defining the Zeeman and isotropic interactions along with a time-dependent radio frequency irradiation of spins, and $\hat{H}_1(t)$ is the stochastic one, which includes the time-dependent stochastic processes which are the source of relaxation. The evolution of the spin system is then described using the density operator formalism and the Liouville–von Neumann equation. To simplify the treatment, the problem is transformed into the interaction frame, which removes the dominant Larmor precession and isolates the effect of the fluctuating perturbation. Within this framework, the time evolution of the density operator is expanded to second order using perturbation theory. The first-order contribution is neglected because, for an ensemble of randomly fluctuating local fields, it averages to zero over time. The treatment then assumes the weak-collision or fast-fluctuation limit, in which the density operator evolves slowly relative to the stochastic perturbations. Under these assumptions, the relaxation process can be expressed in terms of the Redfield relaxation superoperator. Rewriting the interaction Hamiltonian in spherical tensor form allows the fluctuating terms to be connected directly to time-correlation functions $G(t)$, whose Fourier transforms define the spectral density function $J(\omega)$. This spectral density describes how strongly molecular motions at a given frequency contribute to transitions between Zeeman energy levels, and thereby determines the observed longitudinal and transverse relaxation rates. From the correlation function where τ_c is the correlation time,

$$G(t) = \frac{1}{5} e^{-\frac{t}{\tau_c}}$$

[eq.37]

the spectral density function is given by:

$$J(\omega) = \frac{2}{5} \frac{\tau_c}{(1 + \omega^2 \tau_c^2)}$$

[eq.38]

where τ_c is the rotational correlation time and ω is the angular frequency. For a fixed correlation time, the spectral density is largest at zero frequency and decreases as the frequency increases. However, for a given non-zero frequency ω, the contribution $J(\omega)$ is most efficient when the molecular motion occurs on a comparable timescale to the spin transition, approximately when $\omega\tau_c \approx 1$. Thus, two limiting motional regimes can be distinguished: the fast-motion regime, where $\omega\tau_c \ll 1$, and the slow-motion regime, where $\omega\tau_c \gg 1$. For the fast motion regime, the function is written as:

$$J(\omega_0) = \frac{2}{5} \tau_c = J(0),$$

[eq.39]

And for the slow regime:

$$J(\omega_0) = \frac{2}{5} \frac{\tau_c}{\omega^2 \tau_c^2}$$

[eq.40]

Fast-timescale motions (T_1, T_2, hetNOE):

In the fast-motion regime in which many biological phenomena take place like dynamic allostery, bond vibrations and, where $\omega\tau_c \ll 1$, molecular reorientation occurs much more rapidly than spin precession and the spectral density function becomes nearly frequency-independent over the relevant frequencies. Under these conditions, ^{15}N longitudinal and transverse relaxation rates, together with the steady-state heteronuclear NOE, primarily report on picosecond-to-nanosecond motions of the N–H bond vector. The longitudinal and transverse relaxation processes are described by the relaxation rate constants R_1 and R_2. Using the common notation in

which $d = \frac{\mu_0}{4\pi}\frac{\gamma_H \gamma_N \hbar}{r_{NH}^3}$; and $c = \frac{\omega_N \Delta\sigma}{\sqrt{3}}$ denote the dipolar and CSA interaction constants, respectively, the rate expressions are

$$R_1 = \frac{d^2}{4}[J(\omega_H - \omega_N) + 3J(\omega_N) + 6J(\omega_H + \omega_N)] + c^2 J(\omega_N)$$

[eq.41]

$$R_2 = \frac{d^2}{8}[4J(0) + J(\omega_H - \omega_N) + 3J(\omega_N) + 6J(\omega_H) + 6J(\omega_H + \omega_N)] + \frac{c^2}{6}[4J(0) + 3J(\omega_N)] + R_{\text{ex}}$$

[eq.42]

Here, R_{ex} represents an additional exchange contribution to transverse relaxation when motions on slower timescales are present.

For a heteronuclear ^{15}N-^{1}H spin pair, the relaxation rates can be expressed in terms of the spectral density sampled at different angular frequencies. The Nuclear Overhauser Effect (NOE) arises from dipole-dipole cross-relaxation and reflects the transfer of nuclear spin polarization between nearby dipolar-coupled nuclei. In steady-state heteronuclear NOE experiments, continuous irradiation of the proton resonance perturbs the proton spin-state populations away from thermal equilibrium. Through dipolar relaxation pathways, this perturbation is transferred to the attached heteronucleus, altering its signal intensity. The NOE is mediated by zero-quantum and double-quantum relaxation pathways, whose relative efficiencies depend on the molecular tumbling rate and therefore on the spectral density function.

The steady-state heteronuclear NOE may be written as

$$\text{hetNOE} = 1 + \frac{d^2}{4R_1}\frac{\gamma_H}{\gamma_N}[6J(\omega_H + \omega_N) - J(\omega_H - \omega_N)]$$

[eq.43]

Together, R_1, R_2, and heteronuclear NOE provide complementary information on fast internal dynamics because they depend on spectral density values at different frequencies. In folded proteins, rigid backbone amides typically exhibit higher reported heteronuclear NOE ratios, whereas flexible regions with enhanced picosecond-to-nanosecond motion show reduced or negative reported heteronuclear NOE ratios and altered relaxation rates.

Slow-timescale motions (CPMG Relaxation Dispersion)

Major biological processes like breathing of binding pockets, transient structural rearrangements, and exchange between ground and excited states are of particular importance in dynamic allostery, where functional regulation may arise not from a single static conformational change, but from redistribution within a conformational ensemble occur in this time regime (µs-ms). Residues exhibiting significant dispersion therefore identify sites involved in exchange processes that may contribute to long-range communication and regulation. Motions on the microsecond-to-millisecond timescale are commonly assessed using Carr–Purcell–Meiboom–Gill (CPMG) relaxation dispersion experiments, which probe conformational exchange contributions to transverse relaxation[85, 86, 87, 88]. In this regime, nuclei exchange between states with different chemical shifts, leading to additional line broadening. The observed transverse relaxation may therefore be written as

$$R_2 = R_2^0 + R_{\mathrm{ex}}$$

[eq.44]

where R_2^0 is the intrinsic transverse relaxation rate in the absence of exchange and R_{ex} is the exchange-induced contribution. In a two-site exchange process, the interconversion between conformational states A and B is described by the forward and reverse rate constants k_{AB} and k_{BA}, and the overall exchange rate is defined as

$$k_{\mathrm{ex}} = k_{AB} + k_{BA}$$

[eq.45]

with state populations

$$p_A = \frac{k_{BA}}{k_{AB} + k_{BA}}, p_B = \frac{k_{AB}}{k_{AB} + k_{BA}}$$

[eq.46]

such that $p_A + p_B = 1$. The exchange contribution depends on the chemical shift difference between the two states, $\Delta\omega$, their populations, and the exchange rate k_{ex}. In CPMG experiments, a train of refocusing pulses applied at different pulse frequencies partially suppresses exchange broadening, and the resulting effective transverse relaxation rate is measured as

$$R_{2,\mathrm{eff}} = -\frac{1}{T_{\mathrm{relax}}} \ln\left(\frac{I_\nu}{I_0}\right)$$

[eq.47]

where I_ν is the peak intensity measured at a given CPMG pulse frequency ν_{CPMG}, I_0 is the reference intensity, and T_{relax} is the constant relaxation period. If $R_{2,\mathrm{eff}}$ varies as a function of ν_{CPMG}, a relaxation dispersion profile is observed, indicating

conformational exchange on the µs–ms timescale. Fitting these dispersion curves yields k_{ex}, the exchanging populations, and the chemical shift difference between the exchanging states.

Timescales of molecular motion

The functional behaviour of proteins is closely linked to their intrinsic dynamic flexibility. To resolve these motions and to examine the thermodynamic basis of their regulation, complementary NMR experiments (as discussed above in details) are used to probe protein dynamics across different timescales (**Fig.1.7**).

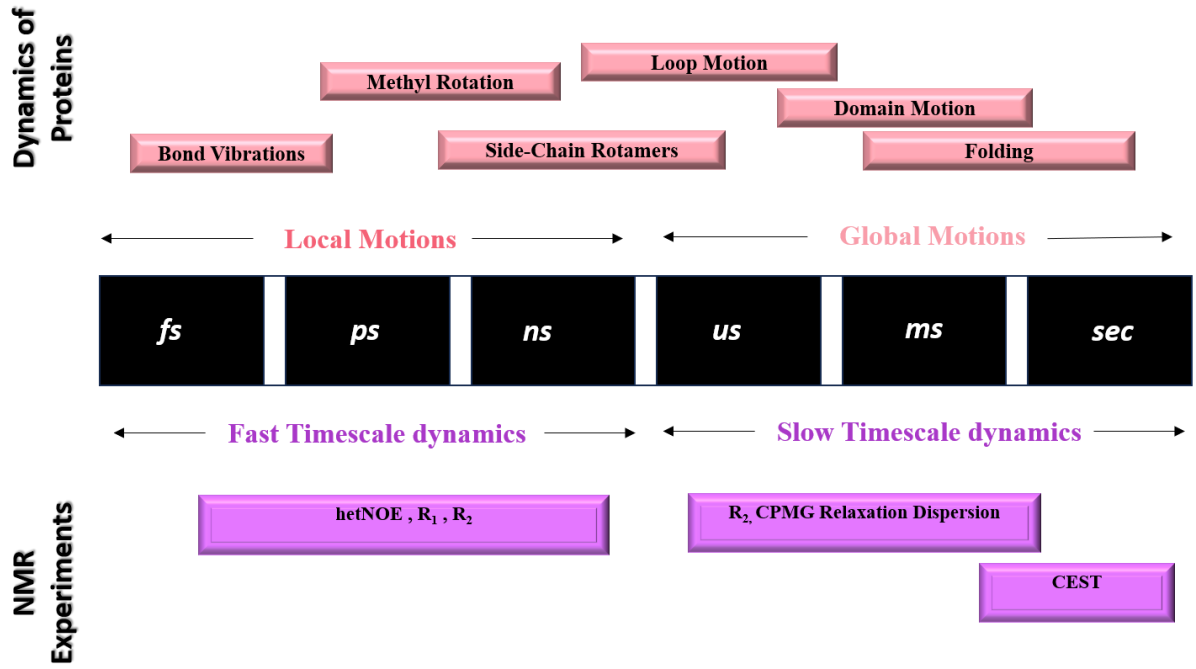

Fig. 1.7 : Schematic figure to elucidate molecular motion at different timescales using NMR experiments.

Solid state NMR

Proteins and other biomolecules are most commonly studied by solution-state NMR, which relies on rapid isotropic molecular tumbling to average anisotropic and interatomic interactions. This averaging is essential for obtaining narrow, well-resolved resonances, but it also imposes practical limitations, particularly for large proteins, oligomeric complexes, and heterogeneous assemblies that tumble slowly or non-uniformly in solution. In such cases, solid-state NMR provides an important complementary approach, as it enables the investigation of systems in which

molecular tumbling is restricted or absent. Because anisotropic interactions are not averaged out under these conditions, solid-state NMR[89, 90] can yield local structural and dynamic information in immobilized or highly ordered samples.

In the present work, solid-state NMR was not used as a general structural method, but in a focused manner in conjunction with hydrogen–deuterium exchange experiments. Here, the protein was examined in the crystalline state, where conformational mobility was reduced relative to solution and rapidly exchanging flexible regions could be stabilized sufficiently for analysis. This made it possible to detect exchangeable and protected regions that were not readily accessible by solution-state NMR alone. In this way, solid-state NMR served as a complementary method to probe solvent exposure, local protection, and conformational stability.

Backbone Resonance assignments

Backbone resonance assignment is essential for residue-specific interpretation of NMR data, as it links individual resonances to defined positions in the protein sequence. In both solution-state and solid-state NMR, this is typically achieved using multidimensional heteronuclear experiments that correlate amide ^{1}H and ^{15}N resonances with backbone carbon chemical shifts. The use of three-dimensional experiments is particularly important because the additional spectral dimension reduces signal overlap and facilitates assignment of individual residues.

In solution-state NMR, backbone assignment is commonly based on triple-resonance experiments that connect the amide ^{1}H and ^{15}N resonances of a given residue to its own $^{13}C_{\alpha}$, $^{13}C_{\beta}$ and carbonyl resonances, as well as to those of adjacent residues. This allows sequential walks along the protein backbone and forms the basis for residue-specific mapping of structural and dynamic observables. In solid-state NMR, analogous assignment strategies are employed, although the magnetization transfer pathways differ because transfer is commonly achieved by cross-polarization rather than INEPT-based coherence transfer. Here, three-dimensional experiments such as hCANH- and hCONH-type correlations provide the corresponding backbone connectivities required for assignment in immobilized samples[91].

1.4 Recombinant Protein Production

To investigate the structure and dynamics of a protein, the availability of highly pure protein is essential. In most cases, such proteins are produced recombinantly. For NMR spectroscopy, isotopically labelled proteins, typically enriched in ^{15}N, ^{13}C, and/or ^{2}H, are required, often at concentrations of approximately 200 μM or higher. Recombinant protein production relies on the introduction of a gene of interest into an expression vector or plasmid, followed by transformation into a suitable host organism (**Fig. 1.8**) . In the case of site-directed mutagenesis, specific mutations are introduced into the parent plasmid by polymerase chain reaction (PCR), after which the template DNA is digested and the mutated plasmid is transformed into *Escherichia coli***.** The resulting construct is then verified, typically by Sanger sequencing, before being used for protein expression.

Because of its rapid growth, well-characterized genetics, and ease of handling, *E. coli* has become one of the most widely used hosts for recombinant protein production. The gene encoding the protein of interest is inserted into an expression vector and introduced into competent cells, which are then selected using the appropriate antibiotic. Protein overexpression is usually induced at a defined cell density, commonly at an optical density (OD_{600}) of 0.6–0.8. In T7 RNA polymerase-based systems under control of the lac operon, isopropyl β-D-1-thiogalactopyranoside (IPTG), a non-metabolizable analogue of allolactose, is commonly used as an inducer. Following expression, the cells are harvested and lysed, and the target protein is purified from other cellular components using one or more chromatographic steps accordingly.

The choice of growth medium is particularly important for isotopic labelling. For labelled protein production, minimal media such as M9 are typically used, supplemented with the required salts, trace elements, vitamins, and isotopically enriched nutrient sources. For the production of deuterated proteins in D_2O-based media, gradual adaptation of the cells is often necessary to maintain robust growth and expression. Thus, the expression strategy, host system, induction conditions, and medium composition together determine the yield, purity, and isotopic enrichment of the final protein sample.

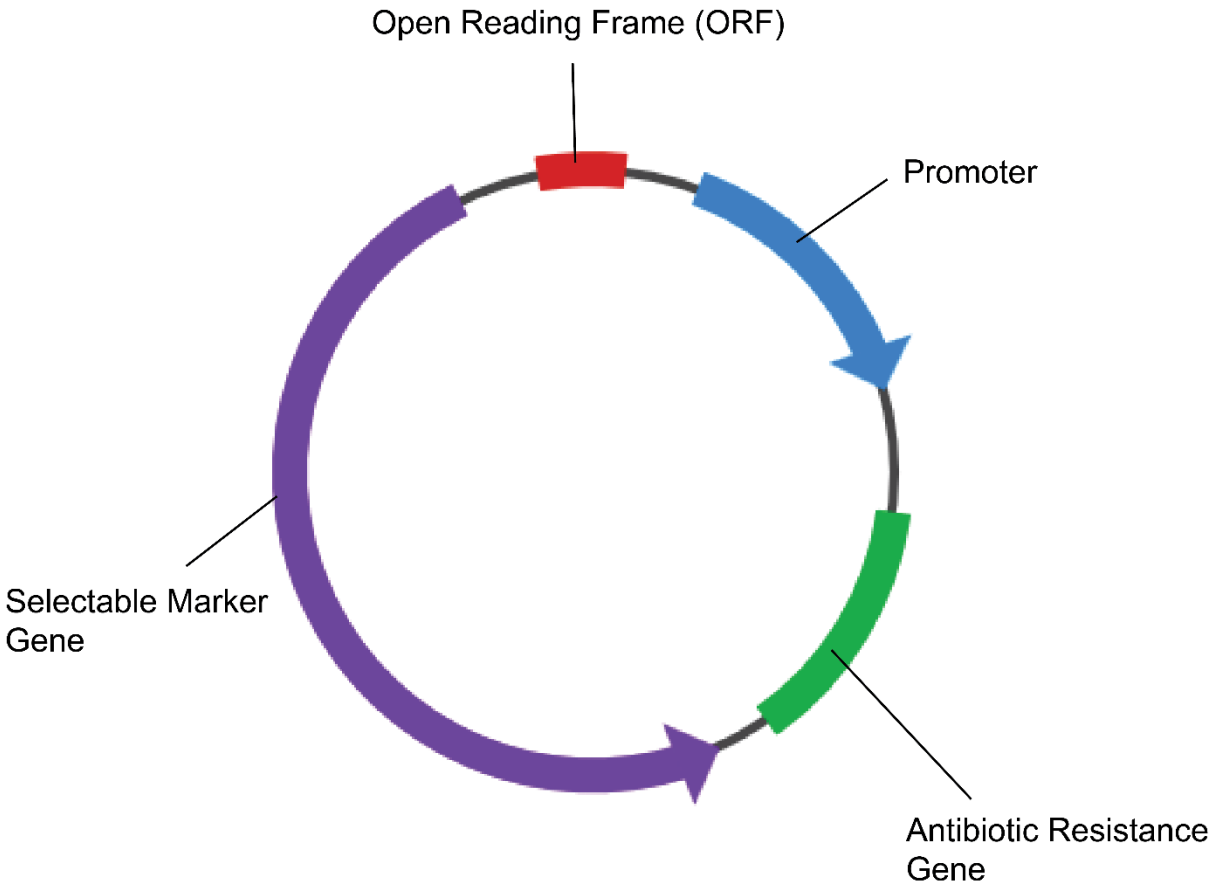

Fig. 1.8. Basic plasmid map portraying different genes required for expression of proteins.

1.5 p38α MAP kinase: biological relevance, inhibition, and structural basis of regulation

The mitogen-activated protein kinase (MAPK) family plays a central role in cellular signal transduction, coordinating responses to a myriad range of extracellular and intracellular cues (**Fig. 1.9**). Within this family, the p38 kinases are particularly important regulators of stress-responsive signalling, and the p38α isoform has attracted considerable interest because of its involvement in inflammation, immune regulation, and cancer-related processes [92, 93]. Unlike classical mitogen-responsive kinases, p38α is primarily activated by environmental and intracellular stress signals, including hyperosmotic stress, oxidative stress, and DNA damage, as well as by physiological stimuli associated with major cellular transitions such as differentiation [94]. Owing to its broad involvement in diverse signalling pathways, dysregulation of p38α has been linked to inflammatory disorders, immune dysfunction, metabolic imbalance, and tumorigenesis, making it an important target for therapeutic intervention[92, 95].

p38 kinases are highly versatile signalling proteins capable of integrating multiple upstream signals and translating them into context-dependent biological responses. Although the individual p38 isoforms share substantial sequence and structural similarity, they differ in tissue distribution, substrate preferences, and sensitivity to chemical inhibition[96, 97]. Activation of p38α most commonly occurs through dual phosphorylation of the conserved *Thr-Gly-Tyr (TGY) motif* in the activation loop by upstream MAPK kinases, particularly MKK3 and MKK6, which themselves are activated by MAP3Ks [98, 99, 100]. In addition to this canonical kinase cascade, p38α can also be activated through non-canonical mechanisms. One such pathway involves binding of TAB1, which promotes p38α autophosphorylation, whereas another, described in T cells, involves phosphorylation at Tyr323 by ZAP70, ultimately leading to autophosphorylation and kinase activation [101, 102, 103, 104, 105]. The exact route of activation also depends on cellular context, with different tissues and signalling environments favoring distinct upstream pathways [98, 99, 100].

Once activated, p38α phosphorylates a broad range of downstream targets, including transcription factors, signalling proteins, and other kinases, thereby influencing

processes such as inflammatory gene expression, cell-cycle regulation, apoptosis, stem-cell behavior, and metabolic adaptation[92, 106, 107]. This central regulatory role initially stimulated extensive efforts to develop p38α inhibitors for inflammatory diseases such as rheumatoid arthritis, chronic obstructive pulmonary disease, and asthma [108, 109]. Early drug discovery campaigns focused primarily on ATP-competitive inhibitors targeting the active site of the kinase in its *DFG-in* conformation. Representative examples include pyridinyl imidazole compounds such as SB203580 and related inhibitors with favorable pharmacokinetic properties [110, 111]. Subsequently, type II inhibitors such as BIRB796, Sorafenib, and Regorafenib were designed to bind a pocket adjacent to the ATP-binding site, stabilizing the DFG-out inactive state and thereby interfering with kinase activation [112, 113, 114].

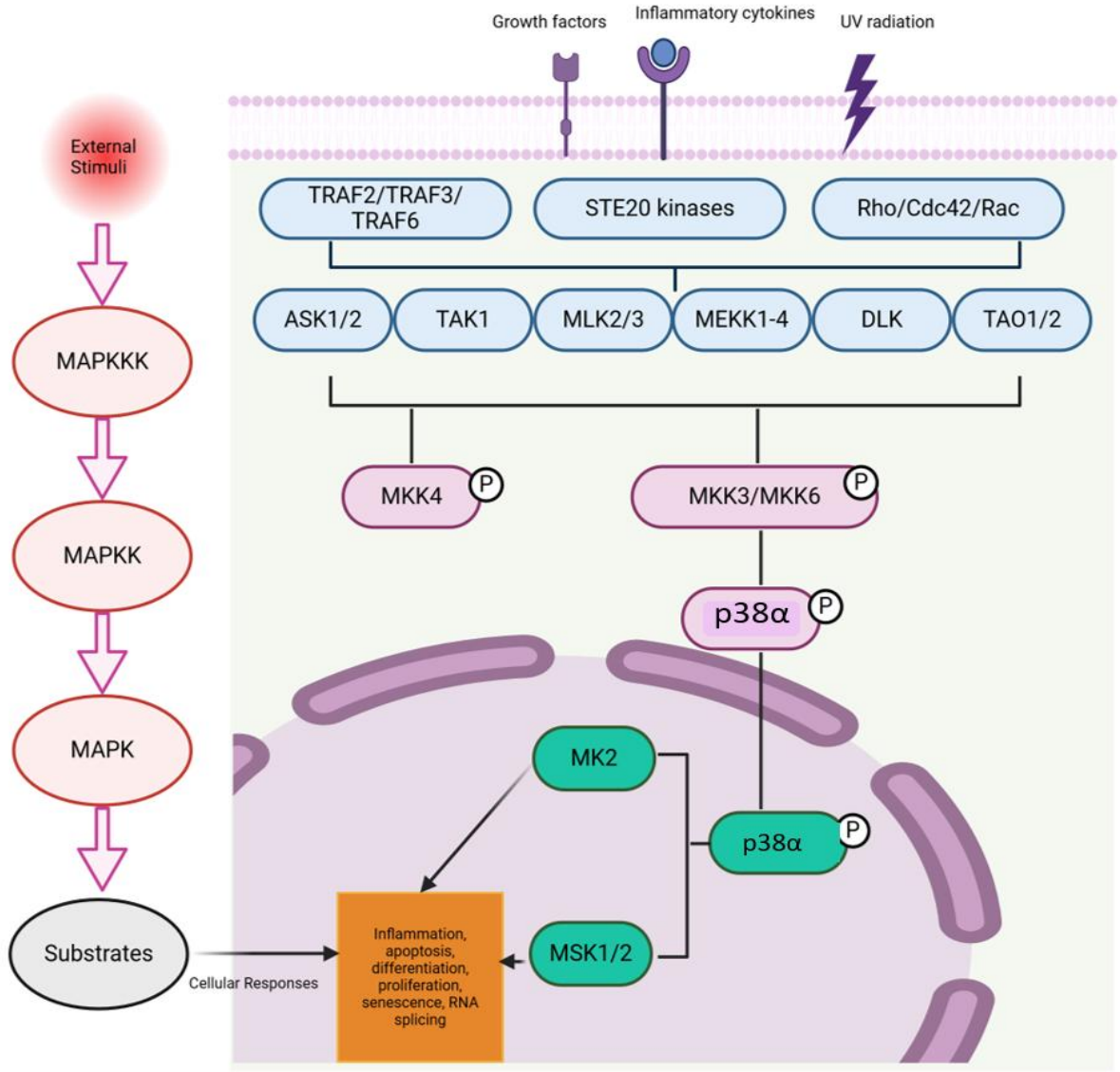

Fig. 1.9: Cellular signalling of the MAP kinase pathway, p38α being the downstream kinase.

Despite their potency, many of these inhibitors have suffered from limited selectivity and dose-limiting toxicity, largely because the ATP-binding cleft and its neighboring structural elements are highly conserved across the kinome[115, 116, 117]. As a result, several compounds originally developed as p38 inhibitors also inhibit multiple other kinases, including members of the Raf family, PDGFR, VEGFR, and c-Kit [118, 119, 120]. Although some type II inhibitors exploit conformational features beyond the canonical ATP pocket, these sites still retain substantial similarity to equivalent regions in related kinases, which restricts the gains in selectivity that can be achieved through ATP-site targeting alone[110, 111, 112, 113, 114, 115, 116, 117]. This limitation has shifted interest toward alternative inhibitory strategies, including the targeting of non-canonical activation routes and the identification of distal allosteric sites that may offer improved specificity [121].

A detailed understanding of p38α structure and dynamics is therefore essential for the rational development of new therapeutic strategies. Like other protein kinases, p38α adopts the conserved bilobal kinase fold, consisting of a smaller N-terminal lobe and a larger C-terminal lobe connected by a flexible hinge region [122, 123, 124, 125]. The N-lobe is composed mainly of β-sheets and contributes to ATP binding, whereas the C-lobe is predominantly α-helical and participates in substrate recognition, catalytic regulation, and effector interactions [123, 124, 125, 126, 127, 128]. The catalytic cleft lies between the two lobes and comprises several highly important structural elements, including the glycine-rich loop, the hinge region, the αC-helix, and the DFG motif within the activation loop. Together, these features define the ATP-binding environment and modulate access to adjacent hydrophobic regions and regulatory pockets[126, 127, 128] (**Fig. 1.10**).

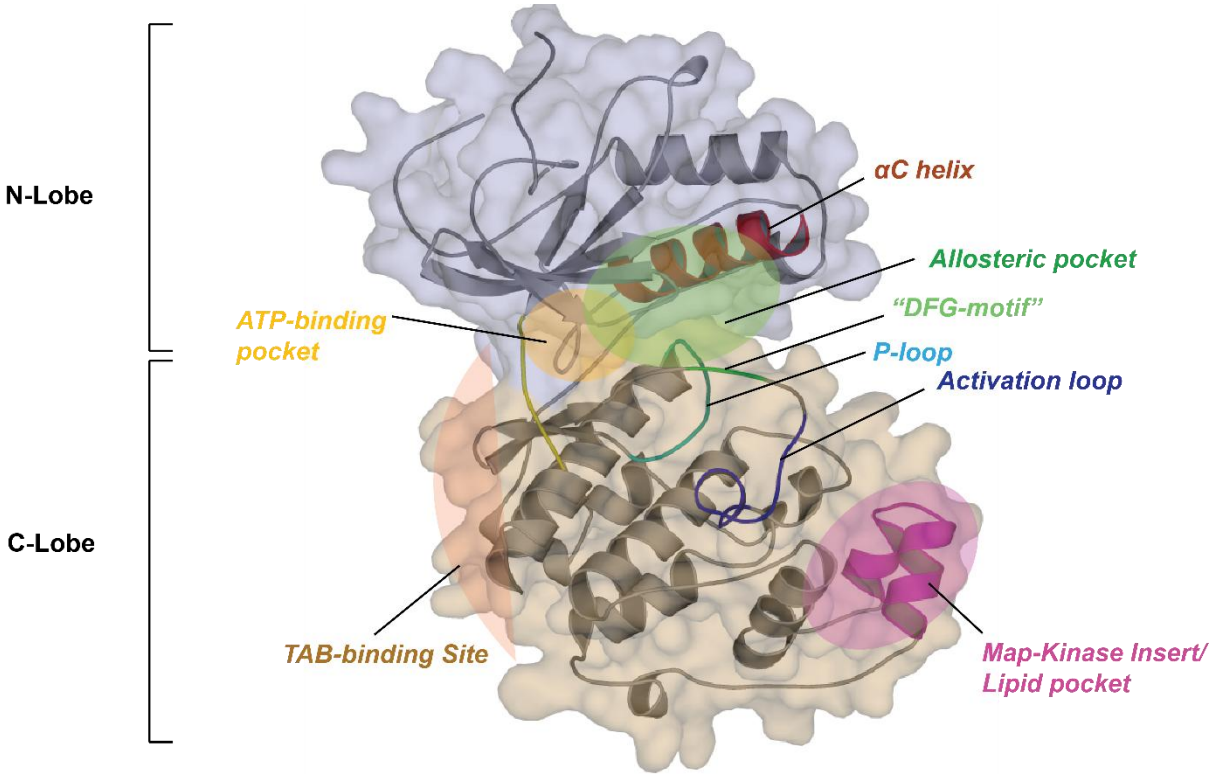

Fig. 1.10. Structural features of p38α.

Beyond the canonical catalytic site, p38α contains several neighboring hydrophobic subregions that have been exploited in inhibitor design. These include hydrophobic regions flanking the ATP-binding site, an allosteric sub pocket associated with the DFG transition[128], and a more distal hydrophobic cavity in the C-lobe often referred to as the lipid pocket or lipid-binding pocket[129, 130, 131, 132]. This latter site has attracted increasing attention because it appears to represent a kinase-specific regulatory feature with potential allosteric relevance. Structural studies have shown that p38α can undergo conformational rearrangements involving both local motif transitions and larger-scale inter-lobe motions. In particular, activation is accompanied by a rigid-body rotation of the N- and C-lobes, typically on the order of several degrees, which enhances catalytic competence and facilitates phosphoryl transfer[133]. In addition, the kinase can adopt different activation-loop conformations, most notably the *DFG-in* and *DFG-out* states. In the DFG-in conformation, the conserved Asp residue is positioned to coordinate Mg^{2+} ions and support ATP binding, whereas in the DFG-out conformation, the phenylalanine side chain is flipped into the active-site region, thereby obstructing catalytically competent ATP binding [134, 135, 136].

These structural transitions are not merely static conformational switches but are part of a broader dynamic ensemble in which communication between distant motifs and domains regulates kinase function. In this sense, p38α is particularly well suited

for analysis in terms of dynamic allostery, where functional regulation arises from correlated motions and coupling between proximal and distal structural elements rather than from a single large structural rearrangement[137, 138, 139, 140]. Increasing evidence suggests that the catalytic site, activation loop, αC-helix, hinge region, and distal lipid-binding domain are dynamically interconnected, forming communication pathways that may be exploited for allosteric regulation[133, 137, 140]. In the present study, these communication pathways were interrogated using dynamical network analysis and complementary computational approaches, with the resulting predictions validated experimentally by solution and solid-state NMR spectroscopy, biophysical assays, and X-ray crystallography. Together, such integrative approaches provide a framework for understanding how long-range dynamic coupling controls p38α function and how this knowledge may guide the discovery of more selective allosteric modulators[141, 142, 143].

2. Research Gap

Despite extensive work on p38α, the mechanistic basis of its dynamic regulation remains incompletely understood. Existing studies have established many important structural, biochemical, and pharmacological features of the kinase, including its activation pathways, catalytic motifs, inhibitor-binding modes, and role in stress and inflammatory signalling. However, these findings do not yet provide a complete explanation of how distant structural regions within p38α are dynamically coupled to regulate activity. This limitation is especially important because p38α, like many kinases, cannot be understood solely in terms of static structural snapshots. Rather, its function appears to depend on an underlying dynamic ensemble in which communication between the N-lobe, C-lobe, activation loop, hinge region, and distal regulatory pockets may collectively determine its conformational preferences and functional output. A clear residue-level understanding of this long-range coupling is still lacking.

This unresolved problem represents a major gap in the field, particularly from the perspective of therapeutic targeting. Kinases remain challenging drug targets because their catalytic cores and ATP-binding sites are highly conserved, often resulting in poor selectivity and dose-limiting off-target effects. For this reason, a deeper understanding of intramolecular communication and dynamic allostery in p38α is not only of fundamental mechanistic interest, but also of direct relevance to the design of more selective modulators. Although distal regulatory regions, including the lipid-binding domain and associated cryptic pockets, have attracted increasing attention, their precise role within the broader allosteric network of the kinase remains insufficiently defined. In particular, it is still unclear which residues function as key communication nodes, how these nodes connect distant functional regions, and how strongly they influence the global dynamic architecture of the protein.

The present study addresses this gap through an integrated structural-biology strategy aimed at defining the intrinsic allosteric network of p38α in quantitative and mechanistic terms. By combining computational and experimental approaches, it seeks to identify dynamically coupled regions, map the network of long-range communication across the kinase, and determine which residues act as central regulators of signal propagation within this network. Rather than focusing

exclusively on large conformational changes, the work examines how dynamic coupling emerges from correlated motions and how these motions link functionally important regions of the protein. In this way, the study moves beyond a purely descriptive account of p38α structure and instead investigates the internal logic by which its dynamics are organized.

Importantly, the work does not stop at computational identification of allosteric pathways. A central objective is to test the biological and structural relevance of the predicted network experimentally, thereby establishing whether the identified residues genuinely contribute to long-range regulation. The study further extends this analysis by perturbing a selected allosteric node through mutation and examining the resulting consequences for solvent dynamics, local stability, and overall structural behavior. This allows the functional importance of a single network element to be assessed within the wider context of the p38α dynamic ensemble. Taken together, the aim is to provide a more complete mechanistic understanding of how p38α is regulated through dynamic allostery and to address questions that have remained insufficiently resolved in earlier studies.

3. Mapping the dynamic allostery of p38α kinase

This section describes the quantification of the p38α dynamic network using an integrative structural-biology approach. The underlying study is currently under revision and is available as an open-access preprint in the journal archive.

3.1 Introduction

The previous section introduced p38α MAP kinase as a central stress-responsive kinase with important roles in inflammation, immune regulation, and cancer-associated signalling. It also described the major structural features of p38α, including the bilobal kinase fold, ATP-binding cleft, activation loop, DFG motif, and distal lipid-binding pocket. The present chapter builds on that background by addressing a more specific question: how are these structural elements dynamically connected within the kinase domain?

Protein kinases are commonly interpreted through changes in static structure, such as transitions between inactive and active conformations or between DFG-in and DFG-out states. Although these structural descriptions are useful, they are insufficient to explain the full regulatory behaviour of p38α. Protein kinase function is strongly coupled to dynamics, with regulatory information distributed across networks of residues rather than being restricted to the catalytic site alone[144, 145]. In this view, kinase regulation emerges from shifts in conformational populations and from changes in the coupling between different regions of the protein.

This concept is central to dynamic allostery. In dynamic allostery, communication between distant sites is mediated not necessarily by large structural rearrangements, but by redistribution of correlated motions across the protein[8]. A perturbation at one site, such as phosphorylation, mutation, ligand binding, or protein interaction, can therefore influence a distant region by changing the internal motional network. For p38α, this is particularly relevant because several functionally important regions are spatially separated but appear to be dynamically linked. These include the activation loop, DFG motif, αC-helix, hinge region, catalytic cleft, inter-lobe interface, and the distal lipid-binding pocket (**Fig. 3.1A**).

Canonical activation of p38α occurs through dual phosphorylation of the Thr-Gly-Tyr motif in the activation loop. However, phosphorylation does not simply switch the kinase from one rigid inactive state into one rigid active state. Enhanced-sampling molecular dynamics simulations showed that phosphorylation, nucleotide binding, and substrate/docking interactions reshape the free-energy landscape of p38α, progressively shifting the conformational ensemble toward active-like states rather than locking the kinase into a single active conformation[146]. This supports an

ensemble-based model in which p38α activity is controlled by population shifts and dynamic coupling between regulatory elements.

The lipid-binding pocket is especially important in this context. Unlike the ATP-binding site, which is highly conserved across the kinome, the lipid pocket is located in a more distal C-lobe region associated with the MAP kinase insert. The pocket was originally identified in crystal structures of p38α bound to n-octyl-β-glucopyranoside, revealing a lipid-binding site formed by the MAP kinase insert[147]. Subsequent studies targeting non-ATP-binding pockets and lipid-pocket-associated regions further supported the idea that distal sites in MAP kinases can influence kinase behaviour and may provide alternative opportunities for allosteric modulation[148, 149]. Structural superimposition of the "DFG-out" p38α complexes bound to Sorafenib alone (PDB 3HEG[150]) and to both Sorafenib and β-OG (PDB 3GCS[151]) reveals a flip of the pyridyl nitrogen and methyl substituent of Sorafenib, despite a separation of more than 30 Å from β-OG bound in the lipid pocket (**Fig. 3.1B).**

Despite this, the residue-level architecture of these communication routes remains incompletely defined. Static structures can reveal where potential regulatory sites are located, but they do not directly explain how dynamic information is transmitted between them. Similarly, global measurements of conformational change provide useful evidence for altered dynamics, but they do not identify which residues act as key mediators of long-range coupling. A central challenge, therefore, is to move from a qualitative description of p38α allostery toward a residue-specific map of its dynamic network (**Fig. 3.1C**).

Molecular dynamics simulations provide a suitable framework for this purpose because they sample correlated motions across the kinase domain over time. When combined with dynamical network analysis, these simulations can be used to represent the protein as a network of interacting residues, where nodes correspond to residues and edges describe the strength of motional coupling between residue pairs. Network analysis based on molecular dynamics trajectories is increasingly used to identify communication pathways and allosteric hotspots in proteins[152]. Dynetan implements generalized-correlation-based dynamical network analysis, using mutual-information-derived correlations to capture both linear and non-linear relationships between residue motions [69].

Computationally predicted networks, however, require experimental validation. NMR spectroscopy is particularly well suited for this task because it provides residue-specific information on both local structure and dynamics in solution. In

MAP kinases, NMR-based approaches have already been used to identify allosteric information flow and communication communities, including in p38γ, where conservative mutations produced long-range chemical-shift perturbations extending across the kinase domain[139]. This supports the use of NMR as a complementary experimental strategy for testing whether predicted communication residues are genuinely involved in kinase allostery.

In this chapter, the intrinsic dynamic network of unphosphorylated apo p38α is mapped using molecular dynamics simulations and dynamical network analysis. Key residues predicted to participate in long-range communication were selected for site-directed mutagenesis, and the effects of these perturbations were examined using NMR spectroscopy and complementary structural and biophysical methods. The aim was to identify residues that connect the activation loop, DFG motif, inter-lobe interface, and lipid-binding region, and to determine whether the lipid pocket is dynamically integrated into the wider regulatory architecture of the kinase.

This analysis reveals that p38α contains an extended dynamic communication network spanning both kinase lobes. Importantly, the network includes not only canonical kinase regulatory elements but also residues associated with the distal lipid-binding pocket. These findings support a model in which p38α regulation is shaped by long-range dynamic coupling across the kinase domain. They also suggest that the lipid pocket should be considered an integral component of the allosteric network rather than an isolated peripheral cavity. By defining this communication architecture at residue-level resolution, this chapter provides a mechanistic basis for understanding p38α dynamic allostery and for exploring distal allosteric sites as potential routes toward more selective kinase modulation.

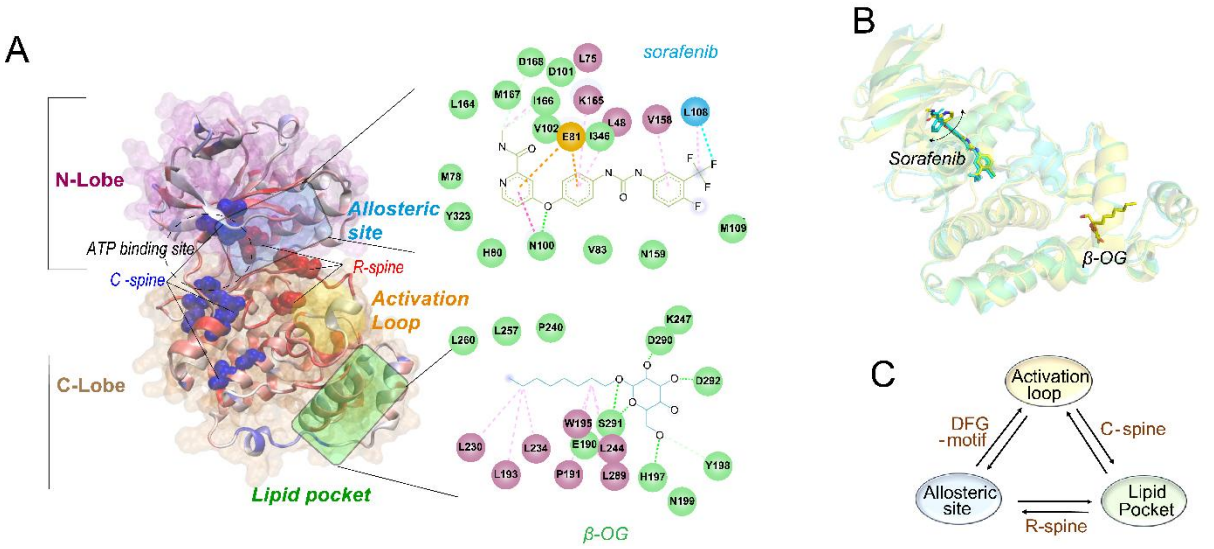

Fig. 3.1 A) Structural representation of p38α kinase, highlighting the interactions of ligands binding to the allosteric pocket (exemplified for sorafenib) and the lipid pocket (shown for β-OG), as produced using Discovery studio. Key structural features such as the activation loop, the catalytic C- spine, and the regulatory R-spine are highlighted. **B**) Observed ring flip of the type-II inhibitor sorafenib between structures in the presence (semi-transparent yellow, PDB 3GCS) or absence (semi-transparent cyan, PDB 3HEG) of a lipid pocket binder (β-OG). **C**) Sketch of the allosteric pathways between the active site, the adjacent, so-called allosteric pocket, and the lipid pocket in question.

3.2 Dynamic network analysis of p38α kinase

Following the workflow summarized in **Fig. 3.2**, this study involved a combination of structural-biology techniques, mainly molecular dynamics simulation and nuclear magnetic resonance, to quantify the allosteric sites of p38α.

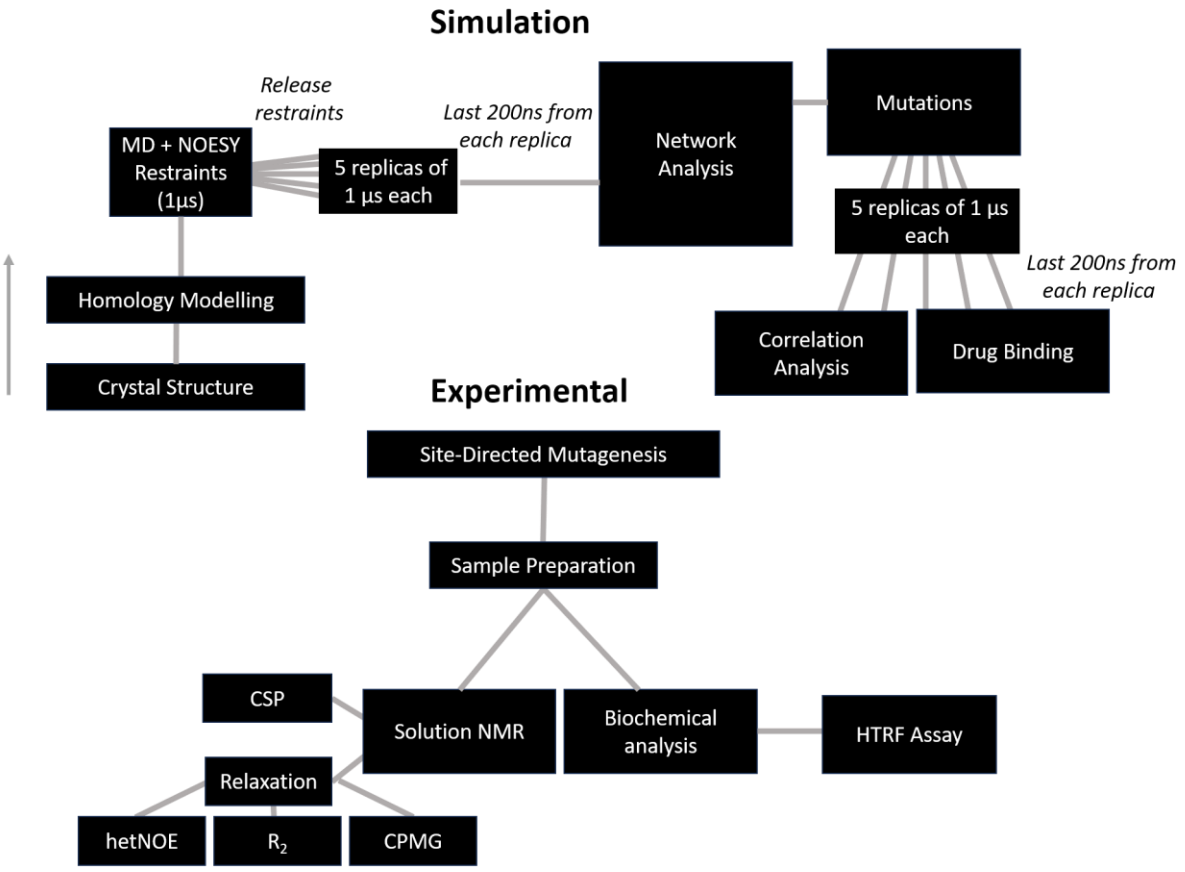

Fig. 3.2 Schematic representation of the methodology to identify the communicators and validate them experimentally and computationally.

Molecular dynamics simulations, along with dynamical network analysis calculations were performed for three unphosphorylated p38α systems: apo p38α, sorafenib-bound p38α, and p38α bound to both sorafenib and β-OG. Simulations were carried out using NAMD 3 with the CHARMM36 force field[34, 59]. The system setup is collectively described in **Table 10.1** (Appendix), with the RMSD and the RMSF values of the trajectory plotted in **Fig. 3.3A** and **Fig. 3.3B** respectively. Dynamical network analysis revealed the change of community structure when the β-OG was in the lipid pocket (**Fig 3.3C**). When the pathway structures were computed from the important locales of the protein, namely the allosteric pocket to activation loop (**Fig. 3.3D**), activation loop to lipid pocket (**Fig 3.3E**) and a direct communication from the allosteric pocket to the lipid pocket (**Fig. 3.3F**), traversing of the pathways were observed, confirming that the occupancy of the lipid pocket indeed changes the dynamic allostery of the protein.

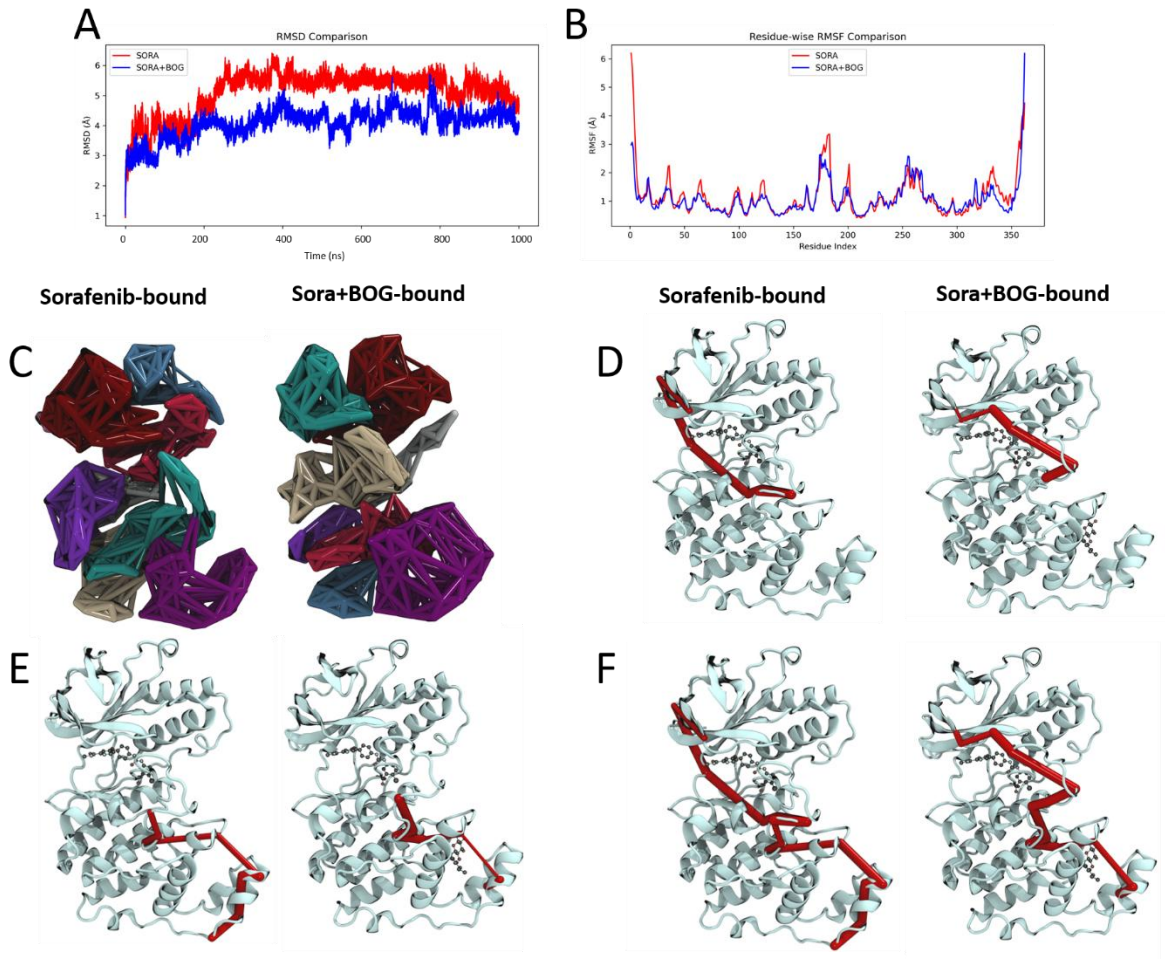

Fig. 3.3 A) RMSD of the simulations using starting crystal structures 3HEG (p38a bound to sorafenib only; red) and 3GCS (Sora + BOG; blue) **B**) RMSF of the simulations using starting crystal structures 3HEG (Sorafenib with p38α; red) and 3GCS (Sora + BOG with p38α ; blue). **C**) Differences in communities when BOG binds to the lipid pocket. **D**) Differences in pathways upon BOG binding from the allosteric pocket to the activation loop. **E**) Differences in pathways upon BOG binding from the lipid pocket to the activation loop. **F**) Differences in pathways upon BOG binding from the lipid pocket directly to the allosteric pocket.

For the apo system, five independent replicas of 1 μs were generated. The root-mean-square deviation over time of the replicas and residue-wise root-mean-square fluctuations are shown in Figs. 3.4A and 3.4B, respectively. The analysis portrayed that not only the loops, but the core helices of p38α, were flexible (Fig.3.4C). For the subsequent network and correlation analyses, the final 200 ns of each replica were concatenated and analysed using Dynetan. The analysis included community detection and quantification of betweenness centrality, allowing the identification of residues with prominent roles in long-range dynamic communication[69, 70].

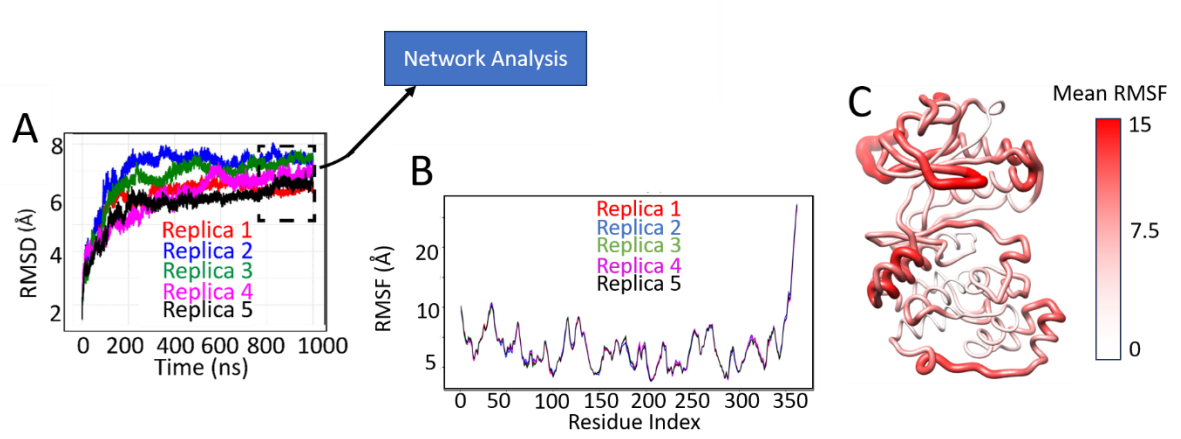

Fig. 3.4: **A**) Backbone RMSD of the apoprotein across five independent 1 μs replicas; the final 200 ns of each replica were used for network analysis. **B**) Overlay of RMSD traces for all five apoprotein replicas, highlighting convergence. **C**) Average per-residue RMSF mapped onto the protein structure to visualize flexibility.

Community detection provides an initial overview of the dynamic organization of the protein by partitioning the residue network into groups that display coherent motions. For the wild-type apo protein, this analysis identified 14 dynamic communities, shown in different colours in **Fig.3.5**. Each community represents a set of residues with stronger internal motional correlations and weaker correlations with residues outside the group. Thus, the communities define regions of coherent dynamical behaviour within the kinase domain.

Despite the approximately 60% sequence identity between p38α and p38γ, and despite the different methodologies used, the communities identified here show notable similarity to the experimentally derived allosteric communities previously reported for p38γ using methyl scanning and chemical-shift perturbation analysis[139]. As in the p38γ study, the N-lobe is divided into distinct regions corresponding to the active-site region, the extended allosteric pocket, and the regulatory and catalytic spine-associated regions. In the present p38α network, these are represented by the magenta, brown, grey, and pink communities, respectively. The C-lobe is divided into several communities, including a green community corresponding to the MAP kinase insert and lipid-binding domain, and a distinct purple community containing the activation loop. This separation is important because it suggests that the lipid-binding domain behaves as a dynamically distinct region rather than simply forming part of the activation-loop community.

Several of these dynamic features also resemble community structures previously identified in protein kinase A using network analysis[144]. In PKA, the N-lobe was partitioned into communities corresponding to the ATP-binding pocket, the αC-

helix region, and the regulatory spine. These regions show qualitative parallels with the active-site, extended allosteric-pocket, and R-spine-associated communities identified here in p38α. Similarly, the C-lobe communities in PKA corresponding to the activation loop, catalytic spine, and substrate-binding region show partial correspondence to the activation-loop, C-spine-associated, and lipid-pocket-associated communities in p38α. However, this comparison should be interpreted cautiously, because p38α contains MAP kinase-specific structural features, including the MAP kinase insert and lipid-binding pocket, that are not directly equivalent to regions in PKA.

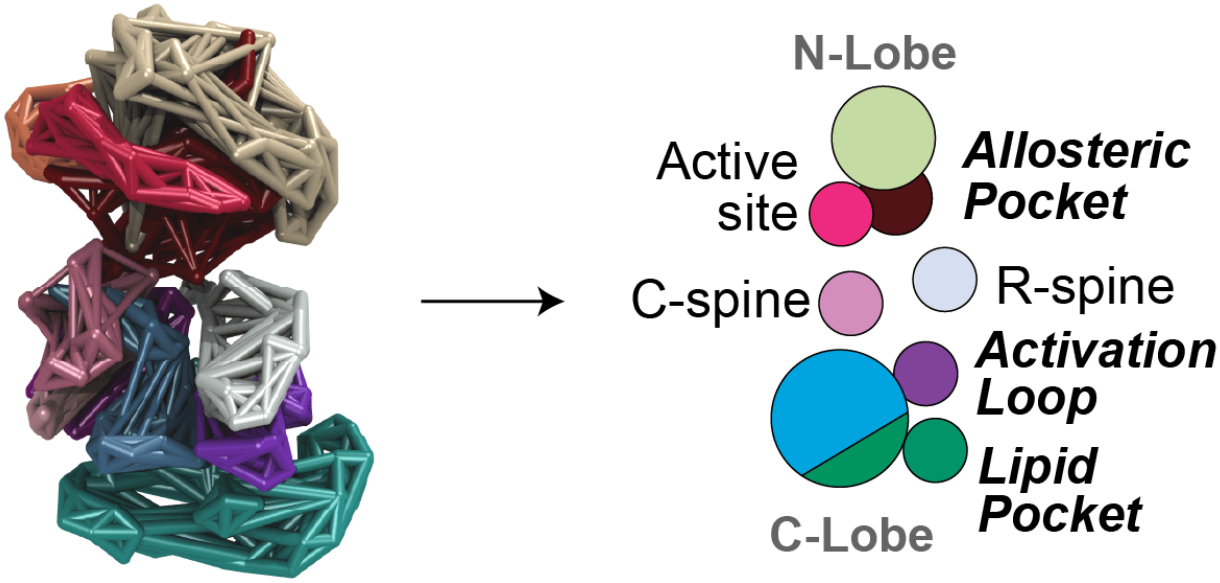

Fig. 3.5 Clustering of the protein into 14 communities, largely reminiscent of the different structural elements of the kinase (right).

To identify residues that may act as communication hubs within the network, betweenness centrality was calculated. Betweenness centrality measures how frequently a residue lies along shortest communication paths between other residues and therefore highlights positions that may contribute disproportionately to long-range information transfer. The results are shown in **Fig. 3.6** and summarized in **Table 10.2** (Appendix). Although direct residue-by-residue comparison with other kinases is limited by sequence and structural differences, several of the high-centrality residues identified here are consistent with previously described allosteric regions in related kinase systems.

One prominent example is D168, the aspartate of the DFG motif. This residue appears as a major motional hotspot in the p38α network. Its central position is consistent with studies of p38γ, where a corresponding node near the DFG motif

was implicated in allosteric communication[139]. Similar observations have also been made in Abl kinase, where the DFG motif contributes to long-range coupling within the kinase domain[153]. In PKA, the neighbouring DFG phenylalanine rather than the aspartate has been emphasized as part of the allosteric communication network[154]. Taken together, these observations suggest that the DFG motif, although not always through the same residue, is a recurrent participant in kinase allostery.

Another high-centrality residue identified in p38α is D150, which belongs to the catalytic HRD motif. This residue is positioned within the conserved catalytic machinery of the kinase. In PKA, the homologous aspartate, D166, has been shown to be critical for preorganizing the substrate phosphoacceptor site for efficient phosphoryl transfer[140]. Homologous catalytic aspartates in other kinases, including Abl and EGFR, also occupy central functional positions [155, 156, 157]. The identification of D150 as a high-centrality node in p38α therefore supports the view that the catalytic loop is not only chemically important for catalysis, but also dynamically integrated into the allosteric communication network.

R49 was also identified as a residue with high betweenness centrality. This residue is located in the extended allosteric pocket of p38α. Unlike the DFG and HRD motifs, this site does not have an obvious universally conserved equivalent with an established allosteric role across other kinases. Its identification therefore appears to reflect a more p38α-specific contribution to the network. This makes R49 particularly interesting, because it may represent a communication node associated with the architecture of the p38α allosteric pocket rather than with the generic kinase catalytic core.

W207 represents another notable high-centrality residue. It is positioned near the substrate-binding groove and faces toward the lipid pocket. In PKA, the homologous W222 has been described as an allosteric hub in the αF/FC region and as a structural keystone stabilizing the C-lobe[126, 145]. Although Abl and EGFR contain hydrophobic residues in related regions, a direct one-to-one analogue is not straightforward to assign. In p38α, the location of W207 is particularly relevant because of its proximity to the lipid pocket, a region previously proposed as a potential site for allosteric modulation[158]. Its high betweenness centrality therefore supports the idea that the lipid pocket is not dynamically isolated, but is connected to the broader allosteric communication network of p38α.

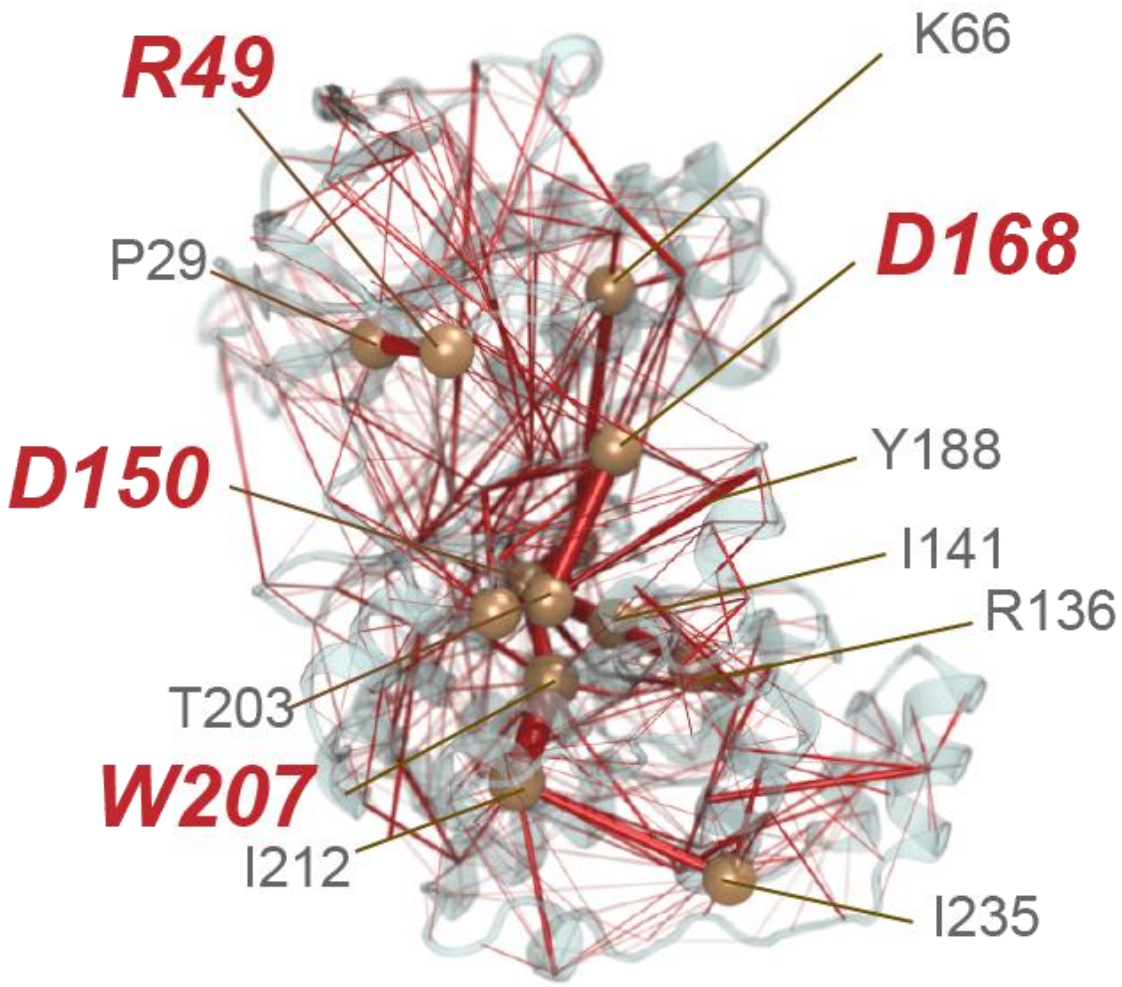

Fig. 3.6 Residues with top betweenness centrality, i.e., the highest degree of information flow traversing them, also highlighting those network sites chosen for mutagenesis studies for network validation (red highlights).

In addition to identifying individual network hotspots, inter-lobe correlations were analysed to examine the broader communication architecture of the kinase. The overall inter-lobe correlation map is shown in **Fig. 3.7** and summarized in **Table 3.2**. As expected, several strong correlations correspond to short-range contacts dictated by the three-dimensional fold of the protein, such as the interaction between R70 and F169. However, longer-range correlations were also observed, including contacts between L104 and L167 and between N102 and K165. These correlations indicate that communication across the two lobes is not limited to local structural packing, but also involves more extended dynamic coupling.

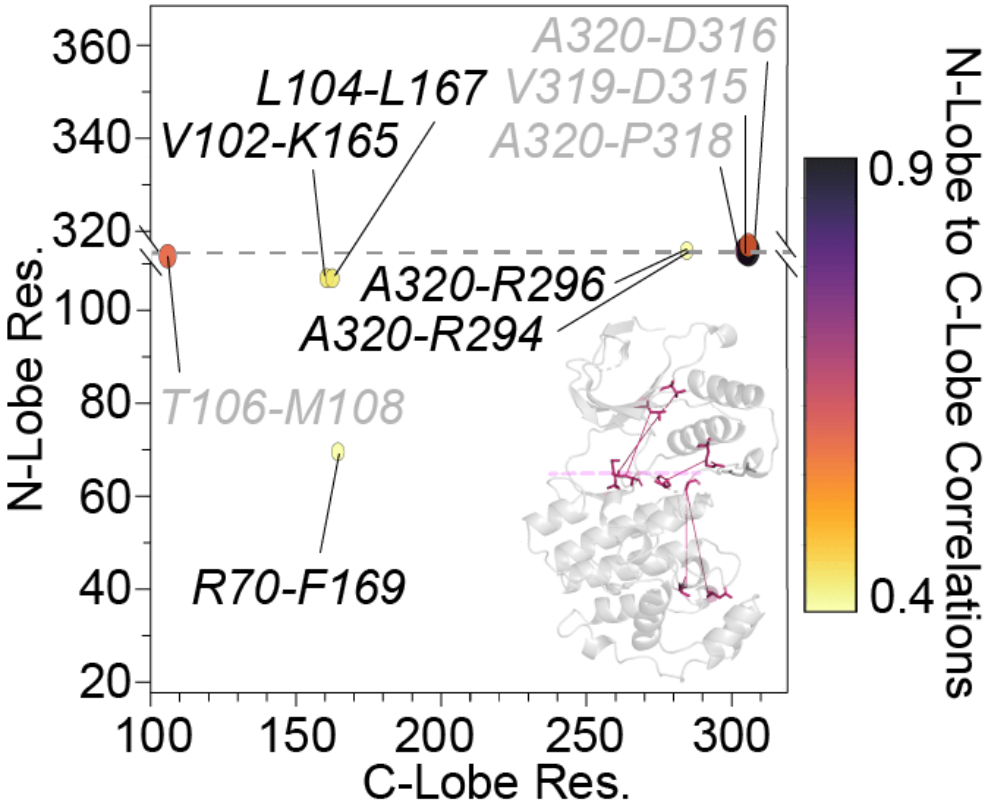

Fig. 3.7 Map of inter-residue dynamic-network correlations, specifically focusing on connections between N- and C-lobe residues. Pairs in black writing denote long-range correlations with a correlation coefficient above 0.3. Note that part of the C-terminal (320-360) lies in the N-Lobe, while the first transition from N- to C-lobe occurs at around residue 107. Correlations involving these covalent linkages are grayed out.

To determine whether the network hotspots identified by the MD-based analysis were already apparent from static crystallographic information, the corresponding residues were examined in terms of crystallographic B-factors derived from apo unphosphorylated p38α structures[159]. Crystallographic B-factors provide an approximate measure of local atomic displacement or structural order within the crystal environment. The B-factor distribution is shown in **Fig. 3.8**, and values for the major network nodes are listed in **Table 1**. Most of the identified allosteric hotspots showed intermediate B-factor values rather than unusually high values. For example, R49, D150, and D168 had normalized B-factor values of 0.509, 0.342, and 0.497, respectively. W207 displayed an even lower value of 0.056, indicating that this residue is well defined in the crystal structure.

These observations indicate that the key dynamic-network residues are not identifiable simply as highly flexible or disordered regions in the crystal structure. Although crystallographic B-factors can sometimes provide useful information

about local mobility, they do not capture the full dynamic coupling present under solution conditions. In particular, residues that are structurally well ordered may still play central roles in long-range communication through correlated motions. Therefore, the allosteric hotspots identified here appear to reflect dynamic network properties rather than static disorder.

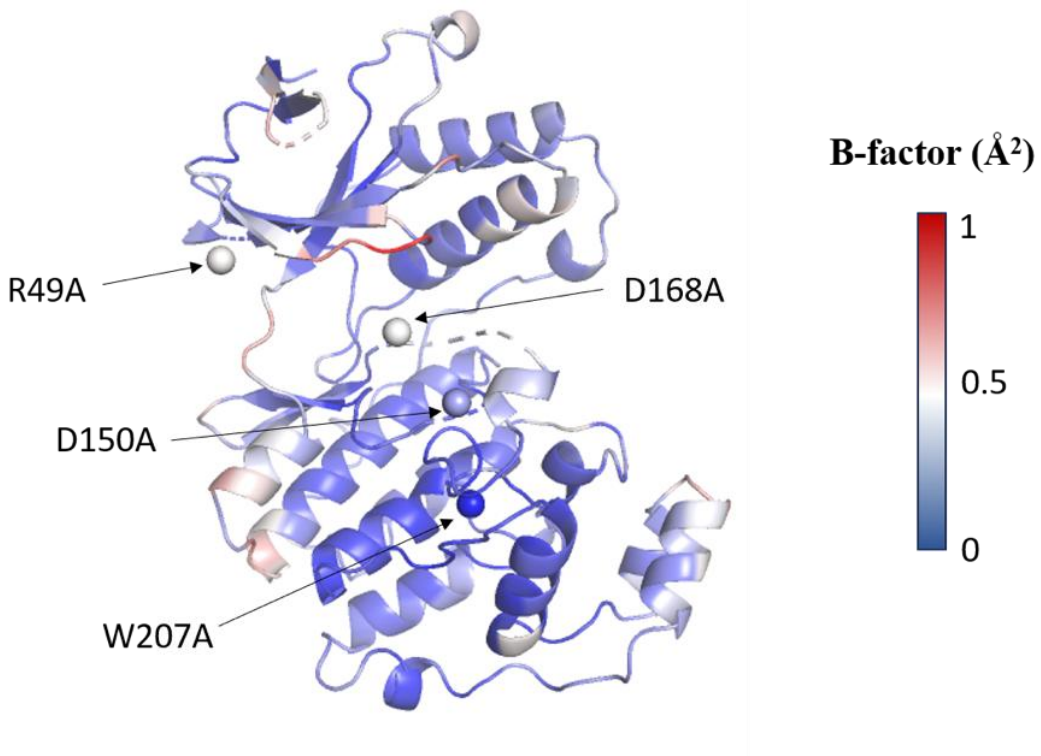

Fig. 3.8 B-factors of X-ray crystal structure along the protein. Temperature B-factors (Debye-Waller factors) are shown for the crystal structure PDB 3HEG.

Table 3.1: B-factors of key network residues, derived from PDB 3HEG.

Residue	**B-factor** (Å²)
PRO29	0.434
ARG49	0.509
LYS66	0.206
ILE141	0.199
ASP150	0.342
ASP168	0.497
TYR188	0.111
THR203	0.207
TRP207	0.056
ILE212	0.107
ILE235	0.098

3.3 Change in the network properties on perturbation

To discern the properties of the network, it was probed by "mutating" residues identified as key nodes based on high betweenness centrality by selecting four of the residues (R49, D150, D168, and W207) and were replaced by alanine. W207 is of particular interest as it forms part of the lipid pocket in the C-lobe. MD data namely the RMSD and the RMSF (five 1 μs trajectories for each of the four mutants) were obtained using similar strategies as for the wild type (**Fig. 3.9**). The trajectories revealed changes in the overall dynamics due to a point mutation.

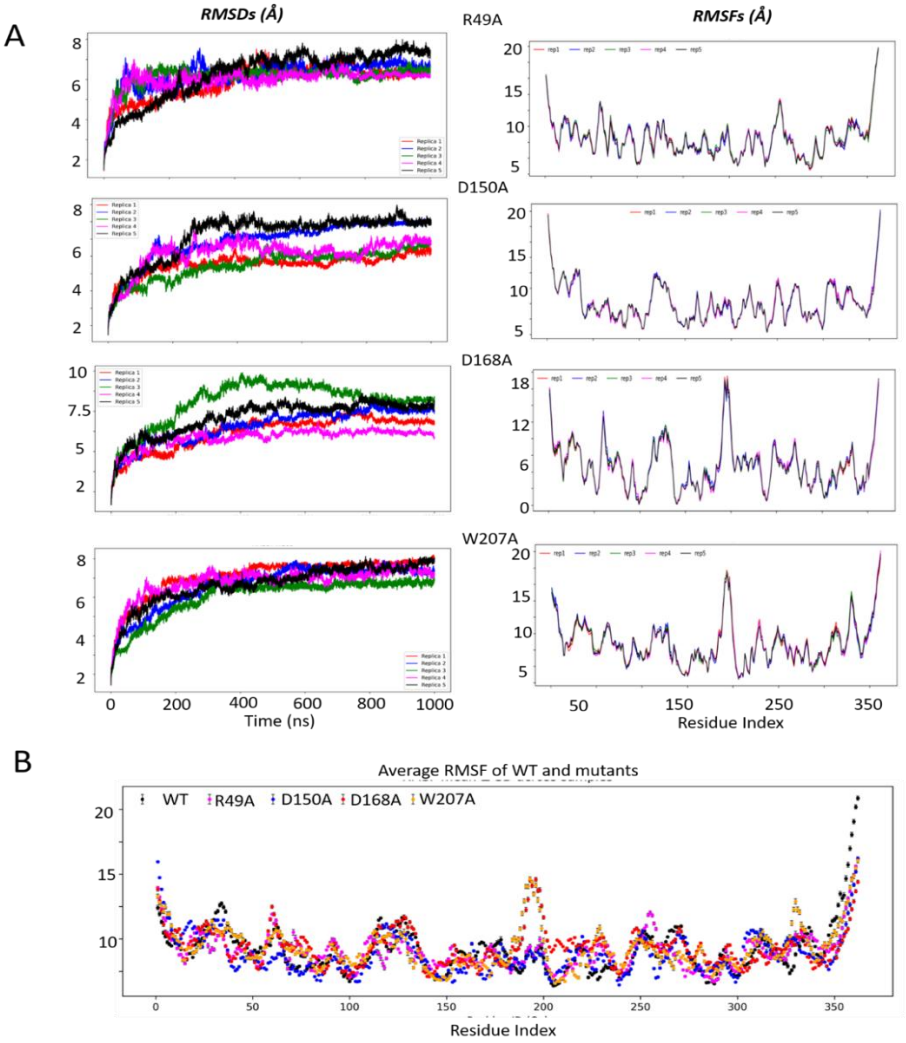

Fig. 3.9 A) RMSDs and RMSFs of five replicas per mutant. The last 200 ns were used for network and correlation analysis. **B)** Mean and SD of all the RMSFs compared with the wildtype.

The mutant trajectories were re-analyzed with the mentioned dynamical network framework. These analyses revealed differences in both betweenness-derived pathways and community structure compared with the wild type (**Fig. 3.10**). The community architecture was different than that of the wildtype. And new shortest paths were established, which featured new residues with maximum betweenness centrality.

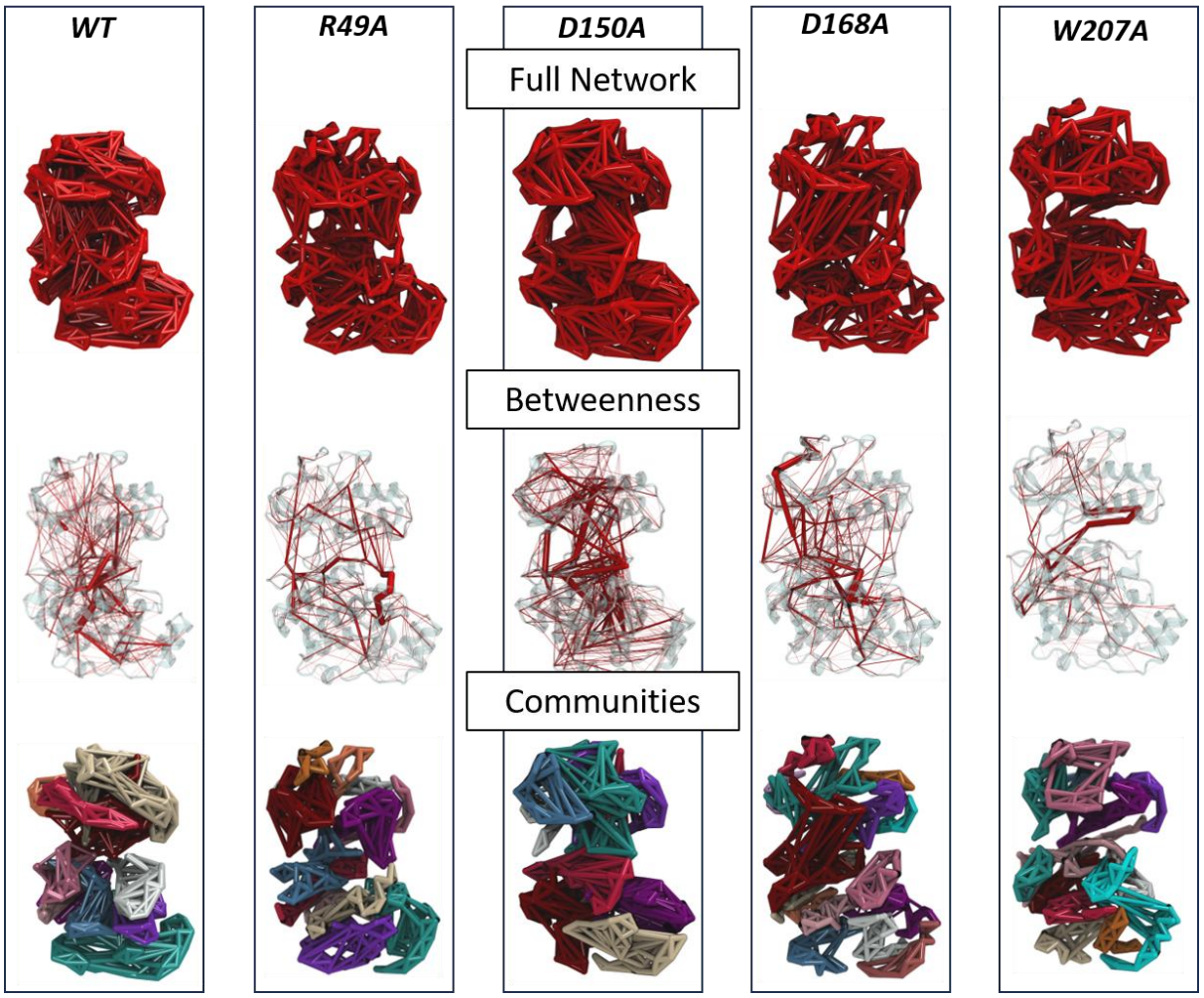

Fig. 3.10: Network analysis by Dynetan, mainly betweenness and communities of the mutants. The top shows the entire network, while the center depicts betweenness, and the bottom shows the clusters found in each of the mutants.

The effects of mutation on long-range communication were also quantified by evaluating inter-lobe (N–C) correlations and correlations along the wild-type-defined shortest communication paths. Total correlation maps for all ensembles are provided in the **Fig. 10.1** (Appendix). The correlations for cross lobe are shown in **Fig. 3.11A**. Whereas the tertiary structure and hence many correlations are necessarily maintained with respect to **Fig. 3.7**, changes with respect to long-range

correlations can be witnessed in each of the cases. (Difference maps (mutant – wild type) are shown in **Fig. 3.11B**.) The correlation pairs are stated below in **Table 3.2**.

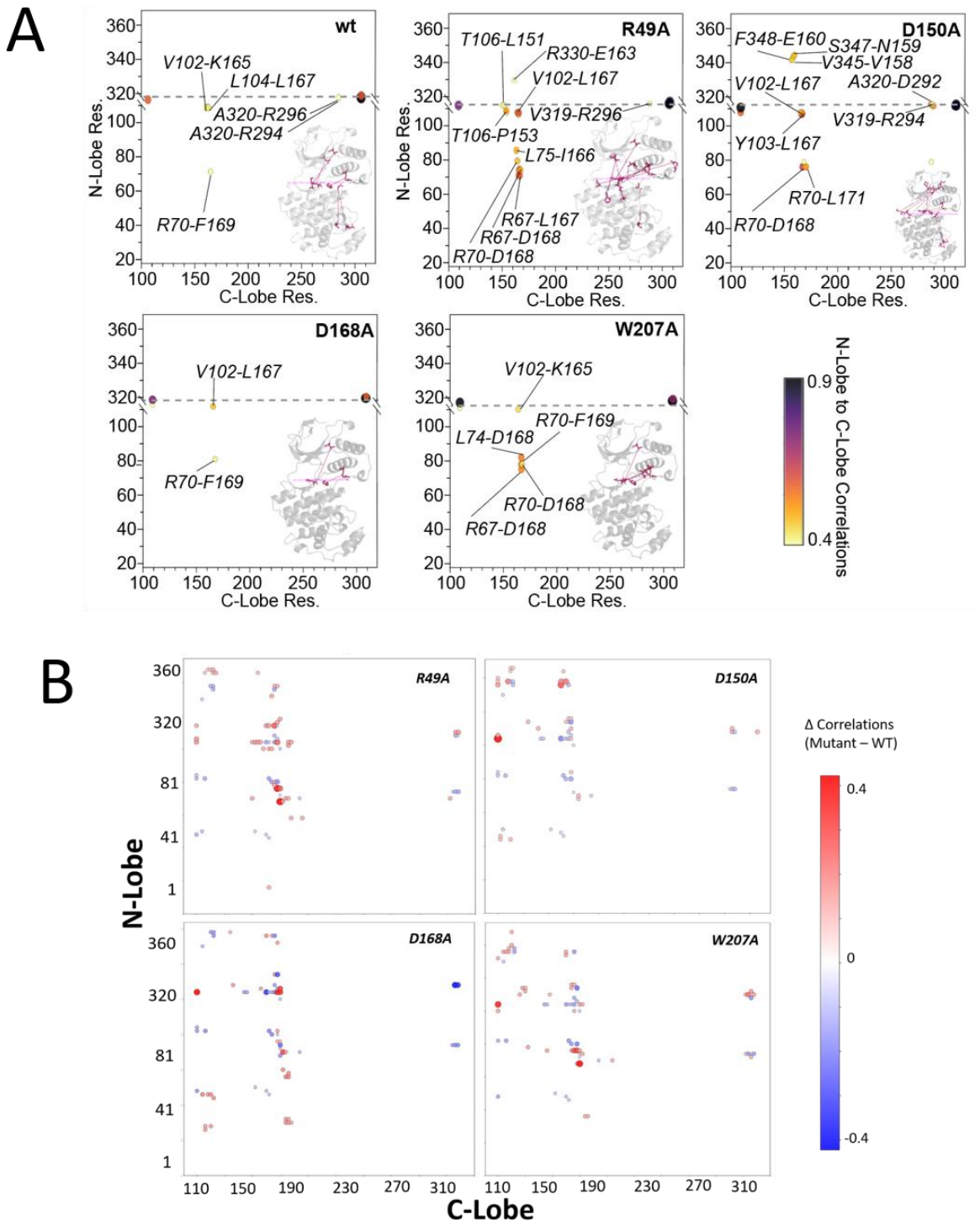

Fig. 3.11. A) N-C lobe correlations of the mutants focusing on the inter-domain regions. B) Differences (mutant – WT) in the correlations from the N to C lobe for each of the mutants.

Table 3.2: Correlation Values Between N-lobe to C-Lobe.

WT	R49A	D150A	D168A	W207A
319–316 (0.96)	319–316 (0.96)	319–316 (0.96)	317–316 (0.96)	317–316 (0.95)
319–315 (0.75)	319–315 (0.94)	106–108 (0.95)	317–315 (0.93)	106–108 (0.94)
106–108 (0.55)	320–316 (0.93)	320–316 (0.91)	106–108 (0.75)	317–315 (0.93)
320–316 (0.55)	106–108 (0.76)	319–315 (0.75)	318–316 (0.55)	318–316 (0.72)
102–165 (0.36)	70–168 (0.58)	102–167 (0.61)	102–167 (0.41)	70–168 (0.53)
102–167 (0.35)	102–167 (0.57)	70–168 (0.59)	70–169 (0.35)	74–168 (0.52)
70–169 (0.31)	67–168 (0.57)	103–108 (0.54)	103–108 (0.32)	67–168 (0.51)
319–294 (0.31)	103–155 (0.46)	319–294 (0.48)		102–165 (0.40)
	70–169 (0.43)	70–171 (0.46)		70–169 (0.38)
	81–165 (0.42)	320–292 (0.46)		103–108 (0.35)
	101–167 (0.41)	103–167 (0.46)		
	102–166 (0.41)	348–160 (0.40)		
	67–167 (0.41)	347–159 (0.39)		
	75–166 (0.41)	345–158 (0.37)		
	319–296 (0.33)	345–157 (0.35)		
	106–153 (0.32)	318–293 (0.31)		
	106–151 (0.32)	73–292 (0.31)		
	330–163 (0.31)	73–169 (0.30)		
	102–155 (0.31)	70–170 (0.30)		
		103–165 (0.30)		

3.4 Validating the dynamic network ensemble

To validate the dynamic allosteric network identified by dynamical network analysis, we used a two-level strategy combining additional computational analyses with experimental validation. This was necessary because different network-analysis approaches can rely on different theoretical assumptions and may therefore emphasize different aspects of residue communication.

In both parts of the validation strategy, the network was probed by perturbing residues identified as key nodes based on high betweenness centrality. Four residues R49, D150, D168, and W207, were selected for alanine substitution, as mentioned in the previous section. These mutants were then used for downstream analyses, including correlation analysis, sorafenib-binding studies, solution NMR chemical-shift perturbation experiments, NMR relaxation measurements, and biochemical assays (**Fig. 3.12**).

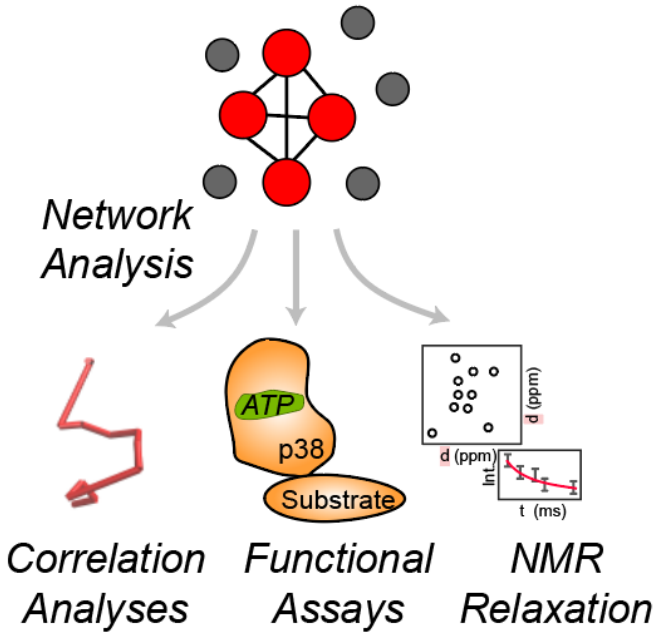

Fig. 3.12 Strategy to verify the results of dynamic-network analyses, using in-silico mutagenesis, functional assays of mutants, and NMR chemical-shift perturbation and relaxation.

3.5 Pathway level changes on network perturbation in apo and holo p38α

To assess how mutation of central network residues affects communication between regulatory regions, shortest-path analyses were also performed for the mutant systems. As in the wild-type analysis, representative residues were selected for each region: K66 for the extended allosteric pocket, Y188 for the activation loop, and I235 for the lipid pocket. For the pathway connecting the allosteric pocket to the activation loop, the communication path traverses the DFG motif, including D168 and G170, consistent with the role of this motif as a central mediator between regulatory regions. This finding also agrees qualitatively with previous observations in p38γ, where the DFG region contributed to communication between distant allosteric sites[139]. The pathway between the activation loop and the lipid pocket was then examined using activation-loop and lipid-pocket residues, including K233 and I235. This analysis revealed a route linking the activation loop to the lipid-binding region of the C-lobe. Finally, pathways between the extended allosteric pocket and the lipid pocket were calculated without imposing passage through the activation loop. These paths also involved the DFG motif but bypassed the activation loop, indicating that communication between the two pockets can be channelled through alternative routes within the kinase domain. The routes are given in **Table 10.3** (Appendix). Together, these analyses reveal a connected allosteric network that spans the N-lobe, C-lobe, activation loop, DFG motif, and lipid-binding domain. Importantly, these computational results support the idea that the lipid-binding domain and lipid pocket are integrated into the dynamic communication architecture of p38α. The lipid pocket therefore should not be considered merely as a peripheral hydrophobic cavity. Instead, it appears to form part of a broader allosteric network connecting distal regulatory sites with the active-site machinery. This provides a mechanistic rationale for the potential modulation of p38α through sites outside the ATP-binding cleft[129, 147].

The shortest path does not by itself define an allosteric pathway. Rather, it represents the most strongly connected communication route between selected residues in the dynamic network. When such a route links known regulatory regions, such as the lipidic pocket, activation loop, catalytic site, or ATP-binding cleft, it can be interpreted as a potential allosteric communication pathway. Therefore, this analysis

was used to identify communication routes and hub residues that may contribute to long-range dynamic coupling in p38α.

The wild-type shortest path was used as the reference, and the cumulative pairwise correlation between consecutive residues along this path was calculated for wild type and each mutant. Uncertainty was estimated from five independent replicas, using bootstrapping hypothesis with each replica further divided into five analysis windows **Table 10.4** (Appendix).

Across all three communication routes – allosteric pocket to activation loop (**Fig. 3.13A**), lipid pocket to activation loop (**Fig. 3.13C**), and allosteric pocket to lipid pocket (**Fig. 3.13E**), the mutants showed consistently reduced cumulative correlations compared with wild-type p38α. This indicates that mutation of high-centrality residues weakens dynamic coupling between distant regulatory regions.

Notably, W207A produced a strong reduction in the allosteric-pocket-to-activation-loop pathway, with an approximately 20% decrease in cumulative correlation (**Fig. 3.3B**). This is particularly informative because W207 is located in the C-lobe and is not directly part of the allosteric pocket. Its mutation therefore suggests that C-lobe residues can influence communication between the allosteric pocket and activation loop, consistent with a densely connected allosteric network.

Conversely, D168A had a pronounced effect on the lipid-pocket-to-activation-loop pathway, reducing cumulative correlation by approximately 10% (**Fig. 3.13D**). D168 is the aspartate of the DFG motif and lies outside the lipid pocket itself, yet its mutation weakens communication between the lipid pocket and activation loop. This supports the role of the DFG motif as a central relay element within the p38α dynamic network.

The strongest and most consistent effects were observed for the direct pathway between the extended allosteric pocket and the lipid pocket. This pathway is also the least studied as it excludes the phosphorylation lip or the activation loop, which is the most important, established regulatory element of p38α. All mutations of central network residues produced substantial decreases in cumulative correlation along this route: R49A by approximately 10%, D150A and D170A by approximately 20%, and W207A by approximately 25% (**Fig. 3.13F**). These reductions were statistically significant and demonstrate that the identified network residues contribute directly to dynamic coupling between the allosteric and lipid-pocket regions. This also validates that a direct coupling between the allosteric pocket and lipid pocket is embedded in the inherent network of the protein and validates the initial hypothesis

that lipid pocket binders cause a major ring flip of Sorafenib, an allosteric pocket binder (**Fig. 3.1C**).

Together, these results show that mutation of high-centrality residues does not merely perturb local structure, but weakens long-range communication between key regulatory sites. The fact that distal mutations affect pathways in which they are not directly located supports the presence of a distributed and interconnected allosteric network in p38α.

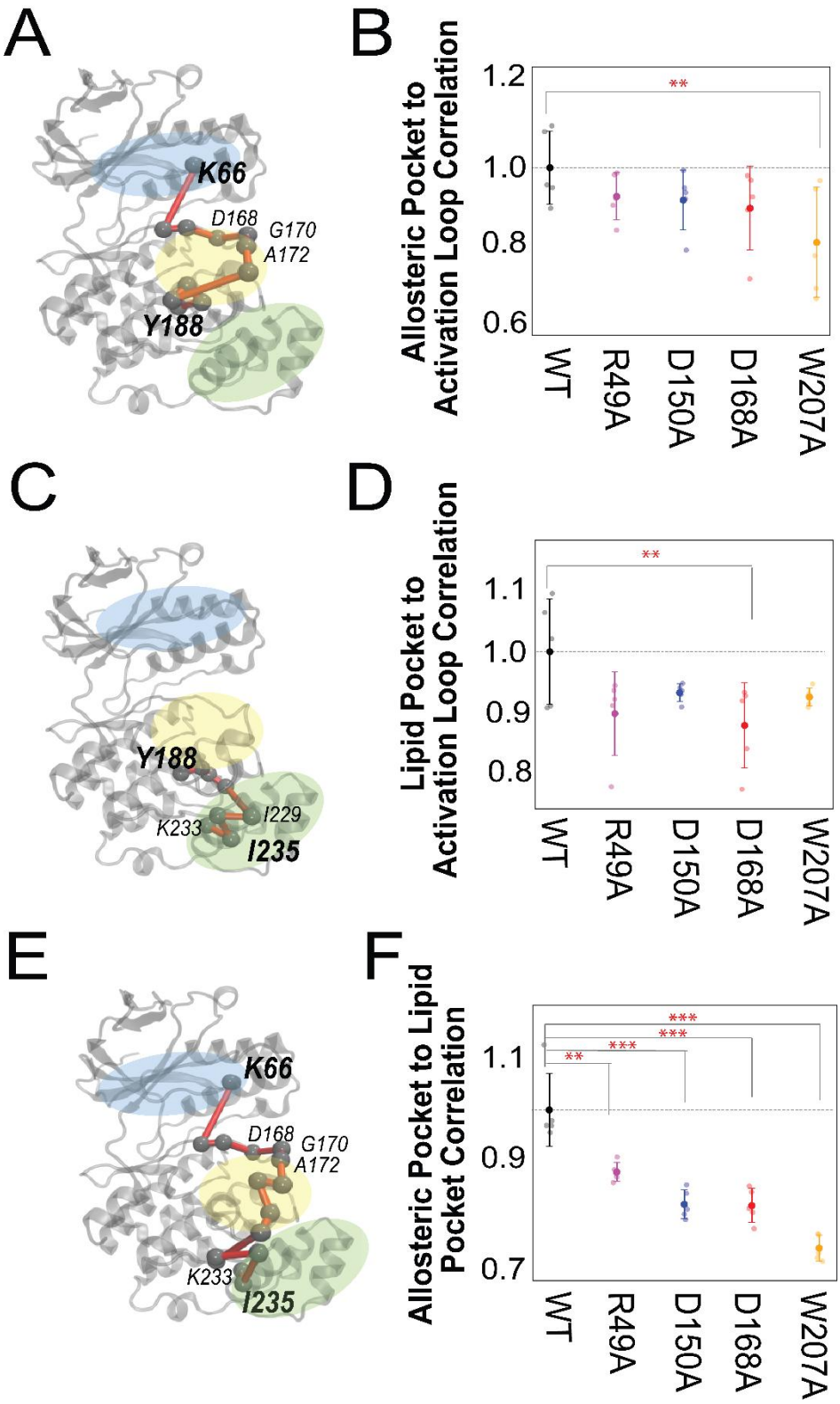

Fig. 3.13 A) Residue-wise depiction of the shortest communication path from the allosteric pocket to the activation loop. **B**) For all the pathways (n=5). Total correlation of residue pairs along the allosteric-pocket-to-activation-loop pathway, normalized to wild-type (WT = 1) and with statistical annotations ** for $p < 0.05$ and *** for $p < 0.01$. Statistical significance was assessed by non-parametric

bootstrap tests, see the Methods for details. A marked reduction is observed in all mutants, with W207A exhibiting the most significant drop ($p = 0.039$). **C**) Shortest path from the lipid pocket to the activation loop with key residues highlighted. **D**) Correlation sums along the lipid-pocket-to-activation-loop pathway, normalized to WT, D168A highlighting a significant decrease ($p = 0.043$). **E**) Residue pathway showing the shortest communication route from the allosteric pocket to the lipid pocket. **F**) Total correlation for the allosteric-pocket-to-lipid-pocket pathway, normalized to WT, with all mutants showing statistically significant reduced correlations ($p = 0.017$ for R49A; $p = 0.0026$ for D150A; $p = 0.0022$ for D168A; $p = 0.005$ for W207A).

In addition to the apo systems, we examined how binding of an active-site/allosteric-site inhibitor affects the p38α dynamic network. For this analysis, the same in silico strategy used for the apo wild-type and mutant proteins was applied to sorafenib-bound p38α, using the X-ray structure 3HEG as the starting model. The binding pose of sorafenib was inspected using Discovery Studio, as shown in **Fig. 3.14**, and the corresponding docking scores are summarized in **Table 3.3**. Molecular dynamics simulations were again performed in five independent replicas for each system (**Fig. 10.2** Appendix).

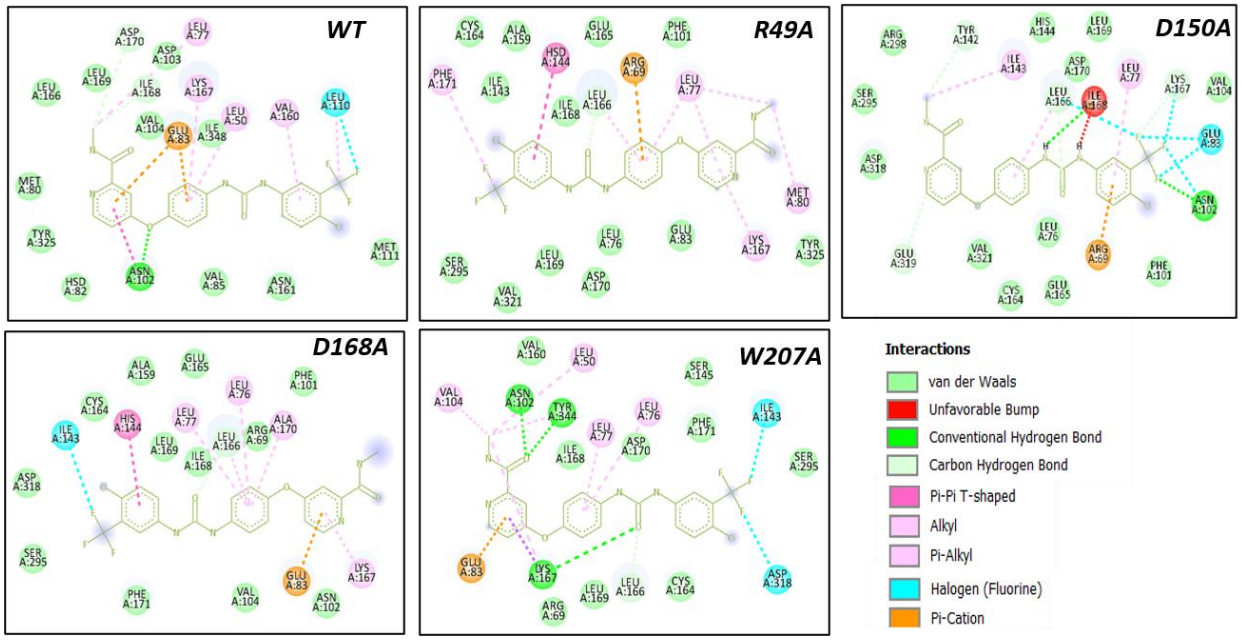

Fig. 3.14: Interacting residues when ligand sorafenib is docked with the WT protein and the mutants as seen through Discovery studio.

Table 3.3: Docking results of WT and mutant with Sorafenib at the allosteric pocket (in kcal/mol).

WT	R49A	D150A	D168A	W207A
-8.74	-3.69	-3.58	-6.56	-3.20
-7.74	-2.70	-3.35	-6.01	-0.35
-7.14		-2.72	-5.67	-0.35
-6.08		-1.70		-0.30
				-0.25

We first assessed motional correlations between p38α and the bound inhibitor. For this purpose, sorafenib was coarse-grained into western and eastern regions, which were analysed separately to simplify interpretation. The resulting protein–ligand correlation maps are shown in **Fig. 3.15**. Overall, mutation caused a modest reduction in cumulative protein–ligand correlation, with the most pronounced decrease observed for D168A. This suggests that mutations of network residues can slightly alter the dynamic coupling between the inhibitor and the kinase.

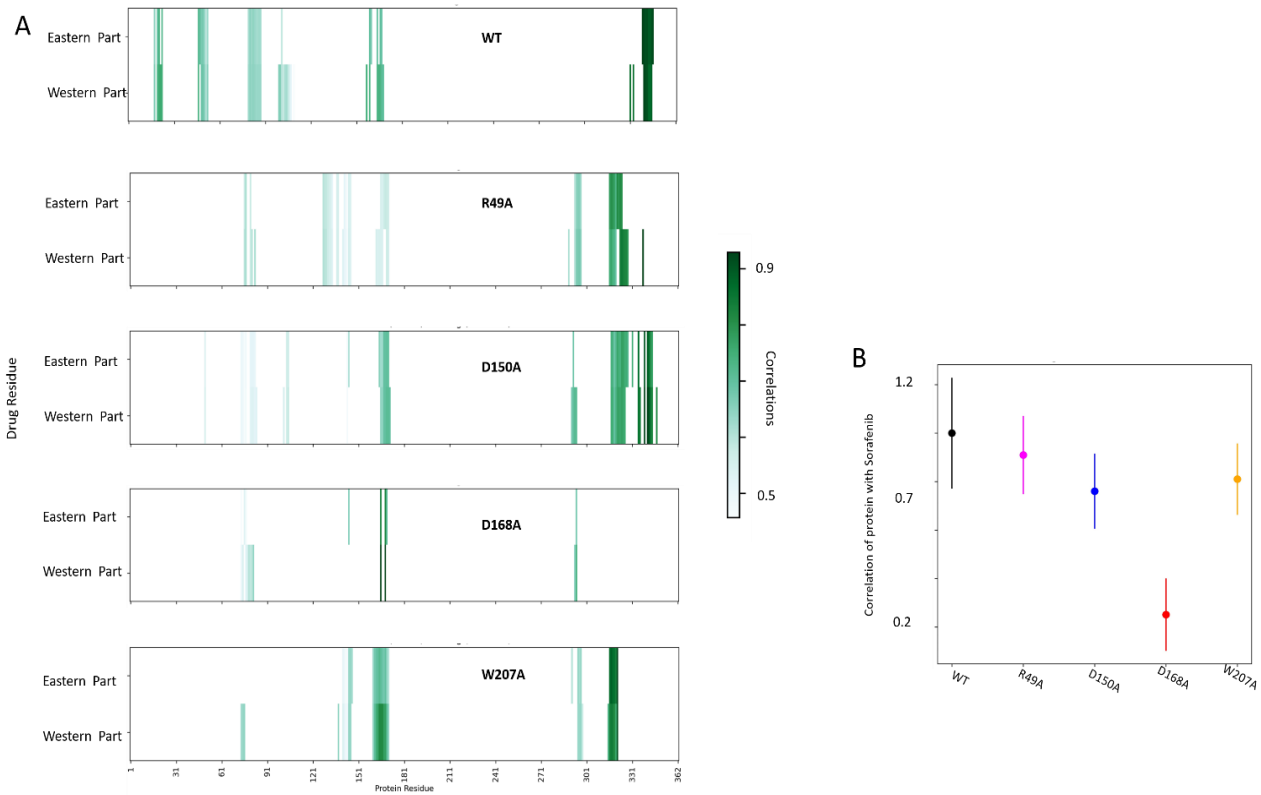

Fig. 3.15 A) Relative correlations between the protein and the ligand (divided into two groups, the eastern and western part), resolved by protein residue. B) Total correlation of the ligand sorafenib with the mutants and the WT (the latter being normalized to 1).

We then examined whether sorafenib binding changes the internal communication routes between the extended allosteric pocket, activation loop, and lipid pocket. For the ligand-bound wild-type protein, shortest communication paths were calculated using the same representative residues as in the apo analysis. Structural representations of these paths are shown in **Fig. 3.16A, C,** and **E**. Compared with the apo protein, sorafenib binding rerouted the preferred communication pathways connecting the allosteric pocket, activation loop, and lipid pocket.

For each ligand-bound system, cumulative pairwise correlations were quantified along the ligand-bound wild-type paths, using the sorafenib-bound wild-type protein as the reference. In contrast to the apo state, alanine substitution of the previously identified network hotspots no longer produced a significant reduction in cumulative correlation along these paths (**Fig. 3.16B, D, F**). This indicates that sorafenib binding alters the dynamic communication architecture of p38α and reduces the dependence of these pathways on the intrinsic apo-state network residues.

Consistently, no systematic gains or losses in cumulative correlations were detected along the ligand-bound communication paths. Together, these results suggest that sorafenib binding reshapes the internal motional network of p38α, rerouting communication between regulatory regions and partially suppressing the intrinsic dynamic network observed in the apo protein.

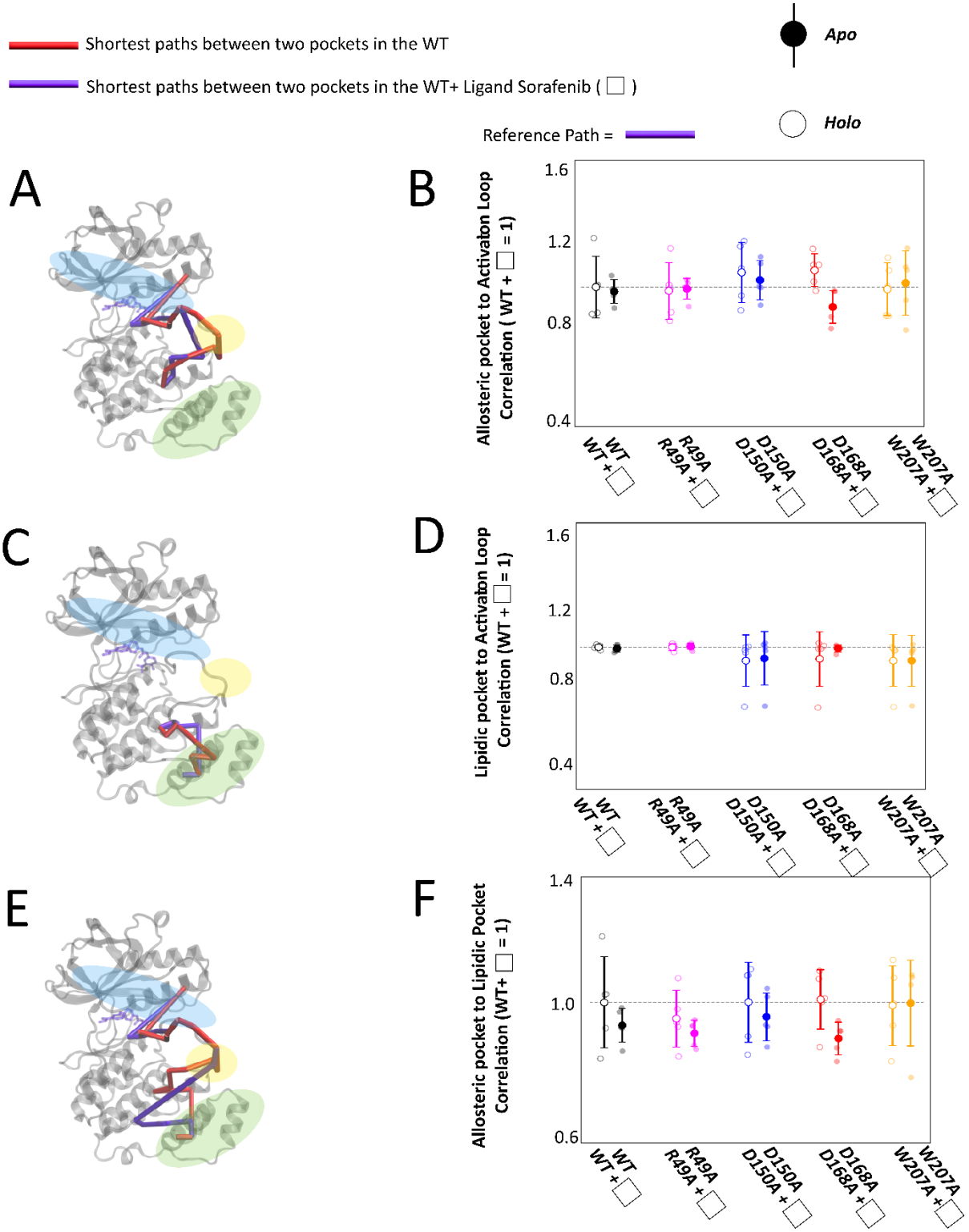

Fig 3.16 A) Structural depiction of the communication pathway from the allosteric pocket to the activation loop in wild-type p38α kinase. The apo WT shortest path is shown in red, while the ligand-bound (holo) WT pathway is depicted in purple, highlighting a shift in the nature of inter-residue motional interactions upon ligand binding. **B**) Correlational changes referenced to the holo WT pathway (purple). **C**) Structure of the lipid-pocket-to-activation-loop pathway, comparing apo (red) and

holo (purple) WT forms. Ligand binding again alters the trajectory of this communication path. **D**) Using the holo WT pathway (purple) as the reference, minor differences in correlations are seen from the lipid pocket to the activation loop. **E**) Structural comparison of the allosteric-to-lipid pocket pathway, red and purple representing shortest paths in apo WT and holo WT, respectively. **F**) Correlation changes for the allosteric-site-to-lipid-pocket pathway.

3.6 Change in biological activity on the absence of network residues

Even with the extensive sampling provided by five independent microsecond-scale MD replicas, the pathway-level correlation analyses retained statistical uncertainty. This limitation highlights the need for experimental validation using ensemble measurements over a much larger number of molecules. To test whether perturbation of the predicted dynamic network has functional consequences, we first assessed the enzymatic integrity of the individual mutants relative to wild-type p38α using Homogeneous Time-Resolved Fluorescence assays (HTRF; **Fig.3.17, 3.18** see Methods)[160].

HTRF is a high-throughput, low-background FRET-based assay format that combines time-resolved fluorescence detection with a homogeneous workflow[160, 161]. Here, HTRF was used to quantitatively compare the activity of wild-type and mutant p38α constructs using GST-tagged activating transcription factor 2 (ATF2) as the substrate. ATF2 is a well-established downstream substrate of p38 MAP kinases and is commonly used in p38α kinase-activity assays[162]. The assay was also used to assess the dependence of kinase activity on ATP concentration, thereby providing an indirect readout of ATP-dependent catalytic competence.

In addition to the wild-type protein, whose expression and purification have been described previously[163], the selected mutants were generated by site-directed mutagenesis. All proteins were recombinantly expressed in E. coli and purified according to established protocols (see Methods for biochemical details)[164]. Reaction rates were measured as a function of either ATP or substrate concentration, providing quantitative proxies for ATP-dependent catalysis and substrate

engagement, respectively. Kinetic characterization was performed using Michaelis–Menten fits, and the resulting apparent K_M values are summarized in Table S8.

The wild-type enzyme showed the strongest apparent binding competence, reflected by the lowest Michaelis–Menten constants. To compare fractional saturation and curve shape independently of differences in absolute signal intensity, HTRF signals were normalized to the fitted v_{max} of each protein variant. All mutants displayed impaired apparent affinity relative to wild type, requiring higher ATP concentrations to reach comparable fractional saturation. This was particularly evident for R49A and D168A, which showed a gradual rightward shift in the ATP-dependent response.

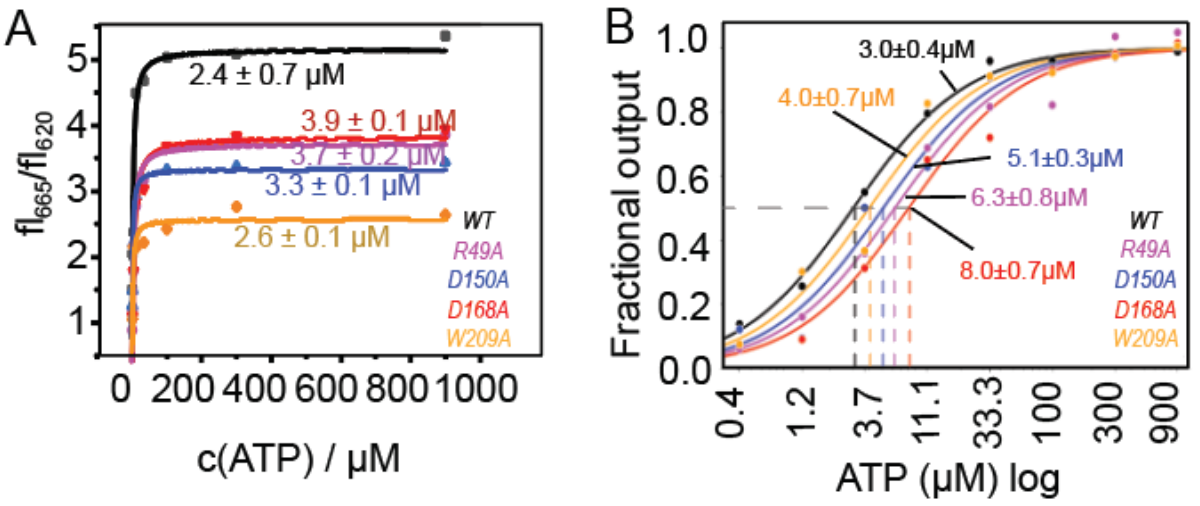

Fig. 3.17 A) HTRF-based ATP titration assay comparing the integrity of ATP binding between wild-type and mutant p38α kinase constructs across a concentration range of 0–1000 µM ATP. The result of a Michaelis-Menten fit of the fluorescence ratio f665/f620 obtained after a given time in the initial-rate regime serves as a quantitative proxy for ATP binding (best-fit KM shown for each curve). **B**) HTRF signals were normalized to the fitted vmax of each protein variant to compare fractional saturation, and were fitted according to Hill equation. The plots highlight differences in the concentration range over which ATP approaches saturation.

A similar trend was observed in the substrate-dependent assay. Wild-type p38α reached saturation efficiently, whereas the mutants showed reduced substrate-dependent response. D150A and R49A were the most strongly affected, as indicated by the pronounced rightward shift of their fitted curves (**Fig. 3.18A**). D150A displayed the most severe phenotype overall, with markedly reduced apparent

substrate engagement and moderately impaired ATP-dependent catalytic competence (**Fig. 3.17A and B**).

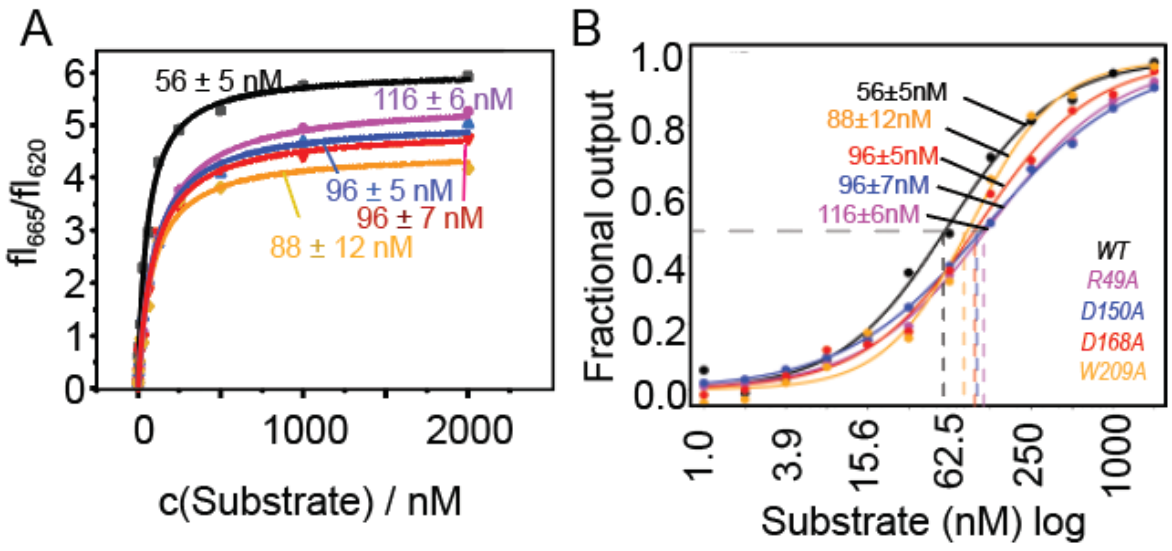

Fig. 3.18. A) HTRF substrate titration assay quantifying substrate binding affinity of wild-type and mutant kinases using increasing concentrations of a GST-tagged activating transcription factor 2 (ATF2) substrate. K_M fit values are again shown for each curve. While wild-type shows high fidelity of substrate association, the data for the dynamic-network mutants consistently indicate slightly impaired ATP and substrate binding competency. **B**) HTRF signals were normalized to the fitted v_{max} of each protein variant to compare fractional saturation, and were fitted according to Hill equation. The plots highlight differences in the concentration range over which substrate approaches saturation.

W207A also showed reduced ATP-dependent regulation and catalytic output, despite the fact that W207 is located deep within the C-lobe and is distant from the canonical catalytic machinery (**Fig 3.17**). Importantly, none of the mutated residues directly participates in the phosphoryl-transfer reaction itself. Therefore, the reduced enzymatic performance of these mutants is consistent with the idea that perturbation of distal allosteric-network residues can impair p38α activity through disruption of long-range dynamic coupling rather than through direct alteration of the active site. All the K_M, v_{max} and EC_{50} values of both the reactions are given in **Table 3.4**.

Table 3.4: K_M, v_{max} and EC values. Note that v_{max} (needs to be read as relative values as the conversion between fluorescence and concentrations is unknown) is not reliable as the protein concentrations and degree of phosphorylation might be slightly different between samples.

Protein	**WT**	**D168A**	**R49A**	**D150A**	**W207A**	
K_M (μM)	2.4+/-0.7	3.9+/-0.1	3.7+/-0.2	3.3+/-0.1	2.6+/-0.1	*from ATP plot*
v_{max} (a.u.)	5.2+/-0.2	4.3+/-0.7	3.3+/-0.8	1.3+/-0.3	1.6+/-0.4	
R-sq	0.93	0.97	0.96	0.94	0.94	
K_M (nM)	56.34 ± 5.0	95.89 ± 4.7	116.24 ± 5.9	95.82 ± 6.5	88.44 ± 11.7	*from substrate plot*
v_{max} (a.u.)	6.03+/-0.3	5.47+/-0.5	5.09+/-0.6	5.98+/-0.4	5.75+/-0.3	
r^2	0.99	0.99	0.99	0.99	0.99	

3.7 Chemical-shift perturbations on network element mutations

If protein motions were purely local and independent, mutation of a single residue would be expected to perturb mainly the substituted site and its immediate structural environment. In contrast, residues embedded within an allosteric communication network can transmit the effect of mutation to distant regions of the protein. Such long-range perturbations are experimentally detectable by NMR spectroscopy as changes in residue-specific chemical shifts, peak intensities, line widths, and relaxation parameters across different motional timescales[139, 161, 162, 164]. Therefore, solution-state NMR provides a powerful experimental strategy to test whether residues identified by dynamical network analysis are genuinely involved in long-range communication within p38α.

To probe these potential long-range effects, we performed solution-state NMR experiments on unphosphorylated apo p38α. Wild-type and mutant proteins were expressed as $^{13}C/^{15}N/^{2}H$-labelled constructs in triple-labelled media and purified

using successive Ni-affinity, anion-exchange, and size-exclusion chromatography steps, following established protocols for recombinant p38α preparation[163]. Despite repeated attempts, the W207A mutant could not be expressed as a stable triple-labelled construct in deuterated minimal media. Consequently, this mutant could not be included in the solution-state NMR analysis, although it was retained in the computational and biochemical parts of the study.

Backbone resonance assignments for wild-type and mutant p38α constructs were obtained using 3D HNCA spectra, complemented by TROSY-HSQC spectra (**Fig. 3.20**) as residue-specific fingerprint spectra (**Fig. 3.19**). Existing backbone assignments deposited in the Biological Magnetic Resonance Data Bank were transferred in a stepwise manner to the spectra recorded here, using BMRB entry 17471 as the reference assignment set[165].

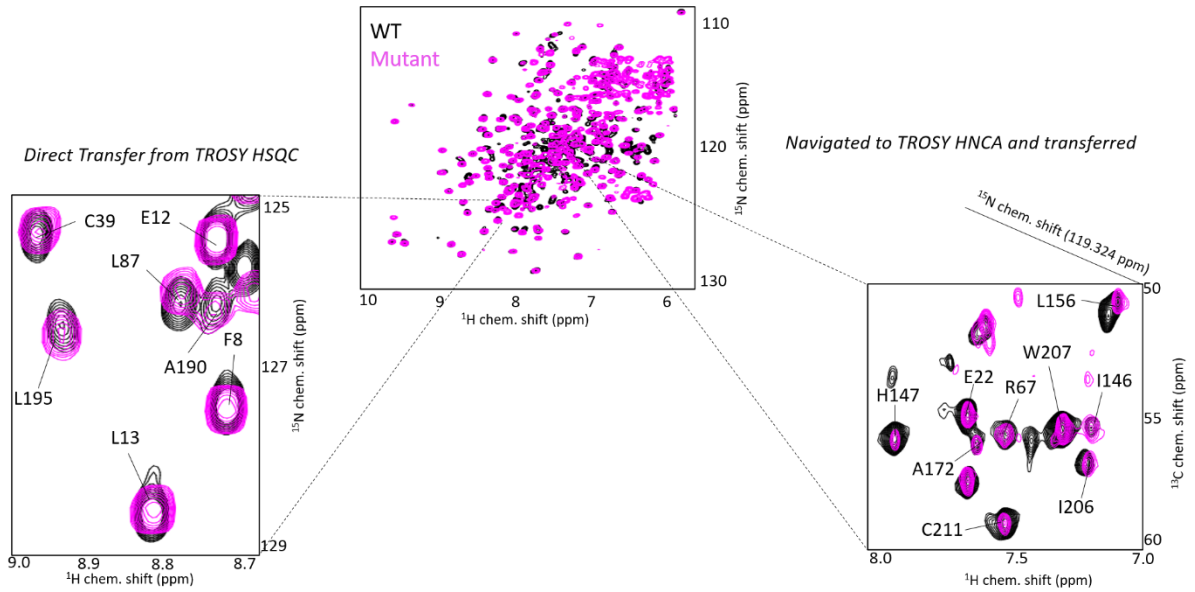

Fig. 3.19 Transfer of assignments using TROSY HSQC and HNCA spectra of the WT. (Chemical shifts of the WT are also available in the BMRB under accession code 17471.)

In addition to the network mutants, V38A was introduced as an experimental negative control. V38 is located within a folded region of the tertiary structure but lies outside the predicted dynamic allosteric network. This mutant therefore allowed us to distinguish ordinary local effects of mutation from broader perturbations associated with disruption of the predicted communication network.

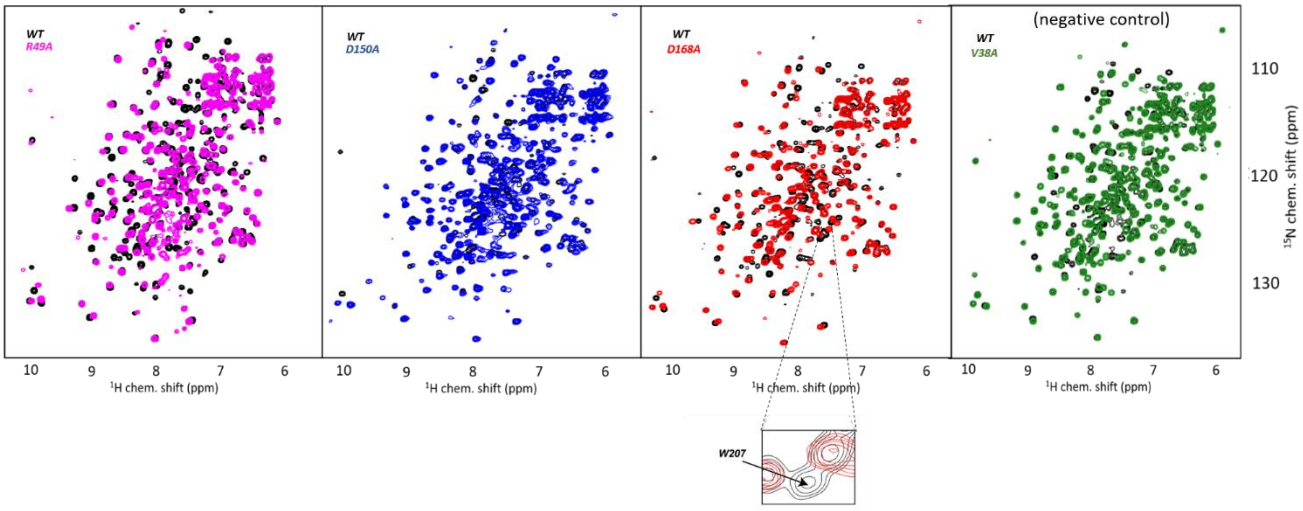

Fig. 3.20 TROSY HSQC of the mutants overlaid with the WT triple labelled proteins

We first used chemical-shift perturbation analysis (**Fig. 3.21**) to assess changes in the average chemical environment of backbone amides throughout the protein. Chemical shifts are highly sensitive reporters of local electronic and structural environments, and therefore provide residue-resolved information on conformational changes, altered hydrogen bonding, modified packing interactions, or changes in local dynamics[139, 161, 162, 164]. If the effects of mutation were restricted to the local structural neighbourhood, substantial chemical-shift changes would be expected mainly around the mutation site. By contrast, widespread chemical-shift perturbations at residues distant from the mutation site would indicate long-range changes in the conformational ensemble.

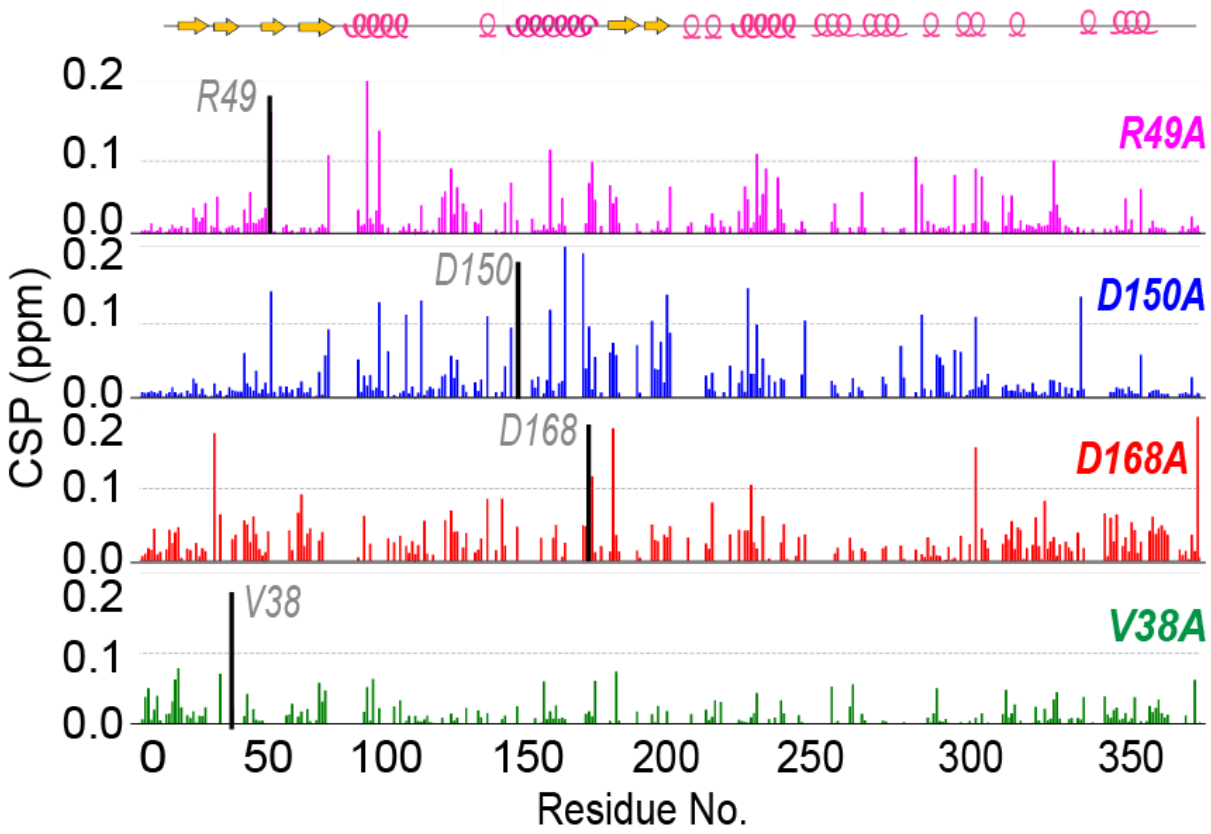

Fig. 3.21 Quantification of chemical-shift perturbations of the dynamic network mutants with the wildtype.

The CSP analysis revealed broad backbone perturbations for the functional mutants targeting predicted allosteric-network residues. Among these, D168A produced the most extensive global perturbation pattern. D168 is the aspartate of the conserved DFG motif and was identified computationally as a major communication hotspot. Its mutation caused chemical-shift changes distributed across the kinase domain, including regions far from the mutation site. Notably, the W207 resonance in the C-lobe disappeared in the D168A spectrum. This is particularly important because W207 was independently identified as a key residue in the dynamic network and is positioned close to the lipid pocket. The disappearance of this resonance therefore supports a strong long-range effect of D168A on the C-lobe and is consistent with dynamic coupling between the DFG motif, inter-lobe communication routes, and the lipid-pocket region.

The distributed nature of the D168A-induced perturbation is illustrated in (**Fig. 3.22**), which maps chemical-shift perturbations onto the p38α structure. Rather than being confined to the DFG motif or activation-loop region, the perturbations extend across multiple structural elements. D150A also produced strong CSP effects, although slightly less extensive than those observed for D168A. Together, these data

indicate that mutation of central network residues alters the conformational ensemble of p38α beyond the immediate mutation site.

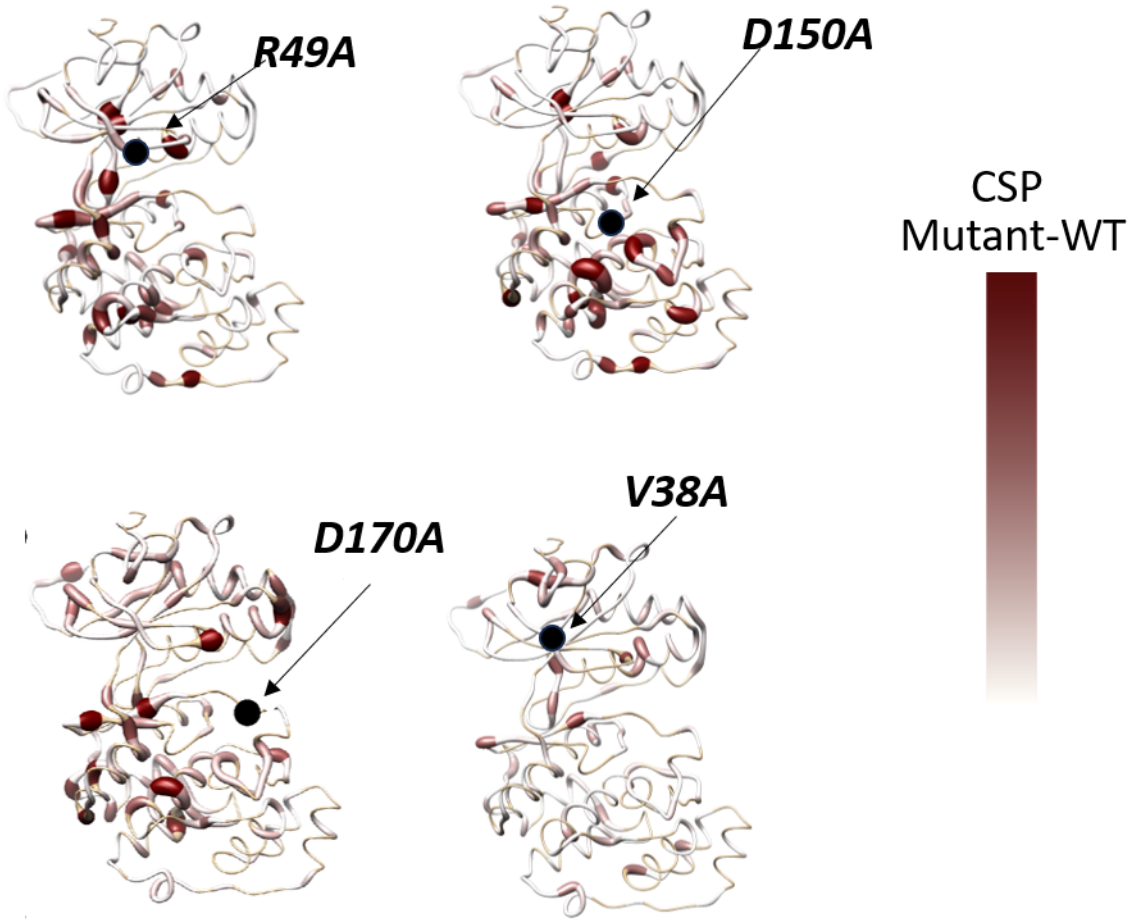

Fig. 3.22 Distribution of chemical shift perturbations across the protein structure.

The CSP patterns showed both shared and mutation-specific features (**Fig. 3.23**; **Table 3.5**). Several regions were repeatedly affected across the network mutants, including the N-lobe/C-lobe interface, the substrate-binding groove in the C-lobe, and N-lobe regulatory elements comprising the P-loop and extended allosteric-pocket region. At the same time, individual mutants produced distinct local and distal perturbation patterns. This combination of shared and mutation-specific effects is consistent with a distributed allosteric network: each mutation perturbs the network in a residue-specific manner, but the recurrence of affected regions indicates that these sites are dynamically coupled rather than behaving as isolated structural elements.

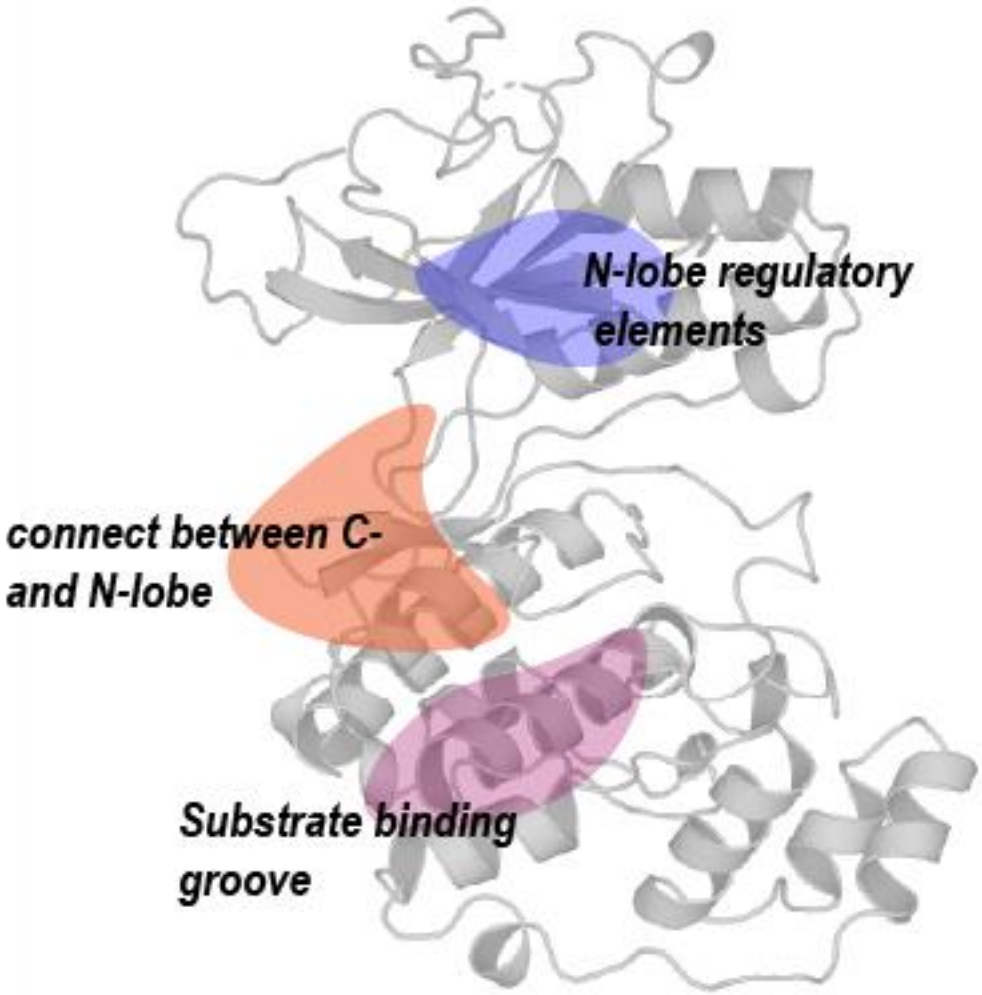

Fig. 3.23 Grouping of structural elements of all the mutants with a perturbed CSP.

In contrast, the negative-control mutant V38A showed only limited chemical-shift changes. This difference is important. V38A lies outside the predicted communication network and therefore provides a control for the general structural consequences of alanine substitution. The restricted CSP pattern of V38A indicates that not every mutation within the folded kinase domain produces widespread spectral changes. Instead, the broad perturbations observed for D150A, D168A, and R49A are specifically associated with mutation of residues predicted to participate in the dynamic allosteric network.

This distinction is further supported by the violin plots shown in **Fig. 3.24**, which compare the distribution of chemical-shift perturbations across the different variants. The network mutants show broader and stronger CSP distributions than V38A, consistent with more extensive remodeling of the conformational ensemble. Therefore, the NMR data experimentally support the computational prediction that

R49, D150, and D168 are not merely local structural residues, but participate in long-range dynamic coupling within p38α.

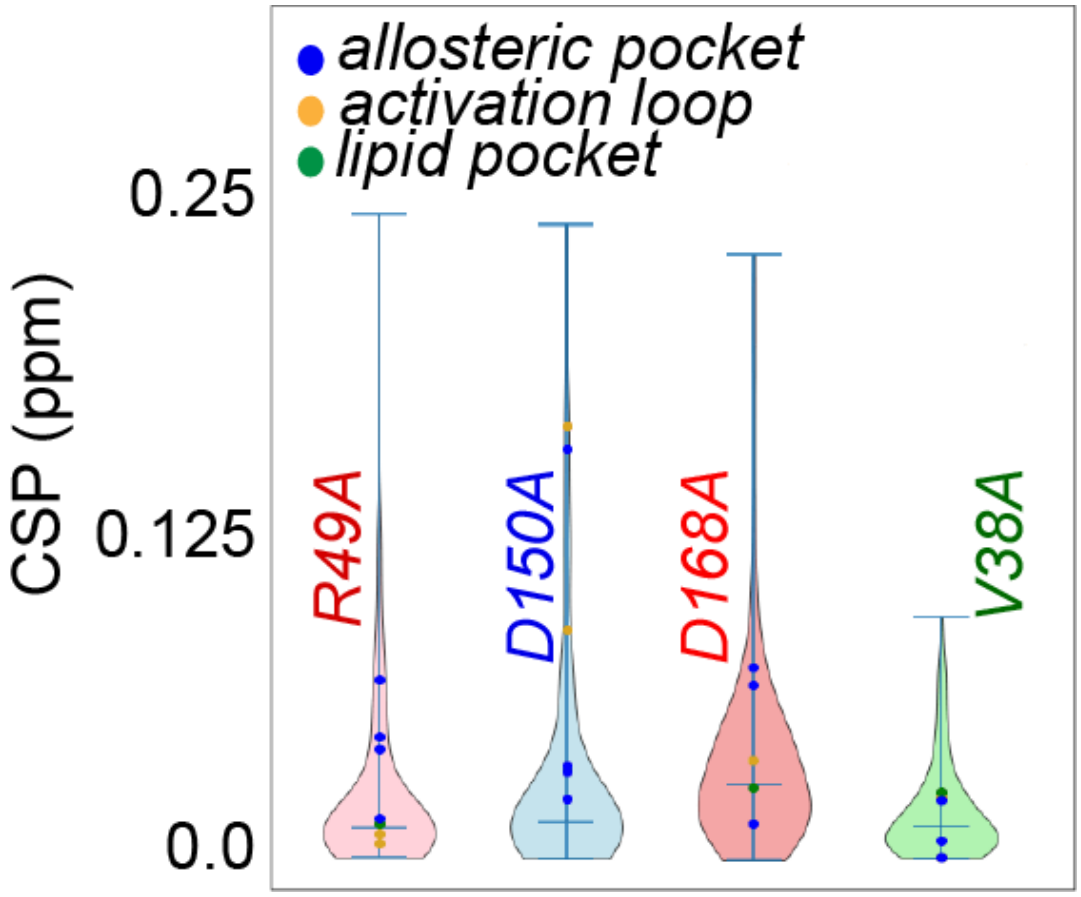

Fig. 3.24 Violin plots summarizing CSP distributions across network mutants (R49A, D150A, D168A) and the control variant (V38A). Blue and red dots mark residues from the lipid pocket and active site, respectively.

Overall, the chemical-shift perturbation analysis provides residue-resolved experimental evidence for allosteric rewiring upon mutation of predicted network hotspots. The widespread CSPs observed for the network mutants, together with the limited perturbation caused by the negative-control V38A mutant, support the conclusion that the identified hotspots contribute to the intrinsic dynamic communication architecture of apo p38α. These findings validate the dynamical network analysis and show that disruption of central communication nodes can reshape the conformational ensemble of the kinase across both lobes.

Table 3.5: Important regions with CSP>0.12 for all mutants

Residue	Mutants	Region
33	D168A	P-loop / glycine-rich loop
52	R49A, D150A	Allosteric pocket / N-lobe pocket
71	R49A	Allosteric pocket / N-lobe pocket
84	R49A	Other / distal region
88	R49A, D150A	Other / distal region
97	D150A	Other / distal region
102	D150A	Other / distal region
124	D150A	Other / distal region
145	R49A, D150A	HRD / catalytic loop region
150	D150A	HRD / catalytic loop region
156	D150A	Other / distal region
159	D168A	Other / distal region
166	D168A	Other / distal region
179	D150A	Other / distal region
184	D150A	Activation loop / phosphorylation region
211	D150A	Other / distal region
212	D168A	Other / distal region
214	R49A	Other / distal region
230	D150A	Lipid pocket / MAP kinase insert
267	R49A	Lipid Pocket connect
269	D150A	Other / distal region
287	D150A, D168A	Other / distal region
313	R49A	Other / distal region
322	D150A	Other / distal region
362	D168A	Other / distal region

3.8 Modulation of protein dynamics in the absence of network elements studied through NMR relaxation

To determine whether the chemical-shift perturbations observed for the network mutants were accompanied by changes in protein dynamics, we next performed solution-state ^{15}N relaxation experiments. Specifically, we measured [^{15}N,^{1}H]-

heteronuclear NOE values and ^{15}N transverse relaxation rates, R_2. These two parameters provide complementary information on backbone dynamics [45–48]. The hetNOE primarily reports on fast local motions on the picosecond-to-nanosecond timescale, with lower values generally indicating increased fast-timescale flexibility in a residue wise manner (**Fig.3.25**)[166].

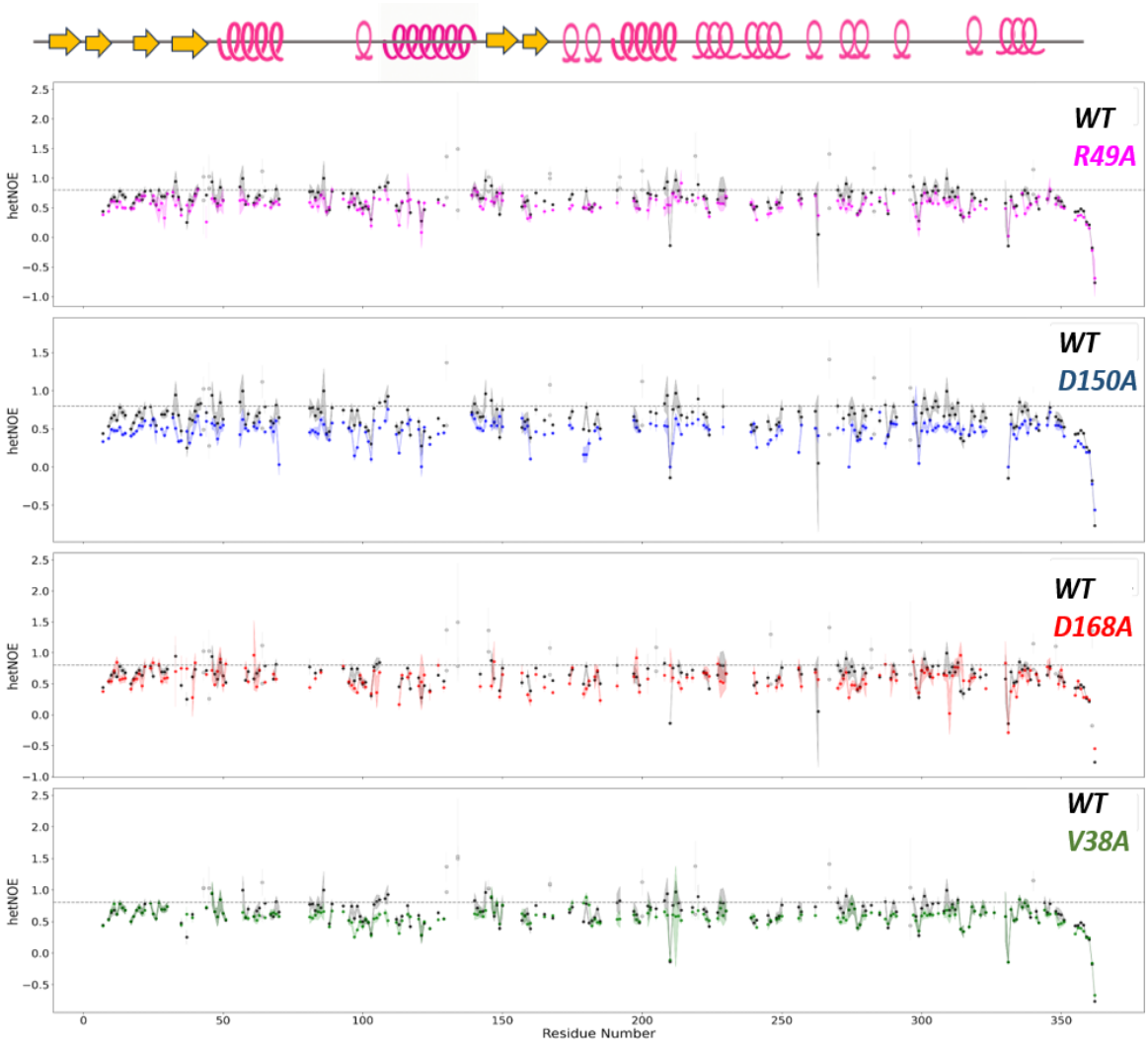

Fig. 3.25 Residue wise hetNOE trends

In contrast, R_2 is sensitive to transverse relaxation and can be influenced by slower conformational exchange processes, typically on the microsecond-to-millisecond timescale, in addition to overall molecular tumbling and local dynamics (**Fig. 3.26**)[167, 168, 169].

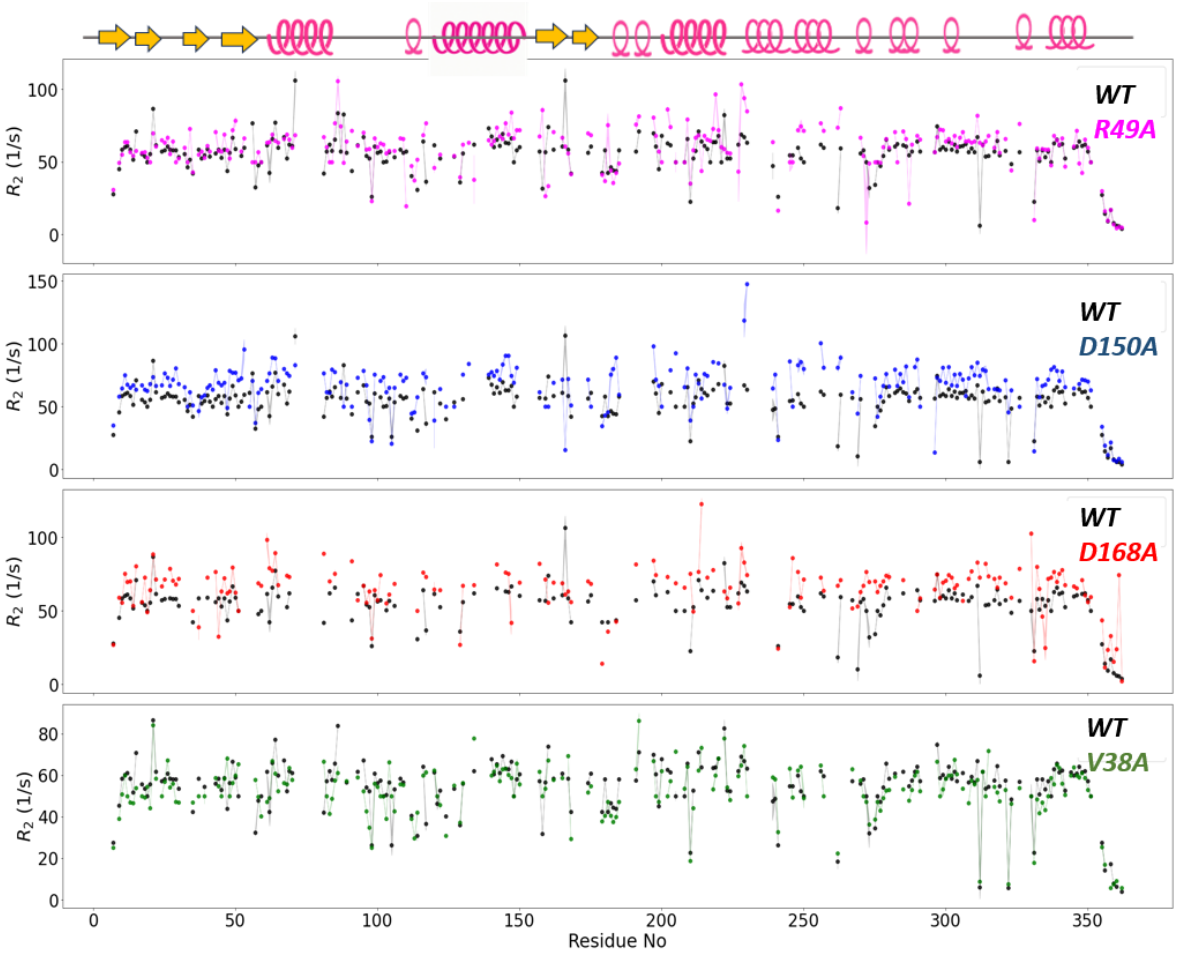

Fig. 3.26 Residue wise R_2 trends

Among the mutants analysed, D150A showed the most pronounced deviations from wild-type p38α across both relaxation datasets. Compared with wild type, D150A displayed reduced hetNOE values at several positions distributed throughout the kinase domain, suggesting increased local backbone flexibility on the fast timescale (**Fig. 3.27**). In parallel, elevated R_2 values were observed at multiple sites, especially in the C-lobe region encompassing residues approximately 200–250, which includes the MAP kinase insert and lipid-pocket region (**Fig. 3.28**). These increased R_2 values suggest enhanced contributions from slower conformational fluctuations and/or conformational exchange. Together, the reduced hetNOE and increased R_2 values indicate that the D150A mutation alters the motional behaviour of p38α across multiple timescales.

The dynamic consequences of D150A were not restricted to the mutation site. Structural mapping of per-residue relaxation differences relative to wild type revealed perturbations extending across both lobes of the kinase (**Fig. 3.27, 3.28**). This is consistent with the CSP analysis, where D150A also produced widespread changes in the backbone chemical environment. The combined CSP and relaxation

data therefore suggest that D150, a catalytic HRD-motif residue identified as a high-centrality node in the dynamic network, contributes not only to local catalytic architecture but also to broader dynamic coupling within the kinase domain.

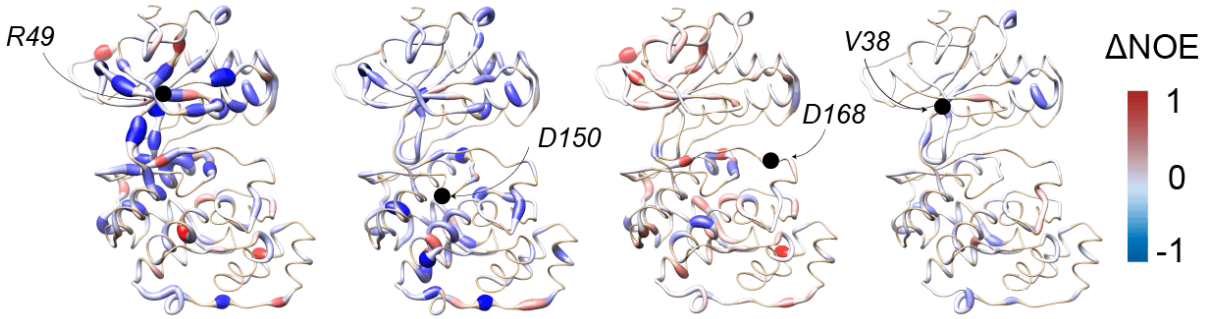

Fig. 3.27 Structural visualization of ΔhetNOE (mutant-WT) values. Blue regions highlight residues with reduced NOE values in the mutants, indicative of enhanced backbone flexibility.

D168A and R49A also showed clear relaxation changes, although their effects were less globally pronounced than those observed for D150A. Both mutants displayed altered R_2 values in the C-lobe, including regions associated with the lipid pocket and MAP kinase insert. More modest changes were also observed in the hetNOE profiles. These effects are important because R49 and D168 are located in different structural regions: R49 lies in the extended allosteric-pocket region, whereas D168 belongs to the DFG motif near the activation loop. Their ability to perturb C-lobe relaxation behaviour supports the idea that these residues participate in long-range allosteric coupling rather than acting as isolated local structural elements.

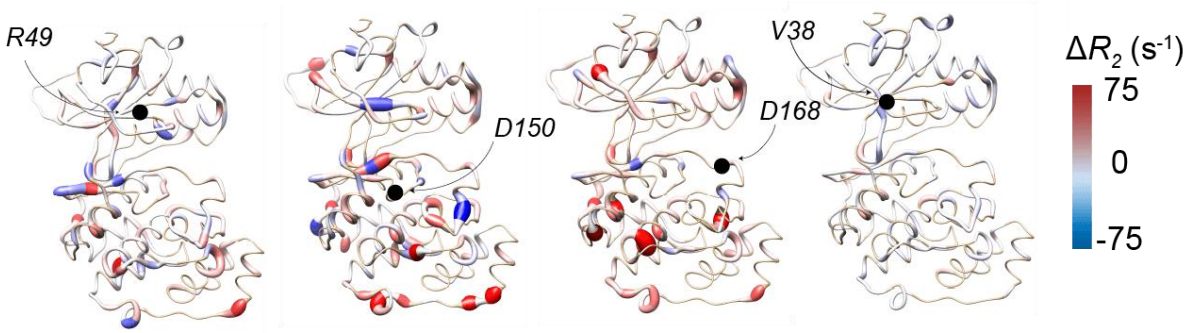

Fig. 3.28 Structural mapping of ΔR_2 (mutant – WT) values onto the three-dimensional structure of p38α kinase. Red regions indicate residues with R_2 higher in the mutants, predominantly localized to the catalytic core and distal C-lobe, supporting widespread conformational exchange.

Comparison of hetNOE differences identified shared perturbations in several regulatory elements, including regions near the activation-loop boundary, the HRD/catalytic-loop region, and the P-loop/glycine-rich loop (**Fig. 3.29; Table 3.6**). These regions are central to kinase regulation and catalytic organization, indicating that mutation of network residues affects not only distal pockets but also canonical kinase-control elements.

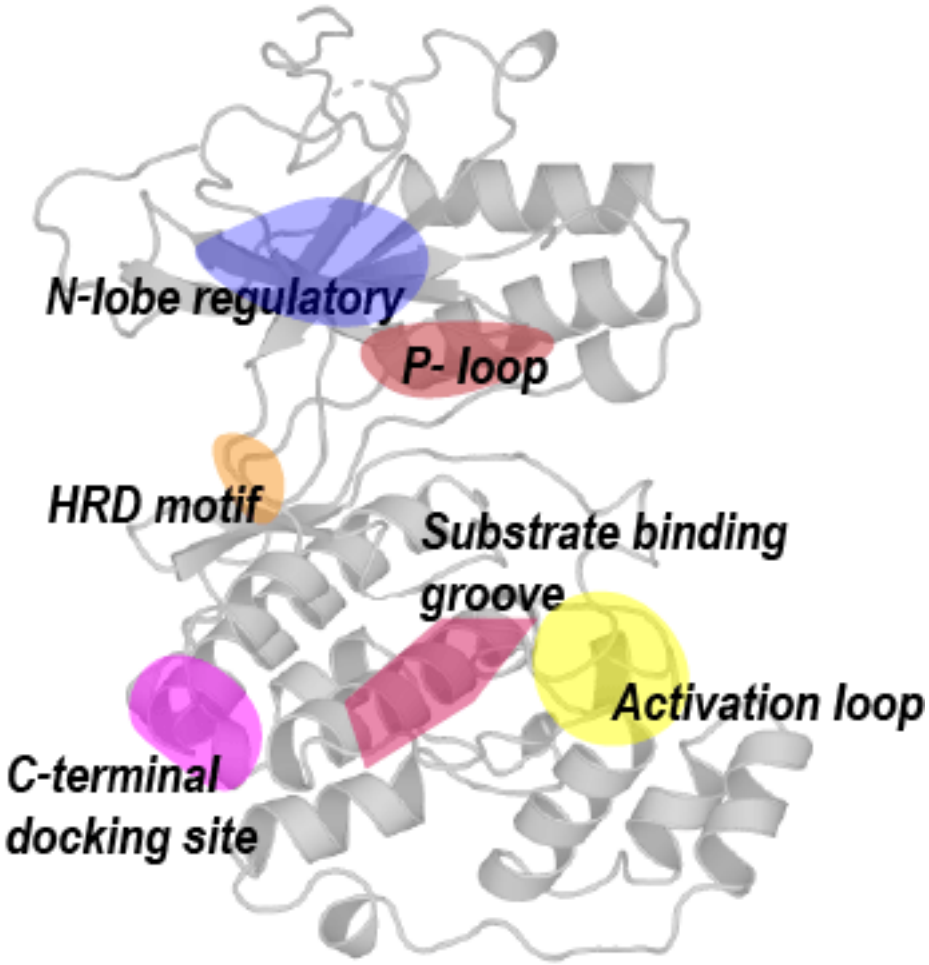

Fig. 3.29 Regions portraying increased fast time-scale dynamics collectively for all dynamic network mutants, specifically the activation loop.

Table 3.6: Important regions around the protein as shown by all mutants determined by difference in hetNOE

Residue	Mutants	Region	Mean_delta_mutant_minus_WT
178	D150A, D168A, R49A	Activation Loop	-0.42479
307	D150A, D168A, R49A	C-terminal docking / common docking region	-0.41298
261	D150A, D168A, R49A	Lipid pocket connector	0.398453
208	D168A, R49A	W207-adjacent substrate-binding groove / C-lobe region	0.809916
272	D150A, D168A	Lipid pocket connector	-0.54573
96	D150A, D168A	Other / distal region	-0.43552
31	D150A, R49A	P-loop / glycine-rich loop	-0.42107
207	D150A, R49A	W207-adjacent substrate-binding groove / C-lobe region	-0.39838
35	D168A, R49A	P-loop / glycine-rich loop	0.39117
84	D150A, R49A	Other / distal region	-0.38912
55	D150A, R49A	N-lobe regulatory / allosteric-pocket-adjacent region	-0.36746
142	D150A, R49A	Other / distal region	-0.3359
157	D168A, R49A	HRD/catalytic-loop-adjacent region	-0.30069
308	D168A	C-terminal docking / common docking region	-0.66113
68	D150A	alphaC-helix region	-0.61569
312	D168A	C-terminal docking / common docking region	0.581011
254	D150A	Lipid pocket / MAP kinase insert	-0.53586
285	D150A	Other / distal region	-0.50107
103	D168A	Other / distal region	-0.45686
42	R49A	Other / distal region	-0.45419

209	D150A	W207-adjacent substrate-binding groove / C-lobe region	-0.44567
54	D150A	N-lobe regulatory / allosteric-pocket-adjacent region	-0.42724
271	R49A	Lipid pocket connector	-0.42172
144	D168A	Other / distal region	-0.41166
40	D150A	P-loop / glycine-rich loop	-0.40812
95	D150A	Other / distal region	-0.39941
335	R49A	Other / distal region	-0.39584
280	D150A	Other / distal region	-0.38341
59	D168A	N-lobe regulatory / allosteric-pocket-adjacent region	0.381286
268	D168A	Lipid pocket connector	-0.36994
44	D150A	Other / distal region	-0.36641
27	R49A	Other / distal region	-0.36142
147	R49A	HRD/catalytic-loop-adjacent region	0.35499
303	D150A	C-terminal docking / common docking region	-0.35133
25	R49A	Other / distal region	-0.33643
37	D168A	P-loop / glycine-rich loop	-0.33586
189	D168A	Other / distal region	-0.33503
206	R49A	W207-adjacent substrate-binding groove / C-lobe region	-0.33385
79	D168A	Other / distal region	-0.33104
330	D168A	Other / distal region	-0.31373
196	D168A	Other / distal region	0.310641
47	R49A	N-lobe regulatory / allosteric-pocket-adjacent region	-0.30215
49	D168A	N-lobe regulatory / allosteric-pocket-adjacent region	0.30025
295	R49A	Other / distal region	-0.29854

Similarly, a collective analysis of R_2 differences relative to wild type revealed recurrent perturbations in the lipid-pocket/MAP kinase insert region across the allosteric mutants (**Fig. 3.30; Table 3.7**). This recurrence supports the interpretation that the lipid pocket is dynamically coupled to the wider p38α kinase network [10, 139].

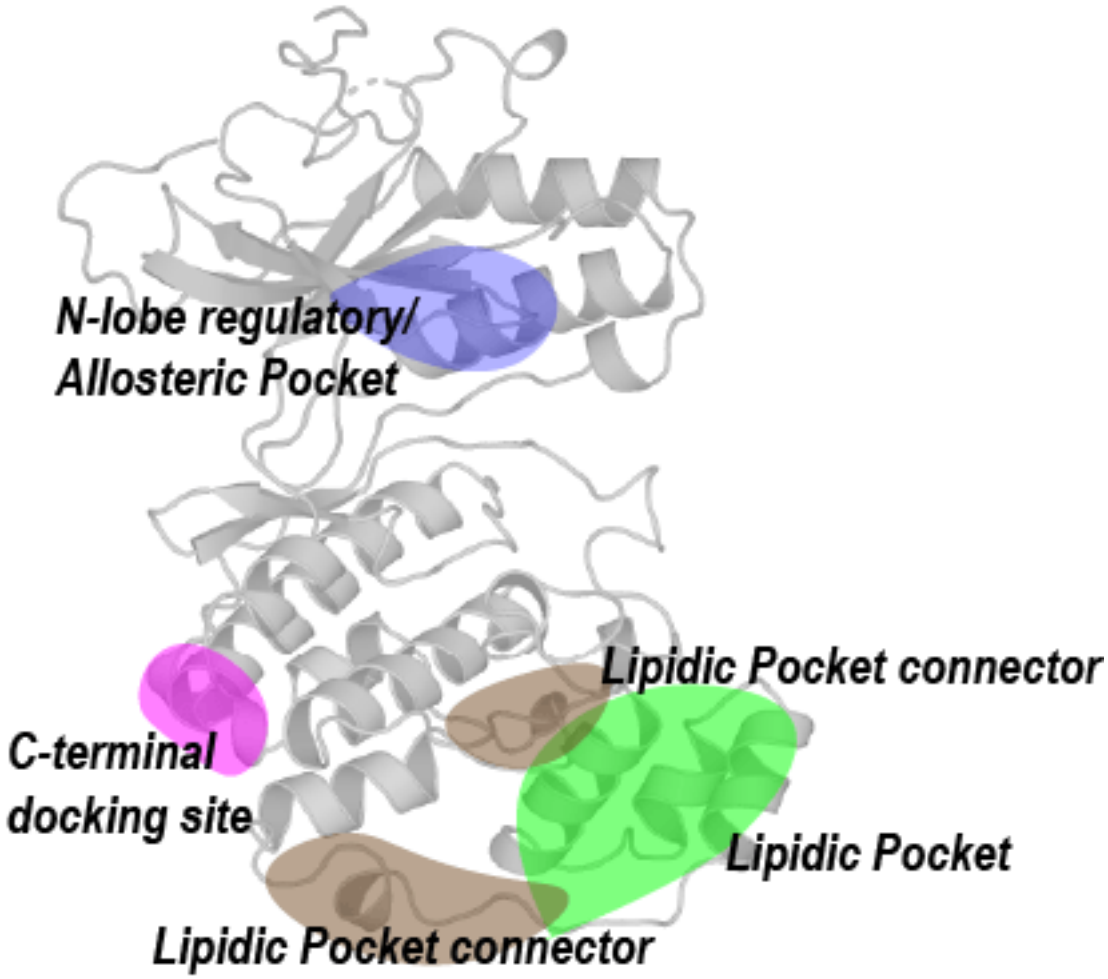

Fig. 3.30 Important regions of protein showing an increased R_2 upon mutation of the dynamic network (R49, D150 and D168), specifically transcending the network to accommodate the lipid pocket

Table 3.7: Important regions around the protein as shown by all mutants determined by difference in R_2

Residue	Mutants	Region	Mean_delta_mutant_minus_WT
310	D150A, D168A, R49A	C-terminal docking / common docking region	64.23073
164	D150A, D168A, R49A	Other / distal region	-60.5253

260	D150A, D168A, R49A	Lipid pocket connector	55.59837
115	D150A, D168A, R49A	Other / distal region	37.86612
79	D150A, D168A, R49A	Other / distal region	35.68239
227	D150A, R49A	Lipid pocket connector	39.281
267	D150A, D168A	Lipid pocket connector	38.34436
273	D150A, D168A	Lipid pocket connector	36.94594
60	D150A, D168A	N-lobe regulatory / allosteric-pocket-adjacent region	35.57432
270	D168A, R49A	Lipid pocket connector	-7.73536
89	D168A, R49A	Other / distal region	33.83916
86	D150A, R49A	Other / distal region	-33.2876
228	D150A	Lipid pocket connector	84.3543
359	D168A	Other / distal region	68.40611
212	D168A	W207-adjacent substrate-binding groove / C-lobe region	58.71044
156	R49A	HRD/catalytic-loop-adjacent region	54.3454
208	D168A	W207-adjacent substrate-binding groove / C-lobe region	52.40458
328	D168A	Other / distal region	52.28157
182	D150A	Activation loop / phosphorylation region	45.21017
294	D150A	Other / distal region	-43.3047
203	D150A	W207-adjacent substrate-binding groove / C-lobe region	42.5236
158	R49A	Other / distal region	-40.7218
320	D150A	C-terminal docking / common docking region	39.67871
254	D150A	Lipid pocket / MAP kinase insert	38.59222
69	R49A	alphaC-helix region	-37.6729
108	R49A	ATP-site hinge region	-37.5516

271	D168A	Lipid pocket connector	37.33149
59	D168A	N-lobe regulatory / allosteric-pocket-adjacent region	36.69748
51	D150A	N-lobe regulatory / allosteric-pocket-adjacent region	35.7457
181	D150A	Activation loop / phosphorylation region	35.425
226	R49A	Lipid pocket connector	34.71639
285	R49A	Lipid pocket connector	-33.5478
247	D150A	Lipid pocket / MAP kinase insert	33.18465
179	R49A	Activation loop / phosphorylation region	32.99165
217	R49A	Other / distal region	32.57734
243	D150A	Lipid pocket / MAP kinase insert	31.54835
244	D168A	Lipid pocket / MAP kinase insert	30.91248
157	R49A	HRD/catalytic-loop-adjacent region	-30.2921
333	D168A	Other / distal region	-28.6189
312	D168A	C-terminal docking / common docking region	28.22658
177	D168A	Other / distal region	-27.9597
261	R49A	Other / distal region	27.84709
54	R49A	N-lobe regulatory / allosteric-pocket-adjacent region	-26.6474

The C-terminal docking groove also showed recurrent perturbations in the relaxation data. This region is functionally relevant because MAP kinases use docking surfaces to engage regulatory proteins and substrates, including interactions involved in non-canonical activation pathways such as TAB1-mediated regulation. The observation that this region is altered in several network mutants suggests that the docking surface is dynamically connected to the broader allosteric architecture of p38α. Therefore, although the global distributions of relaxation parameters partly overlap between wild type and mutants, the residue-specific analysis reveals recurrently affected regulatory sectors. This supports a model in which the lipid pocket, docking groove, activation-loop region, and canonical catalytic elements are dynamically entangled within the p38α allosteric network.

In contrast, the control mutant V38A showed only minimal and mostly local changes. V38 is located outside the predicted dynamic network, and both its hetNOE and R_2 profiles remained largely similar to wild type, apart from subtle

perturbations near the mutation site. This behaviour supports its use as a negative control. The comparison between V38A and the network mutants indicates that widespread relaxation changes are not a generic consequence of alanine substitution within the folded kinase domain, but are associated specifically with mutation of residues predicted to participate in allosteric communication. The overall trends in R_2 and hetNOE are also assessed to produce a global picture. Boxplot comparisons across the variants (**Fig. 3.31**) further support this interpretation. The network mutants generally show a shift toward reduced hetNOE values, and increased R_2 values.

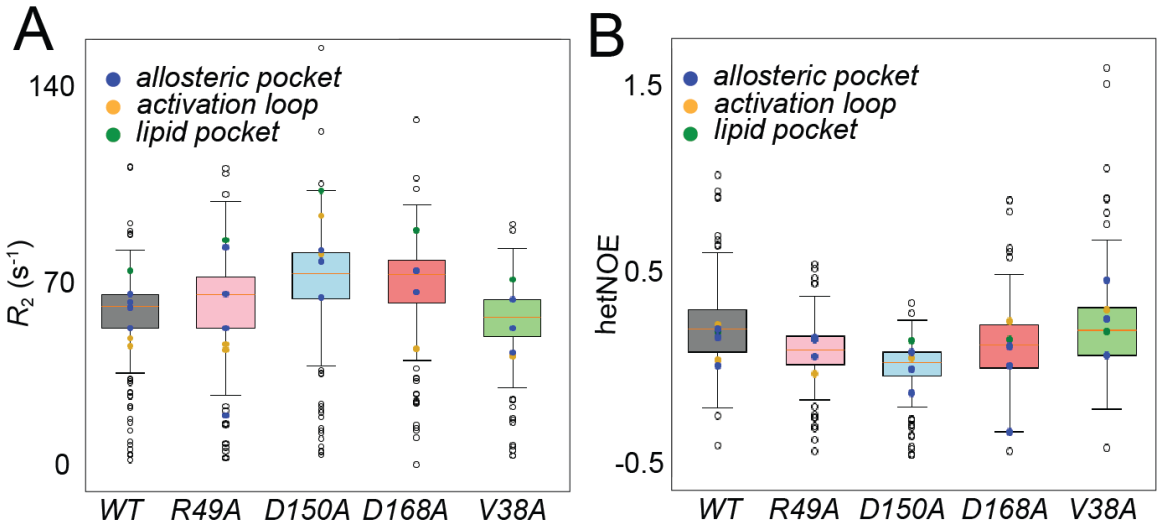

Fig. 3.31 A) Box plot distribution of R_2 values for wild-type, dynamic network mutants (R49A, D168A, D150A), and the negative control (V38A). Active-site residues (red) and lipid pocket residues (blue) are specifically highlighted by colored spheres. All dynamic-network mutants exhibit significantly elevated R_2 values compared to the wild-type and control, consistent with a global enhancement in slow conformational exchange. **B**) Box plots of hetNOE values across the same variants. Dynamic network mutants show a marked reduction in NOE values, reflecting increased local flexibility, including at functionally critical sites. By contrast, the control mutant V38A shows limited perturbation, confirming an impact on the p38 dynamic network to be absent.

To further probe conformational-exchange processes on the microsecond-to-millisecond timescale, we performed ^{15}N CPMG relaxation-dispersion experiments on wild-type p38α and the mutants. The quality of the relaxation-dispersion data did not support a detailed quantitative analysis of exchange parameters for all residues. However, exchange contributions, R_{ex}, to the effective transverse relaxation rates

could be estimated with reasonable accuracy for a subset of residues, allowing residue-specific assessment of transient conformational exchange (**Fig. 3.32**).

In CPMG relaxation-dispersion experiments, R_{ex} is derived from the dependence of $R_{2,eff}$ on the CPMG refocusing frequency[170]. Residues with elevated R_{ex} values undergo chemical exchange between conformational states on the microsecond-to-millisecond timescale[170, 171, 172]. Such exchange can arise from functional loop motions, transient allosteric transitions, domain-breathing motions, or local rearrangements. Importantly, R_{ex} depends both on the population of exchanging states and on the chemical-shift difference between them. Therefore, an increase in R_{ex} does not necessarily mean that a residue is simply more flexible; rather, it indicates stronger detectable exchange between conformational states under the experimental conditions.

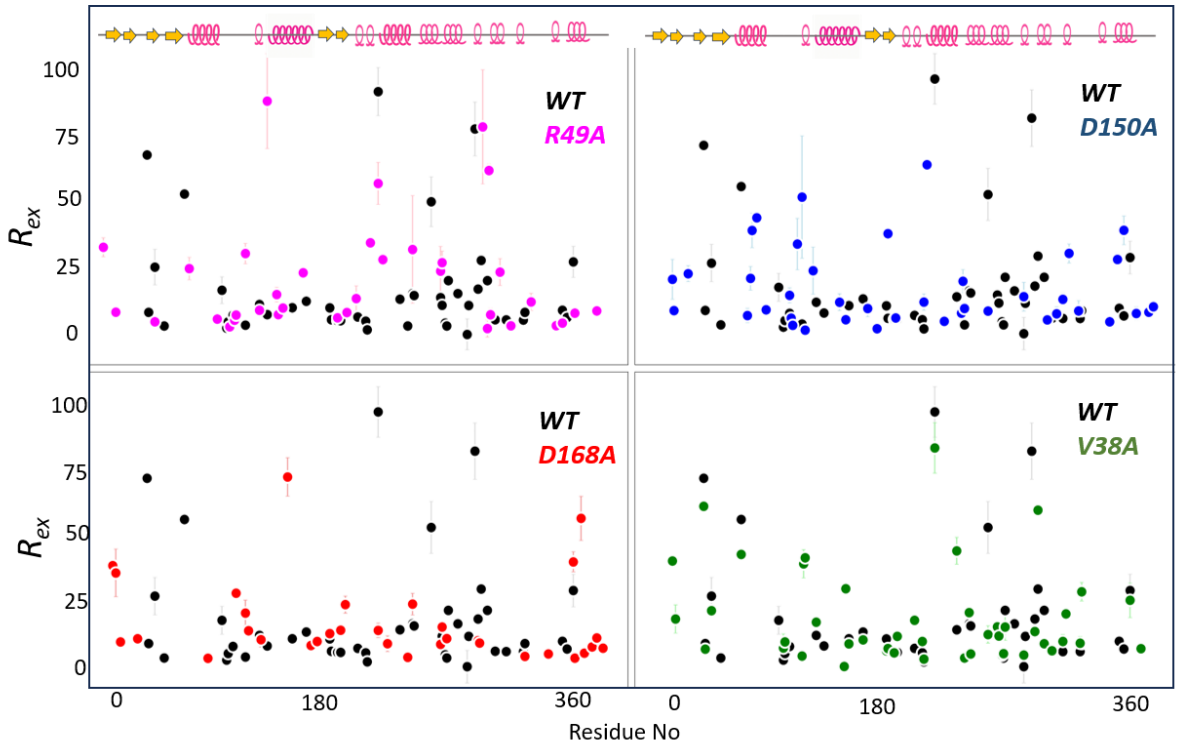

Fig. 3.32 R_{ex} trends residue wise, comparing WT with the mutants

Wild-type p38α displayed significant R_{ex} contributions across residues in both the N-lobe and C-lobe, consistent with widespread conformational plasticity in the apo kinase (**Fig. 3.33**). The V38A control showed a very similar R_{ex} pattern to wild type, both at the residue level and in the histogram distribution of R_{ex} values (**Fig. 3.33**). This agreement is consistent with its location outside the predicted dynamic network and reinforces the interpretation that V38A does not substantially perturb the allosteric communication architecture of p38α.

The network mutants showed more subtle and heterogeneous changes in R_{ex}. R49A displayed a modest reduction in millisecond-timescale exchange in parts of the N-lobe, together with a slight increase in the C-lobe. In contrast, D150A and D168A showed a modest decrease in R_{ex} in parts of the C-lobe and a slight increase in the N-lobe. These changes suggest some redistribution of conformational-exchange behaviour upon mutation, but the effects were not uniform across the kinase and should be interpreted cautiously.

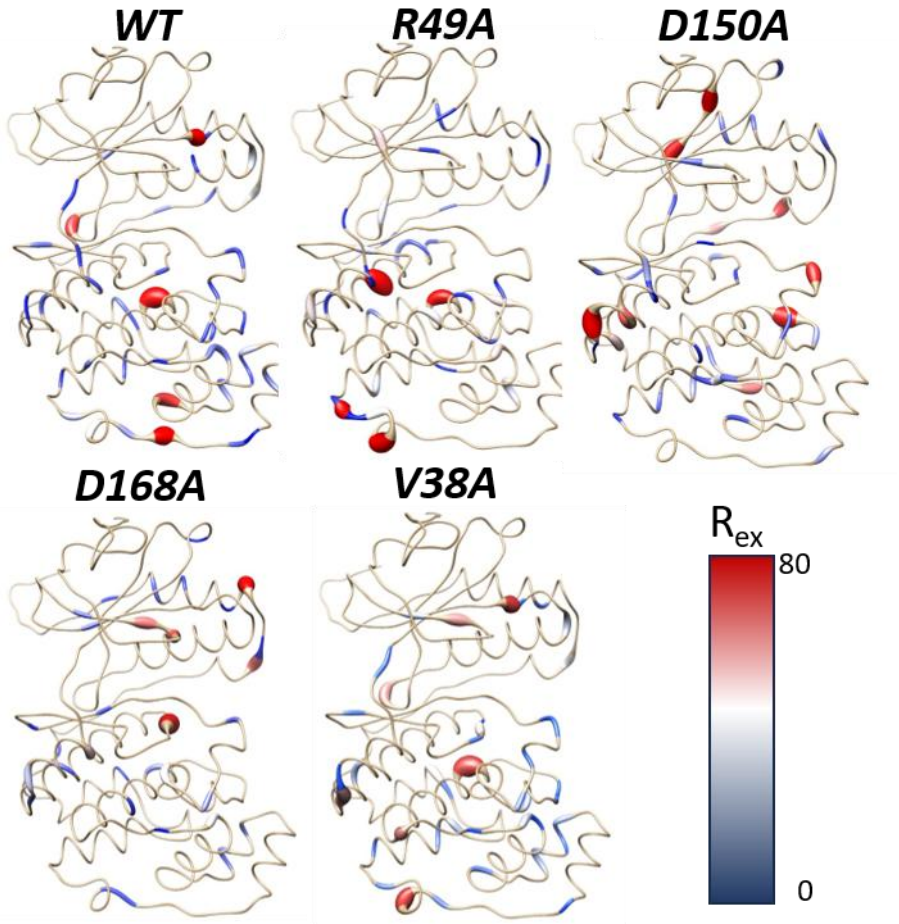

Fig. 3.33 Structural visualization comparing the spatial distribution of R_{ex} values between wild-type and the mutants. Residues exhibiting exchange contributions are highlighted in red. V38A shows minimal deviation from WT, consistent with its dynamic neutrality

The limited clarity of the CPMG-derived trends is partly due to the experimental uncertainty associated with individual $R_{2,eff}$ values. This is illustrated by residue A172, positioned between the DFG motif and the activation loop, where the dispersion curves show noticeable uncertainty across the different samples (**Fig. 3.34**). Additional representative dispersion curves are shown in the **Fig. 10.9** (Appendix). Because of this uncertainty, the CPMG data are best interpreted as supportive rather

than definitive evidence for mutation-induced redistribution of slower exchange processes.

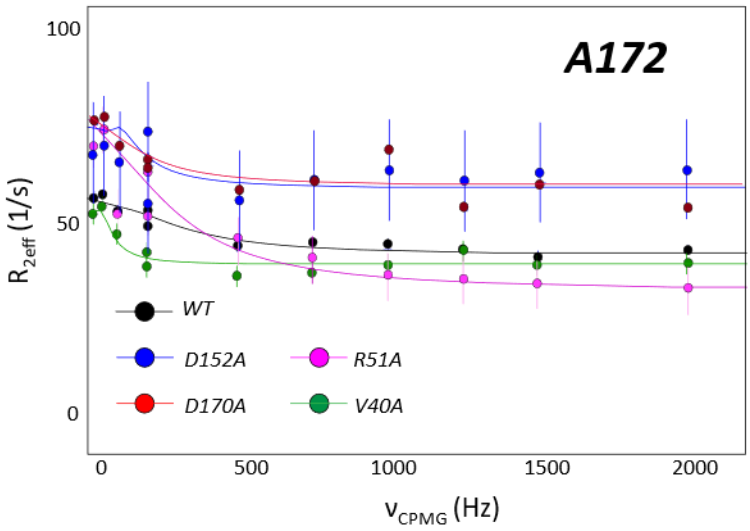

Fig. 3.34 Representative CPMG dispersion curves, shown here for residue A172, a key linker residue bridging the active site to the DFG motif.

Overall, the R_{ex} histograms showed greater similarity between variants than the CSP, hetNOE, and R_2 analyses (**Fig. 3.35**). This suggests that the most robust mutation-induced effects detected here occur primarily in the chemical environment, fast-timescale backbone flexibility, and microsecond-sensitive transverse relaxation regime, rather than as large, uniform changes in millisecond-timescale exchange. Therefore, the CPMG data do not contradict the CSP and relaxation results, but indicate that the strongest dynamic consequences of network mutation are not dominated by a single global millisecond-exchange process.

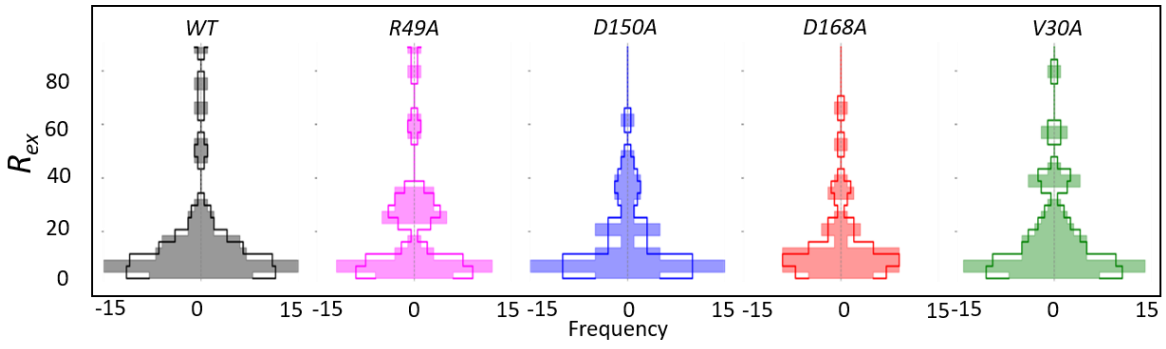

Fig. 3.35 Histogram plots illustrating the global distribution of R_{ex} values across all variants. The wildtype shows a slightly broader distribution of dynamic residues, indicative of a more homogeneous conformational ensemble. In contrast, network-disrupting mutants (e.g., D168A, R49A) display slightly more exchange. The minor

differences hint to any motional changes rather being on timescales faster than the ms regime.

Boxplot comparisons for all the variants (**Fig. 3.36**) show modest changes in R_{ex} distributions. Together, these trends indicate increased backbone plasticity and altered conformational exchange upon mutation of dynamic-network residues. However, the effects are residue-specific and regionally distributed rather than uniformly global.

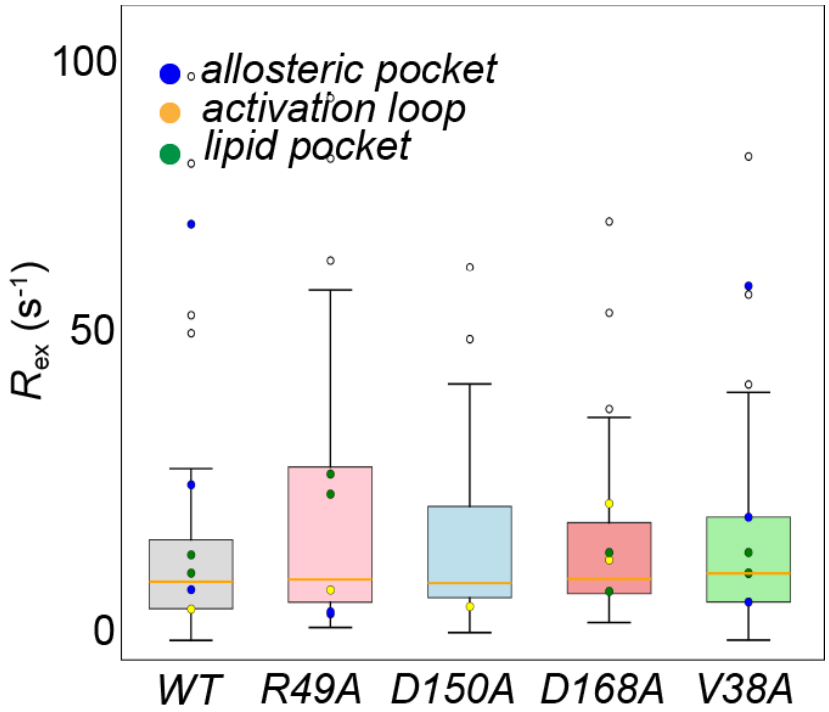

Fig. 3.36 Box plots compare R_{ex} values across WT and mutants, with the median shown in orange. Colored points indicate residues from the activation loop (yellow), allosteric pocket (blue), and lipid pocket/MAP kinase insert region (green), highlighting site-specific contributions of regulatory regions to altered slower-timescale dynamics.

3.9 Conclusion

Together, these results demonstrate that unphosphorylated apo p38α contains an intrinsic dynamic communication network that spans both kinase lobes and includes the MAP kinase insert and lipid-binding pocket. Residues identified as high-centrality nodes by dynamical network analysis were not merely computational

features: their mutation weakened pathway-level correlations and produced broad experimental perturbations in chemical shifts, fast-timescale backbone flexibility, and transverse relaxation behaviour.

The strongest effects were observed for mutations within the predicted network, whereas the V38A control, located outside the network, produced only limited and mostly local changes. This distinction supports the conclusion that the observed perturbations are linked specifically to disruption of allosteric-network residues rather than to alanine substitution in general. The relaxation data further indicate that the effects are regionally distributed rather than uniformly global, with recurrent perturbations in the lipid-pocket/MAP kinase insert region, activation-loop boundary, catalytic-loop region, P-loop/glycine-rich loop, and docking groove.

Ligand-bound simulations showed that sorafenib binding changes the preferred communication routes between regulatory regions and reduces the dependence of these routes on the apo-state network hotspots. Thus, the communication architecture of p38α appears to be state-dependent, with the apo and inhibitor-bound ensembles relying on different patterns of dynamic coupling.

Overall, the combined MD, network-analysis, biochemical, and NMR data support the existence of a residue-level dynamic allosteric network in p38α. These findings provide the basis for the following Discussion, where the implications of this network for kinase regulation, lipid-pocket allostery, and potential allosteric modulation of p38α are considered.

3.10 Discussion

The results presented in this chapter define a residue-resolved dynamic allosteric network within unphosphorylated apo p38α MAP kinase. This network spans both the N- and C-lobes and connects several canonical kinase regulatory elements, including the activation loop, DFG motif, HRD/catalytic-loop region, P-loop, substrate-binding groove, docking groove, and the MAP kinase insert containing the lipid-binding pocket. Importantly, this communication architecture was not inferred from simulations alone. The computationally predicted network was supported by pathway-level correlation analyses, mutational perturbation, biochemical assays, chemical-shift perturbation analysis, and NMR relaxation measurements.

A central conclusion from this work is that p38α regulation cannot be understood solely in terms of local structural elements or static conformational states. Instead, the kinase scaffold appears to be organized as a dynamically coupled system in which residues distributed across distant structural regions contribute to coordinated motion. In the wild-type apo protein, this coupling maintains coherent long-range communication between regulatory sectors. Mutation of high-centrality residues weakens this communication, leading to reduced pathway correlations and altered residue-specific dynamics. This supports a model in which the integrity of the p38α dynamic network depends on a small number of key residues that act as communication relays within the kinase domain.

This framework helps rationalize previous observations on phosphorylation-dependent activation, TAB1-mediated regulation, nucleotide-site control, and kinase dynamic allostery in a residue-specific manner. Local perturbations, such as activation-loop phosphorylation, nucleotide binding, inhibitor binding, or interaction with upstream regulators, can induce changes at distal sites within the kinase by reshaping the underlying conformational ensemble[133]. Because the simulations and experiments described here were performed primarily in the unphosphorylated apo state, they do not reproduce the full phosphorylated, nucleotide-bound, substrate-bound, or TAB1-bound activation pathways. Instead, they define the basal communication architecture from which these regulatory mechanisms may emerge.

This distinction is important. The apo-state network identified here should not be interpreted as a complete model of active p38α signalling. Rather, it represents the intrinsic dynamic wiring of the kinase before regulatory inputs are applied. Such basal wiring may determine how the protein responds to phosphorylation, ligand binding, or protein-protein interactions. In this sense, the network provides a structural-dynamic framework for understanding why perturbations at one site can have consequences at distant regulatory regions.

The effect of mutating central network residues supports this interpretation. In a purely local model of protein dynamics, alanine substitution would be expected to perturb mainly the mutation site and its immediate environment. Instead, mutations at R49, D150, D168, and W207 produced long-range effects on pathway correlations, enzymatic output, chemical shifts, and relaxation parameters. These effects were substantially stronger than those observed for the V38A control, which lies outside the predicted dynamic network. This contrast indicates that the observed perturbations are not a generic consequence of alanine substitution, but are linked

to disruption of residues embedded within the allosteric communication architecture.

The relaxation data further refine this model. Mutation of network residues did not simply destabilize the protein globally. Rather, the effects were regionally distributed and repeatedly involved functionally important sectors, including the lipid-pocket/MAP kinase insert region, activation-loop boundary, catalytic-loop region, P-loop/glycine-rich loop, and docking groove. Reduced heteronuclear NOE values indicate increased fast-timescale flexibility at selected sites, whereas increased R_2 values suggest altered slower conformational fluctuations or exchange contributions. Together, these findings support a model in which disruption of central network residues loosens the coherence of the intrinsic dynamic network, allowing motions in specific regulatory regions to become less coordinated and less constrained.

Several of the identified network nodes have clear functional relevance in p38α biology. D150 is located within the catalytic HRD motif and lies close to the active site. This residue is not only part of the conserved catalytic machinery but has also been implicated in intramolecular interactions relevant for TAB1-induced autoactivation[162]. Its strong effect in the present analysis is therefore consistent with a dual role: it contributes directly to catalytic-site organization and also participates in long-range dynamic coupling.

R49 represents a different type of node. Located in the extended allosteric-pocket region, it is not a canonical catalytic residue, yet its mutation perturbs both computational network properties and experimental dynamics. R49 has also been used as a tool mutation in studies of PRMT1-mediated control of p38α[164]. Its identification here suggests that this region may act as a regulatory communication surface rather than simply as a passive structural element.

D168, the aspartate of the DFG motif, has an especially prominent role. Functionally, this residue is central to the DFG-in/DFG-out switch, ATP/ADP exchange, and catalytic competence[165, 168, 169]. Its mutation is therefore expected to impair kinase function. However, the present data show that the role of D168 extends beyond active-site chemistry. D168A also perturbs distal regions, including the C-lobe and lipid-pocket-associated region. This indicates that the DFG motif is not only a local conformational switch but also a major relay point in the long-range dynamic network of p38α.

W207 provides an important link between the general kinase allostery framework and the MAP kinase-specific lipid-pocket region. W207 lies near the substrate-binding groove and faces the lipid pocket. Its high betweenness centrality, together

with its effect on pathway-level correlations and biochemical output, supports the interpretation that the lipid-pocket region is dynamically integrated into the p38α scaffold. Although W207A could not be analysed by solution-state NMR due to difficulties in expressing a stable triple-labelled construct, the computational and biochemical data still support its role as a key network residue. The absence of NMR data for W207A remains a limitation, but it does not invalidate the broader conclusion that the lipid-pocket region participates in the dynamic network.

The comparison with p38γ and other kinases places the present p38α network within a broader framework of kinase dynamic allostery. Previous studies have shown that conserved kinase motifs, including the DFG segment, HRD motif, hinge region, regulatory spines, and substrate-binding regions, participate in long-range communication[126, 139, 140, 145, 153, 154, 155, 156, 157, 173] . The present work extends this concept to p38α by providing a residue-resolved and experimentally supported dynamic-network map. Importantly, this map explicitly includes the MAP kinase-specific lipid-binding domain and its associated cryptic lipid pocket. Thus, the lipid pocket should not be viewed only as a distal hydrophobic cavity. In the context of apo p38α dynamics, it behaves as part of an integrated communication network coupled to canonical kinase-control elements.

The ligand-bound simulations add another layer to this interpretation. Sorafenib binding altered the preferred communication paths between the allosteric pocket, activation loop, and lipid pocket. In contrast to the apo state, mutation of the same network hotspots did not produce a systematic reduction in cumulative correlations along the ligand-bound wild-type paths. This suggests that inhibitor binding reshapes or partially suppresses the intrinsic apo-state network. Therefore, the communication architecture of p38α is state-dependent. The apo protein and the inhibitor-bound protein do not simply differ by the presence or absence of a ligand; they rely on different patterns of internal dynamic coupling.

This finding is important for interpreting allosteric regulation. It implies that ligand binding can reroute communication through the kinase rather than merely stabilizing or destabilizing pre-existing pathways. However, the present data do not establish whether this rerouting is functionally beneficial, inhibitory, or pharmacologically exploitable in a general sense. That question would require additional ligand series, direct activity measurements under ligand-bound conditions, and pathway-level validation in cellular systems.

The identification of the lipid pocket as part of the dynamic network has potential pharmacological relevance, but this point must be interpreted cautiously. The data

presented here support the conclusion that the lipid-pocket region is dynamically connected to the active-site and regulatory machinery. They do not, by themselves, establish the lipid pocket as a validated drug target. Previous studies showed that lipid-pocket binders can occupy this region, but first-generation or low-affinity ligands have not produced strong effects on kinase activity under all tested conditions[174]. Therefore, the present work should be viewed as providing a mechanistic rationale for further exploration rather than proof of therapeutic tractability.

Nevertheless, the dynamic integration of the lipid pocket makes it an attractive region for future investigation. Unlike the ATP-binding site, which is highly conserved across the kinome, the lipid pocket is associated with the MAP kinase insert and may offer a more kinase-subfamily-specific regulatory surface. The identification of W207 at the rim of this pocket as a high-centrality residue further suggests that this region could be used as a starting point for designing or screening more optimized allosteric modulators. Such efforts would require ligands with improved affinity, defined binding modes, direct functional assays, selectivity profiling, and ideally validation in pathway-specific cellular contexts.

More broadly, this work illustrates how dynamic-network mapping can help identify regulatory regions that may be missed by static structural inspection alone. The residues identified here were not simply the most flexible residues in the crystal structure, nor were they all located in the active site. Instead, their importance emerged from their position within the motional communication network. This highlights the value of integrating molecular dynamics, graph-based network analysis, mutagenesis, biochemical testing, and NMR spectroscopy to study enzyme regulation. Such approaches may be useful not only for identifying allosteric inhibitor sites, but also for engineering enzymes through targeted perturbation of dynamic communication pathways.

Several limitations should also be recognized. First, the MD simulations, although extensive, sample only selected regions of the conformational landscape and were analysed over the final 200 ns of each replica. Second, the network model depends on methodological choices, including residue representation, correlation metrics, community-detection procedures, and path definitions. Third, the NMR analysis could not include W207A due to expression limitations in deuterated minimal media. Fourth, the CPMG relaxation-dispersion data provided only limited support for strong mutation-dependent differences on the millisecond timescale, mainly because of experimental uncertainty in individual dispersion curves. Finally, all experiments

were performed on unphosphorylated apo p38α or selected ligand-bound states in vitro, which does not fully reproduce the cellular context of p38α regulation.

These limitations do not weaken the central conclusion, but they define its scope. The work does not claim to provide a complete model of p38α activation in cells, nor does it prove that the lipid pocket is immediately druggable. Instead, it establishes that unphosphorylated apo p38α contains a measurable and perturbable dynamic communication network, and that this network includes both canonical kinase regulatory motifs and the MAP kinase-specific lipid-pocket region.

In summary, this chapter identifies and maps a dynamic allosteric network within p38α MAP kinase. The network spans both kinase lobes, includes the activation loop and inter-lobe regulatory elements, and explicitly incorporates the MAP kinase insert and lipid-binding pocket. By combining molecular dynamics simulations, dynamical network analysis, mutagenesis, biochemical assays, and NMR spectroscopy, this work identifies specific residues that act as key relays for long-range communication within the kinase scaffold. Mutation of these residues weakens pathway-level correlations and alters residue-specific dynamics across distant regulatory regions, supporting their role as central components of the allosteric network.

These findings provide a residue-level framework for understanding how p38α integrates regulatory signals through coordinated dynamics. They also support the broader view that kinase regulation is not governed only by static active and inactive structures, but by dynamic communication across the conformational ensemble. The identification of the lipid pocket as an integrated component of this network opens a route for future studies aimed at testing whether distal, dynamically coupled sites can be exploited for selective allosteric modulation of p38α.

4. DFG-loop-dependent allostery extends to water dynamics in p38α

This chapter extends the analysis of DFG-loop-dependent allostery by examining how the DFG-mutant alters water dynamics around p38α. In contrast to the previous chapter, which focused primarily on residue-level dynamic communication within the kinase scaffold, this section investigates whether mutation-induced allosteric effects are also reflected in the surrounding hydration environment. The results presented here are unpublished and are currently in preparation. Therefore, this chapter should be considered a preliminary but mechanistically important extension of the broader p38α allostery project.

4.1 Introduction

The conceptual understanding of water in kinase biology has developed substantially over time. Early studies suggested that catalytic competence depends, in part, on water molecules located within highly conserved structural environments[175]. Subsequent structural analyses of protein kinase-A supported this view by identifying recurrent water molecules that maintain similar hydrogen-bonding patterns with conserved catalytic residues as well as with peripheral, non-conserved sites across different crystal forms[176].

More broadly, previous work has shown that water plays an active role in determining biomolecular architecture, topology, and function. Rather than acting merely as a passive solvent in which kinetic and thermodynamic processes occur, water can contribute directly to entropic and enthalpic stabilization of protein structures. Protein stability is therefore closely linked to internal and surface hydrogen-bonding networks, within which ordered water molecules can play important structural and functional roles. Conserved waters should, in this sense, be considered integral components of crystallographic protein models.

The positions of water molecules within hydrogen-bonding networks are often highly ordered rather than random[177]. Even though they usually jump between these defined places on the ns timescale, this supports the view that such waters can act as functional elements that help shape protein structure and influence conformational dynamics[178]. The interplay between site-specific protein motions and hydration-shell behaviour is therefore central to understanding protein dynamics. In particular, fluctuations within the hydration shell are mutually interconnected with the intrinsic dynamical behaviour of proteins[179].

Protein kinase catalysis is tightly linked to intrinsic conformational dynamics, which are coordinated by an interconnected set of regulatory structural elements[180]. A typical protein kinase contains a bilobal catalytic core, with the smaller N-lobe and larger C-lobe forming the ATP-binding cleft between them. Key regulatory elements include the catalytic spine, regulatory spine, activation loop, catalytic loop, glycine-rich P-loop, hinge region, αC-helix, and the inter-lobe connector that couples motions between the two lobes.Within the N-lobe, the P-loop, β-sheet core, αC-helix, and gatekeeper residue play central roles in organizing the nucleotide-binding site. The gatekeeper residue is particularly important because it controls access to a hydrophobic region adjacent to the ATP-binding cleft and strongly influences inhibitor binding. Mutations at this position frequently contribute to resistance against ATP-competitive inhibitors[181]. In addition to its steric role, the gatekeeper

site is also a major determinant of local hydration, because it helps organize conserved water molecules within the kinase active-site environment.

Hydration at the gatekeeper region has emerged as an important regulator of kinase inhibitor binding and resistance. Replacement of a gatekeeper threonine by bulkier hydrophobic residues, commonly isoleucine or phenylalanine, can sterically close the W1/W2 water-containing pocket and displace ordered solvent molecules. This effect has been observed in long-timescale molecular dynamics simulations and supported experimentally by site-selective infrared spectroscopy[182]. A related resistance mechanism involves charge inversion in the activation loop, which can reshape the electrostatic environment that stabilizes internal waters and thereby alter their residence lifetimes[183]. Other mutations may change pocket volume or modify pocket-breathing motions, producing either more persistent, tightly retained hydration waters or faster solvent exchange[184]. In some cases, introduced polar side chains may also partially substitute for the hydrogen-bonding role of conserved water molecules, thereby perturbing ligand-mediated hydrogen-bonding networks and reducing inhibitor affinity[182].

Ligand–water interactions in kinase active sites can be broadly grouped into three major modes. First, in water-bridging interactions, ligands exploit a preorganized solvent network by preserving conserved waters and using them as mediators of hydrogen bonding. For example, inhibitors such as bosutinib can retain conserved W1/W2 waters and complete a hydrogen-bonding network involving the gatekeeper threonine and Asp381[185]. Second, some ligands act through water displacement, hydrophobic or bulky ligand substituents expel structured waters from the pocket. This can release entropically constrained waters into bulk solvent and thereby improve ligand potency, as shown for quinazoline analogues designed to occupy the W1 cavity in cyclin-G-associated kinase[186]. Third, some inhibitors promote water ordering around the binding site. Type II inhibitors, for instance, can clamp the activation loop and immobilize peripheral waters, imposing a more ordered and lower-entropy solvent shell. This entropic penalty contributes to the stronger temperature dependence observed for some type II scaffolds compared with type I inhibitors[181].

Even though in particular for crystallographic studies, the insights are limited to water with fixed position, together, these examples show that kinase regulation and inhibitor binding are not determined only by protein structure and ligand chemistry, but also by the local solvent landscape. Conserved waters, displaced waters, and newly ordered hydration shells can all influence binding thermodynamics, inhibitor selectivity, and resistance. Thus, hydration dynamics at regulatory sites such as the gatekeeper region should be considered an active component of kinase function rather than a passive background feature.

Surface-exposed residues can receive magnetization from water, and the efficiency of this process depends on several factors, including the lifetime of water–protein interactions, local correlation times, and exchange with nearby labile groups such as hydroxyls. In contrast, buried solvent molecules occupy internal hydration sites, where they can form highly ordered hydrogen-bonding networks. Such internal water clusters are increasingly recognized as structural and dynamic elements that influence packing density, modulate loop flexibility, and contribute to the propagation of allosteric signals[187, 188].

High-resolution crystallographic studies of uninhibited kinases, supported by molecular dynamics simulations, have identified recurrent water molecules within conserved kinase environments. Some of these waters are positioned close to the catalytic centre, where they form hydrogen bonds with key functional residues and contribute to active-site stabilization. One such water-associated interaction network involves the magnesium-coordinating aspartate of the DFG motif, corresponding to Asp168 in p38α, which is essential for productive ATP positioning and phosphoryl transfer. Additional ordered waters occupy neighbouring internal pockets, where they help stabilize the substrate-binding cleft and maintain the local conformational architecture required for enzymatic activity[176].

Asp168 forms part of the conserved Asp-Phe-Gly motif, a central regulatory element of the kinase activation loop. The DFG motif acts as a conformational switch whose transition between DFG-in and DFG-out states is tightly coupled to kinase activation and inhibition. In the catalytically competent DFG-in state, the aspartate side chain coordinates the Mg^{2+}-ATP complex and supports phosphoryl transfer (**Fig. 4.1**).

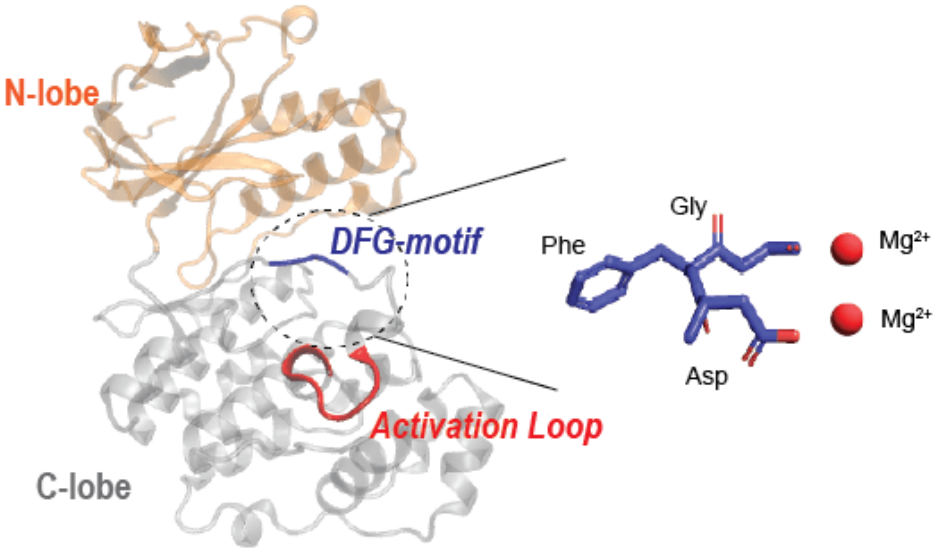

Fig. 4.1 Aspartate of the DFG motif coordinates with Mg^{2+} to support phosphoryl transfer.

In the DFG-out state, the phenylalanine side chain moves away from its active conformation, the nucleotide-binding environment is disrupted, and the activation loop adopts an inactive arrangement[158, 189] (**Fig. 4.2**). Modulation of this conformational switch therefore provides a direct route for controlling kinase activity and allosteric signalling[190]. The differences in crystal waters are also shown in **Fig. 4.2**.

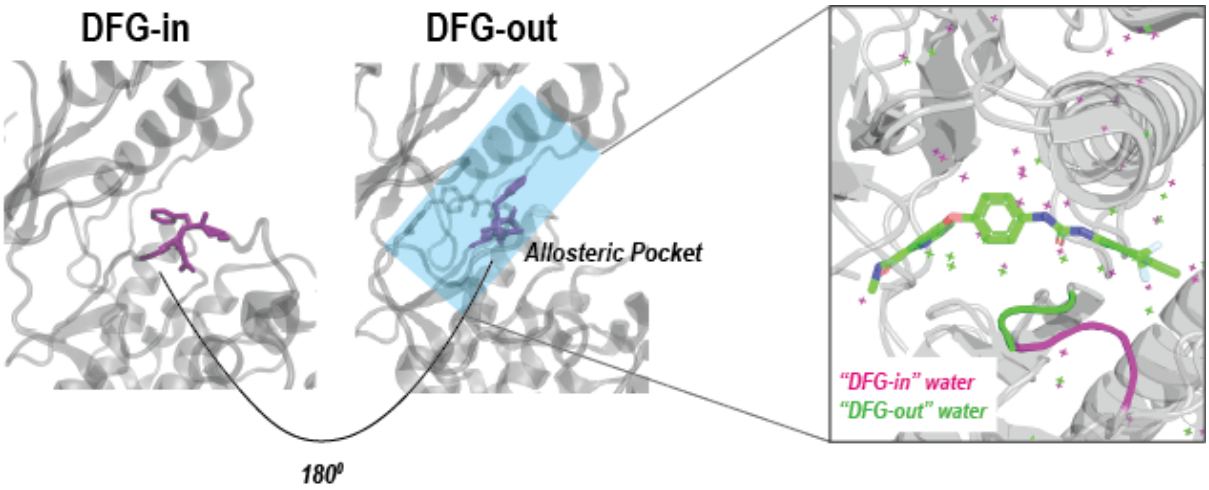

Fig. 4.2 DFG-in/out orientations create the allosteric pocket with different structural crystal waters.

In p38α, the DFG aspartate when mutated to alanine shows the hint of an allosteric coupling when inhibitor-bound crystal structures are studied. Regorafenib acts as our inhibitor here. Mutation causes the pyridyl ring to flip, which corroborates the notion that D168 is an initiator of allosteric coupling (**Fig. 4.3**). Change of the ligand also affects the ring "conformation ensembles" in similar ways (**Fig. 10.10**, Appendix). Thus, the regorafenib ring rearrangement observed here complements the previous chapter, where D168A was shown to perturb dynamic network communication, further supporting D168 as a potential allosteric node in p38α.

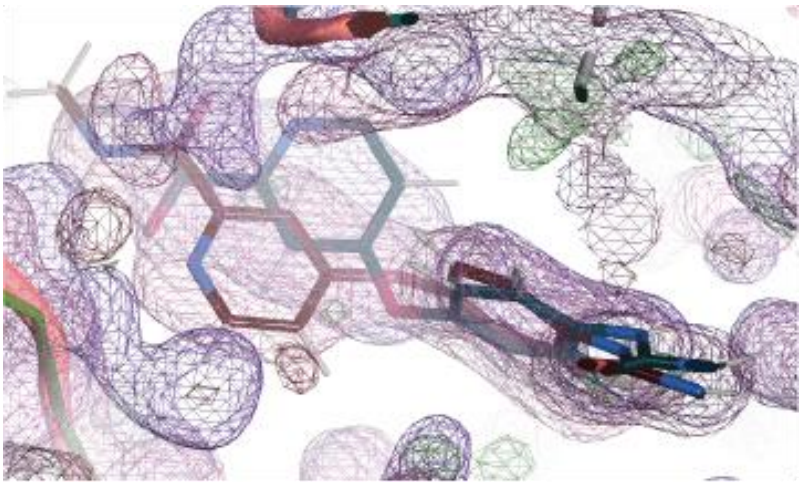

Fig. 4.3 Pyridyl ring flip of regorafenib upon D168A mutation hinting to allostery

When the crystal waters around the allosteric pockets of the wildtype and the mutant are investigated, the crystal waters show some degree of conservation in this region, the ring flip causing some space to be void, allowing substantial water molecules to occupy it for the mutant. Around the lipid pocket, most crystal waters are rearranged in the mutant, suggesting that local water redistribution may reflect the allosteric effect of D168A and serve as a structural reporter of altered coupling. D168 appears to occupy a particularly important position at the interface between catalysis, conformational switching, and hydration. Computational studies, including JAWS and metadynamics-based analyses, have identified high-occupancy water clusters in the ligand-binding region of p38α that form recurrent hydrogen bonds with conserved side-chain and backbone atoms[191, 192]. In these models, D168 can act as a hydrogen-bond acceptor for conserved water molecules and may adopt alternative rotameric states to accommodate the local hydration network. Thus, the DFG aspartate is not only a catalytic residue but may also contribute to organizing the surrounding solvent environment.

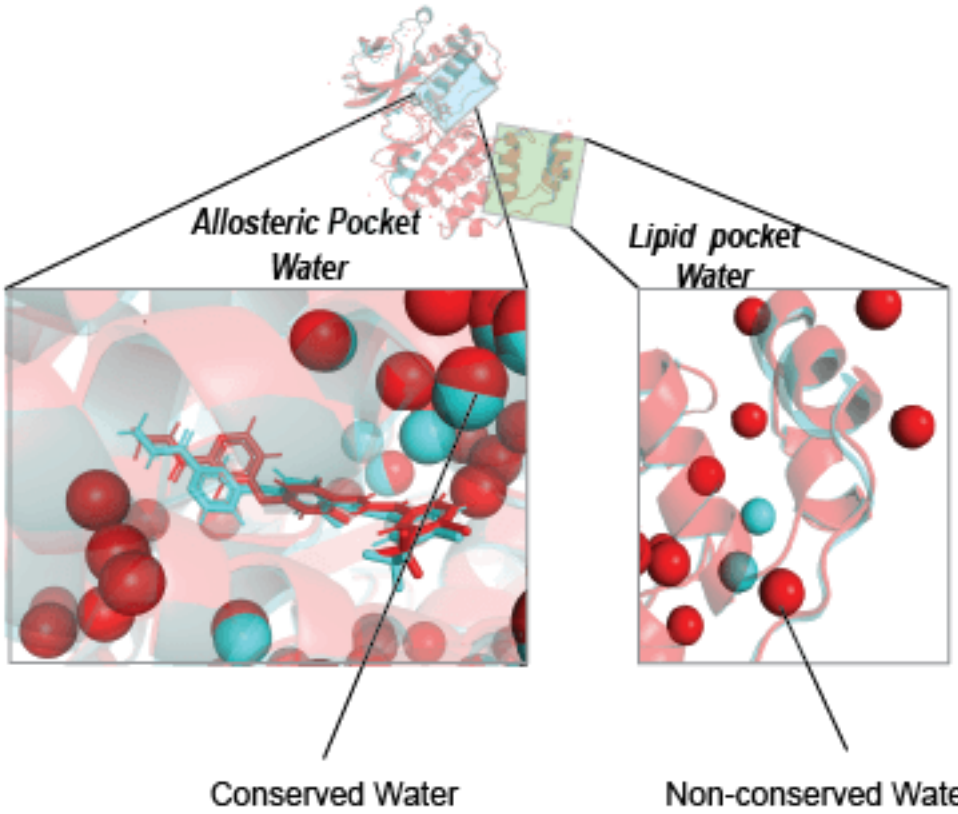

Fig. 4.4 Crystal waters around the allosteric pocket and lipid pocket of the wildtype (blue) and D168A (red) showing the trends in conservation and changes upon mutation.

Because the DFG motif has also been implicated in long-range allosteric communication, we asked whether perturbation of Asp168 affects hydration beyond the above crystallographic insights. In this chapter, we compare wild-type p38α and

the D168A mutant to determine how mutation of this central DFG residue alters site-specific water–protein interactions. By integrating NMR spectroscopy, X-ray crystallography, and molecular dynamics simulations, we examine whether DFG-dependent allostery extends into the hydration shell and whether changes in local catalytic-site hydration are coupled to broader water-dynamic rearrangements around the kinase.

4.2 Differences in thermal stability on DFG-loop mutation

We first examined whether mutation of the DFG-loop aspartate alters the thermal response of p38α using temperature-ramped MD simulations. The systems were heated gradually to 423 K over 1 μs and subsequently maintained at 423 K for an additional 1 μs[193] (**Fig. 4.5A**). Three independent replicas were performed for each system to assess the reproducibility of the observed trends. Across all replicas, D168A displayed lower backbone RMSD values than WT during the elevated-temperature regime, indicating reduced global structural deviation under thermal stress (**Fig. 4.5B**). This suggests that mutation of the conserved DFG-loop aspartate alters the thermal response of the kinase domain and makes the mutant less prone to large-scale temperature-induced conformational excursions within the simulated timescale. Given the established role of the DFG motif as a conformational switch that couples activation-loop organization with kinase-domain dynamics, this altered thermal behaviour is consistent with D168 acting as a key regulator of structural flexibility in p38α. Importantly, these simulations report relative resistance to thermal perturbation rather than direct thermodynamic stability; therefore, the result is interpreted as enhanced apparent structural robustness of D168A under the applied temperature-ramping protocol.

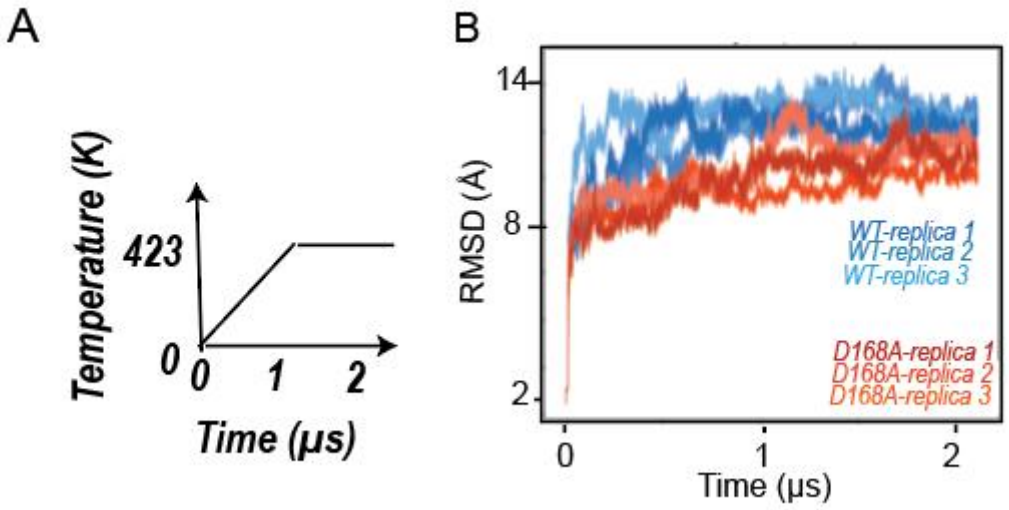

Fig. 4.5 A) Schematic of the temperature-ramping simulation protocol, in which the system was gradually heated to 423 K during the first microsecond and then maintained at 423 K for an additional microsecond to probe high-temperature structural adaptation. **B**) Temperature ramping simulations performed in triplicate for wild-type p38α and the D168A mutant show that the wild type consistently reaches higher RMSD values than D168A, indicating greater structural deviation during heating and suggesting that the mutant better preserves its global fold under thermal stress.

RMSF analysis across the three independent replicas further supported the different thermal responses of WT and D168A p38α. The residue-wise RMSF profiles showed that the WT undergoes a more uniform increase in flexibility upon heating, including within regions that form part of the kinase core **Fig.10.1** (Appendix). To capture how these fluctuations evolve during the temperature-ramping protocol, RMSF-over-time heat maps were generated. Since simulation time is directly coupled to the temperature increase in this protocol, these maps provide a residue-resolved view of how local flexibility changes across the applied temperature range (**Fig. 4.6**). In the WT simulations, increased RMSF was particularly evident around the activation loop and neighbouring core regions, indicating that the native DFG-loop aspartate permits temperature-induced flexibility close to the activation segment. This is consistent with the role of the DFG motif as a structural and dynamic hub that links the activation loop, catalytic spine, and ATP-binding region (**Fig.4.6**). Difference heat maps further showed that RMSF values were generally higher in WT than in D168A, supporting the conclusion that WT is more susceptible to local and global thermal fluctuations under the applied heating protocol. In contrast, D168A showed

a more restricted and redistributed fluctuation pattern. Rather than displaying the same strong increase around the activation loop, the mutant showed greater average RMSF increases around the lipid-pocket region and at the N- and C-terminal segments. This suggests that mutation of the conserved DFG aspartate dampens thermal flexibility near the mutation-proximal activation-loop region, while shifting part of the thermal response toward more distal regions of the kinase domain. Together, these analyses indicate that heating affects WT and D168A through different dynamic pathways. In WT, the strongest temperature-dependent flexibility is concentrated around the DFG/activation-loop region, whereas in D168A, flexibility appears to be redistributed toward distal regions[194], including the lipid pocket and termini. Therefore, the D168A mutation does not simply reduce flexibility globally; rather, it rewires the spatial pattern of thermal fluctuations across the kinase domain.

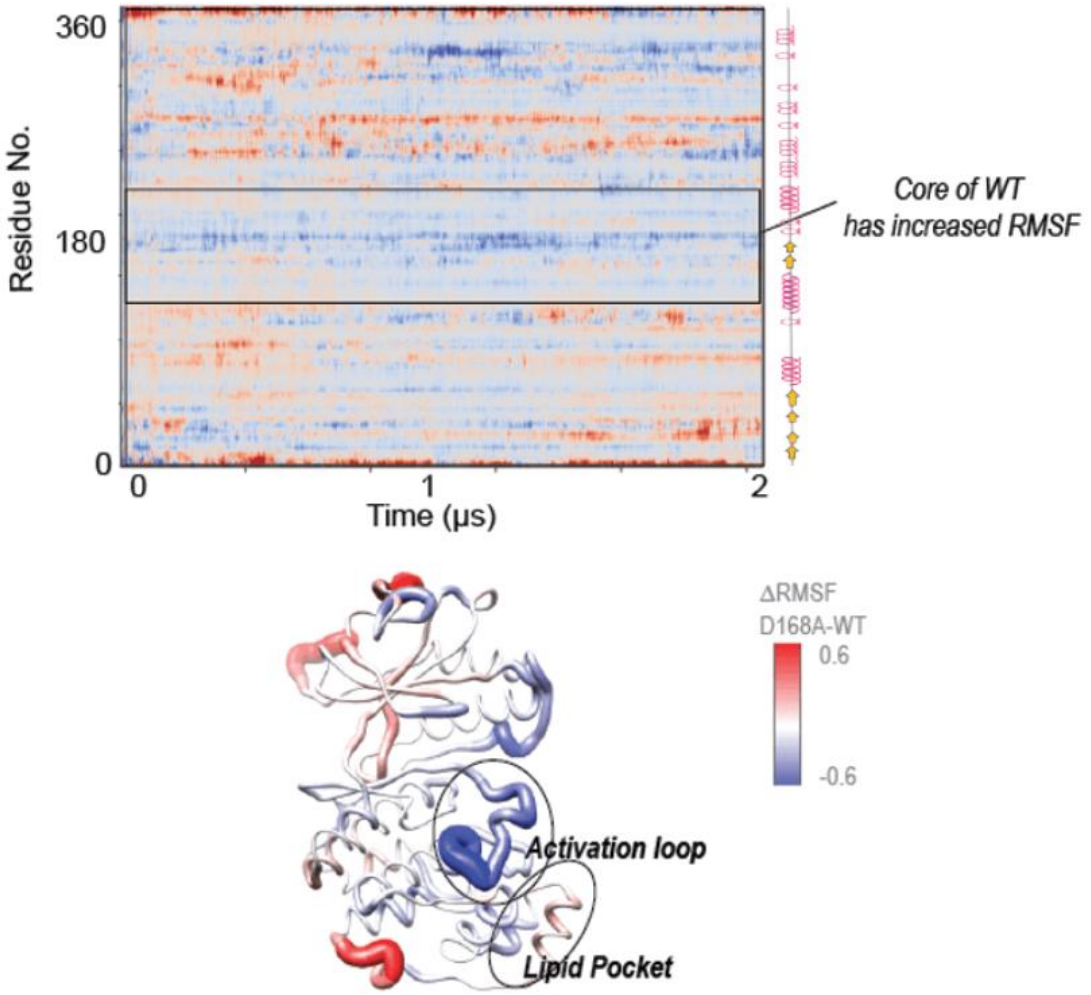

Fig. 4.6 Time-resolved wRMSD/RMSF heatmap analysis further illustrates the differential response to heating. In the wild type, flexibility progressively increases

with temperature, particularly in the core and activation loop. In contrast, the D168A mutant displays more limited temperature-dependent changes, with noticeable increases largely confined to helical regions, suggesting a more thermally resilient structural framework.

When secondary structure was monitored over the full simulation trajectory, D168A retained a higher average helical content than the WT. In the WT simulations, increasing temperature was associated with a marked loss of helical structure, accompanied by a corresponding increase in β-strand content (**Fig.4.7**). This shift suggests that thermal stress promotes partial unfolding or non-native backbone rearrangements in the WT kinase domain. The increase in β-structure may reflect the emergence of aggregation-prone conformational states, although this interpretation should be made cautiously because aggregation itself cannot be directly inferred from a single-protein MD simulation. By contrast, D168A maintained a higher helical fraction throughout the temperature-ramping protocol and showed gain of extended (strand-like) conformations. This indicates that the mutant preserves its native-like secondary-structure elements more effectively under thermal stress. Together with the lower RMSD and redistributed RMSF profile, these data suggest that D168A exhibits enhanced apparent structural robustness during heating. Mechanistically, the D168A substitution may alter the local hydrogen-bonding environment and water-mediated interaction network around the DFG/activation-loop region. This could reduce temperature-induced backbone rearrangements near the kinase core and help preserve helical structure during thermal perturbation.

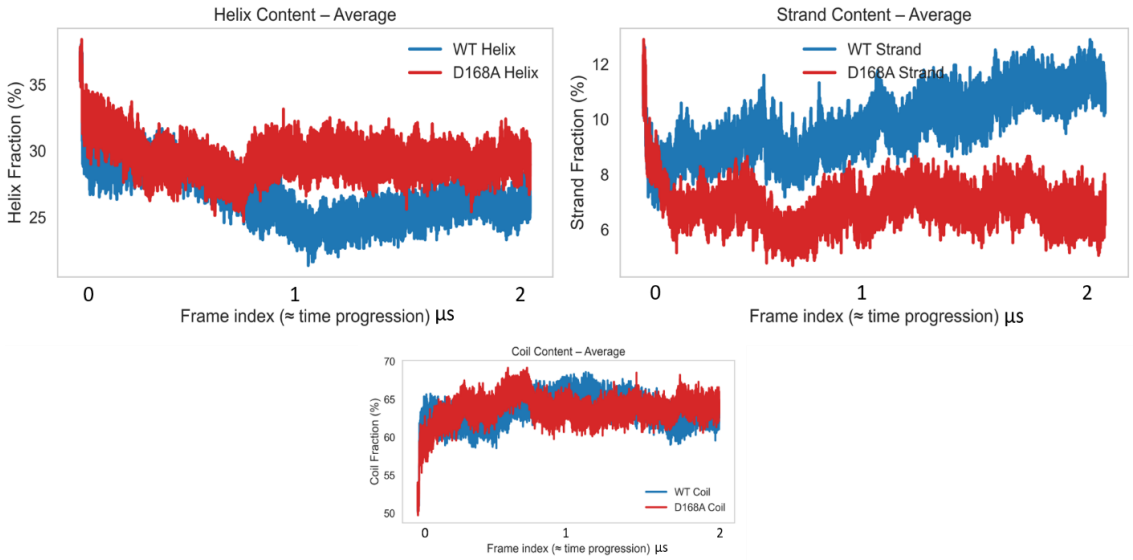

Fig. 4.7 Change in the secondary structure in response to the temperature ramped simulations.

After characterising the general behaviour of the temperature-ramped trajectories, the final 100 ns of each simulation were used for generalised correlation analysis. This time window corresponds to the phase in which the systems were maintained at 423 K, allowing cross-lobe communication to be assessed under sustained thermal stress. Generalised correlations were calculated between residues of the N- and C-lobes and mapped onto the kinase structure (**Fig. 4.8**). To focus specifically on long-range inter-lobe coupling, only residue pairs connecting opposite lobes were visualised. The corresponding correlation values, including the standard deviation across the three replicas, are reported in **Table 4.1**. At 423 K, D168A retained stronger cross-lobe correlations than WT, particularly around the beginning of the C-lobe and the N-terminal region of the DFG motif. The strongest differences were observed near the E163–I166 region, suggesting that mutation of D168 helps preserve communication between the lobes close to the DFG/activation-loop interface under thermal stress. Correlations involving the hinge region were observed in both WT and D168A; however, the correlation values were consistently higher in D168A across the replicas. Together, these results suggest that the D168A mutant does not merely reduce structural fluctuations during heating, but also preserves a higher degree of inter-lobe dynamic coupling at elevated temperature.

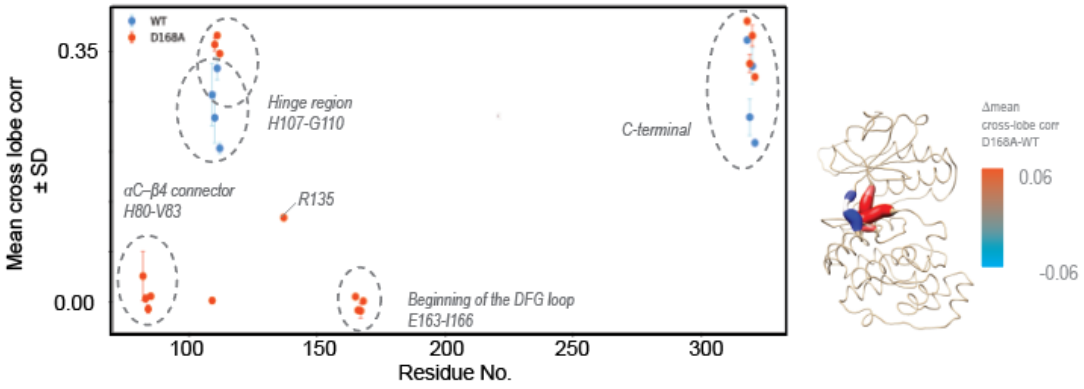

Fig. 4.8 Analysis of cross-lobe correlations at 423 K demonstrates that coupling between the N- and C-lobes, particularly across the hinge region, is stronger in D168A than in the wild type, suggesting that the mutation does not affect long-range intramolecular communication upon temperature rise.

Table 4.1 N-C lobe cross correlation values with errors

Residue	WT_Mean	WT_SD	D168A_Mean	D168A_SD
80	0	0	0.012522	0.007166

81	0	0	0.012119	0.007165
82	0	0	0.01631	0.007783
83	0	0	0.003978	0.003924
107	0.009469	0.006773	0.004695	0.004402
108	0.009103	0.006277	0.009396	0.006479
109	0.012491	0.0085	0.006316	0.006271
110	0.011827	0.00829	0.006143	0.006082
135	0	0	0.005093	0.00537
163	0	0	0.022532	0.011104
164	0	0	0.017205	0.009824
165	0	0	0.010849	0.007519
166	0	0	0.011305	0.007658
316	0.006581	0.006241	0.006633	0.00629
317	0.01202	0.008043	0.012288	0.008222
318	0.008954	0.006435	0.009062	0.006511
319	0.004286	0.0043	0.004408	0.004423

Overall correlation maps were calculated for the final 100 ns of the 2 μs temperature-ramped trajectories, corresponding to the period in which the systems were maintained at 423 K. Difference maps between WT and D168A were then generated to identify mutation-dependent changes in residue–residue coupling under sustained thermal stress (**Fig. 4.9A**). Only statistically significant differences were retained for visualisation in the correlation maps and mapped onto the structure (**Fig. 4.9B**). The correlation values with their respective p values are represented in the **Table 10.9** (Appendix). At 423 K, D168A showed higher correlation values across most regions of the kinase domain compared with WT, suggesting that the mutant preserves a more coordinated dynamic network under thermal stress. Several long-range correlations were particularly prominent in the mutant, including contacts within the N-lobe, such as L87–F99, and within the C-lobe, such as K235–L240. These correlations indicate that D168A does not simply reduce local flexibility near the DFG motif, but also alters dynamic coupling across distal regions of the kinase domain. In contrast, a smaller subset of correlations around the allosteric pocket remained stronger in WT. This suggests that although D168A generally enhances or preserves correlation networks at elevated temperature, some WT-specific coupling around the allosteric pocket is lost or weakened upon mutation. Importantly, the mutant showed increased correlations around the lipid-pocket region, consistent with the RMSF analysis and the earlier observation that D168A redistributes temperature-dependent flexibility toward distal sites. Together, these results support the idea that D168A has a long-range effect on the dynamic architecture of p38α.

Rather than producing a purely local perturbation around the DFG loop, the mutation reshapes the correlation landscape across the kinase domain, enhancing coupling in regions such as the lipid pocket while modifying communication around the allosteric pocket.

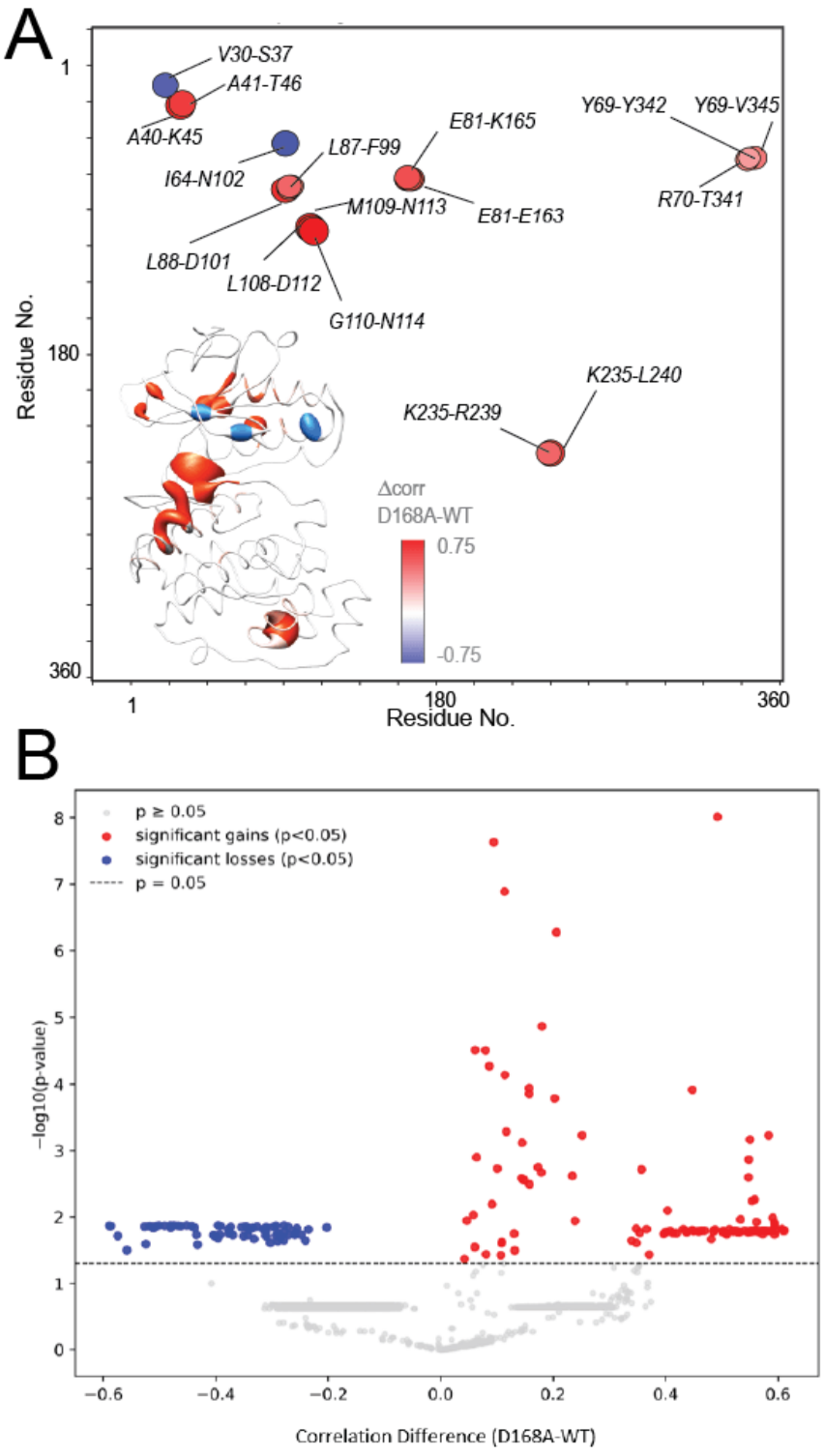

Fig. 4.9 A) Correlation analysis at 423 K reveals clear differences in residue-residue coupling between wild type and D168A. The mutant retains stronger correlated

motions than the wild type, even under high-temperature conditions, indicating preservation of coordinated internal dynamics. **B**) p values to understand significant gains and losses.

Correlation analyses were also performed to compare how WT and D168A respond to elevated temperature. In addition to the temperature-ramped simulations, 2 μs simulations were carried out under standard temperature conditions, and residue–residue correlations were calculated from the final 100 ns of each trajectory. Difference maps were then generated by comparing the normal-temperature simulations with the temperature-ramped simulations, allowing temperature-induced changes in dynamic coupling to be assessed separately for WT and D168A (**Fig. 4.10**). In WT, elevated temperature caused a broad loss of residue–residue correlations, consistent with thermal disruption of coordinated motions across the kinase domain. This loss was particularly evident across several inter-regional contacts, although some correlations were retained or increased around the N-lobe, as well as around the C-lobe contact involving residues 284–288. Overall, the WT response therefore follows the expected trend: increasing temperature weakens coordinated residue motions and disrupts the native dynamic network. The D168A mutant showed a different response. Although some significant correlation losses were also detected, these were fewer than the significant gains assessed using FDR-corrected p-values together with Z-score-based filtering, to reduce false-positive residue-pair correlations. This ensured that only correlation changes showing both statistical significance and sufficient deviation from the overall distribution were retained for interpretation (**Fig. 10.16,** Appendix). The strongest gains were observed around the hinge region and within the C-lobe, particularly near the lipid-pocket region, including the 236–241 contact. This suggests that D168A does not respond to heating simply through a collapse of correlations. Instead, elevated temperature appears to strengthen selected dynamic couplings in the mutant, especially in regions distal to the mutation site. Together, these results indicate that D168A displays an altered temperature-dependent correlation response compared with WT. While WT primarily loses coordinated motions at high temperature, D168A shows a redistribution and partial strengthening of correlations, especially around the hinge and lipid-pocket regions. This behaviour supports the idea that mutation of the DFG-loop aspartate has long-range allosteric consequences, reshaping how the kinase domain responds dynamically to thermal stress.

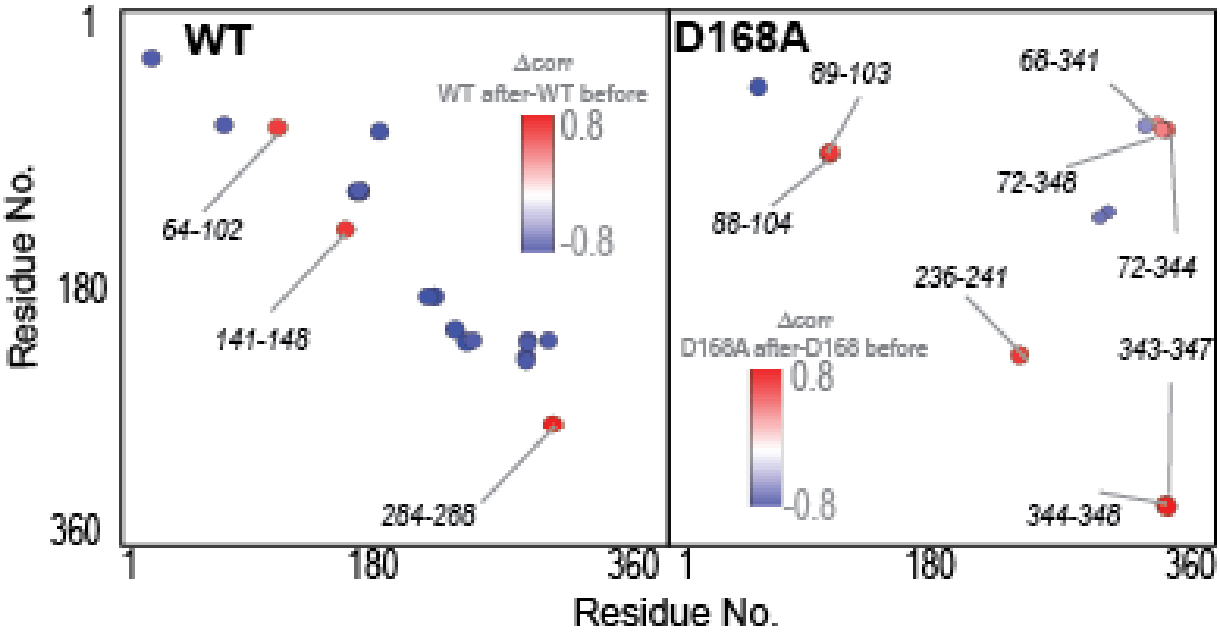

Fig. 4.10 Comparison of correlation patterns before and after heating shows that the wild type loses substantially more correlation upon thermal stress, whereas D168A retains a larger fraction of its original coupling network, consistent with a more robust and less heat-sensitive dynamic architecture.

The simulation-based assessment of thermal response was complemented by experimental melting-temperature measurements using nanoDSF under two buffer conditions. Measurements were performed in HEPES buffer at pH 7 and PBS buffer at pH 8 to test whether the thermal stability of WT and D168A was influenced by pH or buffer composition. During the nanoDSF experiment, the temperature was gradually increased to 90 °C to induce protein unfolding and expose buried aromatic residues. Changes in intrinsic tryptophan and tyrosine fluorescence were monitored, and the fluorescence ratio before and after unfolding was used to determine the melting temperature. The melting temperature was defined as the midpoint of the unfolding transition, corresponding to the temperature at which approximately half of the protein population is unfolded, and was extracted from the first derivative of the fluorescence-ratio curve. Consistent with the temperature-ramped MD simulations, D168A showed a higher melting temperature than WT under both buffer conditions. The mutant displayed melting temperatures of 50.16 °C in HEPES pH 7 and 50.25 °C in PBS pH 8, indicating minimal buffer- or pH-dependent variation. In contrast, WT showed lower melting temperatures of 45.38 °C and 47.45 °C under the same respective conditions, suggesting both reduced thermal stability and a stronger dependence on buffer environment. Together, the nanoDSF data experimentally support the simulation-derived observation that D168A is more resistant to thermal perturbation than WT. While the MD

simulations indicated reduced structural deviation, altered RMSF redistribution, and better preservation of secondary structure in D168A, the nanoDSF measurements confirm that this mutation also increases the apparent melting temperature of the protein. These results suggest that mutation of the DFG-loop aspartate not only perturbs the allosteric communication network of p38α but also rewires the stability landscape of the kinase domain, leading to enhanced thermal resilience.

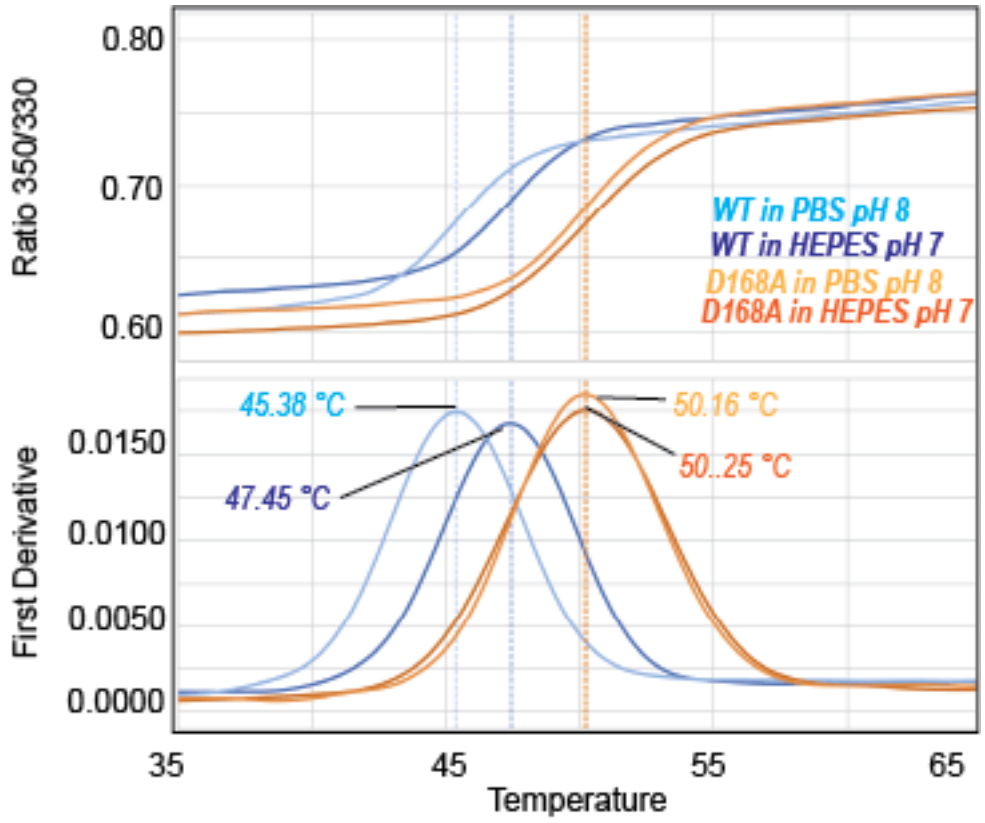

Fig. 4.11 nanoDSF melting analysis shows that D168A has a melting temperature approximately 5 °C higher than the wild type and is less sensitive to pH changes. In contrast, the wild type exhibits a more pronounced pH-dependent shift in thermal stability, indicating greater susceptibility to environmental perturbation.

4.3 Water residence times between different pockets change upon mutation

We extended the stability analysis to examine how the D168A mutation affects local water dynamics. Experimental 3D ^{15}N-edited NOESY provides a powerful approach to detect water molecules that remain in close proximity to specific

backbone amide groups. In NOESY spectra, cross peaks arise from through-space nuclear Overhauser effects between protons that are spatially close. In ^{15}N-edited NOESY experiments, water–amide cross peaks can be observed around the water resonance at approximately 4.6–4.8 ppm, depending on temperature and buffer conditions. It should be noted that hydroxyl-containing side chains or buffer components can also give rise to NOESY cross peaks in this spectral region, and these peaks may not always be easily distinguished from true water–amide cross peaks. However, because the WT and D168A samples have essentially the same protein sequence, apart from the D168A substitution, comparative differences in cross-peak intensity or persistence remain meaningful indicators of altered local hydration or exchange behaviour.

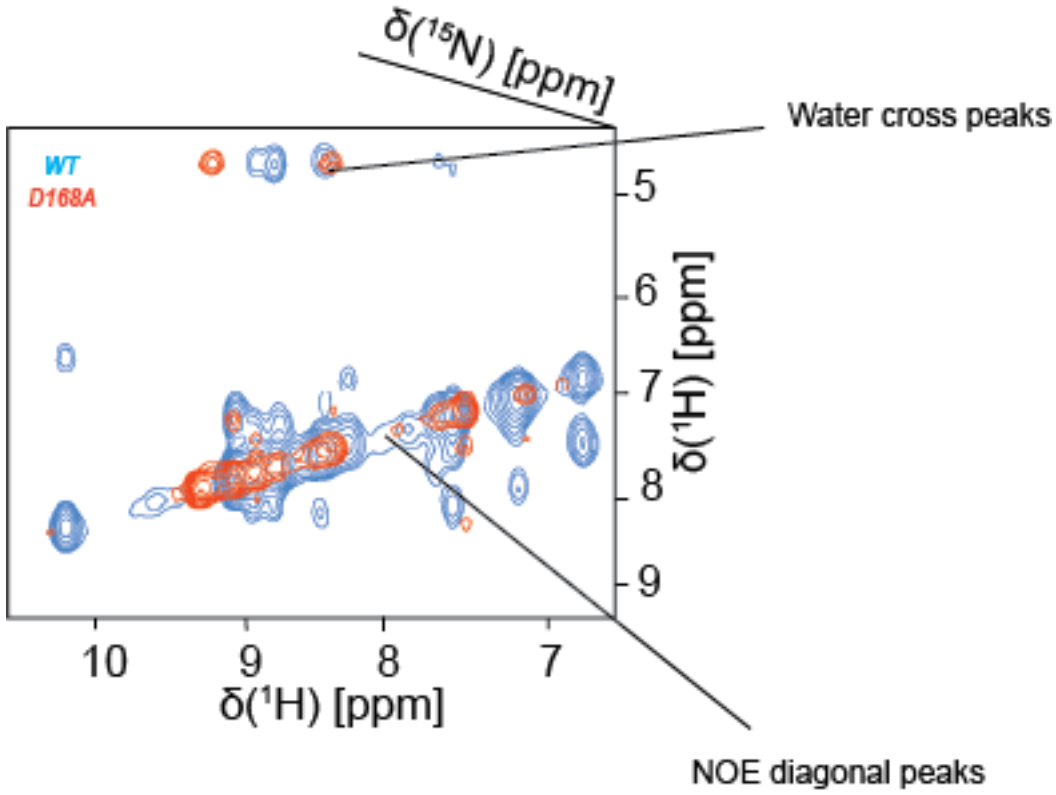

Fig. 4.12 Overlay of NOESY spectra acquired for wild-type p38α and the D168A mutant, highlighting differences in water-related cross peaks between the two proteins.

Quantification of the water–amide cross-peak intensities revealed distinct hydration patterns in WT and D168A. In WT, residues within and around the activation loop showed stronger water-peak intensities than in the mutant, suggesting a greater presence of locally ordered or longer-residing water molecules near this region (**Fig. 4.13**). This indicates that the native DFG-loop aspartate supports a hydration environment around the activation segment that is partially disrupted or weakened

upon mutation. In contrast, residues around the lipid-pocket region showed stronger water-peak intensities in D168A than in WT. This suggests that the mutation does not simply reduce hydration globally, but redistributes the local water environment across the kinase domain. Specifically, D168A appears to reduce water-associated signals near the activation loop while enhancing them around the distal lipid-pocket region. Together, these intensity differences support the idea that the DFG-loop mutation has long-range effects on the hydration landscape of p38α. The altered water-peak intensities are consistent with the simulation-based observation that D168A reshapes the dynamic coupling and flexibility of distal regions. Thus, the mutation appears to reorganize not only the protein's internal dynamic network, but also its surrounding hydration environment.

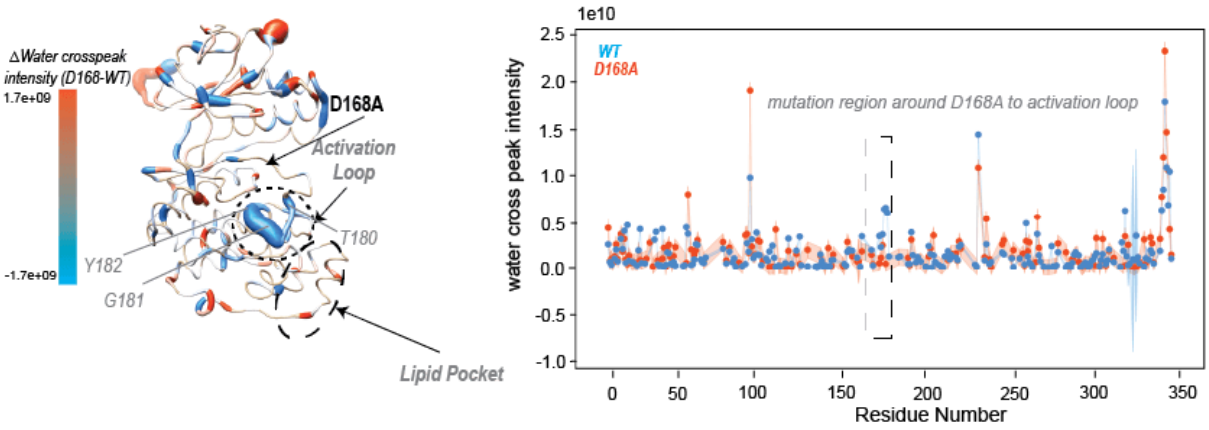

Fig. 4.13 Residue wise water cross peak intensities, also plotted in the protein structure.

To account for differences in sample concentration and overall signal intensity, the water–amide cross-peak intensities were normalised against the corresponding diagonal peak intensities. This ratio-based normalisation reduces the influence of residue-specific peak intensity differences, sample concentration, and general spectral variability, allowing a more reliable comparison of local hydration signatures between WT and D168A, the comparison in the **Fig. 10.17** (Appendix). After normalisation, the activation-loop region still showed stronger water-associated signals in WT than in D168A, indicating that the native protein retains a more pronounced hydration signature around the activation segment (**Fig. 4.14**). In contrast, residues around the lipid pocket displayed higher normalised water–amide intensities in D168A, suggesting an increased contribution from locally ordered or longer-residing water molecules in this distal region. These results confirm that the D168A mutation does not merely alter global signal intensity, but reshapes the

residue-specific hydration landscape of p38α. The mutation reduces the hydration signature around the DFG/activation-loop region while enhancing water-associated signals near the lipid pocket, supporting the idea that perturbation of the DFG-loop aspartate produces long-range effects on both protein dynamics and local solvent organisation.

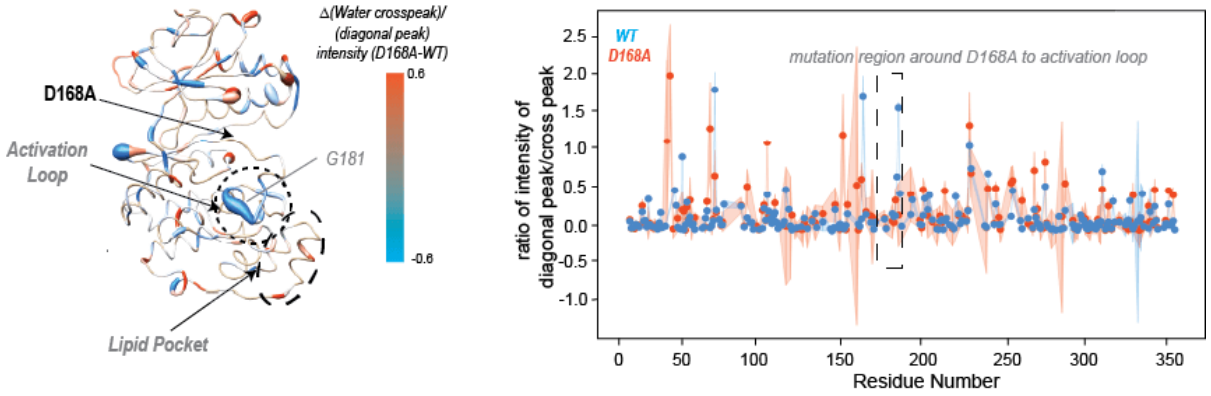

Fig. 4.14 Residue wise water cross peak/NOESY diagonal peak intensities, also plotted in the protein structure.

To complement the NMR-derived hydration analysis, MD simulations of 2 microseconds with three replicas were used to identify long-residing water molecules within the relevant kinase pockets. This allowed us to assess whether the mutation-dependent hydration patterns observed in the NOESY experiments were also reflected in the simulated solvent dynamics. Overall, the MD-derived water residence analysis reproduced the same qualitative trend observed experimentally. The allosteric pocket, which lies closest to the D168A mutation site, did not show major differences in water residence behaviour between WT and D168A. In contrast, clear mutation-dependent differences were observed in the activation-loop and lipid-pocket regions. Consistent with the NOESY analysis, WT displayed a long-residing water event near the activation loop, with a residence time of approximately 160 ns. In D168A, the longest water residence event in the same region was markedly shorter, reaching only around 40 ns (**Fig. 4.15**). This supports the experimental observation that the activation-loop region in WT has a stronger hydration signature than in the mutant. The opposite trend was observed around the lipid pocket, which is distal to the mutation site. In this region, D168A showed a longer water residence event of approximately 60 ns, compared with around 30 ns in WT. This suggests that the mutation redistributes long-residing waters away from the activation-loop region and toward the lipid-pocket region. Together, the MD water residence analysis supports the NOESY-derived hydration data and strengthens the

conclusion that D168A alters the local hydration landscape of p38α. Importantly, these changes are not restricted to the immediate mutation site, but extend to distal regions of the kinase domain, consistent with a long-range allosteric effect of the DFG-loop mutation.

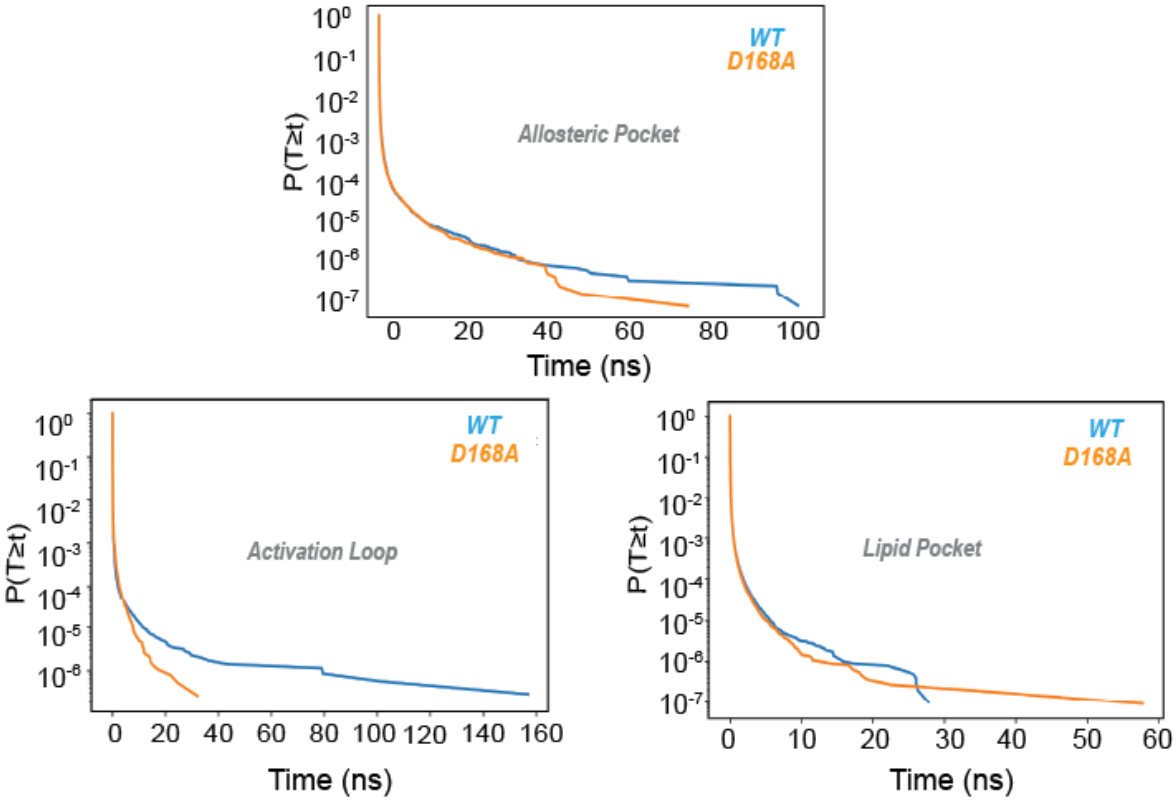

Fig. 4.15 MD-derived water residence-time analysis for the allosteric pocket, activation loop and lipid pocket.

4.4 DFG mutation reshapes water organization around the different pockets

Local water-residence analysis revealed long-range differences in hydration behaviour between WT and D168A. To assess the spatial localization and temporal persistence of water oxygen atoms, radial distribution function analysis was performed for water molecules around the activation-loop, allosteric-pocket, and lipid-pocket regions. This analysis provided a complementary view of solvent organisation by measuring how water density is distributed as a function of distance

from each selected region. The RDF profiles, with mean and SD calculated from three replicas, showed that D168A has a stronger hydration shell than WT around both the activation loop and the lipid pocket. This is interesting because the water-residence analysis had identified a long-residence water event near the activation loop in WT. The RDF results indicate that although WT contains a particularly long-residing water molecule in this region, the broader hydration shell around the activation loop is more populated or more structured in D168A. Therefore, water residence time and hydration-shell density report on related but distinct aspects of solvent behaviour: residence analysis captures the persistence of individual water molecules or events, whereas RDF analysis reflects the average spatial organisation of the surrounding water population. Around the allosteric pocket, the RDF profiles showed only minor differences between WT and D168A, suggesting that the mutation does not substantially alter the average hydration shell in this region. In contrast, the lipid pocket displayed a stronger hydration in D168A, consistent with the NOESY and water-residence analyses showing enhanced water-associated signals and longer water residence in this distal pocket. Water bridges, or coupling of water across two residues, revealed that strong water coupling around the activation loop exist. Overall, these results indicate that mutation-dependent hydration changes are not determined solely by individual long-residing water molecules. Instead, they also depend on the broader exchange and organisation of water molecules entering and leaving each pocket. The stronger hydration shells around the activation loop and lipid pocket in D168A suggest that the mutation reshapes both local and distal solvent architecture. This may contribute to the enhanced apparent thermal stability of the mutant by improving hydration-mediated stabilisation and reducing the tendency for thermally induced structural disruption.

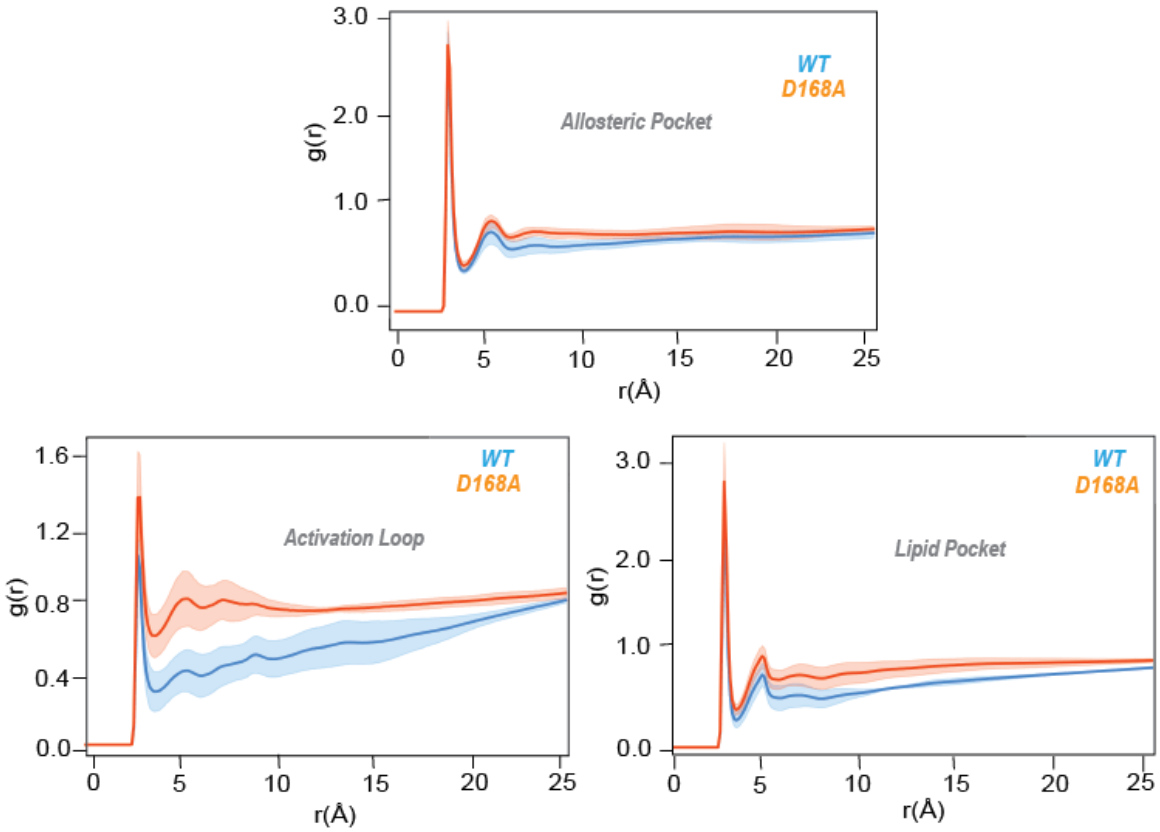

Fig. 4.16 RDF profile comparison of the wildtype and the mutant across different pockets of p38α.

To examine whether water density around the activation loop changed over time in WT and D168A, we analysed solvent distributions across the full 2 μs trajectories. Water molecules within the activation-loop region were extracted and visualised to assess the spatial organisation of the local hydration shell. The solvent shell around the activation loop appeared more centrally localised in D168A than in WT (**Fig. 4.17A**). Density-difference maps further showed that water molecules were more centrally localised within the activation-loop in the mutant, whereas WT displayed stronger water density toward the outer edge of the pocket (**Fig. 4.17B**), slices in the **Fig. 10.19** (Appendix). This suggests that D168A supports a more compact and well-defined hydration shell around the activation loop, while WT shows a more dispersed and fluctuating water distribution. Water oxygen occupancy analysis supported this observation (**Fig. 4.17C**). This analysis was then used as a complementary measure to the RDF analysis. While RDFs quantify the average radial enrichment of water around selected protein atoms, occupancy analysis reports how persistently water oxygen atoms occupy the defined region over the trajectory. In D168A, water oxygen occupancy within the activation-loop pocket remained comparatively stable over the trajectory, whereas WT showed greater

fluctuations. Together, these results indicate that the DFG-loop mutation alters the organisation of water molecules around the activation loop, producing a more persistent and spatially focused hydration environment in the mutant.

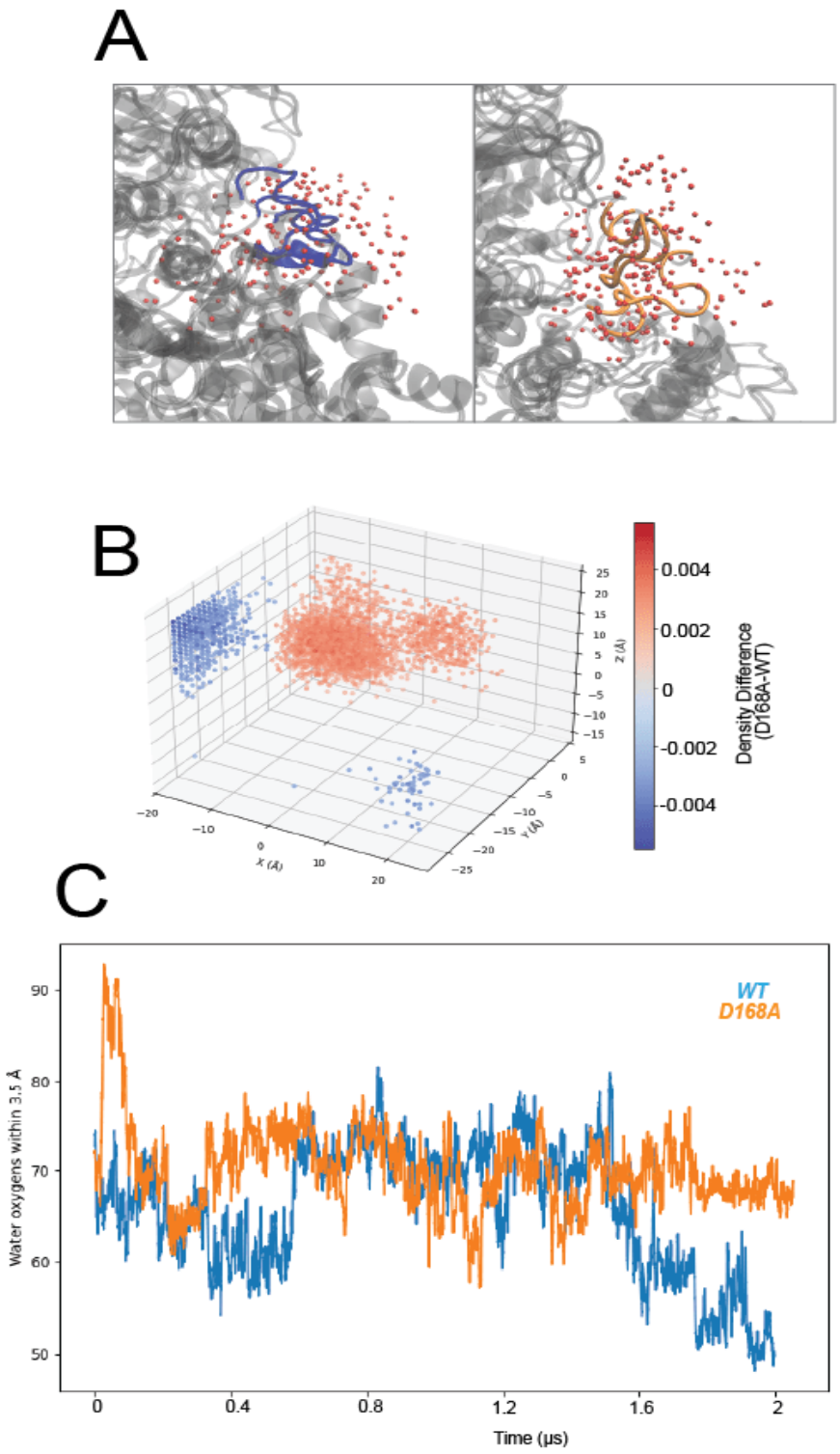

Fig. 4.17 A) Representation of hydration shell around the activation loop across the entire trajectory for the wildtype and D168A. **B**) Density differences mapped in the

water box centring the activation loop. **C**) Water oxygen occupancy around the activation loop.

4.5 DFG mutation rewires the solvent exchange capacities (CLEANEX-PM)

In order to delve deeper into the water dynamics, we performed water exchange studies. CLEANEX-PM experiments were used to probe residues whose backbone amide protons undergo exchange with bulk solvent water. The experiment relies on selective magnetisation transfer from water protons to exchangeable amide protons. Therefore, residues that show signals in the CLEANEX spectrum are those whose amide protons are sufficiently solvent-exposed and exchange-competent on the timescale of the experiment. In this context, stronger CLEANEX intensities indicate higher apparent water–amide proton exchange, which can arise from increased solvent accessibility, local flexibility, transient opening events, or altered hydrogen-bond stability. Comparison of the WT and D168A CLEANEX-TROSY spectra revealed substantial differences in the exchange behaviour of several residues (**Fig. 4.18**). These differences were reflected not only in CLEANEX peak intensities, but also in chemical-shift perturbations **Fig. 10.20** (Appendix) between the corresponding TROSY spectra. In addition, comparison of the reference TROSY spectra before and after the CLEANEX measurements showed that some peaks disappeared or became strongly broadened, suggesting changes in local exchange behaviour, conformational dynamics, or sample stability during the experiment. Importantly, the intensity of the parent TROSY spectrum should not be directly compared with the CLEANEX spectrum without caution, because the two experiments differ in acquisition parameters and measurement time. The longer measurement time of the CLEANEX experiment can partly compensate for weaker signals, meaning that CLEANEX peak intensities should be interpreted as exchange-dependent readouts rather than simple reductions of parent TROSY intensity.

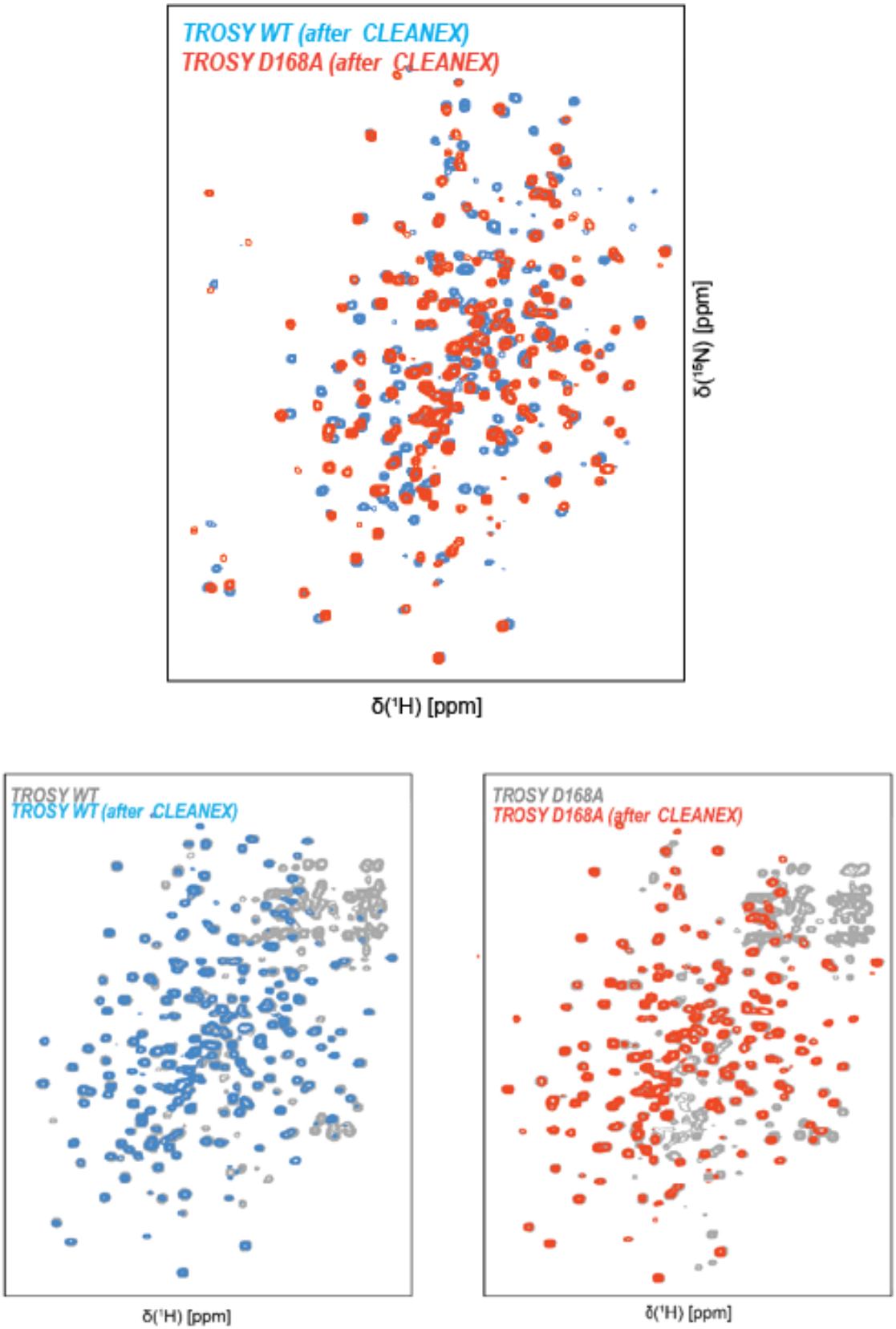

Fig. 4.18 Overlay of CLEANEX-PM spectra with the corresponding reference TROSY spectra. The comparison highlights water-exchange-sensitive amide peaks detected in the CLEANEX experiment. The first panel does not correct for

chemical-shift differences between spectra, but shows the peak distribution used for comparison with the respective TROSY reference.

Quantification of CLEANEX peak intensities was performed to compare residue-specific water–amide exchange between WT and D168A. To minimise artefacts arising from differences in peak intensity, sample concentration, or spectral acquisition, CLEANEX intensities were normalised to the corresponding parent TROSY peak intensities. The resulting intensity ratios were then used as relative measures of apparent solvent-exchange behaviour. The normalised CLEANEX/TROSY intensity ratios showed that D168A displays overall higher water–amide exchange than WT. Difference plots revealed increased CLEANEX intensities across several regions of the mutant, including residues surrounding the lipid pocket as well as broader regions of both the N- and C-lobes. This indicates that D168A has a more exchange-competent backbone environment, consistent with increased solvent accessibility, reduced hydrogen-bond protection, or enhanced local breathing motions in these regions. These findings support the idea that the DFG-loop mutation reshapes the solvent-exchange landscape of p38α. Rather than producing a strictly local effect near the mutation site, D168A increases water–amide exchange across distal regions, including around the lipid pocket. This is consistent with the NOESY, water-residence, RDF, and water-density analyses, which together suggest that the mutation reorganises the hydration environment and promotes a more dynamic solvent shell around selected regions of the kinase domain.

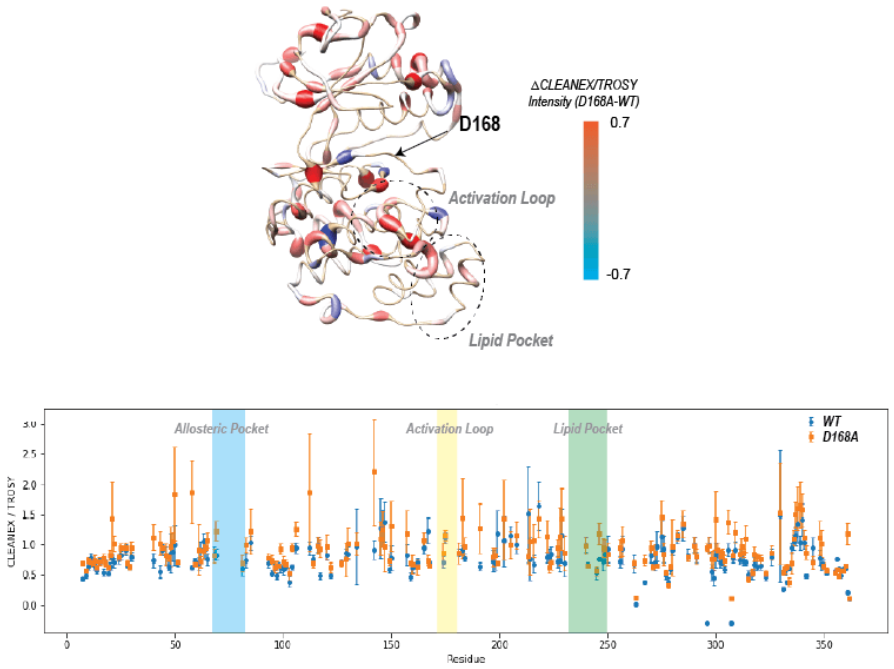

Fig. 4.19 Ratio of CLEANEX/Parent TROSY normalised to see the exchange rates of the amide protons per residue.

4.6 H/D Exchange in Solution NMR

After identifying exchange-competent amide protons using CLEANEX-PM, hydrogen–deuterium exchange was monitored by solution NMR to assess the protection of backbone amide protons. For this experiment, the protein sample was lyophilised and reconstituted in approximately 98% D_2O. TROSY spectra were then recorded at hourly intervals to follow the loss of amide-proton signal intensity as labile backbone NH protons exchanged with deuterium. A decrease in TROSY peak intensity reflects exchange of amide protons with solvent deuterons. Faster intensity loss can indicate weaker hydrogen-bond protection, increased solvent accessibility, local unfolding, or enhanced conformational breathing. Therefore, the time-dependent reduction in peak intensity provides residue-specific information on backbone protection and local structural stability. The first TROSY spectrum recorded after D_2O exchange was overlaid with the parent TROSY spectrum acquired before exchange to visually assess changes in peak position and intensity (**Fig. 4.20**). A substantial loss of signal was observed immediately after reconstitution in D_2O. This loss may partly reflect rapid exchange of highly solvent-accessible amide protons; however, technical effects associated with lyophilisation and reconstitution cannot be excluded. In particular, lyophilisation may have affected sample quality, promoted partial degradation, or caused irreversible loss of folded protein, which could contribute to the reduced signal intensity. Therefore, the HDX-NMR data were interpreted cautiously and primarily as a qualitative indicator of exchange behaviour rather than as a fully quantitative measure of protection.

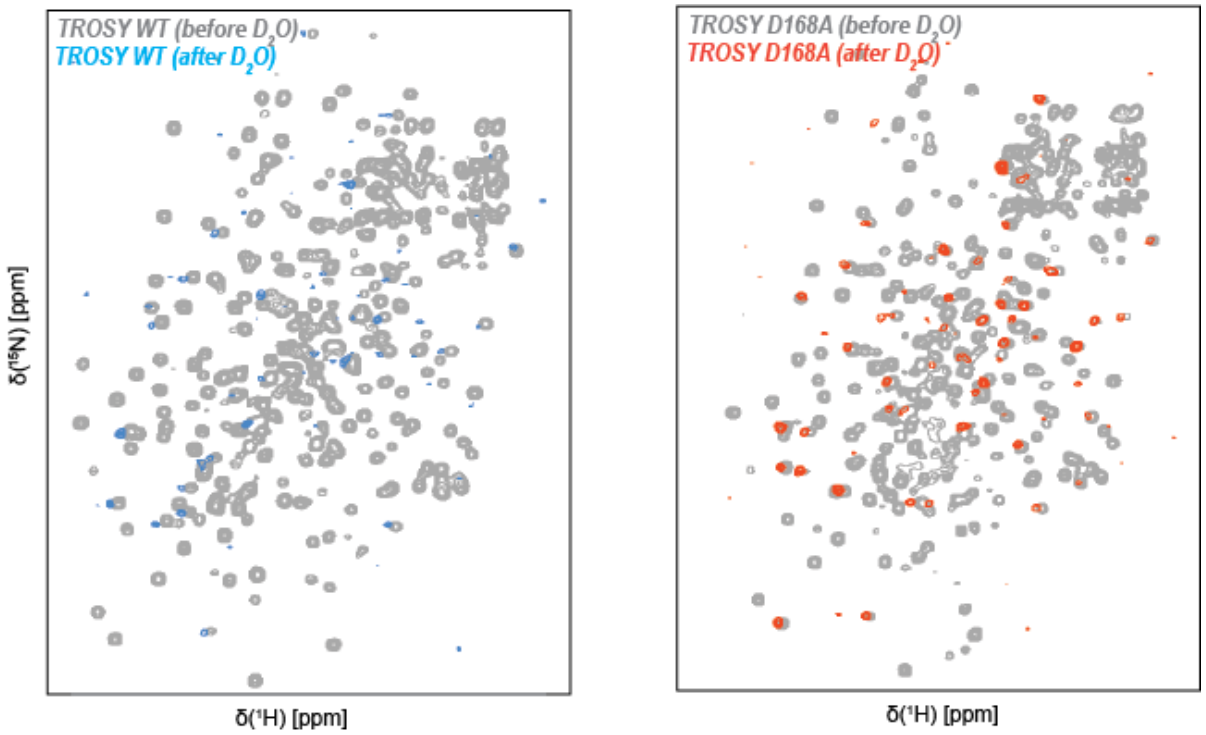

Fig. 4.20 Comparison of TROSY spectra before and after the addition of D_2O for the wildtype and the mutant protein.

The initial HDX-TROSY spectra of WT and D168A were overlaid to assess qualitative differences in backbone amide protection after transfer into D_2O. The D168A spectrum retained a larger number of observable peaks than the WT spectrum, suggesting that a greater fraction of backbone amide protons remained protected from rapid exchange in the mutant during the early phase of the experiment. This observation is consistent with the increased thermal robustness observed for D168A in the temperature-ramped simulations and nanoDSF measurements. At first glance, this may appear to contrast with the CLEANEX-PM results, where D168A showed higher apparent water–amide exchange in several regions. However, the two experiments report on related but distinct aspects of protein hydration and exchange. CLEANEX-PM detects magnetisation transfer from water to exchange-competent amide protons and is sensitive to solvent accessibility, local breathing motions, and water–amide exchange on the experimental timescale. In contrast, HDX-NMR monitors the loss of backbone amide proton signals after transfer into D_2O and reports on the degree of amide protection, which depends on hydrogen bonding, structural stability, local unfolding events, and solvent accessibility on a timescale of hours. Therefore, increased CLEANEX intensity in selected regions does not necessarily contradict stronger global amide protection in HDX. Several residues remained protected in both WT and D168A (**Fig. 4.21A**). V20 was protected in both proteins, suggesting that this

region maintains backbone protection independent of the mutation (**Fig. 4.21B**). T44 and T298 were also retained in both spectra, indicating protection of these residues despite their location in regions that may otherwise be solvent accessible. Charged residues such as D283 and H228 also showed protection, which may reflect stabilising hydrogen-bond interactions or burial within locally structured environments. In WT, the overall HDX spectrum showed markedly reduced signal intensity compared with D168A. This could indicate rapid exchange of a larger fraction of solvent-accessible amide protons in the WT protein. However, technical effects must also be considered. The low WT signal may partly result from sample perturbation during lyophilisation and reconstitution, including partial degradation, aggregation, or loss of folded protein. Therefore, the WT HDX data should be interpreted cautiously. The most defensible conclusion is that D168A retains more observable protected amide signals under the experimental conditions, whereas the WT either exchanges more rapidly or is more strongly affected by the sample-preparation procedure.

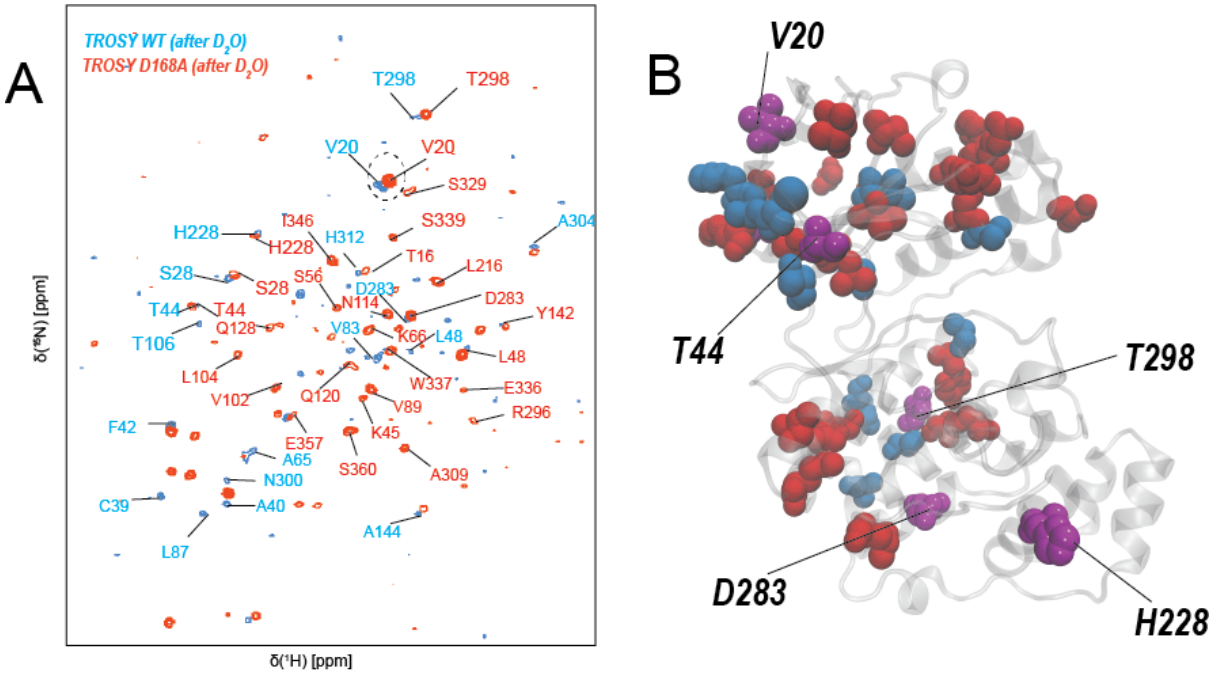

Fig. 4.21 A) Overlay of the first TROSY HSQC of mutant and wildtype after HDX **B**) Representation of residues on the protein structure showed up in the spectra after HDX (red for mutant, blue for wildtype and purple for both).

Peak retention was quantified immediately after HDX and at the final 72 h time point. At the initial time point, D168A retained approximately 9.3% of the parent TROSY peaks, whereas WT retained only around 3.9% (**Fig. 4.22A**). Since peak retention represents a categorical outcome, with each parent TROSY peak classified as either retained or lost after HDX, Fisher's exact test was used to assess whether

the difference in retained peak proportions between WT and D168A was statistically significant. This analysis supported a higher initial peak-retention frequency in D168A compared with WT. This indicates that a larger fraction of amide signals remained observable in the mutant after transfer into D_2O. However, this initial difference may not arise solely from differences in amide protection. It could also reflect differences in sample stability after lyophilisation and reconstitution, with WT potentially being more affected by partial unfolding, aggregation, degradation, or loss of folded protein signal during sample preparation. Therefore, the higher initial peak retention in D168A should be interpreted as a combination of greater early amide protection and/or better preservation of sample quality under the HDX preparation conditions. By 72 h, the retained peak percentages became much closer, with WT retaining approximately 2.6% and D168A approximately 3.0% of the original peaks. Fisher's exact test was again used to compare the retained and lost peak counts at this final time point. In contrast to the initial HDX time point, the retained peak proportions were much more similar after 72 h, indicating convergence of the detectable protected peak population over the full exchange period. Normalised intensity ratios showed a similar trend. Several D168A peaks initially retained ratios above 0.1 relative to the parent TROSY spectrum, but these intensities were substantially reduced during the 72 h time course (Fig. 4.22B). Because the intensity-ratio distributions were not assumed to follow a normal distribution, Mann–Whitney U tests were used to compare WT and D168A intensity ratios at each time point. This allowed the residue-level intensity differences between the two proteins to be assessed independently of the binary retained/lost peak classification. Together, the Fisher's exact test and Mann–Whitney U analysis support a more nuanced interpretation of the HDX data. D168A contains a larger population of initially observable or protected amide signals, but many of these undergo delayed exchange over longer timescales. Therefore, the HDX data support increased early peak retention in the mutant, while also indicating that this initial difference may partly reflect better sample stability after lyophilisation and reconstitution rather than protection alone.

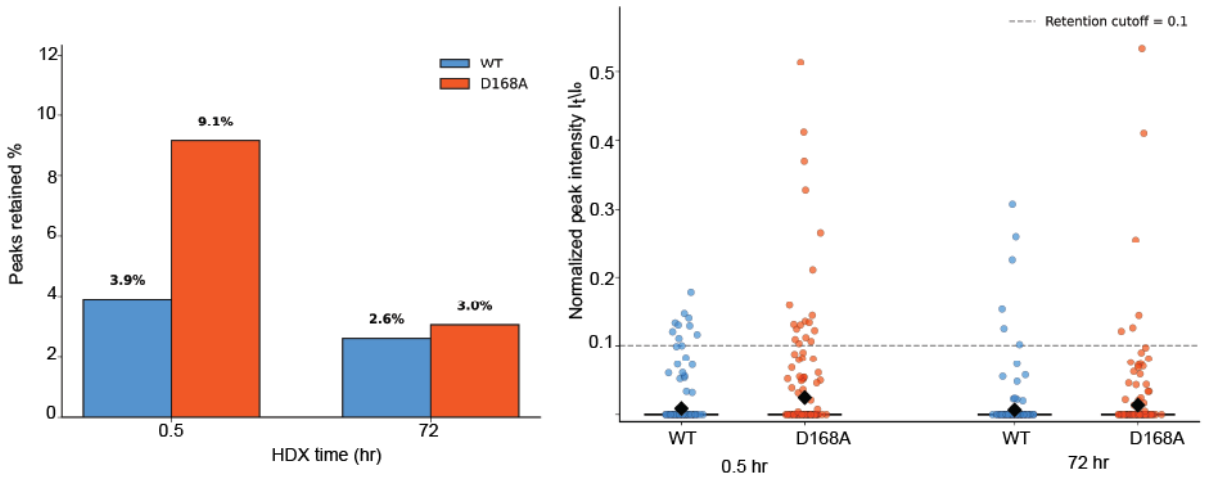

Fig. 4.22 A) Percentage of peaks retained after initial HDX time point and the final time point. **B**) Normalised peak intensities at the initial and final timepoints for WT and D168A.

Table 4.2 : Statistical values for peak counts

Time	Fischer p	Odds ratio	Mann-Whitney p
0.5 hr	0.029	0.403	0.0007
72 hr	0.77	0.849	0.005

When HDX data were quantified across the full-time course, residue-specific differences in exchange behaviour became evident between WT and D168A. Peaks corresponding to V20 and D283 in D168A showed a gradual decrease in intensity, whereas the corresponding WT peaks decayed more rapidly in an exponential-like manner. Although both systems approached similar final intensities by 72 h, D168A retained higher signal intensity during the intermediate stages of the experiment. This indicates that the mutation does not prevent amide exchange, but delays exchange for selected residues. The time-resolved HDX profiles therefore provide information beyond final peak counts alone, revealing slower exchange kinetics in D168A that are consistent with increased local protection or better preservation of folded-state structure during early and intermediate HDX time points.

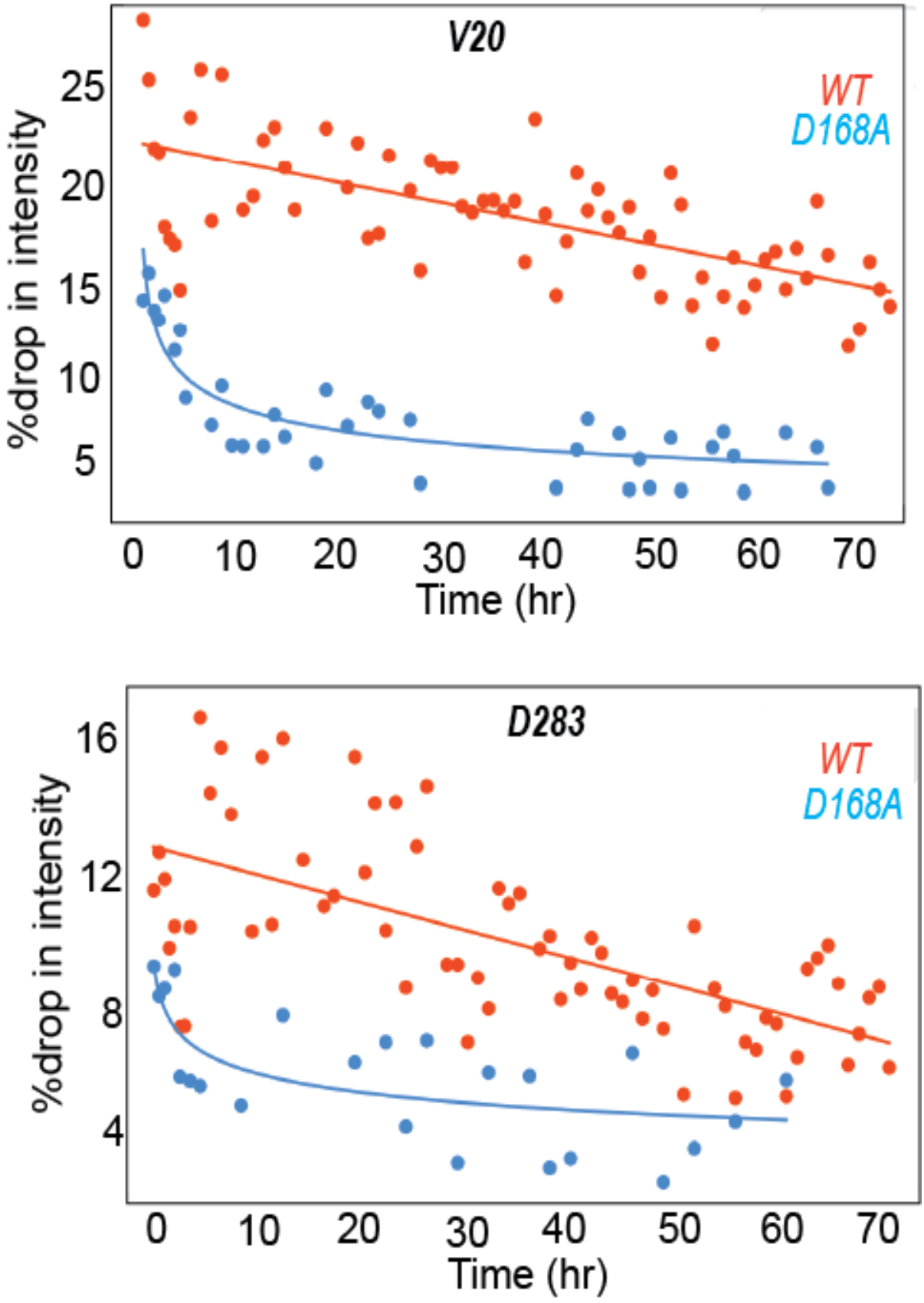

Fig. 4.23 Intensity over time plots for HDX experiment for WT and D168A.

4.7 H/D Exchange in Solid State NMR

Crystalline WT and D168A p38α samples were packed into 1.3 mm solid-state NMR rotors and spun at 55 kHz magic-angle spinning (MAS) to acquire hNH fingerprint spectra. These spectra provide a solid-state equivalent of an amide fingerprint, allowing comparison of the overall fold and residue-specific spectral behaviour of the protein in a crystalline, densely packed environment. The aim was not only to confirm that the protein remains structured in the packed crystals, but also to assess whether the mutation-dependent behaviour observed in solution is preserved, altered, or suppressed under more spatially restricted conditions. Compared with the corresponding solution-state TROSY spectra (**Fig. 4.24**), the solid-state hNH spectra showed broader linewidths and a higher degree of spectral overlap. This is expected in solid-state NMR because proteins in crystals or microcrystalline preparations do not undergo the same rapid isotropic tumbling as proteins in solution. As a result, anisotropic interactions such as dipolar couplings and chemical-shift anisotropy are not naturally averaged to the same extent. MAS at 55 kHz helps reduce these interactions and improves resolution, but it does not completely remove all sources of line broadening. Additional broadening can arise from local conformational heterogeneity, crystal-packing effects, incomplete motional averaging, and small differences in the local environments sampled by individual residues within the packed crystalline lattice. In solution NMR, the protein samples a dynamic ensemble while freely tumbling in solution, which produces sharper averaged resonances under favourable conditions. In solid-state NMR, the protein is conformationally restricted and embedded in a crystal-like packing arrangement. This can preserve structural order while simultaneously increasing local heterogeneity and reducing spectral resolution. Faster MAS frequencies and smaller rotors could further improve resolution by more efficiently averaging anisotropic interactions and reducing linewidths, but the 55 kHz spinning used here was sufficient to obtain solid-state hNH fingerprints for comparison. hCANH spectra were also recorded to assist with backbone assignment. The assignment strategy followed the general logic used for solution-state triple-resonance experiments (see Methods and Chapter 3). However, direct transfer of solution assignments to the solid state is not always straightforward. Even when the global fold is retained, chemical shifts can change between solution and crystalline states because residues experience different hydrogen-bonding patterns, packing contacts, hydration environments, and motional restrictions. Therefore, overlap between solution and

solid-state spectra can support assignment, but differences in peak position are expected and should not automatically be interpreted as structural disruption. Under MAS, orientation-dependent interactions are averaged, and chemical shifts mainly report on the local electronic and structural environment of each nucleus. The inclusion of solid-state NMR therefore provides an additional experimental context for evaluating WT and D168A. While solution NMR reports on the protein in a freely tumbling, hydrated solution ensemble, solid-state NMR allows the protein to be examined in a compact crystalline environment where motions are more restricted and packing interactions become important. This is particularly useful for assessing whether the DFG-loop mutation produces effects that are intrinsic to the kinase fold, or whether some of the observed differences depend on solution-state flexibility and solvent exposure. In this sense, the solid-state spectra serve as a bridge between the solution experiments and the crystalline/compact conformational state of the protein.

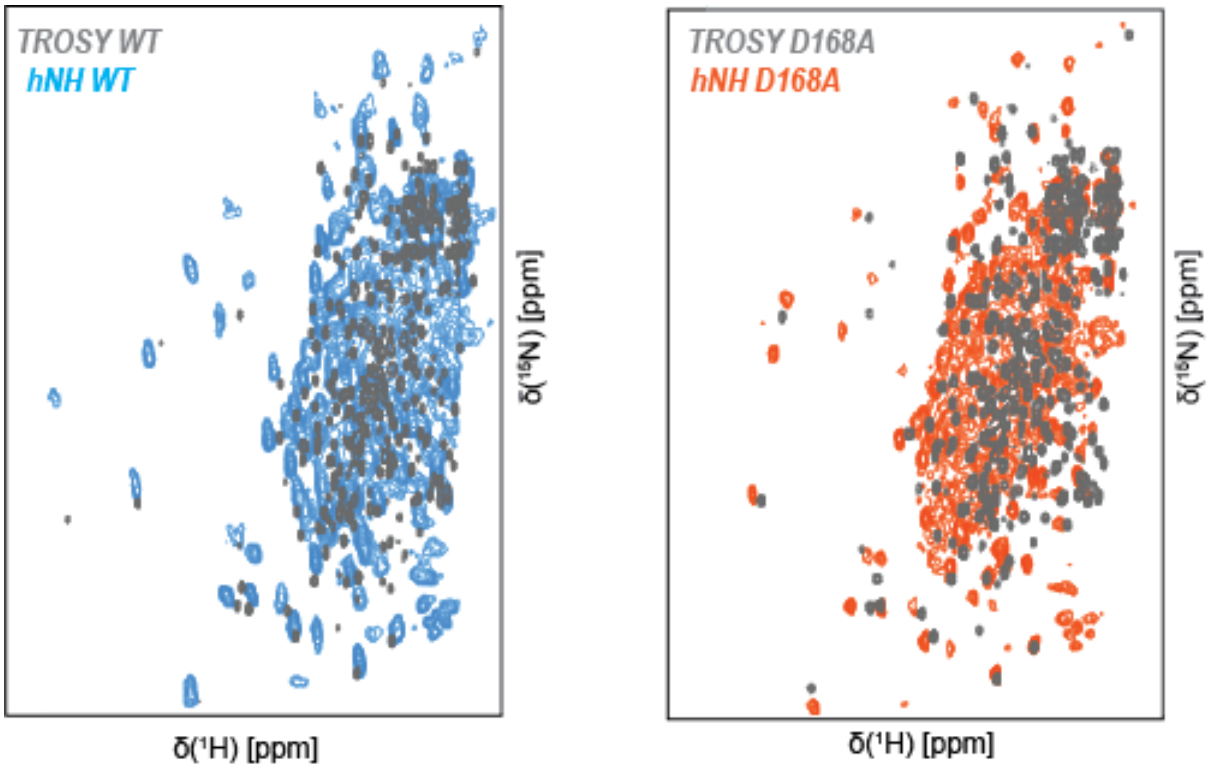

Fig. 4.24 Comparison of spectral fingerprint recorded in solution NMR (TROSY) and solid-state NMR (hNH) for the wildtype and D168A.

Overlay of the solid-state hNH spectra of WT and D168A revealed substantially smaller chemical-shift perturbations (**Fig.4.25**) than those observed in the corresponding solution-state TROSY spectra in **Fig. 10.23** (Appendix). The solid-

state spectra showed fewer disappearing peaks and a highly similar overall spectral pattern between WT and D168A. This suggests that the crystalline packing environment reduces mutation-dependent differences in local chemical environment. In solution, D168A showed pronounced spectral perturbations relative to WT, indicating that the mutation strongly affects the conformational and/or hydration environment of the protein. In contrast, the similar solid-state peak positions suggest that crystal packing and restricted molecular motion may stabilise a more comparable structural ensemble in the two proteins. These observations support the idea that solvation and conformational freedom contribute significantly to the mutation-dependent differences observed in solution. To investigate this further, solid-state HDX measurements were performed to determine whether hydration and exchange behaviour in the densely packed crystalline state resemble those observed in freely solvated solution.

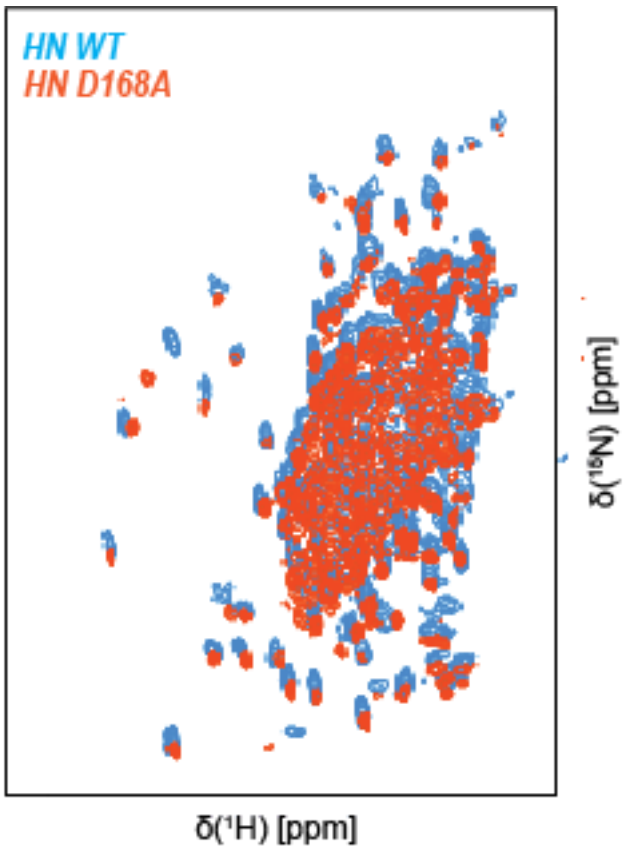

Fig. 4.25 Overlay of the solid state hNH spectra of the wildtype and D168A.

Solid-state HDX was performed to assess whether WT and D168A display different exchange behaviour in the crystalline state. The crystalline samples were exposed stepwise to increasing D_2O content, from approximately 30% to 50%, then 75%, and finally to an overall D_2O concentration of approximately 85–90%. This gradual exchange was used to minimise abrupt perturbation of the crystal sample while

allowing deuterium incorporation into solvent-accessible amide sites. The first hNH spectrum after D_2O exposure was recorded approximately 2.5 h after the initial setup. Because solid-state HDX required stepwise D_2O exchange, sample packing, and transfer into the NMR rotor, the first recorded spectrum represents the earliest experimentally accessible time point rather than the true start of exchange. Therefore, part of the initial exchange may have occurred during sample preparation and equilibration. The crystalline HDX data should therefore be interpreted qualitatively and compared cautiously with the solution-state HDX experiment. When the HDX hNH spectra were overlaid with the corresponding parent hNH spectra, a larger number of peaks disappeared in D168A (**Fig. 4.26B**) than in WT (**Fig. 4.26A**). This observation contrasts with the solution-state HDX experiment, where D168A initially retained a larger fraction of peaks (**Fig. 4.20**). However, this difference is not necessarily contradictory, because proteins can display markedly different exchange behaviour in solution and in crystalline solid-state environments. In the crystalline state, exchange is influenced not only by intrinsic amide protection, but also by crystal packing, solvent channels, local hydration, restricted protein motions, and the ability of D_2O to access exchangeable sites within the packed lattice. Peak matching was performed based on chemical-shift proximity between the parent and HDX hNH spectra with cutoff values of $\pm$0.06 ppm for ^{1}H-dimension and $\pm$0.6 ppm for ^{15}N dimension. Using this criterion, WT retained approximately 66% of its parent hNH peaks, whereas D168A retained only around 28.3% (**Fig. 4.26C**). This suggests that, in the crystalline environment, a larger fraction of D168A peaks are lost after D_2O exposure. One possible interpretation is that the D168A crystal lattice permits greater solvent accessibility or faster exchange for a larger subset of residues than the WT crystal lattice. Conversely, WT may retain more observable peaks because its crystalline packing better protects exchange-sensitive sites or restricts solvent penetration. However, the intensity analysis of matched peaks revealed a more nuanced pattern. Although D168A retained fewer peaks overall, the peaks that remained detectable after D_2O exposure showed higher residual intensities than the corresponding retained WT peaks. This difference was statistically supported by a Mann-Whitney U test, indicating that the distribution of matched-peak intensity ratios differs between WT and D168A (**Fig. 4.26D**). Therefore, D168A appears to contain two distinct populations of peaks in the crystalline state: one population that is rapidly lost after D_2O exposure, and another population that remains strongly protected or less affected once retained. In WT, more peaks remain detectable, but their residual intensities are generally weaker, suggesting broader low-level exchange or partial intensity loss across a larger retained peak population. Together, these results indicate that solid-state HDX does not

simply reproduce the solution-state HDX behaviour. Instead, the crystalline environment changes the exchange landscape. WT retains a larger number of peaks, suggesting broader protection from complete peak loss, whereas D168A retains fewer peaks but preserves stronger intensity among the peaks that remain. This behaviour may reflect differences in crystal packing, solvent-channel architecture, local hydration, and restricted conformational dynamics between WT and D168A. Assignment of the residual peaks will be required to determine whether the retained or lost peaks cluster in specific structural regions, such as the activation loop, allosteric pocket, hinge, or lipid pocket. Additional HDX time points would also be necessary to determine whether the observed behaviour reflects rapid early exchange, delayed exchange, or differential sample stability in the crystalline state.

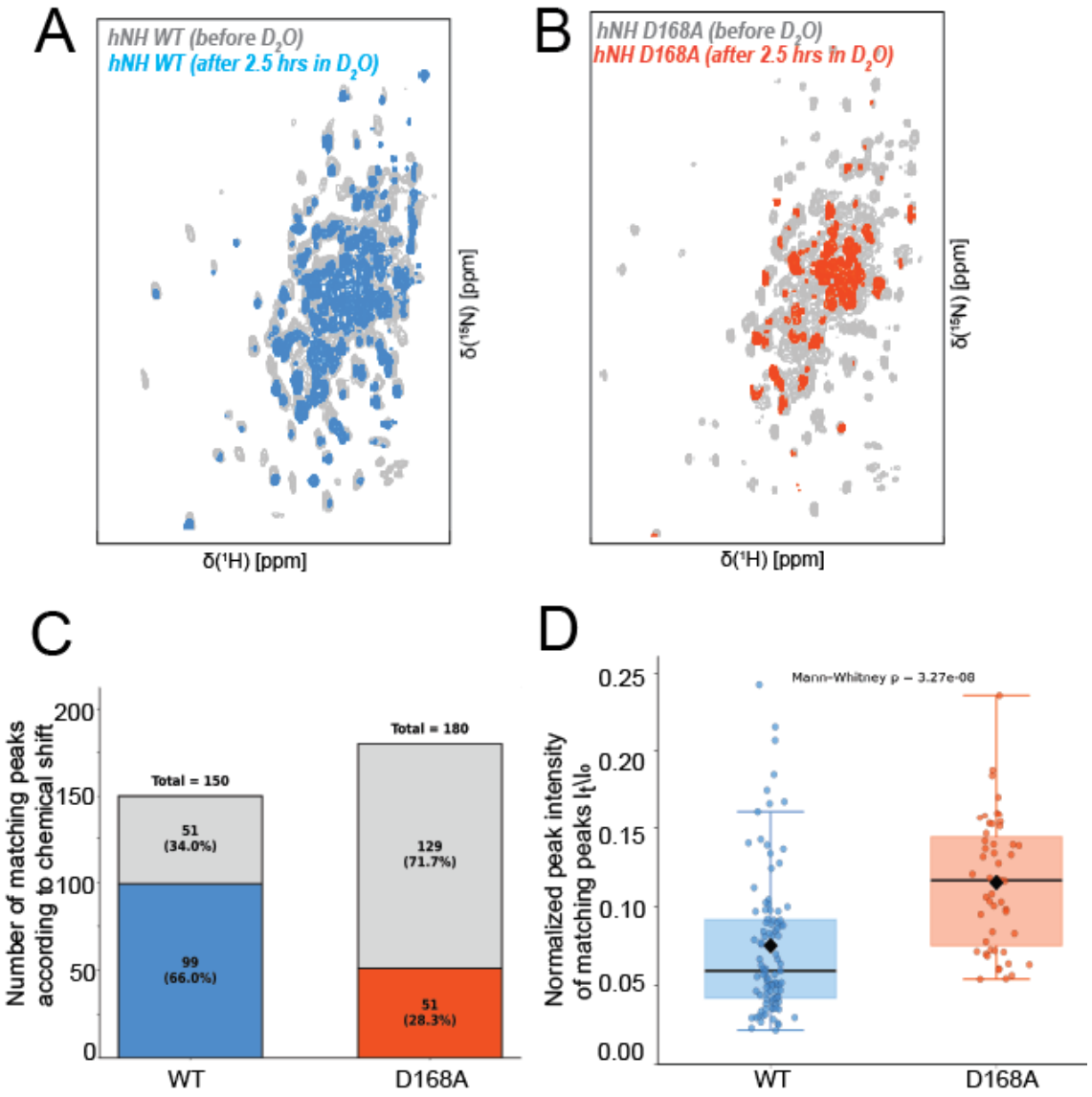

Fig. 4.26 A) Overlay of the hNH spectra before and after 2.5 hrs of adding D_2O of the wildtype p38α. **B**) Overlay of the hNH spectra before and after 2.5 hrs of adding

D_2O of D168A p38α. **C**) Number of matching peaks according to chemical shift cutoff in the wildtype and the mutant (grey indicating peaks missing). **D**) Box plot to understand the overall intensity drop for the matching peaks obtained for wildtype and D168A.

After 78 h of solid-state HDX, both WT and D168A showed additional peak loss relative to their parent hNH spectra. However, the overall trend observed at the earlier time point was still maintained. When the parent hNH spectrum was used as the reference, D168A showed a larger fraction of missing peaks than WT (**Fig.4.27 A & B**). Approximately 72.2% of the D168A peaks were lost after 78 hrs, whereas WT lost approximately 47.3% of its parent peaks (**Fig.4.27C**). This indicates that, in the crystalline state, a larger subset of D168A resonances becomes undetectable upon prolonged exposure to D_2O. When the 2.5 hrs HDX spectrum was used as the reference instead of the parent hNH spectrum, the difference between WT and D168A became smaller but remained evident. From 2.5 hrs to 78 hrs, D168A lost approximately 53.5% of the initially retained peaks, while WT lost approximately 36.2% (**Fig.4.27E**). This suggests that D168A continues to undergo greater progressive peak loss over the extended HDX period, although the strongest difference appears to occur during the early phase of D_2O exposure. The intensity analysis provides a more elaborated interpretation. Although D168A retained fewer peaks overall, the peaks that remained detectable after 78 hrs showed higher residual intensities than those retained in WT (**Fig.4.27 D & F**). This difference was supported by the Mann–Whitney U test, indicating that the distribution of retained peak intensities differs significantly between the two proteins. Therefore, D168A appears to contain a larger population of rapidly exchanging or disappearing peaks, but the subset of peaks that remains observable is comparatively well protected from intensity loss. Together, these results suggest that solid-state HDX separates the D168A resonances into two apparent populations. One population is highly sensitive to D_2O exposure and disappears rapidly or progressively over time. The second population remains detectable and retains relatively strong intensity even after prolonged exchange. In WT, by contrast, more peaks remain detectable, but their residual intensities are generally weaker, suggesting more distributed partial exchange across a larger retained peak population. Thus, the solid-state HDX data do not indicate that D168A is simply more or less protected than WT. Instead, they suggest that the mutation alters the heterogeneity of exchange behaviour in the crystalline state. D168A loses more peaks overall, but the peaks that survive exchange retain stronger intensity. This behaviour may reflect mutation-dependent differences in crystal packing, solvent-channel accessibility, local hydration, or

conformational restriction within the crystalline lattice. Additional intermediate time points and residue-specific assignments will be required to determine whether the lost and retained peaks cluster in specific structural regions.

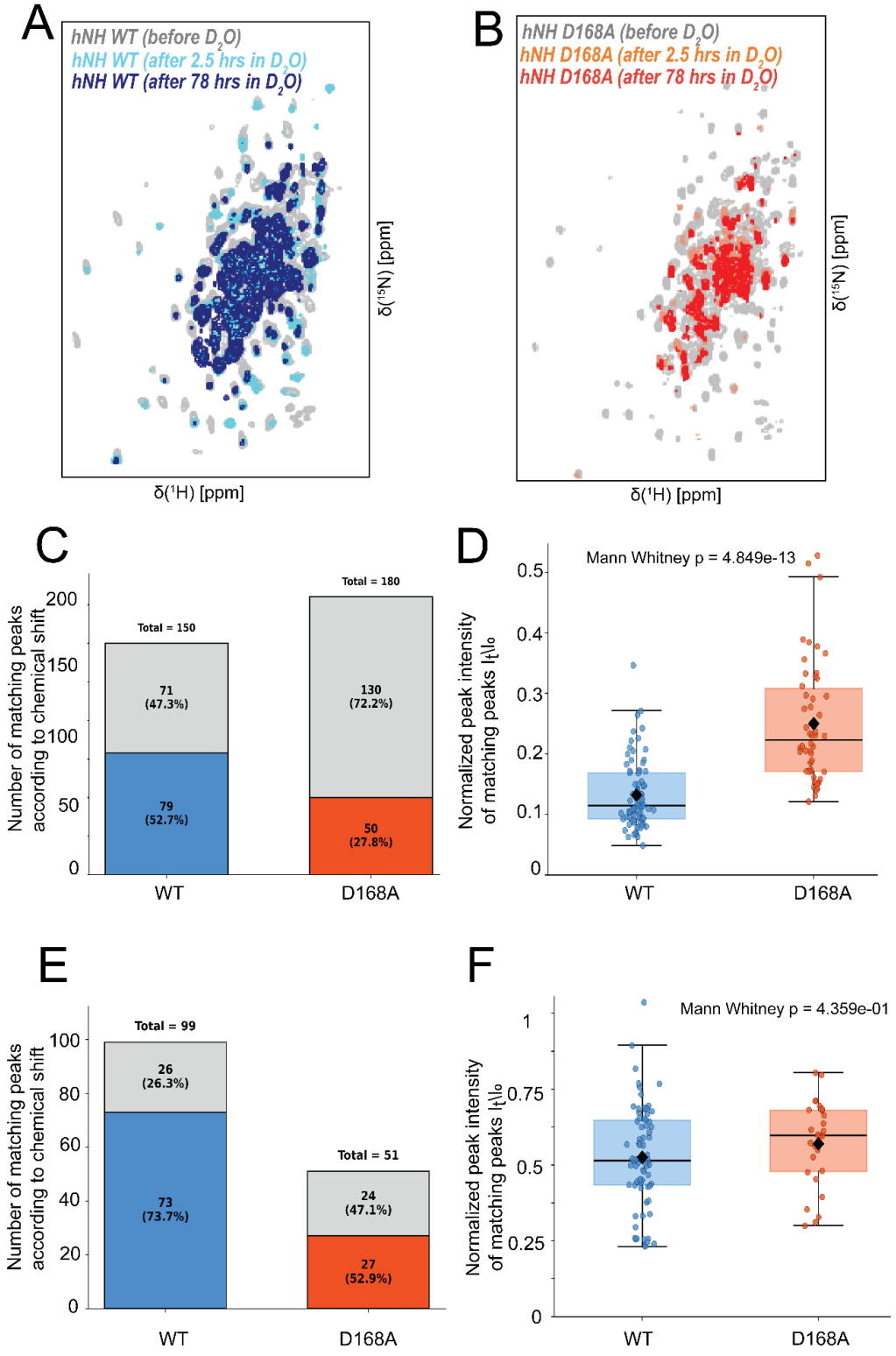

Fig. 4.27 A) hNH overlay before and after adding D_2O after 2.5 hrs and 78 hrs for wildtype protein. **B**) hNH overlay before and after adding D_2O after 2.5 hrs and 78

hrs for D168A protein. **C**) Number of matching peaks according to chemical shift cutoff in the wildtype and the mutant with the reference being before adding D_2O (grey indicating peaks missing). **D**) Box plot to understand the overall intensity drop for the matching peaks obtained for wildtype and D168A with the reference being before adding D_2O. **E**) Number of matching peaks according to chemical shift cutoff in the wildtype and the mutant with the reference being after 2.5 hrs of adding D_2O (grey indicating peaks missing). **F**) Box plot to understand the overall intensity drop for the matching peaks obtained for wildtype and D168A with the reference being after 2.5 hrs of adding D_2O.

4.8 Conclusion

In summary, temperature-dependent simulations, nanoDSF measurements, and hydration analyses collectively show that D168A behaves differently from WT p38α. The mutant displays increased apparent thermal stability, supported by lower structural deviation in temperature-ramped MD simulations and higher melting temperatures in nanoDSF experiments. Hydration-focused analyses further show that this stability is accompanied by a redistribution of the solvent environment. In solution, D168A shows higher apparent water–amide exchange in CLEANEX-PM experiments, particularly around the lipid pocket and across parts of both kinase lobes. However, HDX-NMR indicates that this increased exchange competence does not correspond to complete loss of protection, as D168A initially retains more amide signals and selected residues show more gradual intensity decay over time. MD-based water analyses support this interpretation: while WT contains a long-residing water event near the activation loop, D168A displays stronger average hydration shells around both the activation loop and lipid pocket, as well as longer water residence near the lipid pocket. Thus, the mutation reorganises the hydration landscape rather than simply increasing or decreasing water exposure globally. In the crystalline state, solid-state HDX revealed a different exchange pattern. D168A lost a larger fraction of peaks than WT after D_2O exposure, indicating greater exchange sensitivity for part of the mutant spectrum. However, the retained D168A peaks showed higher residual intensities than those of WT, suggesting that the mutant contains both rapidly exchanging and strongly protected resonance populations. This behaviour likely reflects the influence of crystal packing, solvent-channel accessibility, and restricted dynamics on exchange behaviour. Overall, these results

indicate that D168A does not simply increase or decrease water exposure globally. Instead, the mutation appears to remodel the conformational ensemble of p38α, producing residue-specific changes in hydration, solvent accessibility, and exchange behaviour. In solution, where crystal contacts are absent, these effects are more evident and suggest that D168A reshapes local solvent environments in a region-dependent manner, particularly around the lipid pocket, activation-loop/DFG-loop region, and selected residues across both kinase lobes. The solid-state HDX data further show that exchange behaviour can be modified by crystal packing and restricted solvent channels, highlighting that hydration-dependent allosteric effects depend strongly on the structural environment. Together, the data support a model in which D168A rewires the relationship between thermal stability, water organization, and long-range allosteric communication in p38α.

4.9 Discussion

The functional importance of the conserved DFG aspartate has been demonstrated in several kinases. In Csk protein-tyrosine kinase, the DFG motif is catalytically essential: mutation of D332 to alanine abolished kinase activity toward both polyE4Y and Src, showing that perturbation of this residue can strongly impair catalytic function. This supports the idea that conformational changes propagating to or from the DFG motif can have major consequences for kinase activity[195].In Abl kinase, long-timescale molecular dynamics simulations visualised the DFG flip in atomic-level detail and led to an energetic model in which protonation of the DFG aspartate controls the DFG-in/DFG-out transition. Experimentally, the kinetics of imatinib binding to Abl kinase were shown to be pH-dependent, and this pH dependence disappeared when the DFG aspartate was mutated. These findings indicate that electrostatic changes linked to the catalytic cycle can modulate the DFG flip and allow the kinase to access higher-energy conformational states[196].

In p38α, substitution of the negatively charged DFG aspartate with the smaller, hydrophobic alanine is therefore expected to perturb local interactions within the DFG loop and its neighbouring regulatory regions, including the allosteric pocket. Our thermal-stability data show that the D168A substitution stabilises the kinase fold, consistent with reduced global conformational flexibility under thermal stress. At the same time, the mutation reshapes the conformational ensemble and alters dynamic communication across distal regions of the kinase domain. Such long-range

redistribution of local dynamics is consistent with previous work showing that mutations at network-relevant residues can propagate through kinase allosteric pathways and alter communication between functional sites, as seen in the previous chapter.

However, the consequences of such allosteric perturbations for solvent interactions have been less explored. Allosteric regulation is widespread in biology and can activate or suppress protein function through phosphorylation, substrate binding, ligand association, or interaction with effector proteins. These regulatory events are usually discussed in terms of structural rearrangements, conformational dynamics, and changes in binding-site accessibility. Our results suggest that changes in water organisation may represent an additional layer of allosteric modulation. A mutation that alters the conformational ensemble can also reshape the hydration landscape, changing where water molecules reside, how easily they exchange, and how strongly they are retained within specific pockets.

This has functional implications. Water molecules that are strongly stabilised within a pocket may be more difficult to displace during binding of pharmacological ligands, substrates, or other interaction partners, whereas less favourably organised or more weakly retained waters may be more readily expelled. Therefore, mutation-dependent changes in hydration can influence catalytic activity, ligand binding, and allosteric regulation, even when the mutation is distal from the affected pocket. In this context, water becomes not only a passive solvent component but also a reporter of altered conformational dynamics and allosteric communication.

The NOESY, CLEANEX, HDX, RDF, and water-residence analyses presented here therefore provide complementary views of how D168A reshapes the solvent environment of p38α. Similar to chemical-shift perturbations or NMR relaxation measurements, water-based NMR readouts can report on allosteric effects of mutations. While CSPs reveal changes in local chemical environment and relaxation experiments probe protein motions, water–amide NOEs and HDX measurements provide insight into how mutation-induced dynamic changes are reflected in hydration, solvent accessibility, and backbone protection. Thus, hydration analysis offers an additional experimental window into the long-range allosteric consequences of DFG-motif perturbation.

5. Outlook

In this thesis, we explored the dynamic allosteric ensemble of p38α and investigated how this allostery is reflected in changes to the hydration landscape of the kinase domain. The quantitative understanding gained from molecular dynamics simulations, dynamical network analysis, NMR spectroscopy, thermal-stability measurements, and hydration-focused experiments provides a framework for identifying regions that regulate long-range communication across the protein.

This work highlights that selective kinase modulation may be achieved not only by targeting the conserved ATP-binding site, but also by exploiting distal allosteric regions, communication hubs, and hydration-sensitive pockets. The hydration data further suggest that water organisation can serve both as a reporter and a contributor to allosteric regulation. Understanding where water molecules are stabilised, displaced, or reorganised may therefore support the design of ligands that make use of favourable water-mediated interactions or target pockets where water displacement is energetically accessible.

Overall, this integrative structural-biology approach provides a broader perspective for studying conserved kinase modules. The methodological framework established here can be applied to other kinases and complex protein systems in which function depends on the interplay between conformational dynamics, solvent organisation, and long-range allosteric communication.

6. Methodology

This section describes the methodological framework used in the study, spanning molecular dynamics simulations and dynamical network analysis, followed by protein preparation, solution- and solid-state NMR measurements, and complementary X-ray crystallographic, biochemical, and biophysical experiments.

6.1 Molecular dynamics simulations

All-atom molecular dynamics simulations were performed using NAMD with the CHARMM36 force field[34], and systems were prepared using the QwikMD plugin where applicable[60]. The simulation protocols differed between the two projects because they addressed distinct biological questions. Project 1 focused on mapping dynamic allosteric communication in p38α ensembles whereas Project 2 focused on temperature-dependent structural stability and water architectural differences between p38α and the D168A mutant,

All atomic molecular dynamics simulations

For the dynamic-network analysis, simulations were performed using NAMD 3.0 in combination with QwikMD [59]. To examine ligand-dependent changes in p38α communication pathways, simulations were initiated from crystallographic structures in which the inhibitor ring-flip conformation was observed, corresponding to PDB entries 3HEG[150] and 3GCS[174]. For apo p38α, PDB ID 1WFC[159] was used as the starting model, and missing segments were rebuilt by comparative modelling.

For the apo system, NOESY-derived restraints were applied during the initial preparation phase. Energy minimization was performed for 20,000 steps, followed by gradual heating to 300 K and restrained equilibration. After approximately 1 μs of restrained equilibration, restraints were released and five independent 1 μs production replicas were generated for the wild-type apo system.

Dynamical network analysis of the apo wild-type simulations was then used to identify residues with high betweenness centrality. These residues were selected for alanine-scanning mutagenesis using QwikMD. Each mutant system was subjected to the same minimization, heating, equilibration, and production workflow, followed by five independent 1 μs production replicas.

For the ligand-bound simulations, sorafenib-bound systems were prepared from the relevant crystallographic structures or by docking sorafenib into the allosteric pocket where required. These systems were prepared using the same simulation workflow and simulated in five independent 1 μs replicas. Correlations and communication pathways were then compared across apo wild-type, apo mutant, and ligand-bound p38α ensembles. In total, approximately 50 μs of MD data were generated and analysed for this project.

To understand the behaviour of resident waters and structural water difference as a scope of Project 2, all atomic MD simulations of the wildtype and mutant D168A was carried out for 2 microseconds in three replicas. Radial distribution function and water residence studies were carried out.

Molecular dynamics simulations for thermal-stability analysis

For the thermal-stability analysis, simulations were performed using NAMD 2.6 with the CHARMM36 force field. The QwikMD plugin was used to prepare input systems based on the available crystal structure of p38α kinase, PDB ID 1WFC. Missing segments were rebuilt by comparative modelling. The D168A mutation was introduced using QwikMD.

Initial energy minimization was performed for 20,000 steps, followed by gradual heating to 300 K and equilibration for approximately 10 ns. Three independent 2 μs production replicas were generated to improve sampling. To probe thermal stability, temperature-ramping simulations were performed in which the systems were gradually heated from 300 K to 423 K over 1 μs and then maintained at 423 K for an additional 1 μs, resulting in a total simulation time of 2 μs per trajectory.

Network-analysis and correlation metrics for this project were computed from the final 50 ns of each 2 μs simulation, allowing comparison of the equilibrated high-temperature conformational ensembles. In total, approximately 15 μs of MD data were analysed for this project.

General simulation parameters

Unless otherwise stated, simulations used the CHARMM36 force field for proteins and ligands. Covalent bonds involving hydrogen atoms were constrained using SHAKE, and equations of motion were integrated using a 1 fs timestep. Long-range electrostatic interactions were treated using the particle-mesh Ewald method under periodic boundary conditions. A real-space cutoff of 12 Å and a pair-list distance of 14 Å were used. Systems were equilibrated under NVT conditions for thermalization and then under NPT conditions for pressure coupling before production simulations. Temperature was maintained using Langevin dynamics, and pressure was maintained at 1 atm using the Langevin piston method[58].

6.2 Dynamical network analysis

Topology and trajectory files from the MD simulations were analysed using Dynetan in Python notebooks[69]. Dynetan uses MDAnalysis for trajectory handling and analysis[197]. Contact-detection optimization in the workflow was supported by Numba[198] and Cython[199]. Network statistics and optimal communication paths were calculated using the Floyd–Warshall algorithm implemented in the NetworkX package.

For the dynamic-network project, the final 200 ns of each 1 μs production replica were used for network and correlation analysis unless otherwise stated. For the thermal-stability project, network and correlation metrics were computed from the final 50 ns of each 2 μs trajectory. Differences in correlations were also computed from the temperature ramped as well as normal trajectories for apo and D168A mutant simulations. This difference reflects the distinct aims of the two projects: the former focused on apo and ligand-dependent communication networks under standard conditions, whereas the latter focused on conformational behaviour after temperature ramping.

Dynamical network analysis was first performed on the apo wild-type p38α simulations to identify residues with high betweenness centrality. Betweenness centrality was used to identify residues that frequently occur along shortest communication paths and may therefore act as important communication relays within the protein. These residues were selected for alanine mutagenesis and subsequent comparison with the wild-type network.

For each system, residue-level correlations and communication pathways were calculated and compared across the relevant ensembles. In the dynamic-network project, communication pathways between selected representative residues were used to compare coupling between the extended allosteric pocket, activation loop, and lipid-binding pocket. In the thermal-stability project, correlation metrics were used to assess how elevated temperature influenced structural communication and stability-related dynamics.

Additional analyses were performed using in-house Python and Tcl scripts together with VMD[200]. Residue–residue contact maps were generated using VMD and PyContact. Structural figures from the simulations were rendered in VMD, whereas residue-wise structural properties were mapped and visualized using Chimera attribute files.

For statistical analysis, pathway-level measurements were normalized to the corresponding wild-type or ligand-bound wild-type reference value where applicable. For each variant, the mean value was calculated, and error bars represent the sample standard deviation across replicas. Group comparisons against the reference system were performed using a non-parametric permutation bootstrap. For each comparison, the two groups were pooled, labels were randomly permuted, and the mean difference was recalculated over 10,000 permutations using a two-sided test. The p-value was defined as the proportion of permuted absolute mean differences greater than or equal to the observed absolute mean difference. This approach did not assume normality or equal variances. Statistical analyses and plots were generated using Python notebooks.

6.3 Sample Preparation

The plasmid map of the p38α kinase construct was confirmed by nanopore sequencing to enable the design of mutation-specific primers. Mutagenesis primers were designed so that the target residue was positioned centrally within both the forward and reverse primer sequences. Site-directed mutagenesis was performed by PCR using Phusion™ High-Fidelity DNA Polymerase, which provides high-fidelity amplification suitable for introducing defined point mutations[201]. Following amplification, the parental methylated plasmid template was digested with *DpnI* at 37 °C for 1 h. The digested PCR product was then transformed into *E. coli* XL10-Gold cells and incubated overnight at 37 °C. Individual colonies were selected and grown overnight at 37 °C, after which plasmids were isolated using a PEG Gold miniprep kit (**Fig.6.1**). The resulting plasmids were verified by Sanger sequencing through Eurofins **Fig. 10.3** (Appendix).

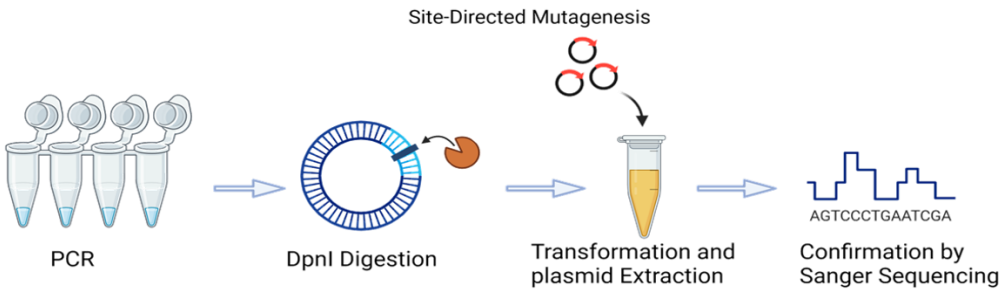

Fig.6.1 Pictorial representation for site directed mutagenesis

Wild-type p38α and the alanine mutants were expressed in BL21(DE3) *E. coli* cells. For NMR assignment and relaxation experiments, proteins were produced using $^{13}C/^{15}N/^{2}H$ isotopic labelling, with deuterated growth conditions used where required for triple-labelled samples[202]. Cultures were adapted to D_2O-containing medium and then grown in 1 L cultures at 37 °C until an OD600 of 0.6–0.7 was reached. The cultures were cooled to room temperature for 30 min and then induced with 1 mM IPTG. Protein expression was carried out overnight for approximately 20 h at 18 °C with shaking at 180 rpm. For the W207A mutant, stable expression in deuterated minimal medium could not be achieved, preventing preparation of a triple-labelled sample suitable for solution-state NMR analysis.

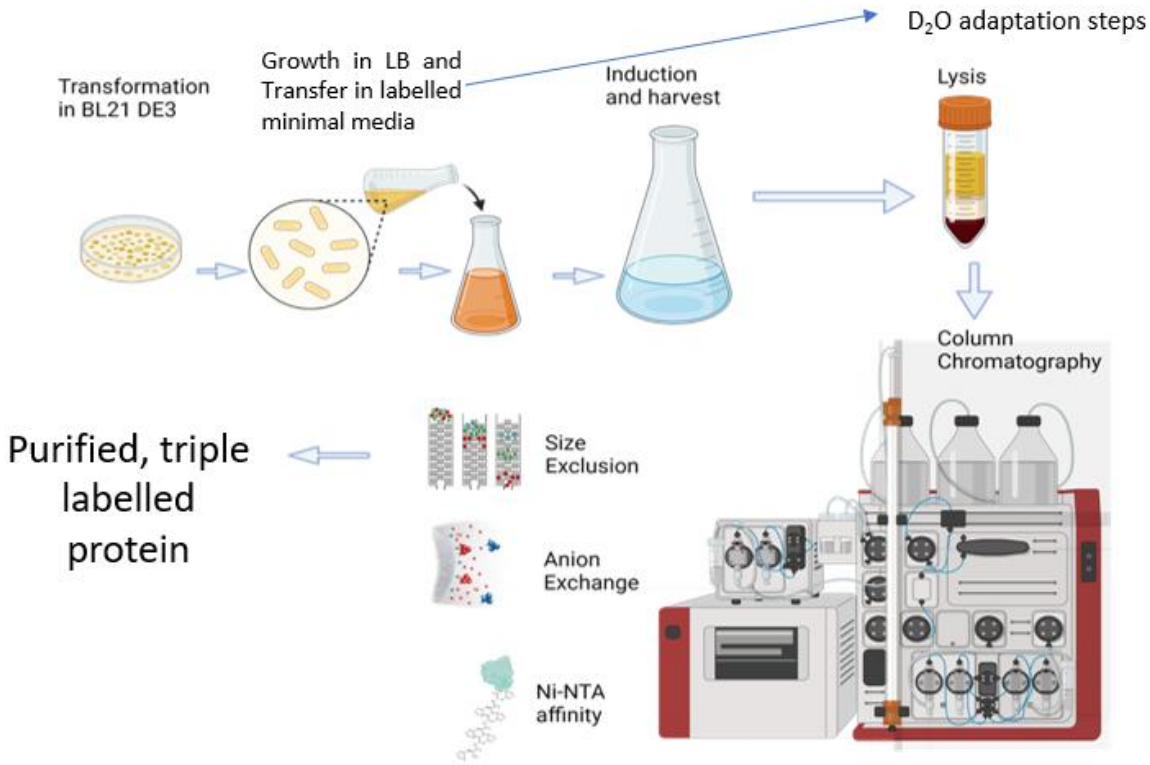

Fig 6.2 Schematic representation of expression and purification of p38α and mutants.

Cells were harvested and lysed in 50 mM Tris buffer supplemented with benzonase, lysozyme, and protease inhibitor. Following centrifugation, the clarified supernatant was subjected to Ni-affinity chromatography using a nickel column. The binding buffer contained 50 mM Tris, 500 mM NaCl, 25 mM imidazole, and 5% glycerol, whereas the elution buffer contained 50 mM Tris, 500 mM NaCl, 500 mM imidazole,

and 5% glycerol. Eluted fractions were dialysed to pH 7 and subjected to overnight thrombin cleavage to remove the affinity tag.

The cleaved protein was further purified by anion-exchange chromatography followed by size-exclusion chromatography, following established p38α purification strategies. For anion exchange, the binding buffer contained 25 mM HEPES and 5% glycerol, and the elution buffer contained 25 mM HEPES, 1 M NaCl, and 5% glycerol. Final polishing was performed by size-exclusion chromatography using buffer containing 20 mM HEPES, 50 mM NaCl, 100 mg/L methionine, and 5% glycerol. Fractions containing pure p38α were pooled and used for subsequent biochemical and NMR experiments (**Fig.6.2**).

6.4 Protein Crystallisation

Crystallization was performed in the presence of regorafenib. The protein solution was supplemented with 50 μM regorafenib dissolved in DMSO and mixed with crystallization buffer containing 100 mM MES and 20% PEG 4000. Crystallization was set up in a 1:3 ratio of crystallization buffer to protein solution using the sitting-drop method.

The crystallization buffer was placed in the reservoir, and drops containing the protein–ligand mixture were prepared for batch crystallization. To promote crystal growth, the drops were seeded with pre-existing crystals. The resulting crystals were used for both solid-state NMR experiments and X-ray crystallographic analysis (**Fig.6.3**).

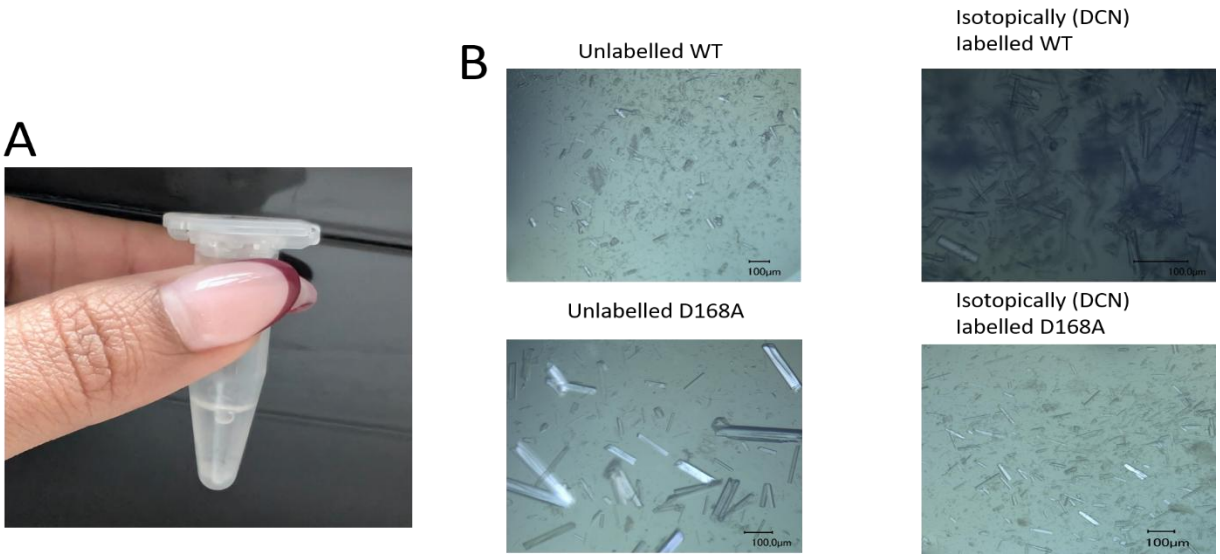

Fig.6.3 A) Batch crystallization of p38α in Eppendorf. **B**) Crystals showing apo and D168A in labelled and unlabelled conditions.

6.5 X-ray diffraction measurements

Crystals of wild-type p38α and the D168A mutant were harvested using 0.1 or 0.05 mm loops, depending on crystal size. The crystals were cryoprotected in precipitant solution supplemented with 10% glycerol and flash-frozen in liquid nitrogen.

Diffraction data were collected at a synchrotron beamline. Data processing and scaling were performed using XDS and XSCALE, respectively. Space-group determination was carried out with Pointless from the CCP4 suite. Model building and refinement were performed using Phenix and Coot.

6.6 HTRF analysis

Unlabelled wild-type and mutant p38α constructs were activated using constitutively active $MKK6^{S207E/T211E}$ (Thermo Scientific, Lot 877061F). Activation was performed in buffer containing 50 mM Tris, 10 mM $MgCl_2$, 1 mM ATP, 1 mM DTT, and 0.001% Tween-20 at pH 7.4. Reactions were incubated at 37 °C for 90 min with shaking at 400 rpm. Following activation, samples were dialysed overnight at 4 °C into storage buffer containing 20 mM HEPES, 50 mM NaCl, and 5% glycerol at pH

7.1. Proteins were then concentrated to approximately 0.2 mg/mL and stored at −80 °C until use.

ATP-dependent kinase activity was measured using the HTRF® KinEASE™ kit (Cisbio) according to the manufacturer's instructions. Activated p38α was added to each well at different amounts depending on the construct and labelling state: 0.04 ng for wild-type p38α, 3.5 ng for unlabelled mutants, and 20 ng for labelled mutants. Reaction times were adjusted accordingly to 10 min for wild type, 10 min for unlabelled mutants, and 20 min for labelled mutants. Reactions were performed in 384-well black flat-bottom plates using 1 μM GST-ATF2 substrate and ATP concentrations ranging from 0.4 to 900 μM.

The reaction buffer contained 50 mM HEPES, 0.1 mM Na_3VO_4, 0.02% NaN_3, 0.01% w/v BSA, 10 mM $MgCl_2$, 1 mM $MnCl_2$, 1 mM DTT, and 0.01% Triton X-100 at pH 7.0. Reactions were stopped by addition of detection solution containing 50 mM HEPES, 0.1% w/v BSA, 800 mM KF, 20 mM EDTA, 0.666 nM anti-phospho-ATF2-Eu(K) antibody, and 100 nM anti-GST-d2 antibody at pH 7.0. Plates were incubated for 60 min at room temperature to allow signal development.

Time-resolved fluorescence was measured using an EnVision 2104 plate reader at emission wavelengths of 620 nm and 665 nm, with readings collected 60 μs after excitation at 317 nm. The HTRF signal was calculated as the 665/620 nm emission ratio. This ratio was plotted as a function of ATP concentration and fitted to the Michaelis–Menten equation using Origin.

6.7 Nano DSF thermal shift analysis

For Project 2, NanoDSF measurements were performed to compare the thermal stability of wild-type p38α and the D168A mutant at different pH conditions. This experiment was designed as a complementary approach to the temperature-dependent MD simulations, allowing experimental comparison of the melting behaviour of the two proteins under defined buffer conditions.

Measurements were carried out in two buffer systems: pH 7.0 HEPES buffer containing 50 mM HEPES, 500 mM NaCl, and 1 mM TCEP, with 137 mM NaCl, 2.7 mM KCl, 10 mM phosphate, pH 8.0.

Protein samples were loaded into nanoDSF capillaries and subjected to a controlled temperature ramp. During heating, intrinsic tryptophan fluorescence was monitored continuously to follow the transition from the folded to unfolded state. The fluorescence ratio, typically reported as the 350/330 nm emission ratio, was used as a readout of changes in the local environment of tryptophan residues during unfolding.

The temperature was increased until 90 °C, at which point all samples were fully unfolded. Melting temperatures were determined from the thermal unfolding curves, allowing comparison of the apparent thermal stability of wild-type p38α and D168A under the tested pH conditions. These NanoDSF data provide an experimental reference for interpreting the temperature-ramping MD simulations and assessing whether the D168A mutation alters the stability of p38α in a pH-dependent manner.

6.8 Solution State NMR

Solution-state NMR spectroscopy was used in both projects to obtain residue-resolved information on p38α structure, dynamics, solvent accessibility, and exchange behaviour. Although both projects used similar sample preparation and assignment-transfer strategies, the experimental focus differed between the two studies. Project 1 focused primarily on solvent accessibility, water interactions, CLEANEX-PM, and hydrogen–deuterium exchange, whereas Project 2 focused on backbone assignment, chemical-shift perturbation analysis, heteronuclear NOE measurements, and CPMG relaxation dispersion.

NMR sample preparation

Protein obtained after size-exclusion chromatography was buffer-exchanged into NMR buffer containing 50 mM HEPES and 150 mM NaCl at approximately pH 6.8. Samples were then concentrated to approximately 450 μM before measurement. NMR spectra were recorded on an 800 MHz Bruker NEO spectrometer at 20 °C.

Backbone assignments were obtained using two-dimensional ^{15}N–^{1}H TROSY-HSQC spectra and three-dimensional TROSY-HNCA experiments. Existing assignments from BMRB entry 17471 were transferred to the mutant spectra in a stepwise manner. Peak assignment and spectral analysis were carried out using CcpNmr Analysis version 3.1[203].

NMR experiments for dynamic network analysis

For Project 1, solution-state NMR was used to assess mutation-induced changes in backbone chemical environment and dynamics. Two-dimensional ^{15}N–^{1}H TROSY-HSQC spectra were recorded for wild-type and mutant p38α constructs and used for chemical-shift perturbation analysis. Three-dimensional TROSY-HNCA experiments were acquired to support backbone assignment transfer from BMRB entry 17471. Mutant peak assignments were performed using CcpNmr Analysis version 3.1.

To probe fast-timescale backbone dynamics, ^{15}N–^{1}H TROSY-based heteronuclear NOE experiments were acquired and analysed using a CcpNmr relaxation-analysis macro. These experiments were used to compare residue-specific fast-timescale motional behaviour between wild-type and mutant proteins.

To assess slower conformational-exchange processes, ^{15}N TROSY-CPMG relaxation-dispersion experiments were acquired in an interleaved manner. The CPMG frequencies were recorded in the following order: 0, 2000, 25, 1500, 1000, 100, 750, 200, 1250, 500, and 200 Hz. The total CPMG delay was 0.022 s, and the recycling delay was 1.5 s. Relaxation-dispersion data were analysed using NESSY software[204] . Additional graphing and downstream analysis were performed using in-house Python scripts.

NMR experiments for water effects in allostery

For Project 2, solution-state NMR was used to probe water accessibility, amide-proton exchange, and protected regions of p38α. Two-dimensional ^{15}N–^{1}H TROSY-HSQC spectra were recorded as fingerprint spectra, and 3D TROSY-HNCA spectra were used to support assignment transfer.

^{15}N-edited NOESY experiments were acquired to identify water–amide cross-peaks and assess residues with detectable interactions with solvent water. CLEANEX-PM experiments were recorded to identify residues undergoing detectable exchange with water, particularly those showing exchange behaviour in the intermediate regime.

For hydrogen–deuterium exchange analysis, the protein was lyophilized after the initial measurements and redissolved in D_2O so that the sample contained approximately 90–95% D_2O, with only minimal residual H_2O. Consecutive ^{15}N–^{1}H TROSY-HSQC spectra were then recorded at hourly intervals over three days. Residues that retained signal intensity over time were interpreted as more protected from solvent exchange, whereas rapidly disappearing peaks were assigned to more solvent-accessible or exchange-prone regions. Peak intensities were extracted for

each time point, and residue-specific decay curves were plotted to monitor the exchange behaviour over time.

6.9 H/D exchange with Solid State NMR

One crystalline protein sample was divided into two Eppendorf tubes and packed into a 1.3 mm solid-state NMR rotor. For the non-exchanged crystalline sample, HNH and CANH experiments were recorded to support resonance assignment.

A second crystalline sample was prepared for hydrogen–deuterium exchange analysis. Before rotor packing, the supernatant buffer was removed, lyophilized, and redissolved in D_2O. The D_2O-containing buffer was then added back to the crystals stepwise, first to approximately 33%, then 75%, and finally 100% D_2O buffer. This resulted in an estimated final D_2O content of approximately 85–90% in the crystal slurry.

The exchanged crystalline sample was then packed into a 1.3 mm rotor (**Fig.6.4**). Two-dimensional hNH spectra were recorded at hourly intervals over three days to monitor time-dependent hydrogen–deuterium exchange in the crystalline protein sample.

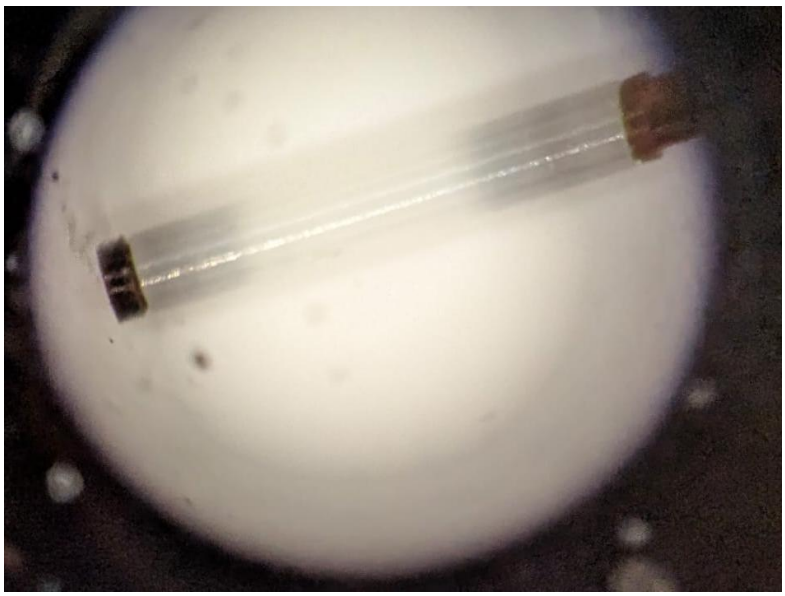

Fig. 6.4. 1.3 mm rotor packed with DCN wt p38α

7. References

1. LaPelusa A, Kaushik R. Physiology, Proteins. In: *StatPearls*). StatPearls Publishing

2. Sun PD, Foster CE, Boyington JC. Overview of protein structural and functional folds. *Curr Protoc Protein Sci* **Chapter 17**, Unit 17.11 (2004).

3. Jane SR. Describing patterns of protein tertiary structure. In: *Diffraction Methods for Biological Macromolecules Part B*). Academic Press (1985).

4. Jiao W, Blackmore NJ, Nazmi AR, Parker EJ. Quaternary structure is an essential component that contributes to the sophisticated allosteric regulation mechanism in a key enzyme from Mycobacterium tuberculosis. *PLoS One* **12**, e0180052 (2017).

5. Jaffe EK. Impact of quaternary structure dynamics on allosteric drug discovery. *Curr Top Med Chem* **13**, 55-63 (2013).

6. Kuriyan J, Eisenberg D. The origin of protein interactions and allostery in colocalization. *Nature* **450**, 983-990 (2007).

7. Monod J, Wyman J, Changeux JP. ON THE NATURE OF ALLOSTERIC TRANSITIONS: A PLAUSIBLE MODEL. *J Mol Biol* **12**, 88-118 (1965).

8. Cooper A, Dryden DT. Allostery without conformational change. A plausible model. *Eur Biophys J* **11**, 103-109 (1984).

9. Campitelli P, Kazan IC, Hamilton S, Ozkan SB. Dynamic Allostery: Evolution's Double-Edged Sword in Protein Function and Disease. *J Mol Biol* **437**, 169175 (2025).

10. Koshland DE, Jr., Némethy G, Filmer D. Comparison of experimental binding data and theoretical models in proteins containing subunits. *Biochemistry* **5**, 365-385 (1966).

11. Kumar S, Ma B, Tsai CJ, Sinha N, Nussinov R. Folding and binding cascades: dynamic landscapes and population shifts. *Protein Sci* **9**, 10-19 (2000).

12. Tzeng SR, Kalodimos CG. Protein dynamics and allostery: an NMR view. *Curr Opin Struct Biol* **21**, 62-67 (2011).

13. Gunasekaran K, Ma B, Nussinov R. Is allostery an intrinsic property of all dynamic proteins? *Proteins* **57**, 433-443 (2004).

14. Motlagh HN, Wrabl JO, Li J, Hilser VJ. The ensemble nature of allostery. *Nature* **508**, 331-339 (2014).

15. Wodak SJ*, et al.* Allostery in Its Many Disguises: From Theory to Applications. *Structure* **27**, 566-578 (2019).

16. Schlick T, Portillo-Ledesma S. Biomolecular modeling thrives in the age of technology. *Nat Comput Sci* **1**, 321-331 (2021).

17. Rohith K*, et al.* Generalized biomolecular modeling and design with RoseTTAFold All-Atom. *Science* **384**, eadl2528 (2024).

18. Schlick T*, et al.* Biomolecular Modeling and Simulation: A Prospering Multidisciplinary Field. *Annu Rev Biophys* **50**, 267-301 (2021).

19. Kosel B, Bigler K, Buchmuller BC, Acharyya SR, Linser R, Summerer D. Evolved Readers of 5-Carboxylcytosine CpG Dyads Reveal a High Versatility of the Methyl-CpG-Binding Domain for Recognition of Noncanonical Epigenetic Marks. *Angewandte Chemie International Edition* **63**, e202318837 (2024).

20. Jo S, Kim T, Iyer VG, Im W. CHARMM-GUI: A web-based graphical user interface for CHARMM. *Journal of Computational Chemistry* **29**, 1859-1865 (2008).

21. Karplus M, McCammon JA. Molecular dynamics simulations of biomolecules. *Nat Struct Biol* **9**, 646-652 (2002).

22. Alder BJ, Wainwright TE. Studies in Molecular Dynamics. I. General Method. *The Journal of Chemical Physics* **31**, 459-466 (1959).

23. Rahman A. Correlations in the Motion of Atoms in Liquid Argon. *Physical Review* **136**, A405-A411 (1964).

24. Karplus M. Molecular dynamics simulations of biomolecules. *Acc Chem Res* **35**, 321-323 (2002).

25. Scott AH, Ron OD. Molecular Dynamics Simulation for All. *Neuron* **99**, 1129-1143 (2018).

26. Kaffash M, Tolou-Shikhzadeh-Yazdi S, Soleimani S, Hoseinpoor S, Saberi MR, Chamani J. Spectroscopy and molecular simulation on the interaction of Nano-Kaempferol prepared by oil-in-water with two carrier proteins: An investigation of protein-protein interaction. *Spectrochim Acta A Mol Biomol Spectrosc* **309**, 123815 (2024).

27. Liang JJ, Pitsillou E, Hung A, Karagiannis TC. A repository of COVID-19 related molecular dynamics simulations and utilisation in the context of nsp10-nsp16 antivirals. *J Mol Graph Model* **126**, 108666 (2024).

28. Patoliya J, Thaker K, Rabadiya K, Patel D, Jain NK, Joshi R. Uncovering the Interaction Interface Between Harpin (Hpa1) and Rice Aquaporin (OsPIP1;3) Through Protein-Protein Docking: An In Silico Approach. *Mol Biotechnol* **66**, 756-768 (2024).

29. Xu B, Liang L, Jiang Y, Zhao Z. Investigating the ibrutinib resistance mechanism of L528W mutation on Bruton's tyrosine kinase via molecular dynamics simulations. *J Mol Graph Model* **126**, 108623 (2024).

30. Guvench O, MacKerell AD. Comparison of Protein Force Fields for Molecular Dynamics Simulations. In: *Molecular Modeling of Proteins* (ed Kukol A). Humana Press (2008).

31. Oostenbrink C, Villa A, Mark AE, van Gunsteren WF. A biomolecular force field based on the free enthalpy of hydration and solvation: the GROMOS force-field parameter sets 53A5 and 53A6. *J Comput Chem* **25**, 1656-1676 (2004).

32. Schmid N*, et al.* Definition and testing of the GROMOS force-field versions 54A7 and 54B7. *Eur Biophys J* **40**, 843-856 (2011).

33. Jorgensen WL, Maxwell DS, Tirado-Rives J. Development and Testing of the OPLS All-Atom Force Field on Conformational Energetics and Properties of Organic Liquids. *Journal of the American Chemical Society* **118**, 11225-11236 (1996).

34. Huang J, MacKerell AD, Jr. CHARMM36 all-atom additive protein force field: validation based on comparison to NMR data. *J Comput Chem* **34**, 2135-2145 (2013).

35. Huang J*, et al.* CHARMM36m: an improved force field for folded and intrinsically disordered proteins. *Nat Methods* **14**, 71-73 (2017).

36. MacKerell AD*, et al.* All-atom empirical potential for molecular modeling and dynamics studies of proteins. *J Phys Chem B* **102**, 3586-3616 (1998).

37. Cornell WD*, et al.* A Second Generation Force Field for the Simulation of Proteins, Nucleic Acids, and Organic Molecules. *Journal of the American Chemical Society* **117**, 5179-5197 (1995).

38. Hornak V, Abel R, Okur A, Strockbine B, Roitberg A, Simmerling C. Comparison of multiple Amber force fields and development of improved protein backbone parameters. *Proteins* **65**, 712-725 (2006).

39. Maier JA, Martinez C, Kasavajhala K, Wickstrom L, Hauser KE, Simmerling C. ff14SB: Improving the Accuracy of Protein Side Chain and Backbone Parameters from ff99SB. *J Chem Theory Comput* **11**, 3696-3713 (2015).

40. Guvench O, MacKerell AD, Jr. Comparison of protein force fields for molecular dynamics simulations. *Methods Mol Biol* **443**, 63-88 (2008).

41. Kopec W, Gapsys V. Periodic boundaries in Molecular Dynamics simulations: why do we need salt? *bioRxiv*, 2022.2010.2018.512672 (2022).

42. Ewald PP. Die Berechnung optischer und elektrostatischer Gitterpotentiale. *Annalen der Physik* **369**, 253-287 (1921).

43. Darden T, York D, Pedersen L. Particle mesh Ewald: An N·log(N) method for Ewald sums in large systems. *The Journal of Chemical Physics* **98**, 10089-10092 (1993).

44. Essmann U, Perera L, Berkowitz ML, Darden T, Lee H, Pedersen LG. A smooth particle mesh Ewald method. *The Journal of Chemical Physics* **103**, 8577-8593 (1995).

45. Hockney RW, Eastwood JW. *Computer Simulation Using Particles* (1981).

46. Lagüe P, Pastor RW, Brooks BR. Pressure-Based Long-Range Correction for Lennard-Jones Interactions in Molecular Dynamics Simulations: Application to Alkanes and Interfaces. *The Journal of Physical Chemistry B* **108**, 363-368 (2004).

47. Sagui C, Darden TA. Molecular dynamics simulations of biomolecules: long-range electrostatic effects. *Annu Rev Biophys Biomol Struct* **28**, 155-179 (1999).

48. Zhang L, Wang H, Muniz MC, Panagiotopoulos AZ, Car R, E W. A deep potential model with long-range electrostatic interactions. *The Journal of Chemical Physics* **156**, (2022).

49. Shūichi N. A molecular dynamics method for simulations in the canonical ensemble. *Molecular Physics* **52**, 255--268 (1984).

50. Berendsen HJC, Postma JPM, van Gunsteren WF, DiNola A, Haak JR. Molecular dynamics with coupling to an external bath. *Journal of Chemical Physics* **81**, 3684-3690 (1984).

51. Nosé S. A molecular dynamics method for simulations in the canonical ensemble. *Molecular Physics* **52**, 255-268 (1984).

52. Hoover WG. Canonical dynamics: Equilibrium phase-space distributions. *Physical Review A* **31**, 1695-1697 (1985).

53. Martyna GJ, Tobias DJ, Klein ML. Constant pressure molecular dynamics algorithms. *The Journal of Chemical Physics* **101**, 4177-4189 (1994).

54. Parrinello M, Rahman A. Polymorphic transitions in single crystals: A new molecular dynamics method. *Journal of Applied Physics* **52**, 7182-7190 (1981).

55. Schneider T, Stoll E. Molecular-dynamics study of a three-dimensional one-component model for distortive phase transitions. *Physical Review B* **17**, 1302-1322 (1978).

56. Verlet L. Computer "Experiments" on Classical Fluids. I. Thermodynamical Properties of Lennard-Jones Molecules. *Physical Review* **159**, 98-103 (1967).

57. Ryckaert J-P, Ciccotti G, Berendsen HJC. Numerical Integration of the Cartesian Equations of Motion of a System with Constraints: Molecular Dynamics of n-Alkanes. *Journal of Computational Physics* **23**, 327-341 (1977).

58. Hess B, Bekker H, Berendsen HJC, Fraaije JGEM. LINCS: A linear constraint solver for molecular simulations. *Journal of Computational Chemistry* **18**, 1463-1472 (1997).

59. Phillips JC*, et al.* Scalable molecular dynamics on CPU and GPU architectures with NAMD. *The Journal of Chemical Physics* **153**, (2020).

60. Phillips JC*, et al.* Scalable molecular dynamics with NAMD. *Journal of Computational Chemistry* **26**, 1781-1802 (2005).

61. Lee T-S*, et al.* GPU-Accelerated Molecular Dynamics and Free Energy Methods in Amber18: Performance Enhancements and New Features. *Journal of Chemical Information and Modeling* **58**, 2043-2050 (2018).

62. Rapid calculation of RMSDs using a quaternion-based characteristic polynomial. *Acta Crystallographica Section A* **61**, 478--480 (2005).

63. Martínez L. Automatic identification of mobile and rigid substructures in molecular dynamics simulations and fractional structural fluctuation analysis. *PLoS One* **10**, e0119264 (2015).

64. Elaheh KG. A review on the radial distribution function: Insights into molecular structure, intermolecular interactions, and thermodynamic properties. *Journal of Molecular Liquids* **433**, 127900 (2025).

65. Levine BG, Stone JE, Kohlmeyer A. Fast Analysis of Molecular Dynamics Trajectories with Graphics Processing Units-Radial Distribution Function Histogramming. *J Comput Phys* **230**, 3556-3569 (2011).

66. Bernetti M, Bosio S, Bresciani V, Falchi F, Masetti M. Probing allosteric communication with combined molecular dynamics simulations and network analysis. *Curr Opin Struct Biol* **86**, 102820 (2024).

67. Eargle J, Luthey-Schulten Z. NetworkView: 3D display and analysis of protein·RNA interaction networks. *Bioinformatics* **28**, 3000-3001 (2012).

68. Feher VA, Durrant JD, Van Wart AT, Amaro RE. Computational approaches to mapping allosteric pathways. *Curr Opin Struct Biol* **25**, 98-103 (2014).

69. Melo MCR, Bernardi RC, de la Fuente-Nunez C, Luthey-Schulten Z. Generalized correlation-based dynamical network analysis: a new high-performance approach for identifying allosteric communications in molecular dynamics trajectories. *J Chem Phys* **153**, 134104 (2020).

70. Sethi A, Eargle J, Black AA, Luthey-Schulten Z. Dynamical networks in tRNA:protein complexes. *Proc Natl Acad Sci U S A* **106**, 6620-6625 (2009).

71. Verkhivker GM, Di Paola L. Dynamic Network Modeling of Allosteric Interactions and Communication Pathways in the SARS-CoV-2 Spike Trimer Mutants: Differential Modulation of Conformational Landscapes and Signal Transmission via Cascades of Regulatory Switches. *J Phys Chem B* **125**, 850-873 (2021).

72. Shannon CE. A Mathematical Theory of Communication. *Bell System Technical Journal* **27**, 379-423 (1948).

73. Floyd RW. Algorithm 97: Shortest path. *Commun ACM* **5**, 345 , numpages = 341 (1962).

74. Warshall S. A Theorem on Boolean Matrices. *J Acm* **9**, 11–12 , numpages = 12 (1962).

75. Blondel VD, Guillaume J-L, Lambiotte R, Lefebvre E. Fast unfolding of communities in large networks. *Journal of Statistical Mechanics: Theory and Experiment* **2008**, P10008 (2008).

76. Girvan M, Newman MEJ. Community structure in social and biological networks. *Proceedings of the National Academy of Sciences* **99**, 7821-7826 (2002).

77. Keeler J. *Understanding NMR Spectroscopy*, 2 edn. Wiley (2010).

78. Cavanagh J, Skelton NJ, Fairbrother WJ, Rance M, Palmer AG, III. *Protein NMR Spectroscopy: Principles and Practice*, 2 edn. Academic Press (2006).

79. Rule GS, Hitchens TK. *Fundamentals of Protein NMR Spectroscopy*. Springer (2005).

80. Palmer AG, III. NMR Characterization of the Dynamics of Biomacromolecules. *Chemical Reviews* **104**, 3623-3640 (2004).

81. Mark WFF, Ananya M, Erik RPZ. Protein NMR relaxation: theory, applications and outlook. *Progress in Nuclear Magnetic Resonance Spectroscopy* **33**, 207-272 (1998).

82. Jarymowycz VA, Stone MJ. Fast Time Scale Dynamics of Protein Backbones: NMR Relaxation Methods, Applications, and Functional Consequences. *Chemical Reviews* **106**, 1624-1671 (2006).

83. Redfield AG. On the theory of relaxation processes. *IBM J Res Dev* **1**, 19–31 , numpages = 13 (1957).

84. Wangsness RK, Bloch F. The Dynamical Theory of Nuclear Induction. *Physical Review* **89**, 728-739 (1953).

85. Abergel D, Palmer AG. Approximate solutions of the Bloch-McConnell equations for two-site chemical exchange. *Chemphyschem* **5**, 787-793 (2004).

86. Carr HY, Purcell EM. Effects of Diffusion on Free Precession in Nuclear Magnetic Resonance Experiments. *Physical Review* **94**, 630-638 (1954).

87. Meiboom S, Gill D. Modified Spin-Echo Method for Measuring Nuclear Relaxation Times. *Review of Scientific Instruments* **29**, 688-691 (1958).

88. Loria JP, Berlow RB, Watt ED. Characterization of Enzyme Motions by Solution NMR Relaxation Dispersion. *Accounts of Chemical Research* **41**, 214-221 (2008).

89. Vasa SK, Rovó P, Linser R. Protons as Versatile Reporters in Solid-State NMR Spectroscopy. *Accounts of Chemical Research* **51**, 1386-1395 (2018).

90. Linser R, Fink U, Reif B. Proton-detected scalar coupling based assignment strategies in MAS solid-state NMR spectroscopy applied to perdeuterated proteins. *J Magn Reson* **193**, 89-93 (2008).

91. Frueh DP. Practical aspects of NMR signal assignment in larger and challenging proteins. *Prog Nucl Magn Reson Spectrosc* **78**, 47-75 (2014).

92. Canovas B, Nebreda AR. Diversity and versatility of p38 kinase signalling in health and disease. *Nat Rev Mol Cell Biol* **22**, 346-366 (2021).

93. Han J, Wu J, Silke J. An overview of mammalian p38 mitogen-activated protein kinases, central regulators of cell stress and receptor signaling. *F1000Res* **9**, (2020).

94. Papaconstantinou J*, et al.* Attenuation of p38α MAPK stress response signaling delays the in vivo aging of skeletal muscle myofibers and progenitor cells. *Aging (Albany NY)* **7**, 718-733 (2015).

95. Nebreda AR. Targeting p38α in cancer: challenges, opportunities, and emerging strategies. *Molecular Oncology* **n/a**, (2026).

96. Sahu V*, et al.* Diagnostic Significance of p38 Isoforms (p38α, p38β, p38γ, p38δ) in Head and Neck Squamous Cell Carcinoma: Comparative Serum Level Evaluation and Design of Novel Peptide Inhibitor Targeting the Same. *Cancer Res Treat* **51**, 313-325 (2019).

97. Uddin S, Ah-Kang J, Ulaszek J, Mahmud D, Wickrema A. Differentiation stage-specific activation of p38 mitogen-activated protein kinase isoforms in primary human erythroid cells. *Proc Natl Acad Sci U S A* **101**, 147-152 (2004).

98. Galan-Moya EM*, et al.* Balance between MKK6 and MKK3 mediates p38 MAPK associated resistance to cisplatin in NSCLC. *PLoS One* **6**, e28406 (2011).

99. Inoue T*, et al.* Mitogen-activated protein kinase kinase 3 is a pivotal pathway regulating p38 activation in inflammatory arthritis. *Proceedings of the National Academy of Sciences* **103**, 5484-5489 (2006).

100. Li Y*, et al.* Activation of Mitogen-activated Protein Kinase Kinase (MKK) 3 and MKK6 by Type I Interferons *. *Journal of Biological Chemistry* **280**, 10001-10010 (2005).

101. Onuma I*, et al.* The stress-activated kinase p38 mediates non-canonical activation of Src and tyrosine phosphorylation of the adapter protein TAB1. *J Biol Chem* **302**, 111200 (2026).

102. Zarubin T, Han J. Activation and signaling of the p38 MAP kinase pathway. *Cell Research* **15**, 11-18 (2005).

103. Ge B*, et al.* MAPKK-Independent Activation of p38α Mediated by TAB1-Dependent Autophosphorylation of p38α. *Science* **295**, 1291-1294 (2002).

104. Mittelstadt PR, Yamaguchi H, Appella E, Ashwell JD. T cell receptor-mediated activation of p38α by mono-phosphorylation of the activation loop results in altered substrate specificity. *J Biol Chem* **284**, 15469-15474 (2009).

105. Jun JE, Kulhanek KR, Chen H, Chakraborty A, Roose JP. Alternative ZAP70-p38 signals prime a classical p38 pathway through LAT and SOS to support regulatory T cell differentiation. *Sci Signal* **12**, (2019).

106. Stadnicki EJ*, et al.* Dual-action kinase inhibitors influence p38α MAP kinase dephosphorylation. *Proceedings of the National Academy of Sciences* **122**, e2415150122 (2025).

107. Trempolec N, Dave-Coll N, Nebreda AR. SnapShot: p38 MAPK Substrates. *Cell* **152**, 924-924.e921 (2013).

108. Heng CKM, Gilad N, Darlyuk-Saadon I, Wong WSF, Engelberg D. Targeting the p38α pathway in chronic inflammatory diseases: Could activation, not inhibition, be the appropriate therapeutic strategy? *Pharmacol Ther* **235**, 108153 (2022).

109. McNamee EN, Collins CB, Lebsack MD, Rivera-Nieves J. Cell-specific inhibition of p38alpha as a therapeutic strategy for inflammatory bowel disease. *Gastroenterology* **138**, 1237-1239 (2010).

110. Birkenkamp KU, Tuyt LM, Lummen C, Wierenga AT, Kruijer W, Vellenga E. The p38 MAP kinase inhibitor SB203580 enhances nuclear factor-kappa B transcriptional activity by a non-specific effect upon the ERK pathway. *Br J Pharmacol* **131**, 99-107 (2000).

111. Young PR*, et al.* Pyridinyl Imidazole Inhibitors of p38 Mitogen-activated Protein Kinase Bind in the ATP Site *. *Journal of Biological Chemistry* **272**, 12116-12121 (1997).

112. Kufareva I, Abagyan R. Type-II kinase inhibitor docking, screening, and profiling using modified structures of active kinase states. *J Med Chem* **51**, 7921-7932 (2008).

113. Liu Y, Gray NS. Rational design of inhibitors that bind to inactive kinase conformations. *Nat Chem Biol* **2**, 358-364 (2006).

114. Wang X, DeFilippis RA, Yan W, Shah NP, Li H-y. Overcoming Secondary Mutations of Type II Kinase Inhibitors. *Journal of Medicinal Chemistry* **67**, 9776-9788 (2024).

115. Ghoreschi K, Laurence A, O'Shea JJ. Selectivity and therapeutic inhibition of kinases: to be or not to be? *Nat Immunol* **10**, 356-360 (2009).

116. Fuwei Y, Li-Jie Z, Qinli X, Jianhui Z. The journey of p38 MAP kinase inhibitors: From bench to bedside in treating inflammatory diseases. *European Journal of Medicinal Chemistry* **280**, 116950 (2024).

117. Ganguly P, Macleod T, Wong C, Harland M, McGonagle D. Revisiting p38 Mitogen-Activated Protein Kinases (MAPK) in Inflammatory Arthritis: A Narrative of the Emergence of MAPK-Activated Protein Kinase Inhibitors (MK2i). *Pharmaceuticals (Basel)* **16**, (2023).

118. Cristina M*, et al.* Effects of the multikinase inhibitors Sorafenib and Regorafenib in PTEN deficient neoplasias. *European Journal of Cancer* **63**, 74-87 (2016).

119. Hamed HA, Tavallai S, Grant S, Poklepovic A, Dent P. Sorafenib/regorafenib and lapatinib interact to kill CNS tumor cells. *J Cell Physiol* **230**, 131-139 (2015).

120. Wilhelm SM*, et al.* Regorafenib (BAY 73-4506): A new oral multikinase inhibitor of angiogenic, stromal and oncogenic receptor tyrosine kinases with potent preclinical antitumor activity. *International Journal of Cancer* **129**, 245-255 (2011).

121. Fan J*, et al.* Harnessing Reversed Allosteric Communication: A Novel Strategy for Allosteric Drug Discovery. *Journal of Medicinal Chemistry* **64**, 17728-17743 (2021).

122. Erika P*, et al.* Structural Basis for the Subversion of MAP Kinase Signaling by an Intrinsically Disordered Parasite Secreted Agonist. *Structure* **25**, 16-26 (2017).

123. Juyoux P*, et al.* Architecture of the MKK6-p38α complex defines the basis of MAPK specificity and activation. *Science* **381**, 1217-1225 (2023).

124. White A, Pargellis CA, Studts JM, Werneburg BG, Farmer BT. Molecular basis of MAPK-activated protein kinase 2:p38 assembly. *Proceedings of the National Academy of Sciences* **104**, 6353-6358 (2007).

125. Pous J*, et al.* Structural basis of a redox-dependent conformational switch that regulates the stress kinase p38α. *Nature Communications* **14**, 7920 (2023).

126. Taylor SS, Kornev AP. Protein kinases: evolution of dynamic regulatory proteins. *Trends Biochem Sci* **36**, 65-77 (2011).

127. Kornev AP, Haste NM, Taylor SS, Ten Eyck LF. Surface comparison of active and inactive protein kinases identifies a conserved activation mechanism. *Proceedings of the National Academy of Sciences* **103**, 17783-17788 (2006).

128. Ung PM-U, Schlessinger A. DFGmodel: Predicting Protein Kinase Structures in Inactive States for Structure-Based Discovery of Type-II Inhibitors. *ACS Chemical Biology* **10**, 269-278 (2015).

129. Perry JJ, Harris RM, Moiani D, Olson AJ, Tainer JA. p38alpha MAP kinase C-terminal domain binding pocket characterized by crystallographic and computational analyses. *J Mol Biol* **391**, 1-11 (2009).

130. Bührmann M, Wiedemann BM, Müller MP, Hardick J, Ecke M, Rauh D. Structure-based design, synthesis and crystallization of 2-arylquinazolines as lipid pocket ligands of p38α MAPK. *PLoS One* **12**, e0184627 (2017).

131. Gomez-Gutierrez P, Rubio-Martinez J, Perez JJ. Identification of Potential Small Molecule Binding Pockets in p38α MAP Kinase. *Journal of Chemical Information and Modeling* **57**, 2566-2574 (2017).

132. Medina Gómez S, Homberg LT, Bührmann M, Rauh D, Linser R. Lipid Pocket Binders Impose Allosteric Changes of Protein Dynamics Around the Active Site of the Protein Kinase p38α. *Angewandte Chemie International Edition* **n/a**, e22665 (2026).

133. Kumar GS*, et al.* Dynamic activation and regulation of the mitogen-activated protein kinase p38. *Proceedings of the National Academy of Sciences* **115**, 4655-4660 (2018).

134. Ung PM, Schlessinger A. DFGmodel: predicting protein kinase structures in inactive states for structure-based discovery of type-II inhibitors. *ACS Chem Biol* **10**, 269-278 (2015).

135. Daniel KT, Neil PS. Ins and Outs of Kinase DFG Motifs. *Chemistry & Biology* **20**, 745-746 (2013).

136. Vijayan RSK*, et al.* Conformational Analysis of the DFG-Out Kinase Motif and Biochemical Profiling of Structurally Validated Type II Inhibitors. *Journal of Medicinal Chemistry* **58**, 466-479 (2015).

137. Pegram LM, Anderson JW, Ahn NG. Dynamic equilibria in protein kinases. *Curr Opin Struct Biol* **71**, 215-222 (2021).

138. Maria-Solano MA, Choi S. Dynamic allosteric networks drive adenosine A\textsubscript 1 receptor activation and G-protein coupling. *eLife* **12**, RP90773 , citation = eLife 92023;90712 RP90773 (2023).

139. Aoto PC, Martin BT, Wright PE. NMR Characterization of Information Flow and Allosteric Communities in the MAP Kinase p38γ. *Scientific Reports* **6**, 28655 (2016).

140. Ahuja LG, Aoto PC, Kornev AP, Veglia G, Taylor SS. Dynamic allostery-based molecular workings of kinase:peptide complexes. *Proceedings of the National Academy of Sciences* **116**, 15052-15061 (2019).

141. Zhang L, Bouguet-Bonnet S, Buck M. Combining NMR and molecular dynamics studies for insights into the allostery of small GTPase-protein interactions. *Methods Mol Biol* **796**, 235-259 (2012).

142. Oxenfarth A*, et al.* Integrated NMR/Molecular Dynamics Determination of the Ensemble Conformation of a Thermodynamically Stable CUUG RNA Tetraloop. *Journal of the American Chemical Society* **145**, 16557-16572 (2023).

143. Papaleo E. Integrating atomistic molecular dynamics simulations, experiments, and network analysis to study protein dynamics: strength in unity. *Frontiers in Molecular Biosciences* **Volume 2 - 2015**, (2015).

144. McClendon CL, Kornev AP, Gilson MK, Taylor SS. Dynamic architecture of a protein kinase. *Proceedings of the National Academy of Sciences* **111**, E4623-E4631 (2014).

145. Kornev AP, Taylor SS. Dynamics-Driven Allostery in Protein Kinases. *Trends Biochem Sci* **40**, 628-647 (2015).

146. Kuzmanic A, Sutto L, Saladino G, Nebreda AR, Gervasio FL, Orozco M. Changes in the free-energy landscape of p38α MAP kinase through its canonical activation and binding events as studied by enhanced molecular dynamics simulations. *eLife* **6**, e22175 , citation = eLife 22017;22176 e22175 (2017).

147. Ron D, David E, Oded L. A Novel Lipid Binding Site Formed by the MAP Kinase Insert in p38α. *Journal of Molecular Biology* **375**, 70-79 (2008).

148. González L*, et al.* Characterization of p38α autophosphorylation inhibitors that target the non-canonical activation pathway. *Nat Commun* **14**, 3318 (2023).

149. Zhang XH*, et al.* Targeting the non-ATP-binding pocket of the MAP kinase p38γ mediates a novel mechanism of cytotoxicity in cutaneous T-cell lymphoma (CTCL). *FEBS Lett* **595**, 2570-2592 (2021).

150. Namboodiri HV, Bukhtiyarova M, Ramcharan J, Karpusas M, Lee Y, Springman EB. Analysis of imatinib and sorafenib binding to p38alpha compared with c-Abl and b-Raf provides structural insights for understanding the selectivity of inhibitors targeting the DFG-out form of protein kinases. *Biochemistry* **49**, 3611-3618 (2010).

151. Simard JR*, et al.* Development of a fluorescent-tagged kinase assay system for the detection and characterization of allosteric kinase inhibitors. *J Am Chem Soc* **131**, 13286-13296 (2009).

152. Mattia B, Stefano B, Veronica B, Federico F, Matteo M. Probing allosteric communication with combined molecular dynamics simulations and network analysis. *Current Opinion in Structural-biology* **86**, 102820 (2024).

153. Krishnan K, Tian H, Tao P, Verkhivker GM. Probing conformational landscapes and mechanisms of allosteric communication in the functional states of the ABL kinase domain using multiscale simulations and network-based mutational profiling of allosteric residue potentials. *J Chem Phys* **157**, 245101 (2022).

154. Taylor SS, Zhang P, Steichen JM, Keshwani MM, Kornev AP. PKA: lessons learned after twenty years. *Biochim Biophys Acta* **1834**, 1271-1278 (2013).

155. Panjarian S, Iacob RE, Chen S, Engen JR, Smithgall TE. Structure and dynamic regulation of Abl kinases. *J Biol Chem* **288**, 5443-5450 (2013).

156. Griswold IJ*, et al.* Kinase domain mutants of Bcr-Abl exhibit altered transformation potency, kinase activity, and substrate utilization, irrespective of sensitivity to imatinib. *Mol Cell Biol* **26**, 6082-6093 (2006).

157. Shan Y*, et al.* Oncogenic mutations counteract intrinsic disorder in the EGFR kinase and promote receptor dimerization. *Cell* **149**, 860-870 (2012).

158. Huse M, Kuriyan J. The conformational plasticity of protein kinases. *Cell* **109**, 275-282 (2002).

159. Wilson KP*, et al.* Crystal structure of p38 mitogen-activated protein kinase. *J Biol Chem* **271**, 27696-27700 (1996).

160. Degorce F, Card A, Soh S, Trinquet E, Knapik GP, Xie B. HTRF: A technology tailored for drug discovery - a review of theoretical aspects and recent applications. *Curr Chem Genomics* **3**, 22-32 (2009).

161. Holliday MJ, Camilloni C, Armstrong GS, Vendruscolo M, Eisenmesser EZ. Networks of Dynamic Allostery Regulate Enzyme Function. *Structure* **25**, 276-286 (2017).

162. Thapa D*, et al.* TAB1-Induced Autoactivation of p38α Mitogen-Activated Protein Kinase Is Crucially Dependent on Threonine 185. *Mol Cell Biol* **38**, (2018).

163. Keesler GA*, et al.* Purification and activation of recombinant p38 isoforms alpha, beta, gamma, and delta. *Protein Expr Purif* **14**, 221-228 (1998).

164. Liu MY, Hua WK, Chen CJ, Lin WJ. The MKK-Dependent Phosphorylation of p38α Is Augmented by Arginine Methylation on Arg49/Arg149 during Erythroid Differentiation. *Int J Mol Sci* **21**, (2020).

165. Ambrosino C*, et al.* Negative feedback regulation of MKK6 mRNA stability by p38alpha mitogen-activated protein kinase. *Mol Cell Biol* **23**, 370-381 (2003).

166. Kharchenko V, Nowakowski M, Jaremko M, Ejchart A, Jaremko Ł. Dynamic $^{15}N^{1}H$ NOE measurements: a tool for studying protein dynamics. *J Biomol NMR* **74**, 707-716 (2020).

167. Bhattacharya S*, et al.* NMR-guided directed evolution. *Nature* **610**, 389-393 (2022).

168. Huang S, New L, Pan Z, Han J, Nemerow GR. Urokinase plasminogen activator/urokinase-specific surface receptor expression and matrix invasion by breast cancer cells requires constitutive p38alpha mitogen-activated protein kinase activity. *J Biol Chem* **275**, 12266-12272 (2000).

169. McLaughlin MM*, et al.* Identification of Mitogen-activated Protein (MAP) Kinase-activated Protein Kinase-3, a Novel Substrate of CSBP p38 MAP Kinase (*). *Journal of Biological Chemistry* **271**, 8488-8492 (1996).

170. Palmer AG, 3rd. NMR characterization of the dynamics of biomacromolecules. *Chem Rev* **104**, 3623-3640 (2004).

171. Palmer AG, 3rd, Kroenke CD, Loria JP. Nuclear magnetic resonance methods for quantifying microsecond-to-millisecond motions in biological macromolecules. *Methods Enzymol* **339**, 204-238 (2001).

172. Loria JP, Rance M, Palmer AG. A Relaxation-Compensated Carr−Purcell−Meiboom−Gill Sequence for Characterizing Chemical Exchange by NMR Spectroscopy. *Journal of the American Chemical Society* **121**, 2331-2332 (1999).

173. Ahuja LG, Kornev AP, McClendon CL, Veglia G, Taylor SS. Mutation of a kinase allosteric node uncouples dynamics linked to phosphotransfer. *Proc Natl Acad Sci U S A* **114**, E931-e940 (2017).

174. Bührmann M, Hardick J, Weisner J, Quambusch L, Rauh D. Covalent Lipid Pocket Ligands Targeting p38α MAPK Mutants. *Angew Chem Int Ed Engl* **56**, 13232-13236 (2017).

175. Singh H*, et al.* Fast Microsecond Dynamics of the Protein–Water Network in the Active Site of Human Carbonic Anhydrase II Studied by Solid-State NMR Spectroscopy. *Journal of the American Chemical Society* **141**, 19276-19288 (2019).

176. Knight JD, Hamelberg D, McCammon JA, Kothary R. The role of conserved water molecules in the catalytic domain of protein kinases. *Proteins* **76**, 527-535 (2009).

177. Fenimore PW, Frauenfelder H, McMahon BH, Parak FG. Slaving: solvent fluctuations dominate protein dynamics and functions. *Proc Natl Acad Sci U S A* **99**, 16047-16051 (2002).

178. Anna Rita B, and Salvatore C. Molecular Dynamics of Water at the Protein-Solvent Interface. *Journal of Physical Chemistry B* **106**, 6617-6633 (2002).

179. Ansari A, Jones CM, Henry ER, Hofrichter J, Eaton WA. The role of solvent viscosity in the dynamics of protein conformational changes. *Science* **256**, 1796-1798 (1992).

180. Gough NR, Kalodimos CG. Exploring the conformational landscape of protein kinases. *Curr Opin Struct Biol* **88**, 102890 (2024).

181. Fabbro D, Cowan-Jacob SW, Moebitz H. Ten things you should know about protein kinases: IUPHAR Review 14. *Br J Pharmacol* **172**, 2675-2700 (2015).

182. Mondal J, Tiwary P, Berne BJ. How a Kinase Inhibitor Withstands Gatekeeper Residue Mutations. *J Am Chem Soc* **138**, 4608-4615 (2016).

183. Teixeira LR, Akella R, Humphreys JM, He H, Goldsmith EJ. Water and chloride as allosteric inhibitors in WNK kinase osmosensing. *Elife* **12**, (2024).

184. Patil K*, et al.* Coupled Solvent Dynamics and Protein Dynamics Help Drive Functional Differences in Exon-19 Deletion Mutants in the Epidermal Growth Factor Receptor (EGFR/ErbB1/HER1) Kinase Domain. *bioRxiv*, (2024).

185. Levinson NM, Boxer SG. A conserved water-mediated hydrogen bond network defines bosutinib's kinase selectivity. *Nat Chem Biol* **10**, 127-132 (2014).

186. Asquith CRM*, et al.* Targeting the Water Network in Cyclin G-Associated Kinase (GAK) with 4-Anilino-quin(az)oline Inhibitors. *ChemMedChem* **15**, 1200-1215 (2020).

187. Williams MA, Goodfellow JM, Thornton JM. Buried waters and internal cavities in monomeric proteins. *Protein Sci* **3**, 1224-1235 (1994).

188. Carugo O. Structure and function of water molecules buried in the protein core. *Curr Protein Pept Sci* **16**, 259-265 (2015).

189. Klein T*, et al.* Structural and dynamic insights into the energetics of activation loop rearrangement in FGFR1 kinase. *Nat Commun* **6**, 7877 (2015).

190. Xie T, Saleh T, Rossi P, Kalodimos CG. Conformational states dynamically populated by a kinase determine its function. *Science* **370**, (2020).

191. Casasnovas R, Limongelli V, Tiwary P, Carloni P, Parrinello M. Unbinding Kinetics of a p38 MAP Kinase Type II Inhibitor from Metadynamics Simulations. *J Am Chem Soc* **139**, 4780-4788 (2017).

192. Luccarelli J, Michel J, Tirado-Rives J, Jorgensen WL. Effects of Water Placement on Predictions of Binding Affinities for p38α MAP Kinase Inhibitors. *J Chem Theory Comput* **6**, 3850-3856 (2010).

193. Gómez-Flores AK, López-Pérez E, Alas-Guardado SJ. Molecular Dynamics Simulations of HPr Proteins from a Thermophilic and a Mesophilic Organism: A Comparative Thermal Study. *Int J Mol Sci* **24**, (2023).

194. Yu H, Dalby PA. Exploiting correlated molecular-dynamics networks to counteract enzyme activity–stability trade-off. *Proceedings of the National Academy of Sciences* **115**, E12192-E12200 (2018).

195. Lin X, Lee S, Sun G. Functions of the activation loop in Csk protein-tyrosine kinase. *J Biol Chem* **278**, 24072-24077 (2003).

196. Shan Y*, et al.* A conserved protonation-dependent switch controls drug binding in the Abl kinase. *Proceedings of the National Academy of Sciences* **106**, 139-144 (2009).

197. Michaud-Agrawal N, Denning EJ, Woolf TB, Beckstein O. MDAnalysis: a toolkit for the analysis of molecular dynamics simulations. *J Comput Chem* **32**, 2319-2327 (2011).

198. Lam SK, Pitrou A, Seibert S. Numba: a LLVM-based Python JIT compiler. In: *Proceedings of the Second Workshop on the LLVM Compiler Infrastructure in HPC , articleno = 7 , numpages = 6*). Association for Computing Machinery (2015).

199. Behnel S, Bradshaw R, Citro C, Dalcin L, Seljebotn DS, Smith K. Cython: The Best of Both Worlds. *Computing in Science and Engg* **13**, 31–39 , numpages = 39 (2011).

200. Humphrey W, Dalke A, Schulten K. VMD: visual molecular dynamics. *J Mol Graph* **14**, 33-38, 27-38 (1996).

201. Carter P. Site-directed mutagenesis. *Biochem J* **237**, 1-7 (1986).

202. Kainosho M, Torizawa T, Iwashita Y, Terauchi T, Mei Ono A, Güntert P. Optimal isotope labelling for NMR protein structure determinations. *Nature* **440**, 52-57 (2006).

203. Skinner SP, Fogh RH, Boucher W, Ragan TJ, Mureddu LG, Vuister GW. CcpNmr AnalysisAssign: a flexible platform for integrated NMR analysis. *J Biomol NMR* **66**, 111-124 (2016).

204. Bieri M, Gooley PR. Automated NMR relaxation dispersion data analysis using NESSY. *BMC Bioinformatics* **12**, 421 (2011).

8. List of Figures

Fig.1.1 : Illustration of the hierarchical levels of protein structure, including the primary, secondary, tertiary, and quaternary levels……15

Fig.1.2 Entropy- or dynamics-driven allostery model. Distinct residue communities that move coherently as semi-rigid bodies are highlighted in different colors, while intermediate residues that cannot be assigned to a specific community are represented as white circles. Information flux passes through dynamic motions of the semi rigid bodies from the allosteric to the active site…….17

Fig. 1.3. A, B) Models of KLTR (**A**) and GMRN (**B**) interacting with caC/caC/dyad. Mutants in green, superimposed MeCP2 wt (pdb 3c2i) in white. Retained, canonical interactions found in both wt and mutant in yellow, new interactions uniquely occurring in mutants in red. **C**) Contact arrays for KLTR and GMRN with caC/caC and mC/caC. Note canonical, wt-like interactions of R111/133 with Gs (numbered in white), and new interactions of mutant-specific residues (numbered in black). Favorable interactions to C 5-substituents marked with green arrow–GMRN cannot interact with mC 5-methyl (red arrow), explaining its high selectivity for caC/caC. Interaction color code on the right (HB=hydrogen bond; CA: contact area)……20

Fig 1.4 A) Root mean square deviations **B**) Root mean square fluctuations **C**) Radius of gyration **D**) Solvent Accessible Surface Area of the wildtype in Na ions, wildtype in Cs ions and the mutant 2b9 in Na ions…….26

Fig. 1.5. Angular momentum I of the spin -$\frac{1}{2}$ along with its Z-component, rotating about an external magnetic field……31

Fig. 1.6. Pulse sequence for HSQC showing refocussed INEPT. It starts with a 90°_{x} pulse on antiphase state on spin I, transferred to spin S with 90°_{y}, and evolves into in-phase magnetisation, with optimum delays τ_1 and τ_2 being $1/4J_{IS}$……..36

Fig.1.7 : Schematic figure to elucidate molecular motion at different timescales using NMR experiments……43

Fig. 1.8. Basic plasmid map portraying different genes required for expression of proteins……46

Fig. 1.9: Cellular signalling of the MAP kinase pathway, p38α being the downstream kinase……...48

Fig. 1.10. Structural features of p38α……49

Fig. 3.1 A) Structural representation of p38α kinase, highlighting the interactions of ligands binding to the allosteric pocket (exemplified for sorafenib) and the lipid pocket (shown for β-OG), as produced using Discovery studio. Key structural features such as the activation loop, the catalytic C- spine, and the regulatory R-spine are highlighted. **B**) Observed ring flip of the type-II inhibitor sorafenib between structures in the presence (semi-transparent yellow, PDB 3GCS) or absence (semi-transparent cyan, PDB 3HEG) of a lipid pocket binder (β-OG). **C**) Sketch of the allosteric pathways between the active site, the adjacent, so-called allosteric pocket, and the lipid pocket in question……58

Fig. 3.2 Schematic representation of the methodology to identify the communicators and validate them experimentally and computationally……59

Fig. 3.3 A) RMSD of the simulations using starting crystal structures 3HEG (p38a bound to sorafenib only; red) and 3GCS (Sora + BOG; blue) **B**) RMSF of the simulations using starting crystal structures 3HEG (Sorafenib with p38α; red) and 3GCS (Sora + BOG with p38α ; blue). **C**) Differences in communities when BOG binds to the lipid pocket. **D**) Differences in pathways upon BOG binding from the allosteric pocket to the activation loop. **E**) Differences in pathways upon BOG binding from the lipid pocket to the activation loop. **F**) Differences in pathways upon BOG binding from the lipid pocket directly to the allosteric pocket……60

Fig. 3.4: **A**) Backbone RMSD of the apoprotein across five independent 1 μs replicas; the final 200 ns of each replica were used for network analysis. **B**) Overlay of RMSD traces for all five apoprotein replicas, highlighting convergence. **C**) Average per-residue RMSF mapped onto the protein structure to visualize flexibility.

…….61

Fig. 3.5 Clustering of the protein into 14 communities, largely reminiscent of the different structural elements of the kinase (right)……..62

Fig. 3.6 Residues with top betweenness centrality, i.e., the highest degree of information flow traversing them, also highlighting those network sites chosen for mutagenesis studies for network validation (red highlights)……..64

Fig.3.7 Map of inter-residue dynamic-network correlations, specifically focusing on connections between N- and C-lobe residues. Pairs in black writing denote long-range correlations with a correlation coefficient above 0.3. Note that part of the C-terminal (320-360) lies in the N-Lobe, while the first transition from N- to C-lobe

occurs at around residue 107. Correlations involving these covalent linkages are grayed out…….65

Fig. 3.8 B-factors of X-ray crystal structure along the protein. Temperature B-factors (Debye-Waller factors) are shown for the crystal structure PDB 3HEG…66

Fig. 3.9 A) RMSDs and RMSFs of five replicas per mutant. The last 200 ns were used for network and correlation analysis. **B)** Mean and SD of all the RMSFs compared with the wildtype……..67

Fig. 3.10: Network analysis by Dynetan, mainly betweenness and communities of the mutants. The top shows the entire network, while the center depicts betweenness, and the bottom shows the clusters found in each of the mutants…68

Fig. 3.11. A) N-C lobe correlations of the mutants focusing on the inter-domain regions. B) Differences (mutant – WT) in the correlations from the N to C lobe for each of the mutants……...69

Fig. 3.12 Strategy to verify the results of dynamic-network analyses, using in-silico mutagenesis, functional assays of mutants, and NMR chemical-shift perturbation and relaxation……...72

Fig. 3.13 A) Residue-wise depiction of the shortest communication path from the allosteric pocket to the activation loop. **B**) For all the pathways (n=5).Total correlation of residue pairs along the allosteric-pocket-to-activation-loop pathway, normalized to wild-type (WT = 1) and with statistical annotations ** for $p < 0.05$ and *** for $p < 0.01$. Statistical significance was assessed by non-parametric bootstrap tests, see the Methods for details. A marked reduction is observed in all mutants, with W207A exhibiting the most significant drop ($p = 0.039$). **C**) Shortest path from the lipid pocket to the activation loop with key residues highlighted. **D**) Correlation sums along the lipid-pocket-to-activation-loop pathway, normalized to WT, D168A highlighting a significant decrease ($p = 0.043$). **E**) Residue pathway showing the shortest communication route from the allosteric pocket to the lipid pocket. **F**) Total correlation for the allosteric-pocket-to-lipid-pocket pathway, normalized to WT, with all mutants showing statistically significant reduced correlations ($p = 0.017$ for R49A; $p = 0.0026$ for D150A; $p = 0.0022$ for D168A; $p = 0.005$ for W207A)……..75

Fig. 3.14: Interacting residues when ligand sorafenib is docked with the WT protein and the mutants as seen through Discovery studio……76

Fig. 3.15: A) Relative correlations between the protein and the ligand (divided into two groups, the eastern and western part), resolved by protein residue. B) Total

correlation of the ligand sorafenib with the mutants and the WT (the latter being normalized to 1)……77

Fig 3.16: A) Structural depiction of the communication pathway from the allosteric pocket to the activation loop in wild-type p38α kinase. The apo WT shortest path is shown in red, while the ligand-bound (holo) WT pathway is depicted in purple, highlighting a shift in the nature of inter-residue motional interactions upon ligand binding. **B**) Correlational changes referenced to the holo WT pathway (purple). **C**) Structure of the lipid-pocket-to-activation-loop pathway, comparing apo (red) and holo (purple) WT forms. Ligand binding again alters the trajectory of this communication path. **D**) Using the holo WT pathway (purple) as the reference, minor differences in correlations are seen from the lipid pocket to the activation loop. **E**) Structural comparison of the allosteric-to-lipid pocket pathway, red and purple representing shortest paths in apo WT and holo WT, respectively. **F**) Correlation changes for the allosteric-site-to-lipid-pocket pathway……79

Fig.3.17 A) HTRF-based ATP titration assay comparing the integrity of ATP binding between wild-type and mutant p38α kinase constructs across a concentration range of 0–1000 μM ATP. The result of a Michaelis-Menten fit of the fluorescence ratio f665/f620 obtained after a given time in the initial-rate regime serves as a quantitative proxy for ATP binding (best-fit KM shown for each curve). **B**) HTRF signals were normalized to the fitted vmax of each protein variant to compare fractional saturation, and were fitted according to Hill equation. The plots highlight differences in the concentration range over which ATP approaches saturation……..81

Fig. 3.18. A) HTRF substrate titration assay quantifying substrate binding affinity of wild-type and mutant kinases using increasing concentrations of a GST-tagged activating transcription factor 2 (ATF2) substrate. KM fit values are again shown for each curve. While wild-type shows high fidelity of substrate association, the data for the dynamic-network mutants consistently indicate slightly impaired ATP and substrate binding competency. **B**) HTRF signals were normalized to the fitted vmax of each protein variant to compare fractional saturation, and were fitted according to Hill equation. The plots highlight differences in the concentration range over which substrate approaches saturation……..82

Fig.3.19 Transfer of assignments using TROSY HSQC and HNCA spectra of the WT. (Chemical shifts of the WT are also available in the BMRB under accession code 17471.)……84

Fig.3.20 TROSY HSQC of the mutants overlaid with the WT triple labelled proteins……85

Fig.3.21 Quantification of chemical shift perturbations of the dynamic network mutants with the wildtype……86

Fig.3.22 Distribution of chemical shift perturbations across the protein structure.87

Fig.3.23 Grouping of structural elements of all the mutants with a perturbed CSP.88

Fig.3.24 Violin plots summarizing CSP distributions across network mutants (R49A, D150A, D168A) and the control variant (V38A). Blue and red dots mark residues from the lipid pocket and active site, respectively……89

Fig.3.25 Residue wise hetNOE trends……..91

Fig.3.26 Residue wise R_2 trends……92

Fig.3.27 Structural visualization of ΔhetNOE (mutant-WT) values. Blue regions highlight residues with reduced NOE values in the mutants, indicative of enhanced backbone flexibility……...93

Fig.3.28 Structural mapping of ΔR_2 (mutant – WT) values onto the three-dimensional structure of p38α kinase. Red regions indicate residues with R_2 higher in the mutants, predominantly localized to the catalytic core and distal C-lobe, supporting widespread conformational exchange……93

Fig.3.29 Regions portraying increased fast time-scale dynamics collectively for all dynamic network mutants, specifically the activation loop……94

Fig.3.30 Important regions of protein showing an increased R2 upon mutation of the dynamic network (R49, D150 and D168), specifically transcending the network to accommodate the lipid pocket……..97

Fig.3.31 A) Box plot distribution of R_2 values for wild-type, dynamic network mutants (R49A, D168A, D150A), and the negative control (V38A). Active-site residues (red) and lipid pocket residues (blue) are specifically highlighted by colored spheres. All dynamic-network mutants exhibit significantly elevated R_2 values compared to the wild-type and control, consistent with a global enhancement in slow conformational exchange. **B**) Box plots of hetNOE values across the same variants. Dynamic network mutants show a marked reduction in NOE values, reflecting increased local flexibility, including at functionally critical sites. By contrast, the control mutant V38A shows limited perturbation, confirming an impact on the p38 dynamic network to be absent……100

Fig.3.32 R_{ex} trends residue wise, comparing WT with the mutants……..101

Fig.3.33 Structural visualization comparing the spatial distribution of Rex values between wild-type and the mutants. Residues exhibiting exchange contributions are highlighted in red. V38A shows minimal deviation from WT, consistent with its dynamic neutrality……...102

Fig.3.34 Representative CPMG dispersion curves, shown here for residue A172, a key linker residue bridging the active site to the DFG motif……103

Fig.3.35 Histogram plots illustrating the global frequency distribution of R_{ex} values across all variants. The wildtype shows a slightly broader distribution of dynamic residues, indicative of a more homogeneous conformational ensemble. In contrast, network-disrupting mutants (e.g., D168A, R49A) display slightly more exchange.103

Fig.3.36 Box plots compare Rex values across WT and mutants, with the median shown in orange. Colored points indicate residues from the activation loop (yellow), allosteric pocket (blue), and lipid pocket/MAP kinase insert region (green), highlighting site-specific contributions of regulatory regions to altered slower-timescale dynamics……..104

Fig.4.1 Aspartate of the DFG motif coordinates with Mg^{2+} to support phosphoryl transfer……...114

Fig.4.2 DFG-in/out orientations create the allosteric pocket with different structural crystal waters……..115

Fig. 4.3 Pyridyl ring flip of regorafenib on D168A mutation hinting to allostery.115

Fig.4.4 Crystal waters around the allosteric pocket and lipid pocket of the wildtype (blue) and D168A (red) showing the trends in conservation and changes upon mutation…….116

Fig.4.5 A) Schematic of the temperature-ramping simulation protocol, in which the system was gradually heated to 423 K during the first microsecond and then maintained at 423 K for an additional microsecond to probe high-temperature structural adaptation. **B**) Temperature ramping simulations performed in triplicate for wild-type p38α and the D168A mutant show that the wild type consistently reaches higher RMSD values than D168A, indicating greater structural deviation during heating and suggesting that the mutant better preserves its global fold under thermal stress…….118

Fig.4.6 Time-resolved wRMSD/RMSF heatmap analysis further illustrates the differential response to heating. In the wild type, flexibility progressively increases

with temperature, particularly in the core and activation loop. In contrast, the D168A mutant displays more limited temperature-dependent changes, with noticeable increases largely confined to helical regions, suggesting a more thermally resilient structural framework……..119

Fig.4.7 Change in the secondary structure in response to the temperature ramped simulations……120

Fig.4.8 Analysis of cross-lobe correlations at 423 K demonstrates that coupling between the N- and C-lobes, particularly across the hinge region, is stronger in D168A than in the wild type, suggesting that the mutation does not affect long-range intramolecular communication on temperature rise…….121

Fig.4.9 A) Correlation analysis at 423 K reveals clear differences in residue-residue coupling between wild type and D168A. The mutant retains stronger correlated motions than the wild type, even under high-temperature conditions, indicating preservation of coordinated internal dynamics. **B**) p- values to understand significant gains and losses……..123

Fig.4.10 Comparison of correlation patterns before and after heating shows that the wild type loses substantially more correlation upon thermal stress, whereas D168A retains a larger fraction of its original coupling network, consistent with a more robust and less heat-sensitive dynamic architecture…….125

Fig.4.11 nanoDSF melting analysis shows that D168A has a melting temperature approximately 5 °C higher than the wild type and is less sensitive to pH changes. In contrast, the wild type exhibits a more pronounced pH-dependent shift in thermal stability, indicating greater susceptibility to environmental perturbation……..126

Fig.4.12 Overlay of NOESY spectra acquired for wild-type p38α and the D168A mutant, highlighting differences in water-related cross peaks between the two proteins……..127

Fig.4.13 Residue wise water cross peak intensities, also plotted in the protein structure…….128

Fig.4.14 Residue wise water cross peak/NOESY diagonal peak intensities, also plotted in the protein structure……129

Fig.4.15 MD-derived water residence-time analysis for the allosteric pocket, activation loop and lipid pocket……..130

Fig.4.16 RDF profile comparison of the wildtype and the mutant across different pockets of p38α……..132

Fig.4.17 A) Representation of hydration shell around the activation loop across the entire trajectory for the wildtype and D168A. **B**) Density differences mapped in the water box centring the activation loop. **C**) Water oxygen occupancy around the activation loop……133

Fig.4.18 TROSY spectra comparing the peaks after CLEANEX, as well as comparing before and after undergoing clean chemical exchange……135

Fig.4.19 Ratio of CLEANEX/Parent TROSY normalised to see the exchange rates of the amide protons per residue……137

Fig.4.20 Comparison of TROSY spectra before and after the addition of D_2O for the wildtype and the mutant protein……...138

Fig.4.21 A) Overlay of the first TROSY HSQC of mutant and wildtype after HDX **B**) Representation of residues on the protein structure showed up in the spectra after HDX (red for mutant, blue for wildtype and purple for both)……140

Fig.4.22 A) percentage of peaks retained after initial HDX time point and the final time point. **B**) Normalised peak intensities at the initial and final timepoints for WT and D168A……..141

Fig.4.23 Intensity over time plots for HDX experiment for WT and D168A….143

Fig. 4.24 Comparison of spectral fingerprint recorded in solution NMR (TROSY) and solid-state NMR (hNH) for the wildtype and D168A……145

Fig.4.25 Overlay of the solid state hNH spectra of the wildtype and D168A…..146

Fig.4.26 A) Overlay of the hNH spectra before and after 2.5 hrs of adding D_2O of the wildtype p38α. **B**) Overlay of the hNH spectra before and after 2.5 hrs of adding D_2O of D168A p38α. **C**) Number of matching peaks according to chemical shift cutoff in the wildtype and the mutant. **D**) Box plot to understand the overall intensity drop for the matching peaks obtained for wildtype and D168A……..148

Fig.4.27 A) hNH overlay before and after adding D_2O after 2.5 hrs and 78 hrs for wildtype protein. **B**) hNH overlay before and after adding D_2O after 2.5 hrs and 78 hrs for D168A protein. **C**) Number of matching peaks according to chemical shift cutoff in the wildtype and the mutant with the reference being before adding D_2O **D**) Box plot to understand the overall intensity drop for the matching peaks obtained for wildtype and D168A with the reference being before adding D_2O. **E**) Number of matching peaks according to chemical shift cutoff in the wildtype and the mutant with the reference being after 2.5 hrs of adding D_2O **F**) Box plot to understand the

overall intensity drop for the matching peaks obtained for wildtype and D168A with the reference being after 2.5 hrs of adding D_2O……..150

Fig.6.1 Pictorial representation for site directed mutagenesis……..159

Fig 6.2 Schematic representation of expression and purification of p38α and mutants……...160

Fig.6.3 A) Batch crystallization of p38α in Eppendorf. **B**) Crystals showing apo and D168A in labelled and unlabelled conditions……...162

Fig. 6.4. 1.3 mm rotor packed with DCN wt p38α……..166

9. List of Tables

Table 3.1: B-factors of key network residues, derived from PDB 3HEG……..66

Table 3.2: Correlation Values Between N-lobe to C-Lobe……70

Table 3.3: Docking results of WT and mutant with Sorafenib at the allosteric pocket (in kcal/mol)……77

Table 3.4: K_M, v_{max} and EC values. Note that v_{max} (needs to be read as relative values as the conversion between fluorescence and concentrations is unknown) is not reliable as the protein concentrations and degree of phosphorylation might be slightly different between samples……83

Table 3.5: Important regions with CSP>0.12 for all mutants……90

Table 3.6: Important regions around the protein as shown by all mutants determined by difference in hetNOE……95

Table 3.7: Important regions around the protein as shown by all mutants determined by difference in R_2……97

Table 4.1 N-C lobe cross correlation values with errors after heating……121

Table 4.2 : Statistical values for peak counts……141

10. Appendix

10.1 Appendix Figures

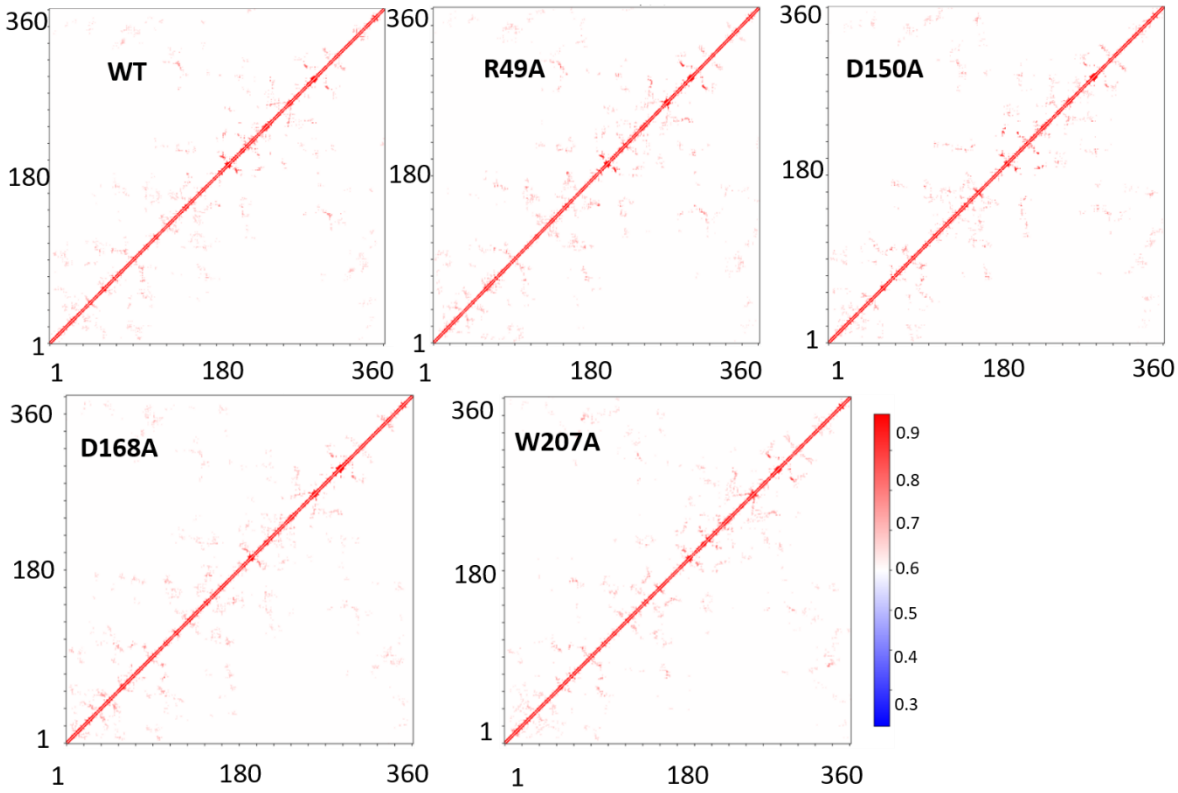

Fig.10.1 Total correlation maps for wildtype and the mutants.

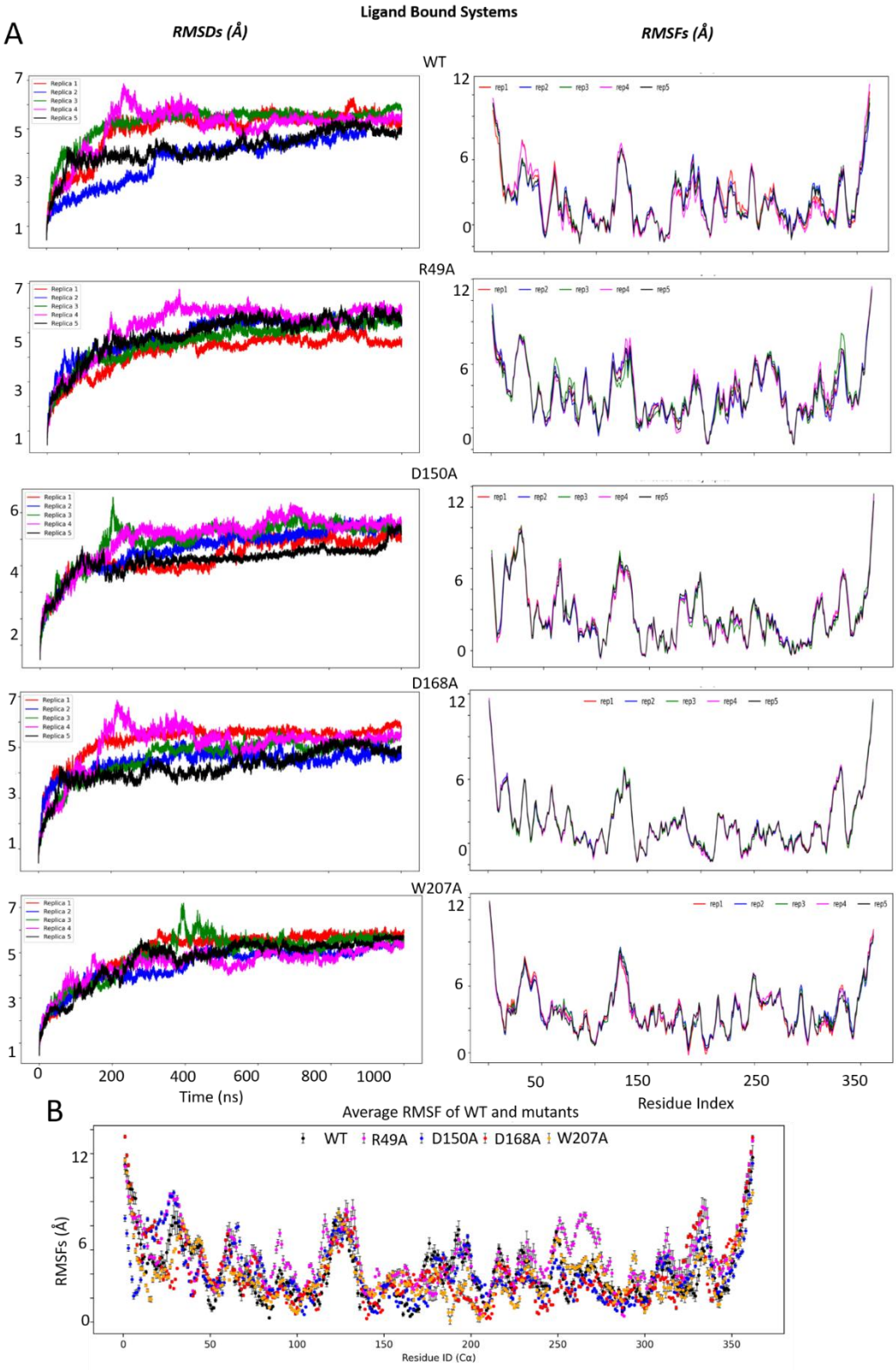

Fig. 10.2: **A**) RMSDs and RMSFs of five replicas per ligand-bound mutant. The last 200 ns each were used for network and correlation analysis. **B**) Mean and standard deviation of the RMSFs of the ligand-bound ensembles compared to each other.

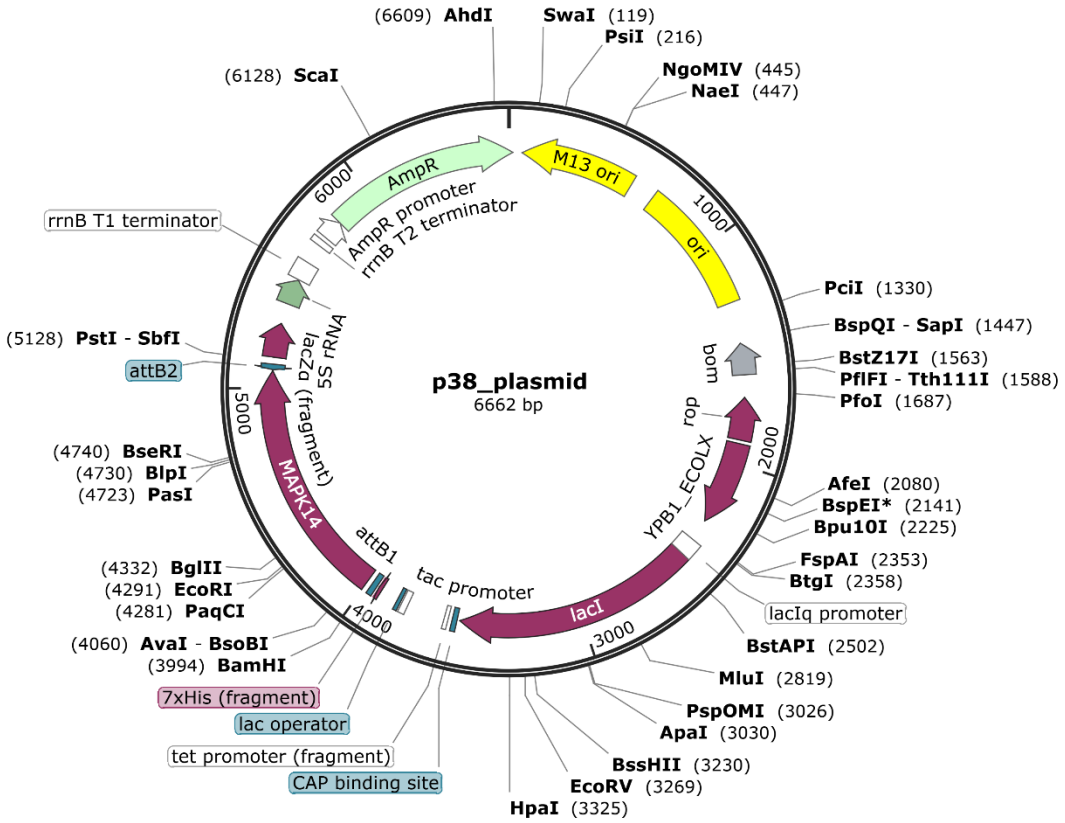

Fig.10.3 Plasmid map of p38α from nanopore sequencing

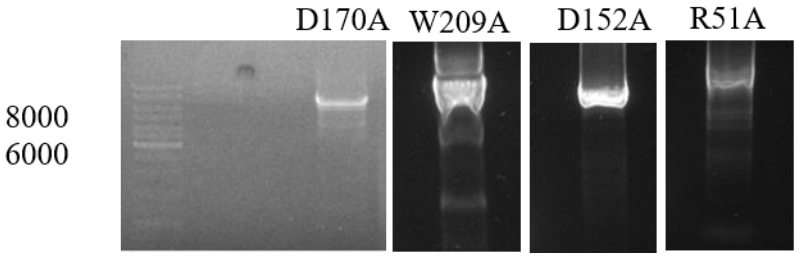

Fig.10.4 Agarose gel electrophoresis showing mutant DNA

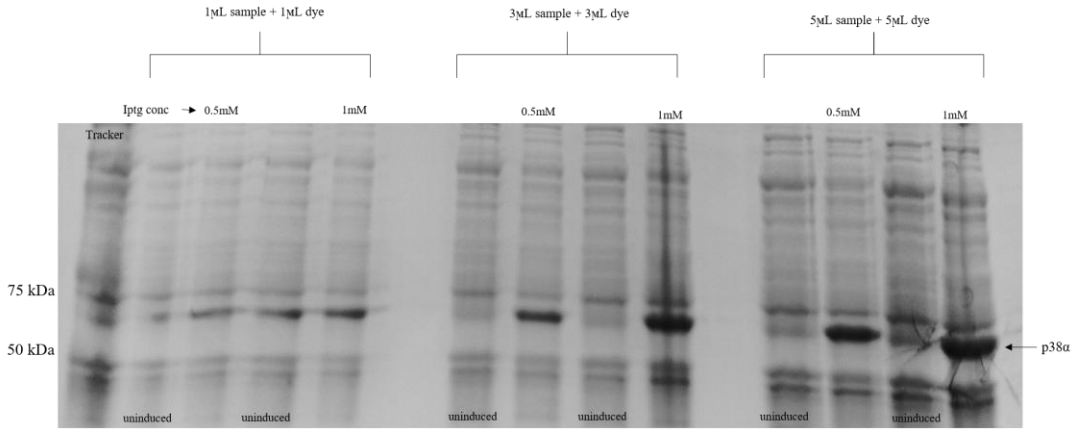

Fig.10.5 Expression optimization of p38α at different IPTG concentrations

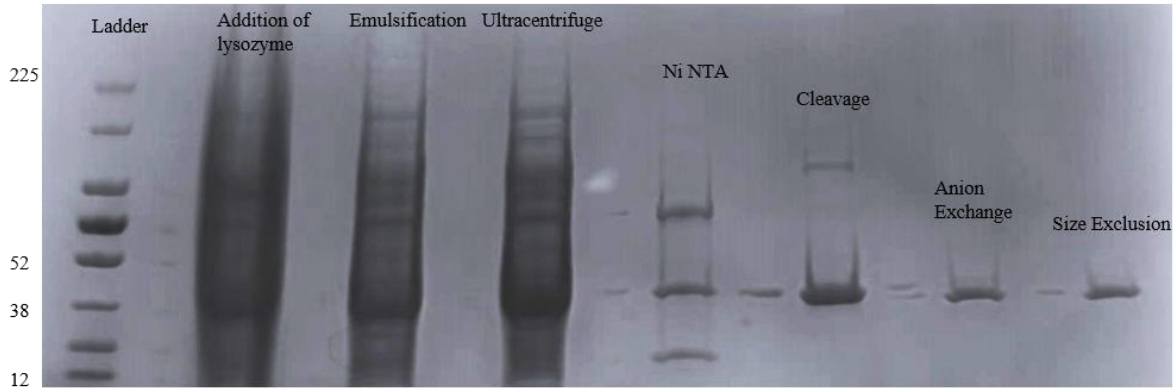

Fig.10.6 SDS page run of the purification procedure

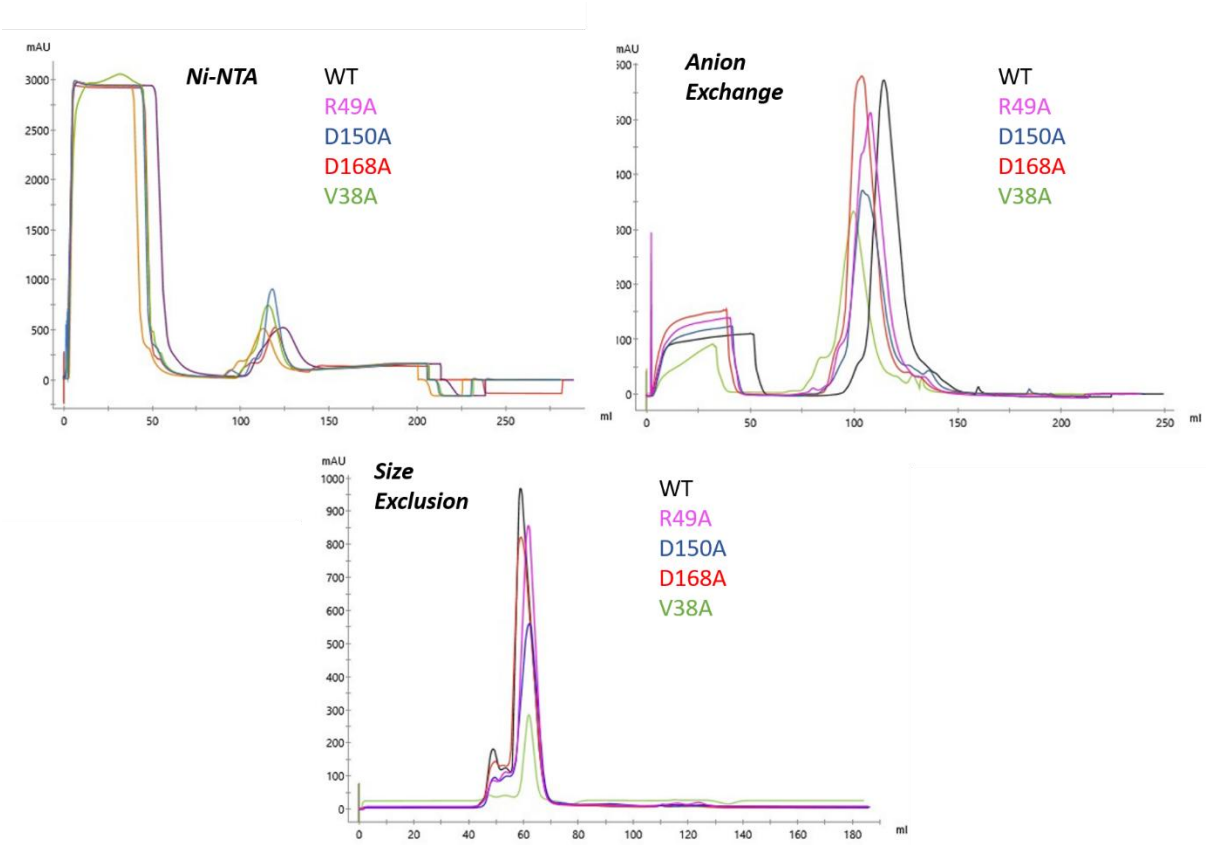

Fig.10.7 Chromatograms at different stages of p38 purification

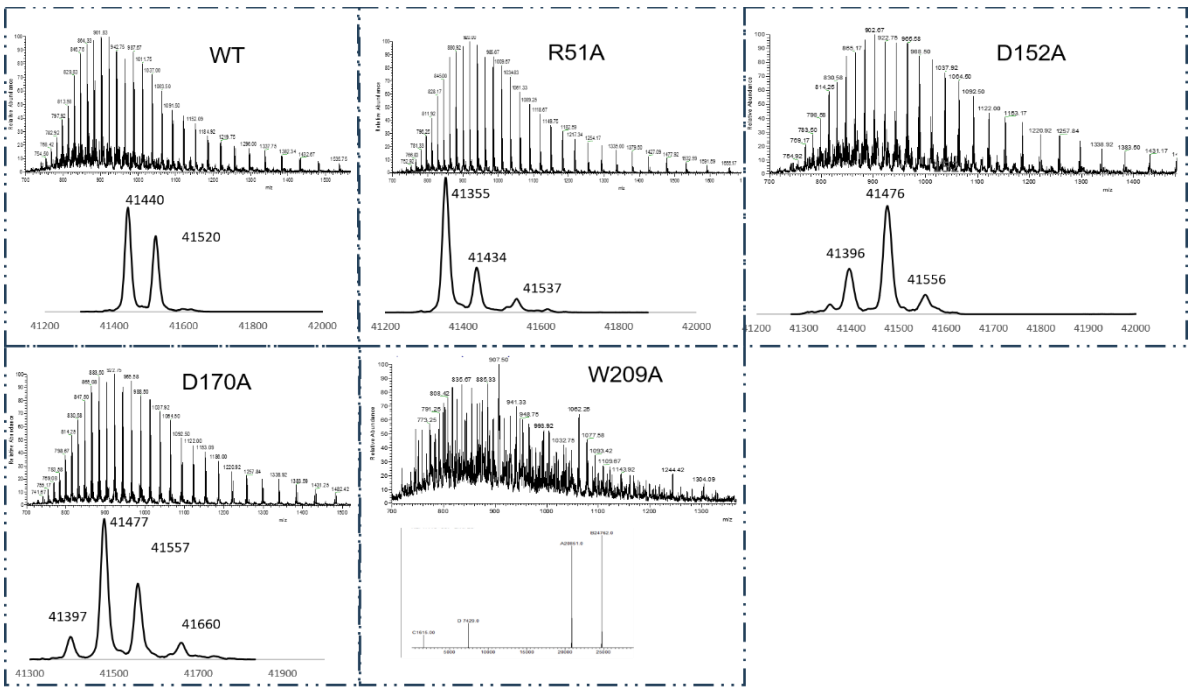

Fig.10.8 Mass spectrometry data for p38α and mutants

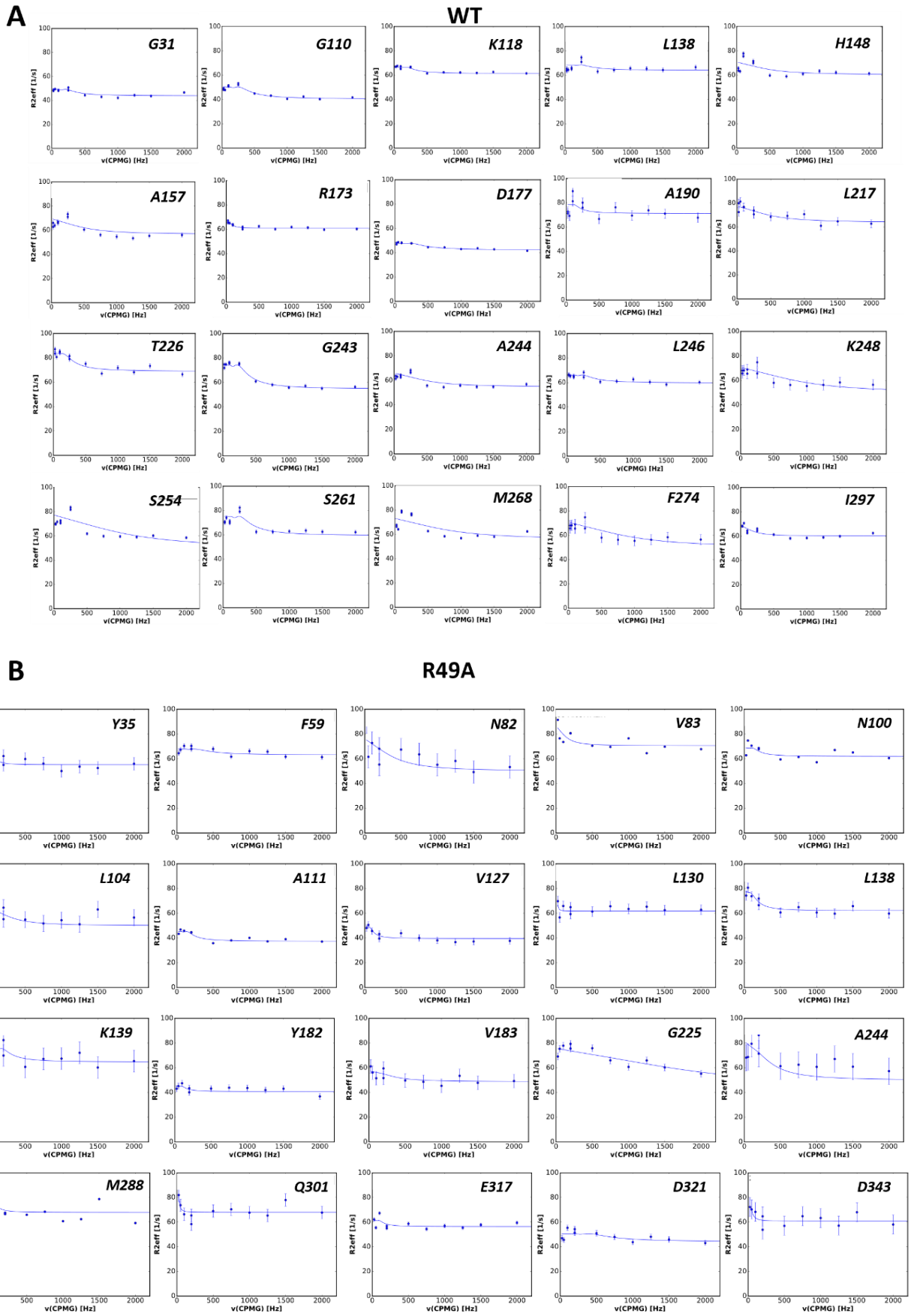
A
WT
G31
G110
K118
L138
H148
A157
R173
D177
A190
L217
T226
G243
A244
L246
K248
S254
S261
M268
F274
I297
B
R49A
Y35
F59
N82
V83
N100
L104
A111
V127
L130
L138
K139
Y182
V183
G225
A244
M288
Q301
E317
D321
D343
R2eff [1/s]
v(CPMG) [Hz]

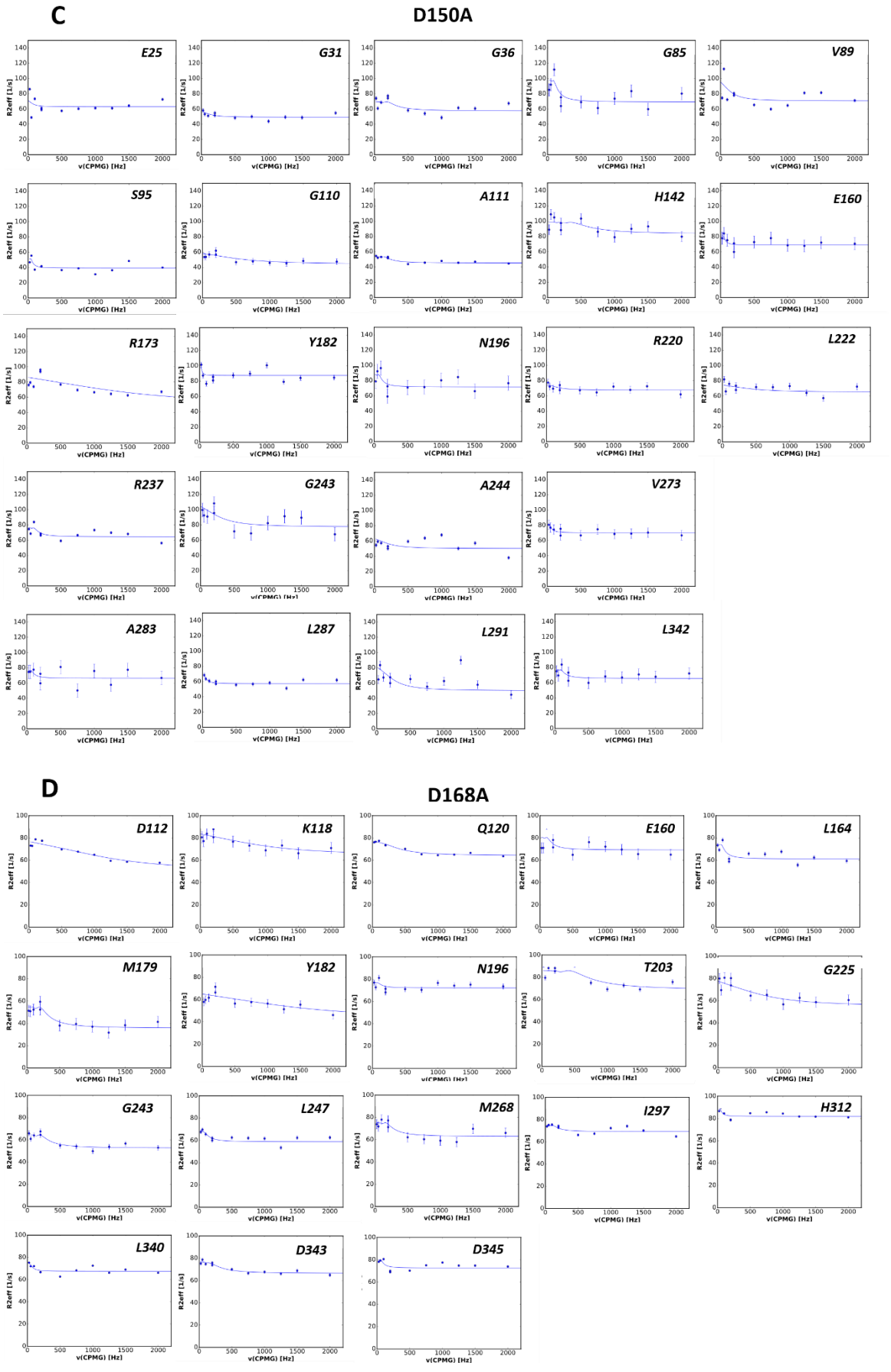
C
D150A
E25
G31
G36
G85
V89
S95
G110
A111
H142
E160
R173
Y182
N196
R220
L222
R237
G243
A244
V273
A283
L287
L291
L342
D
D168A
D112
K118
Q120
E160
L164
M179
Y182
N196
T203
G225
G243
L247
M268
I297
H312
L340
D343
D345
R2eff [1/s]
ν(CPMG) [Hz]

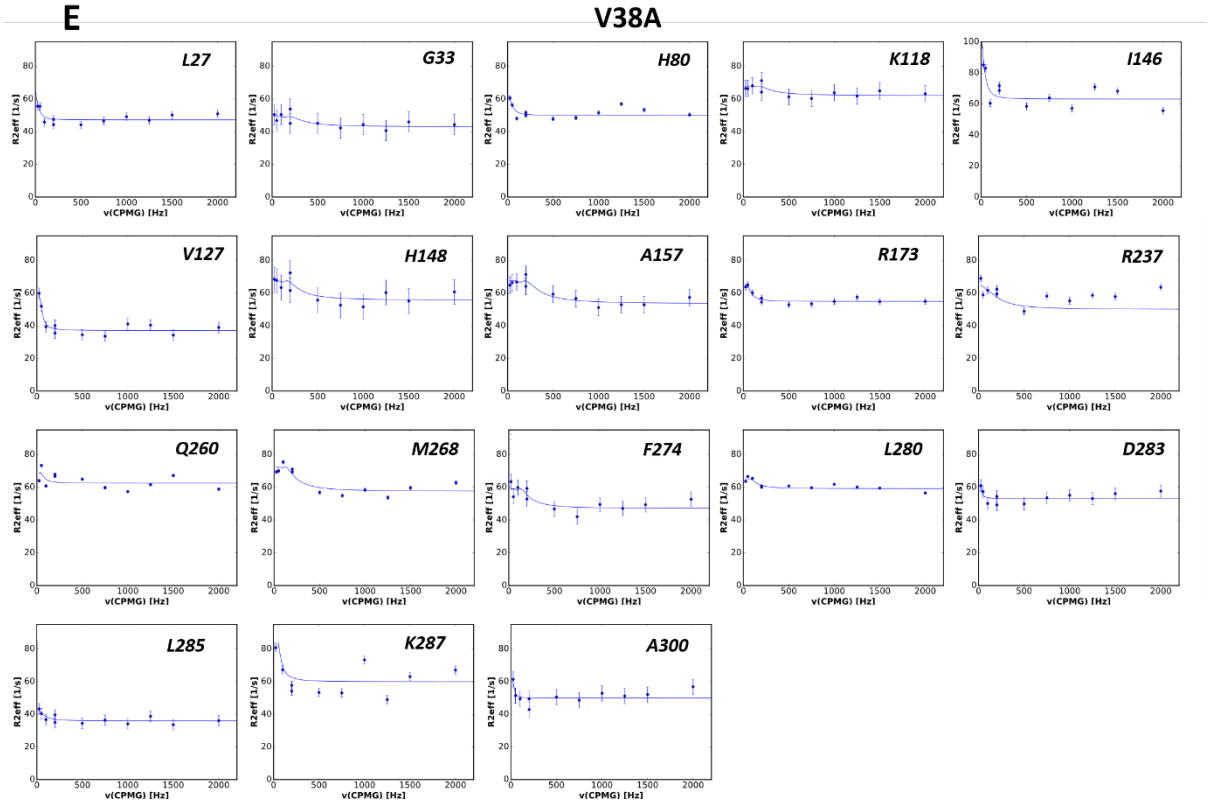

Fig. 10.9 A) CPMG curves of some residues for the WT. **B**) CPMG curves of some residues of the R49A protein. **C**) CPMG curves of some residues from D150A. **D**) CPMG curves of some residues from D168A. **E**) CPMG curves of some residues in V38A.

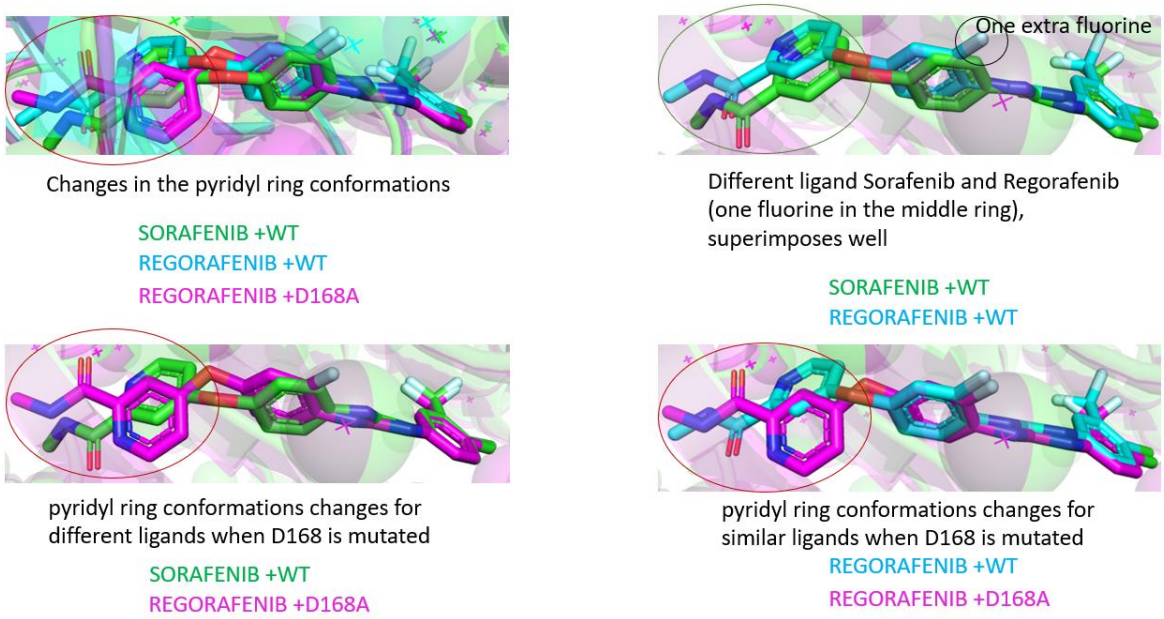

Fig.10.10 Changes in ligand conformational distributions on mutation. Change in the ligand from Regorafenib to Sorafenib in the crystal structure does not affect the predominant ring conformations.

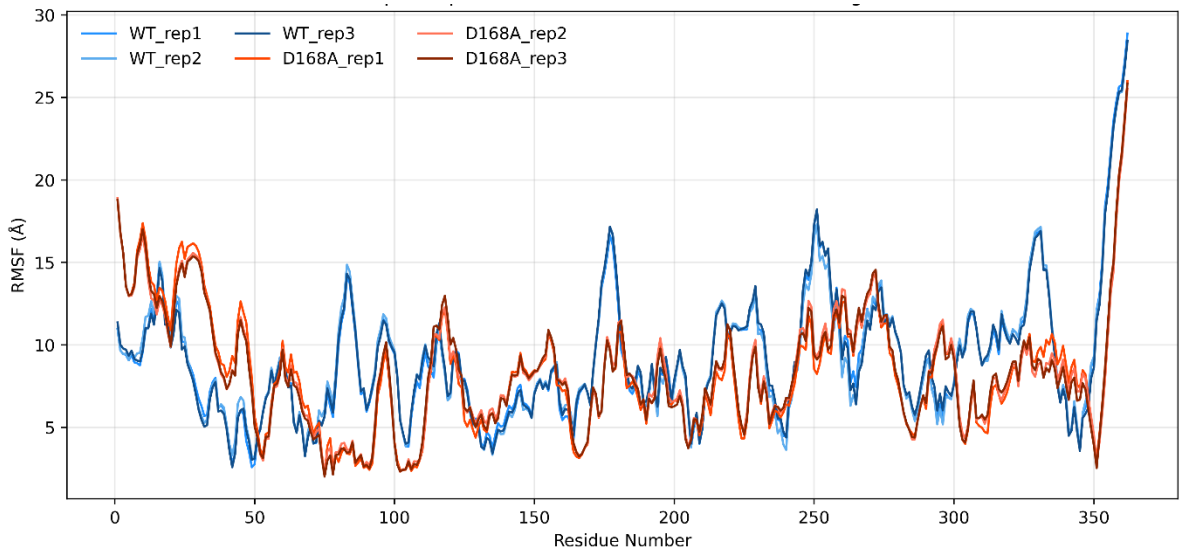

Fig.10.11 Residue wise RMSF of 3 replicas of temperature ramped simulations for WT and D168A.

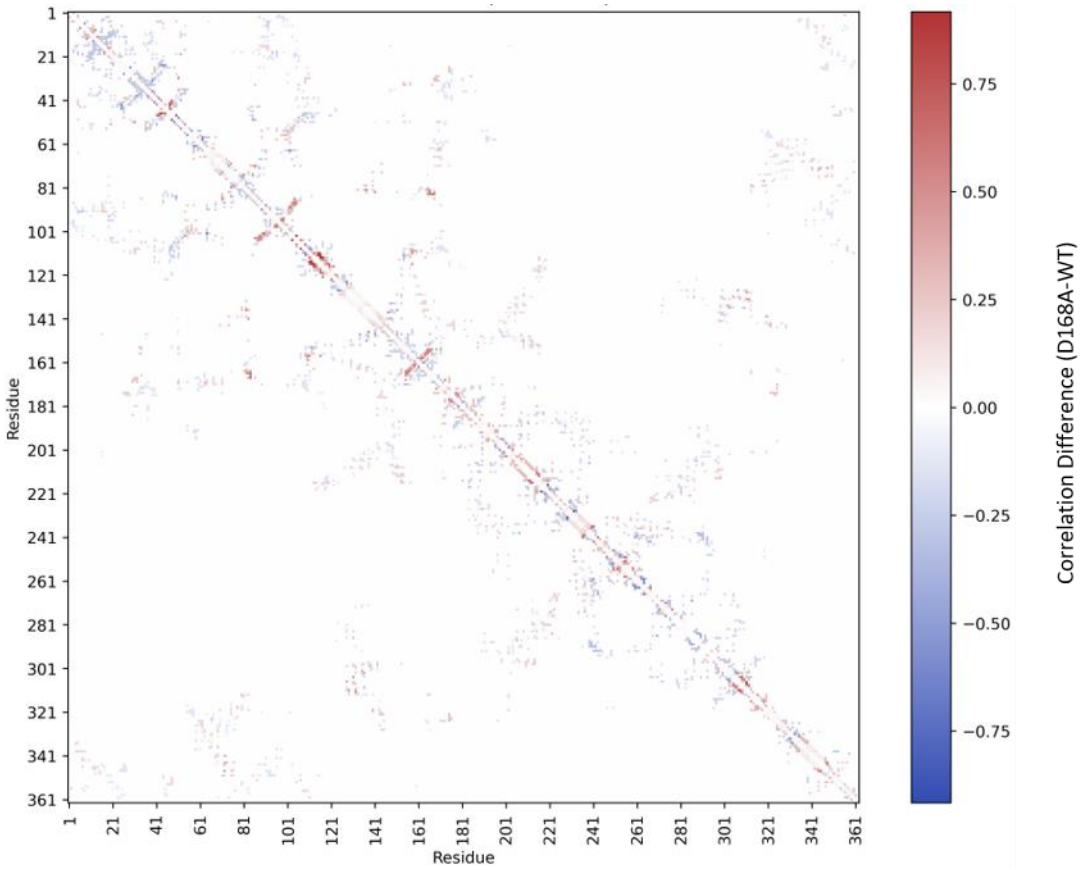

Fig.10.12 Total Correlation Difference Matrix (D168A-WT)

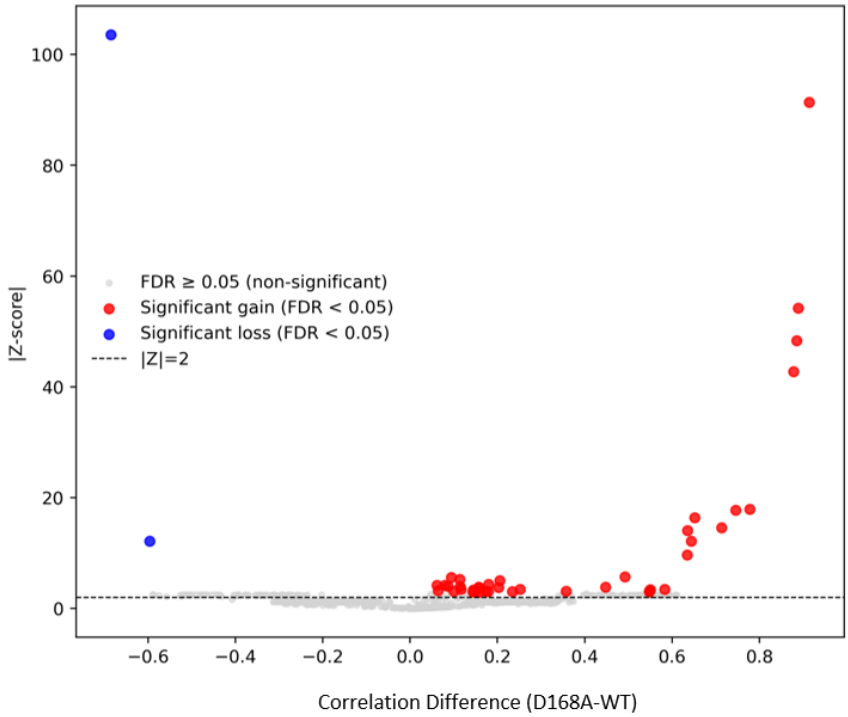

Fig.10.13 Z-scores of correlation difference values (D168A-WT)

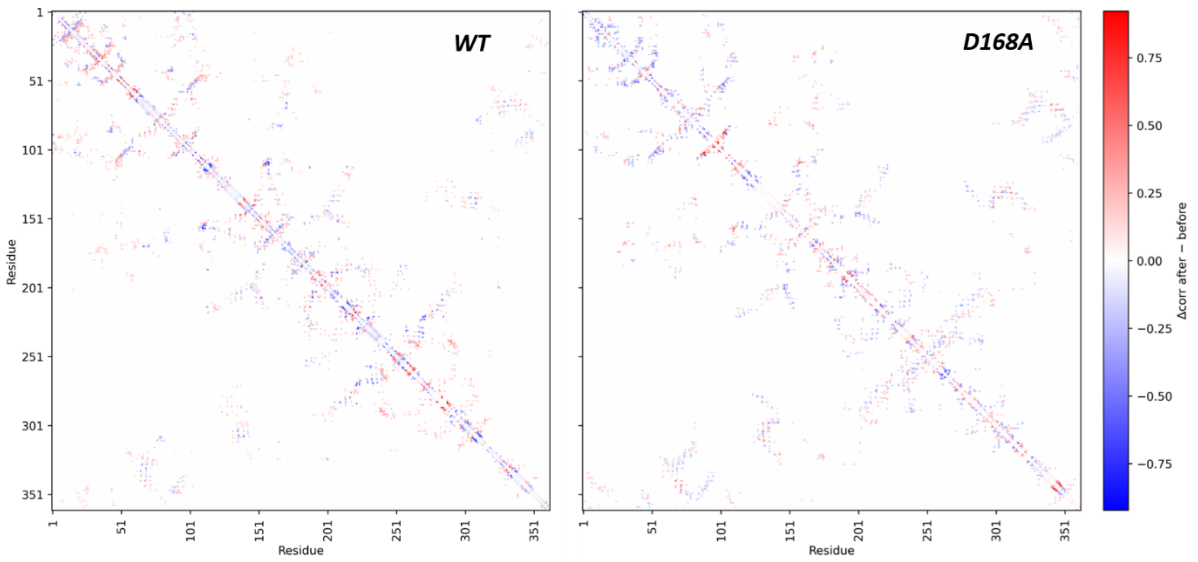

Fig.10.14 Total correlation matrix difference under before to after heating conditions for WT and D168A

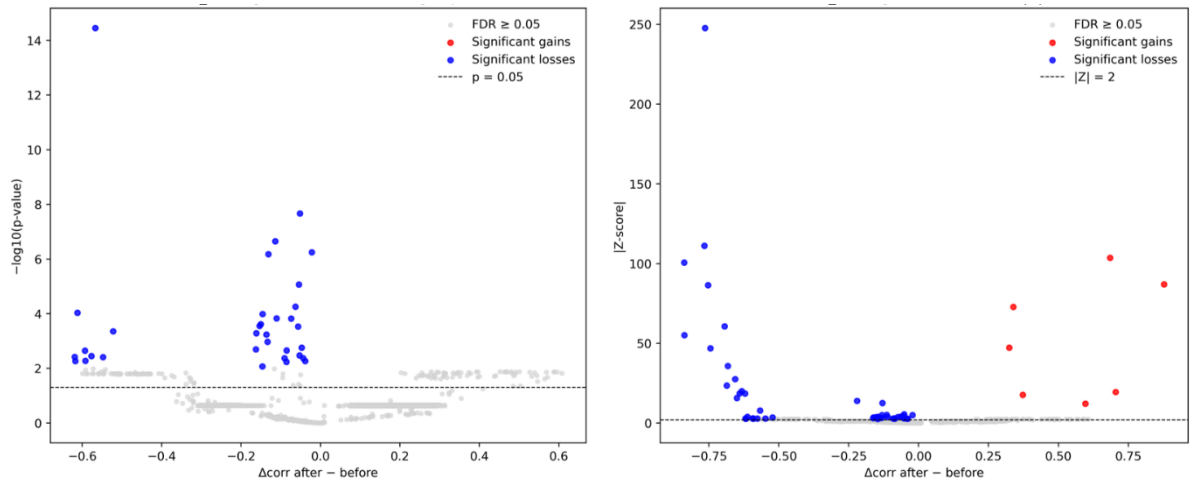

Fig.10.15 Statistical scores for correlation differences in WT before and after heating

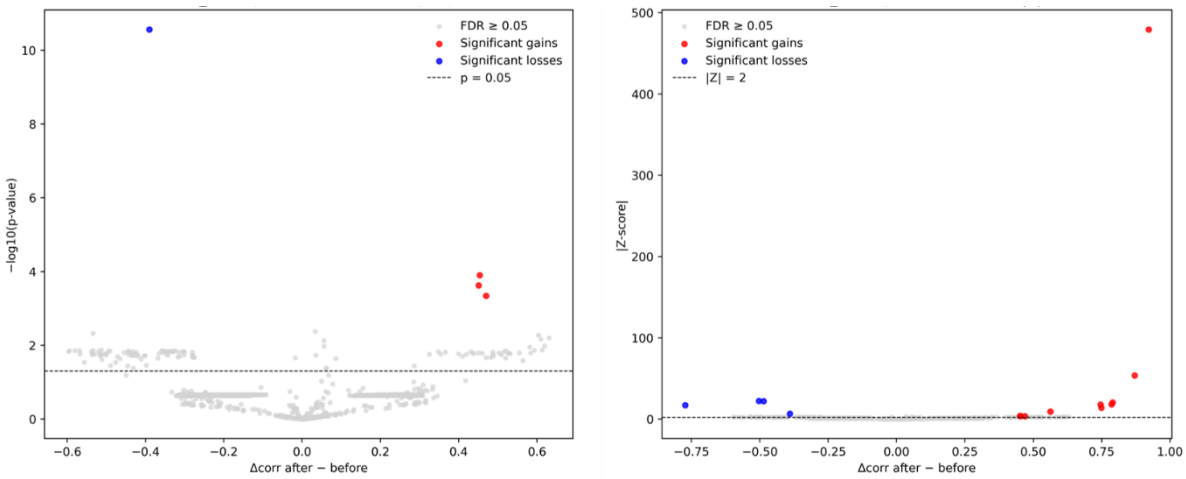

Fig.10.16 Statistical scores for correlation differences in D168A before and after heating

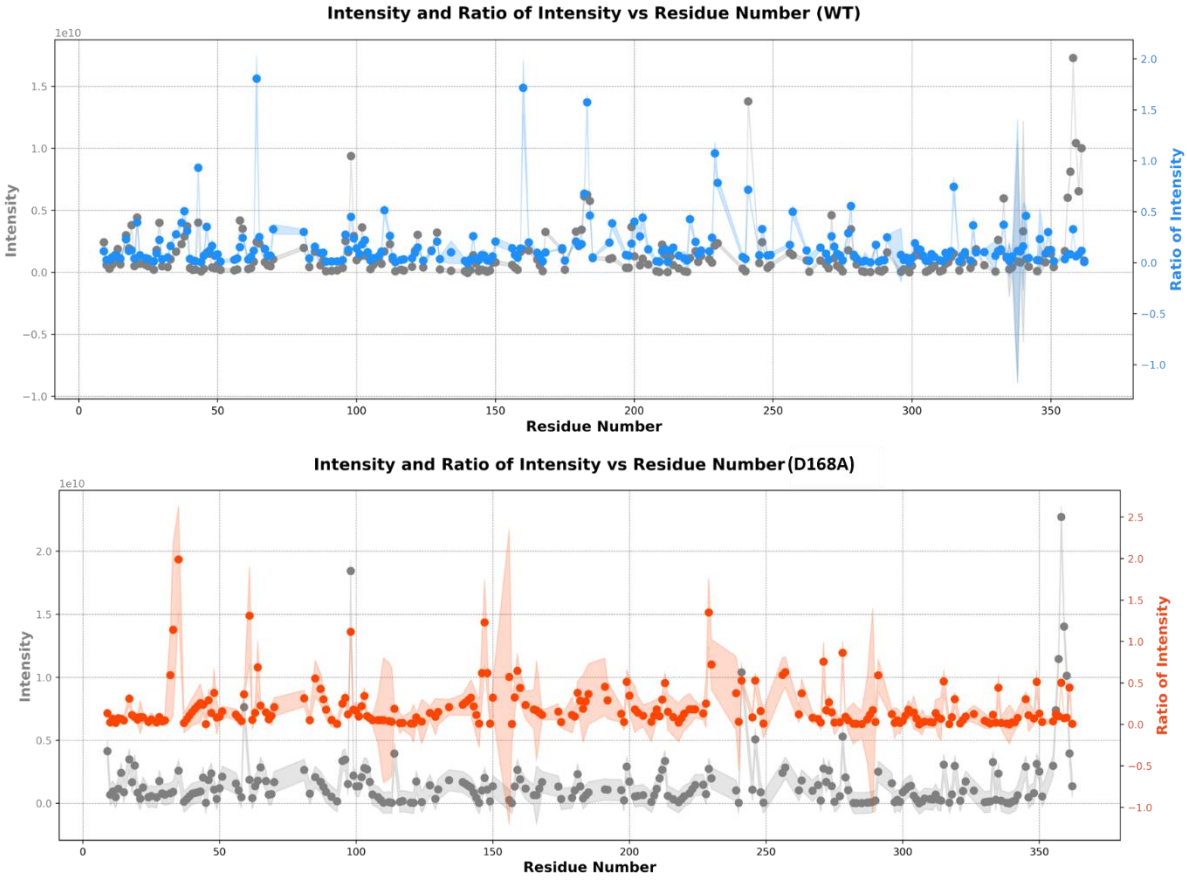

Fig.10.17 Intensity of the water cross peaks compared to the ratio of intensity with the NOESY diagonal for the wildtype and the mutant D168A.

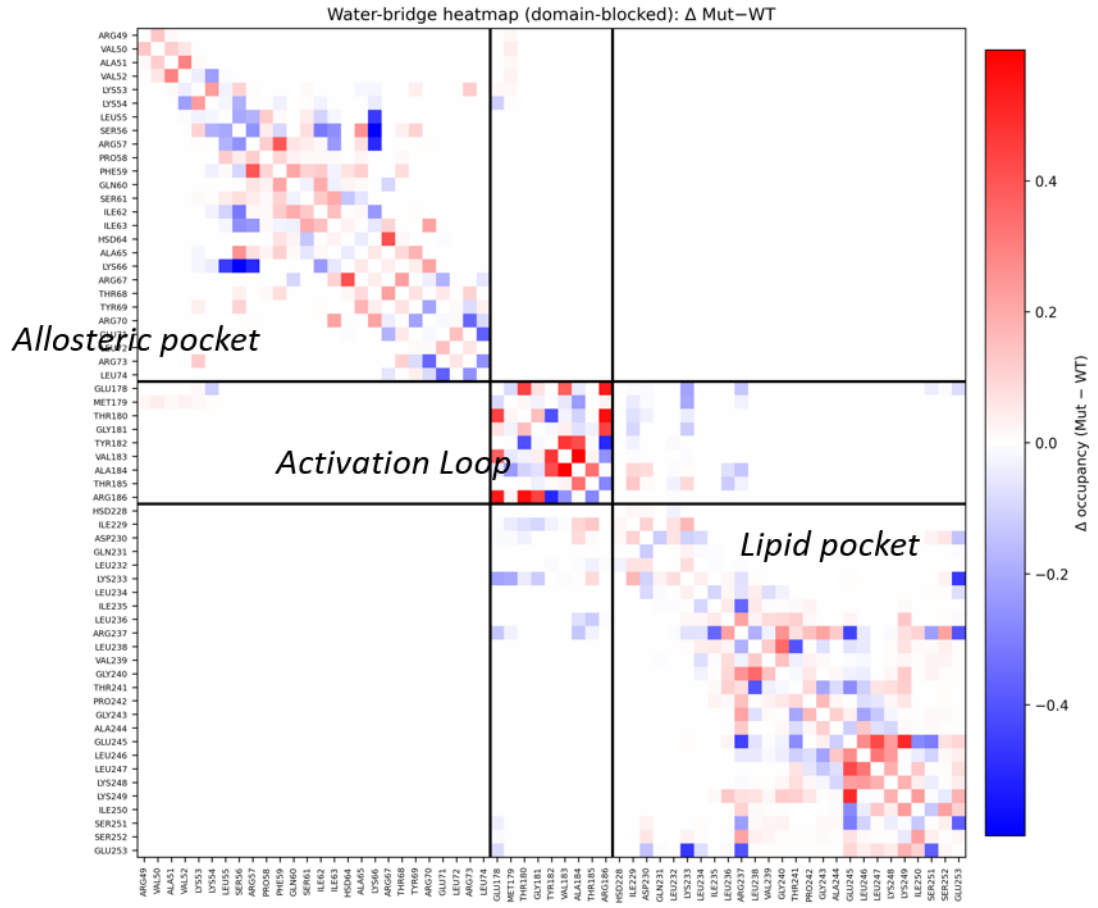

Fig.10.18 Coupled waters creating water bridges at different pocket

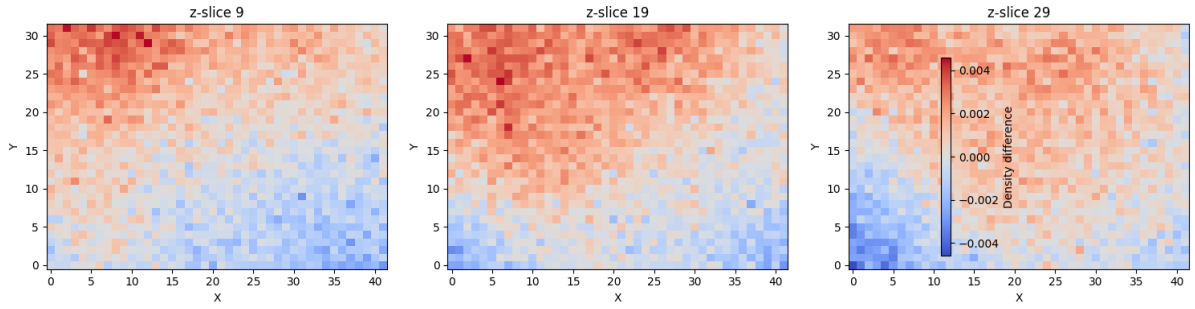

Fig.10.19 Slices of density slices for difference between mutant and wildtype in the activation loop area.

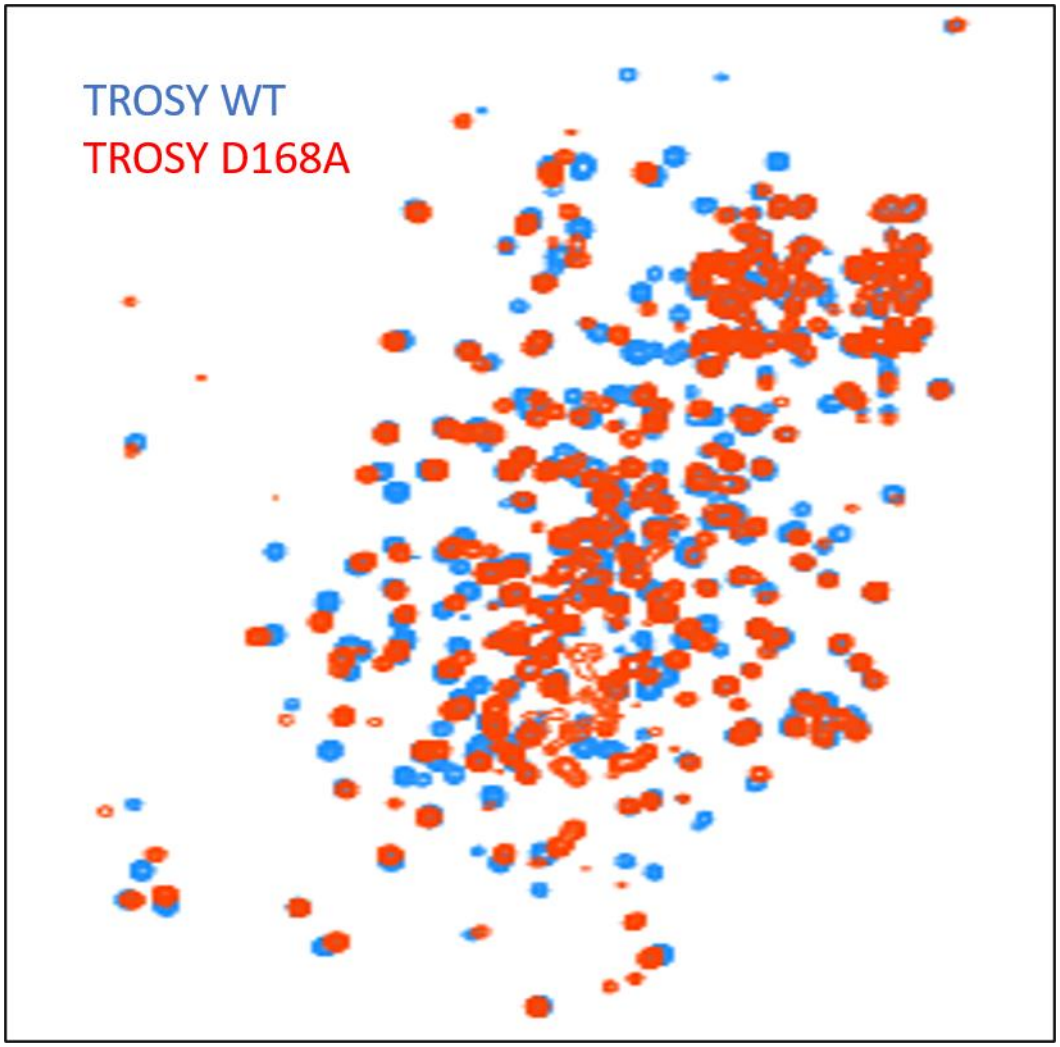

Fig.10.20 TROSY overlay of WT and D168A showing chemical shift perturbations

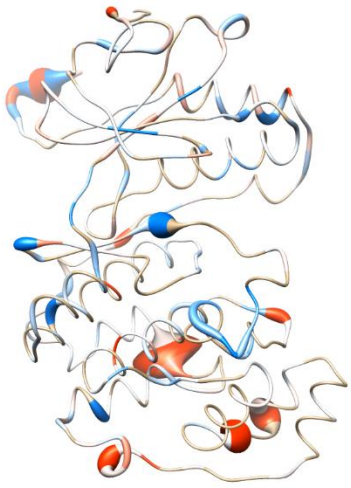

Fig.10.21 CLEANEX absolute intensity differences plotted.

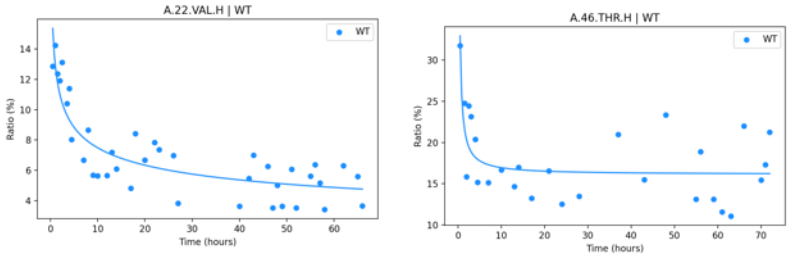

Fig.10.22 Solution NMR HDX curves for the wildtype of some residues

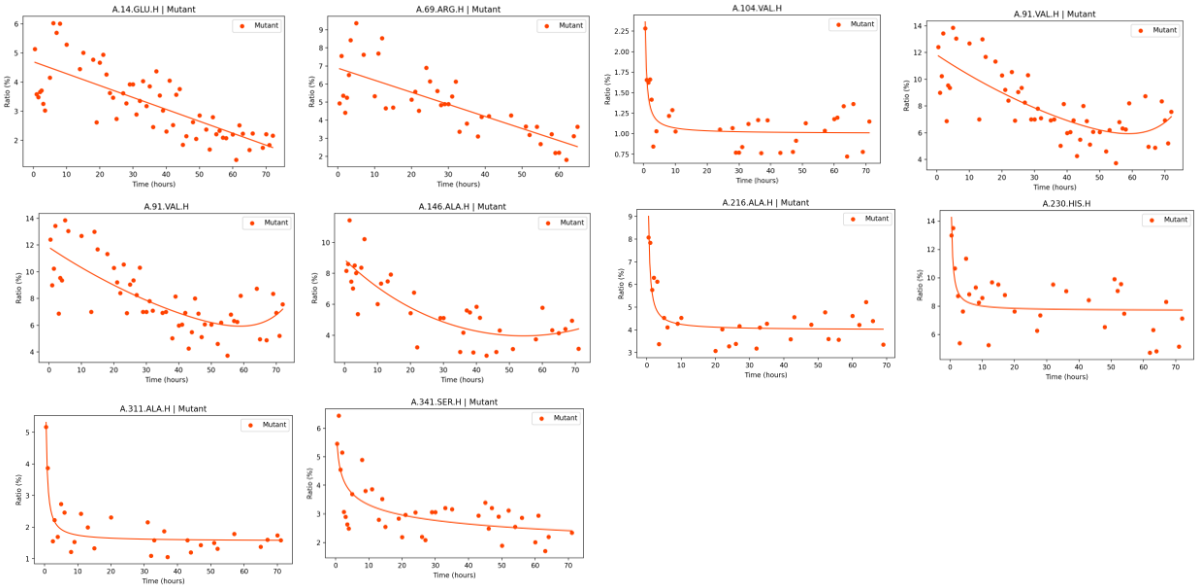

Fig.10.23 Solution NMR HDX curves for mutant for some residues

10.1 Appendix Tables

Table 10.1: Summary of Molecular Dynamics system parameters.

System	**Box** (Å)	**Total No. of Atoms**	**Salt Pairs (NaCl)**	**Salt Concentration** (M)	**No. of Water Molecules**
Wildtype apo	63.65 * 100.91* 84.81	66,679	56	0.151	19,896
R49A apo	79.60* 102.97 * 81.84	68,577	58	0.146	20,883
D150A apo	79.59 * 102.97* 81.84	68,593	59	0.146	20,885
D168A apo	79.85 * 102.87 * 81.35	68,566	59	0.147	20,678
W207A apo	79.61* 102.99 * 81.85	68,576	59	0.146	20,883
Wildtype holo	106.46 * 70.03 * 90.98	69,469	60	0.147	21,159
R49A holo	102.93 * 85.05 * 71.93	64,445	55	0.145	19,492
D150A holo	101.80 * 84.49 * 71.93	63,037	54	0.145	19,020
D168A holo	100.66 * 85.60 * 71.41	62,995	54	0.146	19,006
W207A holo	102.50 * 85.11 * 72.13	64,201	55	0.145	19,411
3HEG (crystal structure	96.32 * 76.65 * 67.13	50,932	42	0.140	14,979

with Sorafenib)					
3GCS (crystal structure with Sorafenib and β-OG)	94.64 * 68.08 * 74.74	49,421	41	0.141	14,489

Table 10.2: Residues showing highest betweenness centrality for the wildtype and mutants (with decreasing values from top to bottom in each of the columns).

WT	**R49A**	**D150A**	**D168A**	**W207A**
W207, I212	L135, N155	K165, D343	I131, D343	R14, I52
R136, I141	R149, T185	V105, L156	I131, L135	E141, L166
R136, T203	N155, N159	D205, S208	G210, L236	L205, V236
D150, D168	N14, E160	S154, R173	L135, G210	R139, E141
P29, R49	V117, I134	S154, S208	V102, I142	R135, M165
R136, W207	N14, N159	Y140, M288	I134, G137	I52, E66
K66, I141	I116, V158	K338, D343	N100, V102	E141, T167
W205, I210	I134, G137	H142, L280	G47, V102	G145, G170
Y140, D205	K66, K165	H142, L156	L236, S254	E274, T293
Y188, T203	G137, V273	H80, C162	C39, G47	E48, I102

Table 10.3: Pathways to and from different pockets.

Apo Pathway (red)	Allosteric Pocket to Activation Loop	{ K66 R67 } { R67 L167 } { L167 D168 } { D168 G170 } { G170 A172 } { A172 R173 } { R173 T175 } { T175 Y182 } { Y182 V183 } { V183 A184 } { A184 Y188 }
	Lipid Pocket to Activation Loop	{ R186 W187 } { W187 Y188 } { Y188 R189 } { R189 D227 } { D227 I229 } { I229 Q231 } { Q231 K233 } { K233 I235}
	Allosteric Pocket to lipid Pocket	{ K66 R67 } { R67 L167 } { L167 D168 } { D168 G170 } { G170 A172 } { A172 R173 } { R173 T175 } { T175 A176 } { A176 G178 } { G178 M179 } { M179 T221 } { T221 L222 } { L222 P224 } { P224 L232 } { L232 I235 }
Holo Pathway (purple)	Allosteric Pocket to Activation Loop	{ K66 D168 } { D168 F169 } { F169 L171 } { L171 R173 } { R173 T175 } { T175 A176 }

		{ A176 G178 } { G178 T180 } { T180 G181 } { G181 V183 } { V183 T185 } { T185 Y188 }
	Lipid Pocket to Activation Loop	{ Y188 R189 } { R189 Y188 } { Y188 T221 } { T221 K233 } { K233 I235 }
	Allosteric Pocket to lipid Pocket	{ K66 D168 } { D168 F169 } { F169 L171 } { L171 R173 } { R173 T175 } { T175 A176 } { A176 G178 } { G178 T180 } { T180 G181 } { G181 V183 } { V183 A184 } { A184 R186 } { R186 Y188 } { Y188 T221 } { T221 K233 } { K233 I235 }

Table 10.4 Statistical values for shortest-path analysis.

Apo protein pathway							
Pathway	**Comparison**	**Variant mean norm**	**Mean diff**	**95% CI low**	**95% CI high**	**Hedges' g**	**Bootstrap p**
Allosteric → Activation	WT vs 51	0.95	-0.05	-0.1	0.01	-0.84	0.1862

	WT vs 152	0.95	-0.05	-0.11	0	-0.87	0.1664
	WT vs 170	0.93	-0.07	-0.14	0	-0.93	0.1414
	WT vs 209	0.88	-0.12	-0.2	-0.04	-1.44	0.0394
Activation → Lipid	WT vs 51	0.9	-0.1	-0.19	-0.02	-1.17	0.0701
	WT vs 152	0.93	-0.07	-0.14	0	-0.98	0.1582
	WT vs 170	0.88	-0.12	-0.21	-0.04	-1.39	0.0425
	WT vs 209	0.92	-0.08	-0.14	-0.01	-1.08	0.1273
Allosteric → Lipid	WT vs 51	0.9	-0.1	-0.16	-0.06	-2.1	0.0171
	WT vs 152	0.85	-0.15	-0.21	-0.11	-3.06	0.0026
	WT vs 170	0.84	-0.16	-0.21	-0.11	-3.03	0.0022
	WT vs 209	0.78	-0.22	-0.28	-0.18	-4.55	0.0005
Sorafenib bound protein pathway							
Pathway	**Comparison**	**Variant mean norm**	**Mean diff**	**95% CI low**	**95% CI high**	**Hedges' g**	**Bootstrap p**
Allosteric → Activation	LWT vs WT	0.98	-0.02	-0.14	0.08	-0.17	0.7758
	LWT vs L51	0.98	-0.02	-0.16	0.13	-0.11	0.8465
	LWT vs 51	0.99	-0.01	-0.13	0.09	-0.07	0.9056
	LWT vs L152	1.06	0.06	-0.09	0.2	0.44	0.4681
	LWT vs 152	1.03	0.03	-0.1	0.15	0.25	0.6795
	LWT vs L170	1.07	0.07	-0.05	0.18	0.62	0.3202

	LWT vs 170	0.91	-0.09	-0.22	0.02	-0.73	0.2472
	LWT vs L209	0.99	-0.01	-0.15	0.12	-0.07	0.9079
	LWT vs 209	1.02	0.02	-0.14	0.16	0.11	0.8481
Activation → Lipid	LWT vs WT	0.99	-0.01	-0.02	0.01	-0.39	0.5132
	LWT vs L51	1	0	-0.02	0.02	0	1
	LWT vs 51	1	0	-0.01	0.02	0.24	0.6847
	LWT vs L152	0.93	-0.07	-0.19	0	-0.67	0.3079
	LWT vs 152	0.94	-0.06	-0.19	0.02	-0.53	0.407
	LWT vs L170	0.94	-0.06	-0.19	0.01	-0.55	0.3925
	LWT vs 170	0.99	-0.01	-0.03	0.01	-0.38	0.5226
	LWT vs L209	0.93	-0.07	-0.2	0	-0.66	0.3135
	LWT vs 209	0.93	-0.07	-0.19	0	-0.68	0.3013
Allosteric → Lipid	LWT vs WT	0.93	-0.07	-0.19	0.04	-0.6	0.3397
	LWT vs L51	0.95	-0.05	-0.18	0.07	-0.38	0.5246
	LWT vs 51	0.91	-0.09	-0.21	0.01	-0.83	0.2093
	LWT vs L152	1	0	-0.15	0.13	0	0.9953
	LWT vs 152	0.96	-0.04	-0.17	0.07	-0.36	0.554
	LWT vs L170	1.01	0.01	-0.12	0.13	0.07	0.9076
	LWT vs 170	0.89	-0.11	-0.23	0	-0.95	0.1568
	LWT vs L209	0.99	-0.01	-0.16	0.13	-0.07	0.9113
	LWT vs 209	1	0	-0.16	0.13	-0.02	0.9789

Table 10.5 Chemical shifts of R49A (BMRB nomenclature is i+2)

Assign F1	Assign F2	Assign F3	Pos F1	Pos F2	Pos F3
A.7.ARG.H	A.7.ARG.N	A.7.ARG.CA	8.387421	125.7773	51.05425
A.9.THR.H	A.9.THR.N	A.9.THR.CA	8.40445	117.4269	59.95926
A.9.THR.H	A.9.THR.N	A.10.PHE.CA	8.752186	127.3751	53.87534
A.11.TYR.H	A.11.TYR.N	A.11.TYR.CA	9.064844	120.1719	52.79029
A.12.ARG.H	A.12.ARG.N	A.12.ARG.CA	8.382833	120.1795	51.37223
A.13.GLN.H	A.13.GLN.N	A.13.GLN.CA	8.865685	122.3663	51.66029
A.14.GLU.H	A.14.GLU.N	A.14.GLU.CA	8.773679	125.4867	52.23986
A.15.LEU.H	A.15.LEU.N	A.15.LEU.CA	8.920161	128.5961	50.75807
A.17.LYS.H	A.17.LYS.N	A.17.LYS.CA	8.815916	110.0472	54.65605
A.18.THR.H	A.18.THR.N	A.18.THR.CA	7.768081	115.8017	58.25398
A.19.ILE.H	A.19.ILE.N	A.19.ILE.CA	8.541429	125.7501	57.01436
A.20.TRP.H	A.20.TRP.N	A.20.TRP.CA	9.202969	131.0972	53.81717
A.21.GLU.H	A.21.GLU.N	A.21.GLU.CA	8.244663	128.5366	51.80873
A.22.VAL.H	A.22.VAL.N	A.22.VAL.CA	7.564269	112.3152	53.15492
A.24.GLU.H	A.24.GLU.N	A.24.GLU.CA	8.070641	119.2404	55.51167
A.25.ARG.H	A.25.ARG.N	A.25.ARG.CA	7.430792	117.2988	54.60217
A.26.TYR.H	A.26.TYR.N	A.26.TYR.CA	7.701333	118.5652	54.26266
A.27.GLN.H	A.27.GLN.N	A.27.GLN.CA	9.087523	122.7895	50.52803
A.28.ASN.H	A.28.ASN.N	A.28.ASN.CA	8.719637	117.4044	50.46545
A.29.LEU.H	A.29.LEU.N	A.29.LEU.CA	8.414585	120.1479	54.04925
A.30.SER.H	A.30.SER.N	A.30.SER.CA	8.717724	116.4294	51.48061
A.32.VAL.H	A.32.VAL.N	A.32.VAL.CA	8.56372	120.9326	61.35404
A.33.GLY.H	A.33.GLY.N	A.33.GLY.CA	7.707134	108.6133	42.53187
A.34.SER.H	A.34.SER.N	A.34.SER.CA	8.31226	115.7972	54.15593
A.35.GLY.H	A.35.GLY.N	A.35.GLY.CA	8.095381	110.4977	41.71339
A.37.TYR.H	A.37.TYR.N	A.37.TYR.CA	8.000425	113.6078	54.09182
A.38.GLY.H	A.38.GLY.N	A.38.GLY.CA	7.240478	108.6211	42.47934
A.39.SER.H	A.39.SER.N	A.39.SER.CA	8.079057	116.078	54.79124
A.40.VAL.H	A.40.VAL.N	A.40.VAL.CA	8.600684	122.6154	58.30318
A.41.CYS.H	A.41.CYS.N	A.41.CYS.CA	9.179073	125.4544	54.96375
A.42.ALA.H	A.42.ALA.N	A.42.ALA.CA	8.703002	125.4821	48.29102
A.43.ALA.H	A.43.ALA.N	A.43.ALA.CA	9.004147	120.7417	47.58038
A.44.PHE.H	A.44.PHE.N	A.44.PHE.CA	9.09569	122.7506	54.39182
A.45.ASP.H	A.45.ASP.N	A.45.ASP.CA	8.231055	126.3968	48.43618
A.46.THR.H	A.46.THR.N	A.46.THR.CA	8.940954	117.5291	60.67422
A.47.LYS.H	A.47.LYS.N	A.47.LYS.CA	7.753608	121.3973	55.37344
A.48.THR.H	A.48.THR.N	A.48.THR.CA	6.466809	104.8872	58.55395
A.49.GLY.H	A.49.GLY.N	A.49.GLY.CA	8.240489	112.2928	42.9791
A.50.LEU.H	A.50.LEU.N	A.50.LEU.CA	7.041676	119.5468	50.62933
A.51.ARG.H	A.51.ARG.N	A.51.ARG.CA	8.215315	119.5717	52.84555
A.52.VAL.H	A.52.VAL.N	A.52.VAL.CA	8.719009	116.7248	54.13123
A.53.ALA.H	A.53.ALA.N	A.53.ALA.CA	8.727397	122.9006	46.96427

A.55.LYS.H	A.55.LYS.N	A.55.LYS.CA	9.471439	129.2405	50.95941
A.56.LYS.H	A.56.LYS.N	A.56.LYS.CA	8.580573	128.5754	51.06115
A.57.LEU.H	A.57.LEU.N	A.57.LEU.CA	7.925266	128.5968	52.21437
A.58.SER.H	A.58.SER.N	A.58.SER.CA	7.9421	117.9629	53.95269
A.59.ARG.H	A.59.ARG.N	A.59.ARG.CA	8.680974	123.2823	53.14349
A.61.PHE.H	A.61.PHE.N	A.61.PHE.CA	7.834333	112.4351	51.40882
A.62.GLN.H	A.62.GLN.N	A.62.GLN.CA	6.988401	115.5422	54.45721
A.63.SER.H	A.63.SER.N	A.63.SER.CA	7.348562	110.6046	53.56417
A.64.ILE.H	A.64.ILE.N	A.64.ILE.CA	9.103647	123.2871	62.69556
A.65.ILE.H	A.65.ILE.N	A.65.ILE.CA	7.527207	118.8995	61.19806
A.67.ALA.H	A.67.ALA.N	A.67.ALA.CA	8.541768	123.6243	52.06099
A.68.LYS.H	A.68.LYS.N	A.68.LYS.CA	7.751098	118.3039	56.38614
A.69.ARG.H	A.69.ARG.N	A.69.ARG.CA	7.37028	119.2346	56.22373
A.70.THR.H	A.70.THR.N	A.70.THR.CA	8.368578	120.2379	63.90454
A.71.TYR.H	A.71.TYR.N	A.71.TYR.CA	7.529273	121.6717	59.48114
A.81.LYS.H	A.81.LYS.N	A.81.LYS.CA	8.441486	128.1362	51.34939
A.82.HIS.H	A.82.HIS.N	A.82.HIS.CA	8.601665	124.1507	54.23804
A.83.GLU.H	A.83.GLU.N	A.83.GLU.CA	7.959391	125.4884	56.41538
A.85.VAL.H	A.85.VAL.N	A.85.VAL.CA	7.631095	119.8329	58.24591
A.87.GLY.H	A.87.GLY.N	A.87.GLY.CA	7.531509	110.0376	40.36556
A.88.LEU.H	A.88.LEU.N	A.88.LEU.CA	8.28737	121.4033	51.40987
A.89.LEU.H	A.89.LEU.N	A.89.LEU.CA	8.855995	126.1398	52.03035
A.91.VAL.H	A.91.VAL.N	A.91.VAL.CA	7.77147	121.0742	56.42158
A.93.THR.H	A.93.THR.N	A.93.THR.CA	8.882024	113.6628	54.16942
A.95.ALA.H	A.95.ALA.N	A.95.ALA.CA	7.633072	122.3413	49.73605
A.96.ARG.H	A.96.ARG.N	A.96.ARG.CA	9.200533	121.337	52.91924
A.97.SER.H	A.97.SER.N	A.97.SER.CA	7.293001	111.4036	53.45527
A.98.LEU.H	A.98.LEU.N	A.98.LEU.CA	8.386128	122.4114	53.27569
A.99.GLU.H	A.99.GLU.N	A.99.GLU.CA	8.217475	117.3567	56.30861
A.100.GLU.H	A.100.GLU.N	A.100.GLU.CA	6.927759	115.4191	51.7646
A.101.PHE.H	A.101.PHE.N	A.101.PHE.CA	7.219078	122.3157	53.90543
A.102.ASN.H	A.102.ASN.N	A.102.ASN.CA	8.490935	125.7883	51.19527
A.103.ASP.H	A.103.ASP.N	A.103.ASP.CA	7.507063	115.8185	50.20955
A.104.VAL.H	A.104.VAL.N	A.104.VAL.CA	8.387933	121.069	58.53109
A.106.LEU.H	A.106.LEU.N	A.106.LEU.CA	8.66925	119.825	49.74222
A.108.THR.H	A.108.THR.N	A.108.THR.CA	8.869282	118.1972	56.4392
A.109.HIS.H	A.109.HIS.N	A.109.HIS.CA	8.957862	119.7092	56.06645
A.110.LEU.H	A.110.LEU.N	A.110.LEU.CA	8.095529	124.5852	52.22716
A.112.GLY.H	A.112.GLY.N	A.112.GLY.CA	8.091563	108.4151	42.57059
A.113.ALA.H	A.113.ALA.N	A.113.ALA.CA	7.800885	123.9109	48.4631
A.114.ASP.H	A.114.ASP.N	A.114.ASP.CA	7.908341	118.6318	49.26975
A.116.ASN.H	A.116.ASN.N	A.116.ASN.CA	7.601906	117.2388	53.02249
A.117.ASN.H	A.117.ASN.N	A.117.ASN.CA	7.811315	118.2622	54.89669
A.120.LYS.H	A.120.LYS.N	A.120.LYS.CA	7.303634	117.3651	54.0356
A.121.CYS.H	A.121.CYS.N	A.121.CYS.CA	7.577267	113.661	55.22155
A.122.GLN.H	A.122.GLN.N	A.122.GLN.CA	7.864457	119.8993	50.92634

A.124.LEU.H	A.124.LEU.N	A.124.LEU.CA	8.646466	129.8513	51.00994
A.127.ASP.H	A.127.ASP.N	A.127.ASP.CA	7.767366	115.7899	54.66503
A.129.VAL.H	A.129.VAL.N	A.129.VAL.CA	8.061735	119.8541	64.63946
A.130.GLN.H	A.130.GLN.N	A.130.GLN.CA	8.33496	118.2695	56.22049
A.132.LEU.H	A.132.LEU.N	A.132.LEU.CA	8.819068	120.4531	55.18766
A.134.TYR.H	A.134.TYR.N	A.134.TYR.CA	8.874623	120.1663	54.6767
A.139.GLY.H	A.139.GLY.N	A.139.GLY.CA	8.047624	107.3275	43.88711
A.140.LEU.H	A.140.LEU.N	A.140.LEU.CA	8.594906	121.5454	53.62551
A.141.LYS.H	A.141.LYS.N	A.141.LYS.CA	8.611542	119.5044	56.74948
A.142.TYR.H	A.142.TYR.N	A.142.TYR.CA	6.735686	118.2377	58.71721
A.143.ILE.H	A.143.ILE.N	A.143.ILE.CA	8.368578	120.2379	63.90454
A.144.HIS.H	A.144.HIS.N	A.144.HIS.CA	9.449081	119.8276	54.12449
A.145.SER.H	A.145.SER.N	A.145.SER.CA	7.792234	115.8116	58.26434
A.146.ALA.H	A.146.ALA.N	A.146.ALA.CA	7.321997	126.4517	48.3147
A.147.ASP.H	A.147.ASP.N	A.147.ASP.CA	8.120589	115.3755	52.46334
A.148.ILE.H	A.148.ILE.N	A.148.ILE.CA	7.161913	119.2458	56.25616
A.149.ILE.H	A.149.ILE.N	A.149.ILE.CA	7.782328	123.2113	56.87646
A.150.HIS.H	A.150.HIS.N	A.150.HIS.CA	7.287962	121.0417	59.64616
A.156.SER.H	A.156.SER.N	A.156.SER.CA	7.786735	105.7589	58.16461
A.157.ASN.H	A.157.ASN.N	A.157.ASN.CA	7.699571	119.0985	49.63858
A.158.LEU.H	A.158.LEU.N	A.158.LEU.CA	6.963797	119.2443	49.83825
A.159.ALA.H	A.159.ALA.N	A.159.ALA.CA	8.391782	125.4726	47.33085
A.160.VAL.H	A.160.VAL.N	A.160.VAL.CA	8.163342	117.2082	56.23339
A.162.GLU.H	A.162.GLU.N	A.162.GLU.CA	8.506532	116.4071	56.11605
A.165.GLU.H	A.165.GLU.N	A.165.GLU.CA	7.422889	118.6323	51.33622
A.166.LEU.H	A.166.LEU.N	A.166.LEU.CA	7.945639	125.8908	50.60352
A.167.LYS.H	A.167.LYS.N	A.167.LYS.CA	8.864142	122.663	51.97644
A.168.ILE.H	A.168.ILE.N	A.168.ILE.CA	8.136425	122.127	59.64654
A.174.ALA.H	A.174.ALA.N	A.174.ALA.CA	8.008601	119.3877	56.69946
A.175.ARG.H	A.175.ARG.N	A.175.ARG.CA	8.335872	117.0922	52.63111
A.179.ASP.H	A.179.ASP.N	A.179.ASP.CA	8.007086	120.0265	51.90442
A.180.GLU.H	A.180.GLU.N	A.180.GLU.CA	8.032752	120.5076	54.03161
A.181.MET.H	A.181.MET.N	A.181.MET.CA	8.030413	120.0671	52.22047
A.182.THR.H	A.182.THR.N	A.182.THR.CA	7.858066	114.1888	59.43118
A.183.GLY.H	A.183.GLY.N	A.183.GLY.CA	8.190983	111.3867	42.25542
A.184.TYR.H	A.184.TYR.N	A.184.TYR.CA	7.784779	121.0524	54.98445
A.185.VAL.H	A.185.VAL.N	A.185.VAL.CA	7.713685	123.3273	59.23077
A.191.ARG.H	A.191.ARG.N	A.191.ARG.CA	7.247859	122.4658	52.71995
A.192.ALA.H	A.192.ALA.N	A.192.ALA.CA	8.776436	126.3127	47.01003
A.197.LEU.H	A.197.LEU.N	A.197.LEU.CA	9.129339	126.6104	55.00242
A.198.ASN.H	A.198.ASN.N	A.198.ASN.CA	7.810093	115.3788	50.67772
A.199.TRP.H	A.199.TRP.N	A.199.TRP.CA	8.525442	125.4433	51.09634
A.200.MET.H	A.200.MET.N	A.200.MET.CA	8.607158	120.1782	59.07851
A.202.TYR.H	A.202.TYR.N	A.202.TYR.CA	10.05549	127.0715	49.83121
A.203.ASN.H	A.203.ASN.N	A.203.ASN.CA	8.702264	124.8443	53.42454
A.208.ILE.H	A.208.ILE.N	A.208.ILE.CA	7.180682	119.2609	57.96908

A.209.TRP.H	A.209.TRP.N	A.209.TRP.CA	7.439725	120.9819	58.27944
A.210.SER.H	A.210.SER.N	A.210.SER.CA	7.4981	112.6667	59.23569
A.211.VAL.H	A.211.VAL.N	A.211.VAL.CA	7.908189	119.9027	64.40242
A.212.GLY.H	A.212.GLY.N	A.212.GLY.CA	8.441059	110.4099	45.00745
A.213.CYS.H	A.213.CYS.N	A.213.CYS.CA	7.802347	119.286	60.97017
A.214.ILE.H	A.214.ILE.N	A.214.ILE.CA	8.353252	124.2248	62.77326
A.215.MET.H	A.215.MET.N	A.215.MET.CA	9.219001	120.5222	57.33655
A.216.ALA.H	A.216.ALA.N	A.216.ALA.CA	8.069899	118.5405	52.44355
A.217.GLU.H	A.217.GLU.N	A.217.GLU.CA	7.008964	120.5046	54.16716
A.218.LEU.H	A.218.LEU.N	A.218.LEU.CA	7.19003	116.4169	54.3649
A.219.LEU.H	A.219.LEU.N	A.219.LEU.CA	8.480618	118.5566	54.02217
A.220.THR.H	A.220.THR.N	A.220.THR.CA	7.883462	106.1002	59.07888
A.221.GLY.H	A.221.GLY.N	A.221.GLY.CA	8.395288	113.6051	42.40132
A.222.ARG.H	A.222.ARG.N	A.222.ARG.CA	7.937809	119.198	50.91894
A.223.THR.H	A.223.THR.N	A.223.THR.CA	7.862857	119.8915	60.41566
A.224.LEU.H	A.224.LEU.N	A.224.LEU.CA	7.775305	117.9483	49.98409
A.227.GLY.H	A.227.GLY.N	A.227.GLY.CA	8.269577	113.6857	42.47739
A.230.HIS.H	A.230.HIS.N	A.230.HIS.CA	8.497704	114.456	49.16909
A.239.ARG.H	A.239.ARG.N	A.239.ARG.CA	8.1649	116.7731	56.37137
A.240.LEU.H	A.240.LEU.N	A.240.LEU.CA	7.508357	117.7729	54.51022
A.241.VAL.H	A.241.VAL.N	A.241.VAL.CA	8.368266	122.3942	55.4076
A.245.GLY.H	A.245.GLY.N	A.245.GLY.CA	8.224234	108.8555	40.71062
A.246.ALA.H	A.246.ALA.N	A.246.ALA.CA	8.28737	121.4033	51.40987
A.248.LEU.H	A.248.LEU.N	A.248.LEU.CA	7.398521	120.4937	53.74965
A.249.LEU.H	A.249.LEU.N	A.249.LEU.CA	7.835646	118.3093	54.46906
A.250.LYS.H	A.250.LYS.N	A.250.LYS.CA	7.533832	120.7695	52.96523
A.256.SER.H	A.256.SER.N	A.256.SER.CA	8.285134	113.9099	57.87701
A.257.ALA.H	A.257.ALA.N	A.257.ALA.CA	7.624708	125.7843	51.66527
A.262.GLN.H	A.262.GLN.N	A.262.GLN.CA	8.013743	118.2813	55.02805
A.263.SER.H	A.263.SER.N	A.263.SER.CA	7.353929	113.9531	56.27198
A.264.LEU.H	A.264.LEU.N		6.87474	122.9769	51.30061
A.267.MET.H	A.267.MET.N	A.267.MET.CA	8.619354	124.8507	53.58703
A.269.LYS.H	A.269.LYS.N	A.269.LYS.CA	8.199232	120.7878	53.99614
A.270.MET.H	A.270.MET.N	A.270.MET.CA	8.328227	126.0958	52.94882
A.271.ASN.H	A.271.ASN.N	A.271.ASN.CA	8.492022	120.4258	49.75321
A.272.PHE.H	A.272.PHE.N	A.272.PHE.CA	9.329122	129.9836	56.77875
A.273.ALA.H	A.273.ALA.N	A.273.ALA.CA	8.464278	122.3624	51.6055
A.274.ASN.H	A.274.ASN.N	A.274.ASN.CA	7.372293	113.1744	50.61602
A.275.VAL.H	A.275.VAL.N	A.275.VAL.CA	7.123302	120.131	61.21496
A.276.PHE.H	A.276.PHE.N	A.276.PHE.CA	7.533832	120.7695	52.96523
A.277.ILE.H	A.277.ILE.N	A.277.ILE.CA	6.796073	121.027	59.27023
A.278.GLY.H	A.278.GLY.N	A.278.GLY.CA	8.933163	116.4061	42.00684
A.279.ALA.H	A.279.ALA.N	A.279.ALA.CA	7.314566	122.0356	48.08325
A.280.ASN.H	A.280.ASN.N	A.280.ASN.CA	9.017936	122.6328	48.27927
A.282.LEU.H	A.282.LEU.N	A.282.LEU.CA	8.342377	117.1082	54.08974
A.283.ALA.H	A.283.ALA.N	A.283.ALA.CA	7.017473	121.0888	50.94258

A.284.VAL.H	A.284.VAL.N	A.284.VAL.CA	6.99312	116.422	63.69952
A.285.ASP.H	A.285.ASP.N	A.285.ASP.CA	7.400253	117.9752	54.71461
A.286.LEU.H	A.286.LEU.N	A.286.LEU.CA	7.021573	117.6297	54.71639
A.287.LEU.H	A.287.LEU.N	A.287.LEU.CA	8.054185	120.4484	55.80322
A.288.GLU.H	A.288.GLU.N	A.288.GLU.CA	7.895772	117.61	55.62306
A.289.LYS.H	A.289.LYS.N	A.289.LYS.CA	7.254119	116.0997	54.29335
A.290.MET.H	A.290.MET.N	A.290.MET.CA	7.547902	117.7074	55.86261
A.291.LEU.H	A.291.LEU.N	A.291.LEU.CA	7.79517	119.1412	56.56485
A.296.ASP.H	A.296.ASP.N	A.296.ASP.CA	8.378028	121.0875	53.33903
A.297.LYS.H	A.297.LYS.N	A.297.LYS.CA	7.561489	117.5683	51.78211
A.298.ARG.H	A.298.ARG.N	A.298.ARG.CA	6.96175	122.5371	54.28487
A.299.ILE.H	A.299.ILE.N	A.299.ILE.CA	7.004657	125.1826	59.21291
A.300.THR.H	A.300.THR.N	A.300.THR.CA	7.305903	109.5068	57.21353
A.301.ALA.H	A.301.ALA.N	A.301.ALA.CA	9.446821	122.2789	53.27407
A.302.ALA.H	A.302.ALA.N	A.302.ALA.CA	8.557499	116.3541	52.22311
A.303.GLN.H	A.303.GLN.N	A.303.GLN.CA	7.354053	116.1297	55.25307
A.304.ALA.H	A.304.ALA.N	A.304.ALA.CA	8.618392	123.939	52.02214
A.305.LEU.H	A.305.LEU.N	A.305.LEU.CA	7.581305	116.38	54.63303
A.306.ALA.H	A.306.ALA.N	A.306.ALA.CA	6.564594	115.4132	48.01124
A.307.HIS.H	A.307.HIS.N	A.307.HIS.CA	7.884027	122.77	55.77318
A.308.ALA.H	A.308.ALA.N	A.307.HIS.CA	8.278398	132.8855	55.7722
A.308.ALA.H	A.308.ALA.N	A.308.ALA.CA	8.279288	132.9087	52.23459
A.309.TYR.H	A.309.TYR.N	A.309.TYR.CA	11.63151	125.1847	57.43937
A.310.PHE.H	A.310.PHE.N	A.310.PHE.CA	7.568125	110.4675	53.13366
A.311.ALA.H	A.311.ALA.N	A.311.ALA.CA	7.450304	123.6251	52.88996
A.312.GLN.H	A.312.GLN.N	A.312.GLN.CA	8.585749	113.9839	54.25029
A.313.TYR.H	A.313.TYR.N	A.313.TYR.CA	7.354053	116.1297	55.25307
A.314.HIS.H	A.314.HIS.N	A.314.HIS.CA	7.748603	115.5099	52.97459
A.315.ASP.H	A.315.ASP.N	A.315.ASP.CA	7.332039	125.1329	47.9628
A.317.ASP.H	A.317.ASP.N	A.317.ASP.CA	7.883211	117.4102	52.31035
A.318.ASP.H	A.318.ASP.N	A.318.ASP.CA	7.904558	121.1533	49.64214
A.319.GLU.H	A.319.GLU.N	A.319.GLU.CA	7.74133	121.4567	50.60538
A.321.VAL.H	A.321.VAL.N	A.321.VAL.CA	7.7757	109.0877	56.46189
A.322.ALA.H	A.322.ALA.N	A.322.ALA.CA	8.261487	123.6837	47.98298
A.323.ASP.H	A.323.ASP.N	A.323.ASP.CA	8.008401	121.1459	50.20323
A.326.ASP.H	A.326.ASP.N	A.326.ASP.CA	6.87474	122.9769	51.30061
A.330.GLU.H	A.330.GLU.N	A.330.GLU.CA	9.847678	114.8663	56.35469
A.331.SER.H	A.331.SER.N	A.331.SER.CA	7.435253	112.7036	54.92073
A.332.ARG.H	A.332.ARG.N	A.332.ARG.CA	7.542747	121.9959	53.16682
A.333.ASP.H	A.333.ASP.N	A.333.ASP.CA	8.487249	124.6021	50.30483
A.334.LEU.H	A.334.LEU.N	A.334.LEU.CA	7.736607	123.0224	49.82457
A.335.LEU.H	A.335.LEU.N	A.335.LEU.CA	8.669675	119.8361	50.99085
A.336.ILE.H	A.336.ILE.N	A.336.ILE.CA	8.873068	121.7267	63.9391
A.337.ASP.H	A.337.ASP.N	A.337.ASP.CA	8.31226	115.7972	54.15593
A.338.GLU.H	A.338.GLU.N	A.338.GLU.CA	7.009056	120.5157	55.61378
A.339.TRP.H	A.339.TRP.N	A.339.TRP.CA	7.60343	119.5618	56.98141

A.340.LYS.H	A.340.LYS.N	A.340.LYS.CA	8.683377	121.44	57.32619
A.341.SER.H	A.341.SER.N	A.341.SER.CA	7.518914	114.5007	58.04963
A.342.LEU.H	A.342.LEU.N	A.342.LEU.CA	7.85874	120.1997	54.71126
A.345.ASP.H	A.345.ASP.N	A.345.ASP.CA	8.017697	117.3976	54.26638
A.346.GLU.H	A.346.GLU.N	A.346.GLU.CA	7.459426	118.2504	54.83979
A.347.VAL.H	A.347.VAL.N	A.347.VAL.CA	7.981782	121.6835	63.16855
A.348.ILE.H	A.348.ILE.N	A.348.ILE.CA	7.951949	115.3991	60.1112
A.349.SER.H	A.349.SER.N	A.349.SER.CA	7.357424	112.0078	55.10434
A.350.PHE.H	A.350.PHE.N	A.350.PHE.CA	7.034582	124.1924	56.60092
A.351.VAL.H	A.351.VAL.N	A.351.VAL.CA	7.750843	131.3591	55.5995
A.355.LEU.H	A.355.LEU.N	A.355.LEU.CA	8.207426	123.5741	51.71477
A.356.ASP.H	A.356.ASP.N	A.356.ASP.CA	8.210951	121.4144	51.51834
A.357.GLN.H	A.357.GLN.N	A.357.GLN.CA	8.155836	120.2047	52.63775
A.358.GLU.H	A.358.GLU.N	A.358.GLU.CA	8.249368	122.9584	53.02011
A.359.GLU.H	A.359.GLU.N	A.359.GLU.CA	8.283479	122.3312	53.49065
A.360.MET.H	A.360.MET.N	A.360.MET.CA	8.23075	122.1201	52.2606
A.361.GLU.H	A.361.GLU.N	A.361.GLU.CA	8.302817	122.8653	53.18869
A.362.SER.H	A.362.SER.N	A.362.SER.CA	7.859086	123.008	56.86469

Table 10.6 Chemical shifts of D150A (BMRB nomenclature is i+2)

Assign F1	Assign F2	Assign F3	Pos F1	Pos F2	Pos F3
A.7.ARG.H	A.7.ARG.N	A.7.ARG.CA	8.381256	125.7735	50.94958
A.9.THR.H	A.9.THR.N	A.10.PHE.CA	8.747751	127.3657	53.80888
A.9.THR.H	A.9.THR.N	A.9.THR.CA	8.405871	117.429	59.84844
A.11.TYR.H	A.11.TYR.N	A.11.TYR.CA	9.064062	120.1823	52.70681
A.12.ARG.H	A.12.ARG.N	A.12.ARG.CA	8.382203	120.1791	51.27361
A.13.GLN.H	A.13.GLN.N	A.13.GLN.CA	8.865487	122.357	51.54043
A.14.GLU.H	A.14.GLU.N	A.14.GLU.CA	8.774586	125.4808	52.11905
A.15.LEU.H	A.15.LEU.N	A.15.LEU.CA	8.919832	128.6035	50.69834
A.17.LYS.H	A.17.LYS.N	A.17.LYS.CA	8.816931	110.0811	54.56448
A.18.THR.H	A.18.THR.N	A.18.THR.CA	7.768332	115.8146	58.19529
A.19.ILE.H	A.19.ILE.N	A.19.ILE.CA	8.540393	125.7452	56.9527
A.20.TRP.H	A.20.TRP.N	A.20.TRP.CA	9.204672	131.0973	53.73928
A.21.GLU.H	A.21.GLU.N	A.21.GLU.CA	8.242506	128.5087	51.77186
A.22.VAL.H	A.22.VAL.N	A.22.VAL.CA	7.564733	112.2094	53.04839
A.24.GLU.H	A.24.GLU.N	A.24.GLU.CA	8.061763	119.2192	55.46138
A.25.ARG.H	A.25.ARG.N	A.25.ARG.CA	7.426201	117.2964	54.5458
A.26.TYR.H	A.26.TYR.N	A.26.TYR.CA	7.683454	118.3831	54.16074
A.27.GLN.H	A.27.GLN.N	A.27.GLN.CA	9.120395	122.8762	50.46948
A.28.ASN.H	A.28.ASN.N	A.28.ASN.CA	8.736856	117.4323	50.41564

A.29.LEU.H	A.29.LEU.N	A.29.LEU.CA	8.446315	120.2326	53.97159
A.29.LEU.H	A.29.LEU.N	A.29.LEU.CA	8.444256	120.4243	37.77055
A.30.SER.H	A.30.SER.N	A.30.SER.CA	8.685935	116.2059	51.38415
A.32.VAL.H	A.32.VAL.N	A.32.VAL.CA	8.578082	121.021	61.34055
A.33.GLY.H	A.33.GLY.N	A.33.GLY.CA	7.680334	108.5491	42.30726
A.34.SER.H	A.34.SER.N	A.34.SER.CA	8.336162	115.4084	54.82602
A.35.GLY.H	A.35.GLY.N	A.35.GLY.CA	8.091197	110.4911	41.55809
A.37.TYR.H	A.37.TYR.N	A.37.TYR.CA	8.003035	113.575	54.03423
A.38.GLY.H	A.38.GLY.N	A.38.GLY.CA	7.2339	108.6355	42.31821
A.39.SER.H	A.39.SER.N	A.39.SER.CA	8.066736	115.9985	54.75701
A.40.VAL.H	A.40.VAL.N	A.40.VAL.CA	8.622473	122.492	58.22664
A.41.CYS.H	A.41.CYS.N	A.41.CYS.CA	9.182983	125.4861	54.87284
A.42.ALA.H	A.42.ALA.N	A.42.ALA.CA	8.710202	125.7879	47.4821
A.43.ALA.H	A.43.ALA.N	A.43.ALA.CA	8.964267	120.8082	47.64778
A.44.PHE.H	A.44.PHE.N	A.44.PHE.CA	9.106066	122.5794	53.92141
A.45.ASP.H	A.45.ASP.N	A.45.ASP.CA	8.215129	125.8626	48.77967
A.46.THR.H	A.46.THR.N	A.46.THR.CA	8.959443	117.5043	60.5739
A.47.LYS.H	A.47.LYS.N	A.47.LYS.CA	7.744056	121.4101	55.28024
A.48.THR.H	A.48.THR.N	A.48.THR.CA	6.465724	104.7256	58.68911
A.49.GLY.H	A.49.GLY.N	A.49.GLY.CA	8.250205	112.0652	42.75746
A.50.LEU.H	A.50.LEU.N	A.50.LEU.CA	7.031661	119.6023	50.41306
A.51.ARG.H	A.51.ARG.N	A.51.ARG.CA	8.163382	119.8546	52.80693
A.52.VAL.H	A.52.VAL.N	A.52.VAL.CA	8.705079	116.6087	55.98133
A.53.ALA.H	A.53.ALA.N	A.53.ALA.CA	8.74688	122.9801	47.10763
A.55.LYS.H	A.55.LYS.N	A.55.LYS.CA	9.518535	129.5436	50.51358
A.56.LYS.H	A.56.LYS.N	A.56.LYS.CA	8.547955	128.3456	51.22936
A.57.LEU.H	A.57.LEU.N	A.57.LEU.CA	7.90885	128.5992	52.15796
A.58.SER.H	A.58.SER.N	A.58.SER.CA	7.942055	117.9728	53.82709
A.59.ARG.H	A.59.ARG.N	A.59.ARG.CA	8.687976	123.2951	53.23661
A.62.GLN.H	A.62.GLN.N	A.62.GLN.CA	6.990684	115.4907	54.38226
A.63.SER.H	A.63.SER.N	A.63.SER.CA	7.349213	110.7439	53.52722
A.64.ILE.H	A.64.ILE.N	A.64.ILE.CA	9.10643	123.2623	62.77798
A.65.ILE.H	A.65.ILE.N	A.65.ILE.CA	7.512849	118.9218	61.15625
A.67.ALA.H	A.67.ALA.N	A.67.ALA.CA	8.549217	123.6027	51.98982
A.68.LYS.H	A.68.LYS.N	A.68.LYS.CA	7.749147	118.3154	56.34073
A.69.ARG.H	A.69.ARG.N	A.69.ARG.CA	7.375151	119.2352	56.20194
A.70.THR.H	A.70.THR.N	A.70.THR.CA	8.34514	119.8274	63.88836
A.71.TYR.H	A.71.TYR.N	A.71.TYR.CA	7.523292	121.6579	59.47251
A.81.LYS.H	A.81.LYS.N	A.81.LYS.CA	8.4343	128.2884	51.90804
A.82.HIS.H	A.82.HIS.N	A.82.HIS.CA	8.603701	123.9537	54.23685
A.83.GLU.H	A.83.GLU.N	A.83.GLU.CA	7.963109	125.546	56.3805
A.85.VAL.H	A.85.VAL.N		7.636335	119.8747	58.28683
A.87.GLY.H	A.87.GLY.N	A.87.GLY.CA	7.560864	109.8958	40.20474
A.88.LEU.H	A.88.LEU.N	A.88.LEU.CA	8.276366	121.1048	51.17178
A.89.LEU.H	A.89.LEU.N	A.89.LEU.CA	8.849951	126.11	52.10812
A.91.VAL.H	A.91.VAL.N	A.91.VAL.CA	7.723834	120.7908	56.34139

A.93.THR.H	A.93.THR.N	A.93.THR.CA	8.879463	113.6698	54.13616
A.95.ALA.H	A.95.ALA.N	A.95.ALA.CA	7.637074	122.3336	49.60563
A.96.ARG.H	A.96.ARG.N	A.96.ARG.CA	9.189263	121.1565	52.88867
A.97.SER.H	A.97.SER.N	A.97.SER.CA	7.292887	111.3995	53.374
A.98.LEU.H	A.98.LEU.N	A.98.LEU.CA	8.355738	122.3583	53.20197
A.99.GLU.H	A.99.GLU.N	A.99.GLU.CA	8.216622	117.3607	56.23008
A.100.GLU.H	A.100.GLU.N	A.100.GLU.CA	6.928959	115.419	51.67673
A.101.PHE.H	A.101.PHE.N	A.101.PHE.CA	7.217779	122.2934	53.84277
A.102.ASN.H	A.102.ASN.N	A.102.ASN.CA	8.468726	125.793	50.80057
A.103.ASP.H	A.103.ASP.N	A.103.ASP.CA	7.514817	115.8701	50.13345
A.104.VAL.H	A.104.VAL.N	A.104.VAL.CA	8.390791	121.0637	58.44071
A.106.LEU.H	A.106.LEU.N	A.106.LEU.CA	8.669605	119.8266	49.67226
A.108.THR.H	A.108.THR.N	A.108.THR.CA	8.887051	118.0218	56.33742
A.109.HIS.H	A.109.HIS.N	A.109.HIS.CA	8.89307	119.589	55.97919
A.110.LEU.H	A.110.LEU.N	A.110.LEU.CA	8.082351	125.491	51.46124
A.112.GLY.H	A.112.GLY.N	A.112.GLY.CA	8.07707	108.288	42.2067
A.113.ALA.H	A.113.ALA.N	A.113.ALA.CA	7.80539	123.88	48.25409
A.114.ASP.H	A.114.ASP.N	A.114.ASP.CA	7.913331	118.5916	49.27547
A.116.ASN.H	A.116.ASN.N	A.116.ASN.CA	7.592793	117.7308	53.03097
A.117.ASN.H	A.117.ASN.N	A.117.ASN.CA	7.808518	118.2455	54.75804
A.120.LYS.H	A.120.LYS.N	A.120.LYS.CA	7.304028	117.4993	54.3291
A.121.CYS.H	A.121.CYS.N	A.121.CYS.CA	7.512171	113.5384	55.01824
A.122.GLN.H	A.122.GLN.N	A.122.GLN.CA	7.881	119.8694	50.78777
A.124.LEU.H	A.124.LEU.N	A.124.LEU.CA	8.531535	128.3456	49.60787
A.127.ASP.H	A.127.ASP.N	A.127.ASP.CA	7.76882	115.8086	54.58662
A.129.VAL.H	A.129.VAL.N	A.129.VAL.CA	8.107714	118.3319	64.14968
A.130.GLN.H	A.130.GLN.N	A.130.GLN.CA	8.343888	118.279	56.16107
A.132.LEU.H	A.132.LEU.N	A.132.LEU.CA	8.812319	120.5053	55.18766
A.134.TYR.H	A.134.TYR.N	A.134.TYR.CA	8.824057	119.8912	54.60069
A.139.GLY.H	A.139.GLY.N	A.139.GLY.CA	8.047213	107.305	43.72874
A.140.LEU.H	A.140.LEU.N	A.140.LEU.CA	8.596534	121.6604	53.57156
A.141.LYS.H	A.141.LYS.N	A.141.LYS.CA	8.61104	119.5479	56.75068
A.142.TYR.H	A.142.TYR.N	A.142.TYR.CA	6.724332	118.2673	58.63148
A.143.ILE.H	A.143.ILE.N	A.143.ILE.CA	8.370801	120.2659	64.34205
A.144.HIS.H	A.144.HIS.N	A.144.HIS.CA	9.500256	120.1389	53.72579
A.145.SER.H	A.145.SER.N	A.145.SER.CA	7.781081	116.4166	58.06498
A.146.ALA.H	A.146.ALA.N	A.146.ALA.CA	7.319086	126.4197	48.23522
A.147.ASP.H	A.147.ASP.N	A.147.ASP.CA	8.117555	115.4218	52.35491
A.148.ILE.H	A.148.ILE.N	A.148.ILE.CA	7.134744	119.2122	56.34889
A.149.ILE.H	A.149.ILE.N	A.149.ILE.CA	7.786856	123.5186	56.77062
A.150.HIS.H	A.150.HIS.N	A.150.HIS.CA	7.303392	120.8187	59.25746
A.156.SER.H	A.156.SER.N	A.156.SER.CA	7.804352	105.8314	58.18143
A.157.ASN.H	A.157.ASN.N	A.157.ASN.CA	7.710862	118.856	49.57402
A.158.LEU.H	A.158.LEU.N	A.158.LEU.CA	6.948422	119.1916	49.96538
A.159.ALA.H	A.159.ALA.N	A.159.ALA.CA	8.412704	125.6207	47.13071
A.160.VAL.H	A.160.VAL.N	A.160.VAL.CA	8.163653	116.8165	56.14823

A.162.GLU.H	A.162.GLU.N	A.162.GLU.CA	8.485842	116.3659	55.88532
A.165.GLU.H	A.165.GLU.N	A.165.GLU.CA	7.421799	118.6395	51.1756
A.166.LEU.H	A.166.LEU.N	A.166.LEU.CA	7.917637	125.8398	50.06305
A.167.LYS.H	A.167.LYS.N	A.167.LYS.CA	8.875465	122.6676	52.07324
A.168.ILE.H	A.168.ILE.N	A.168.ILE.CA	8.134185	121.7515	59.33738
A.174.ALA.H	A.174.ALA.N	A.174.ALA.CA	7.996227	119.316	56.99484
A.175.ARG.H	A.175.ARG.N	A.175.ARG.CA	8.352842	117.0497	52.70574
A.179.ASP.H	A.179.ASP.N	A.179.ASP.CA	7.98837	120.8757	51.7131
A.180.GLU.H	A.180.GLU.N	A.180.GLU.CA	8.05124	120.801	53.7747
A.181.MET.H	A.181.MET.N	A.181.MET.CA	8.01469	120.286	51.54637
A.182.THR.H	A.182.THR.N	A.182.THR.CA	7.821948	114.1374	59.09247
A.183.GLY.H	A.183.GLY.N	A.183.GLY.CA	8.198926	111.6086	42.26478
A.184.TYR.H	A.184.TYR.N	A.184.TYR.CA	7.780367	120.2152	54.553
A.185.VAL.H	A.185.VAL.N	A.185.VAL.CA	7.712386	123.1527	58.68404
A.191.ARG.H	A.191.ARG.N	A.191.ARG.CA	7.264362	122.6763	52.77703
A.192.ALA.H	A.192.ALA.N	A.192.ALA.CA	8.76104	126.0871	47.07413
A.197.LEU.H	A.197.LEU.N	A.197.LEU.CA	9.087664	126.4176	54.88588
A.198.ASN.H	A.198.ASN.N	A.198.ASN.CA	7.798604	115.4592	50.53765
A.199.TRP.H	A.199.TRP.N	A.199.TRP.CA	8.526317	125.3626	51.30616
A.200.MET.H	A.200.MET.N	A.200.MET.CA	8.60549	120.3751	59.62305
A.202.TYR.H	A.202.TYR.N	A.202.TYR.CA	10.07059	126.9877	49.89764
A.203.ASN.H	A.203.ASN.N	A.203.ASN.CA	8.717512	124.8884	53.30717
A.205.THR.H	A.205.THR.N	A.205.THR.CA	8.276469	114.828	56.40752
A.208.ILE.H	A.208.ILE.N	A.208.ILE.CA	7.138722	119.4653	57.98322
A.209.TRP.H	A.209.TRP.N	A.209.TRP.CA	7.489955	121.0792	58.27416
A.210.SER.H	A.210.SER.N	A.210.SER.CA	7.488112	112.6957	59.12577
A.211.VAL.H	A.211.VAL.N	A.211.VAL.CA	7.928055	120.1605	64.41585
A.212.GLY.H	A.212.GLY.N	A.212.GLY.CA	8.482305	110.4738	44.94197
A.213.CYS.H	A.213.CYS.N	A.213.CYS.CA	7.810391	119.2916	60.99739
A.214.ILE.H	A.214.ILE.N	A.214.ILE.CA	8.375225	124.5003	62.75887
A.215.MET.H	A.215.MET.N	A.215.MET.CA	9.212521	120.7382	57.31271
A.216.ALA.H	A.216.ALA.N	A.216.ALA.CA	8.063504	118.579	52.30179
A.217.GLU.H	A.217.GLU.N	A.217.GLU.CA	7.042062	120.4129	55.07716
A.218.LEU.H	A.218.LEU.N	A.218.LEU.CA	7.215207	116.4407	54.29123
A.219.LEU.H	A.219.LEU.N	A.219.LEU.CA	8.428148	118.3031	53.63341
A.220.THR.H	A.220.THR.N	A.220.THR.CA	7.890926	106.2051	59.14631
A.221.GLY.H	A.221.GLY.N	A.221.GLY.CA	8.369505	113.4055	42.93112
A.222.ARG.H	A.222.ARG.N	A.222.ARG.CA	7.931684	119.1447	50.79334
A.223.THR.H	A.223.THR.N	A.223.THR.CA	7.878496	119.8646	60.4088
A.224.LEU.H	A.224.LEU.N	A.224.LEU.CA	7.707201	118.0545	49.90352
A.227.GLY.H	A.227.GLY.N	A.227.GLY.CA	8.308504	114.5154	42.30211
A.230.HIS.H	A.230.HIS.N	A.230.HIS.CA	8.495175	112.9786	49.25006
A.239.ARG.H	A.239.ARG.N	A.239.ARG.CA	8.179645	116.8307	56.18872
A.240.LEU.H	A.240.LEU.N	A.240.LEU.CA	7.507407	117.519	53.64815
A.241.VAL.H	A.241.VAL.N	A.241.VAL.CA	8.361053	123.2927	55.23342
A.245.GLY.H	A.245.GLY.N	A.245.GLY.CA	8.241774	108.8158	40.60212

A.246.ALA.H	A.246.ALA.N	A.246.ALA.CA	8.262353	121.4131	51.39198
A.248.LEU.H	A.248.LEU.N	A.248.LEU.CA	7.389063	120.5809	53.54813
A.249.LEU.H	A.249.LEU.N	A.249.LEU.CA	7.808518	118.2455	54.75804
A.250.LYS.H	A.250.LYS.N	A.250.LYS.CA	7.579746	120.7477	52.58009
A.256.SER.H	A.256.SER.N	A.256.SER.CA	8.280716	114.0041	57.9197
A.257.ALA.H	A.257.ALA.N	A.257.ALA.CA	7.62465	125.7779	51.52237
A.262.GLN.H	A.262.GLN.N	A.262.GLN.CA	8.009717	118.2411	54.8784
A.263.SER.H	A.263.SER.N	A.263.SER.CA	7.336473	113.9162	55.71398
A.264.LEU.H	A.264.LEU.N		6.871856	122.9427	51.17668
A.267.MET.H	A.267.MET.N	A.267.MET.CA	8.612025	124.7605	53.93427
A.269.LYS.H	A.269.LYS.N	A.269.LYS.CA	8.2251	120.7557	53.61234
A.270.MET.H	A.270.MET.N	A.270.MET.CA	8.380062	125.7755	53.04257
A.271.ASN.H	A.271.ASN.N	A.271.ASN.CA	8.497576	120.4783	49.6887
A.272.PHE.H	A.272.PHE.N	A.272.PHE.CA	9.299018	130.1711	56.67735
A.273.ALA.H	A.273.ALA.N	A.273.ALA.CA	8.451303	122.3337	51.95185
A.274.ASN.H	A.274.ASN.N	A.274.ASN.CA	7.376454	113.0878	50.5722
A.275.VAL.H	A.275.VAL.N	A.275.VAL.CA	7.110035	120.1123	60.99874
A.276.PHE.H	A.276.PHE.N	A.276.PHE.CA	7.533473	120.792	53.09203
A.277.ILE.H	A.277.ILE.N	A.277.ILE.CA	6.804534	121.016	59.21477
A.278.GLY.H	A.278.GLY.N	A.278.GLY.CA	8.93615	116.4024	41.89142
A.279.ALA.H	A.279.ALA.N	A.279.ALA.CA	7.312287	122.0299	47.99832
A.280.ASN.H	A.280.ASN.N	A.280.ASN.CA	9.044831	122.6797	48.15695
A.282.LEU.H	A.282.LEU.N	A.282.LEU.CA	8.360645	117.078	54.00207
A.283.ALA.H	A.283.ALA.N	A.283.ALA.CA	7.019278	121.1096	50.80077
A.284.VAL.H	A.284.VAL.N	A.284.VAL.CA	6.985273	116.4371	63.66961
A.285.ASP.H	A.285.ASP.N	A.285.ASP.CA	7.412466	117.9934	54.67395
A.286.LEU.H	A.286.LEU.N	A.286.LEU.CA	7.026228	117.6071	54.69937
A.287.LEU.H	A.287.LEU.N	A.287.LEU.CA	8.040771	120.3984	55.65901
A.288.GLU.H	A.288.GLU.N	A.288.GLU.CA	7.907125	117.3883	55.68267
A.289.LYS.H	A.289.LYS.N	A.289.LYS.CA	7.215207	116.4407	54.29123
A.290.MET.H	A.290.MET.N	A.290.MET.CA	7.555573	117.7409	56.34771
A.291.LEU.H	A.291.LEU.N	A.291.LEU.CA	7.770221	118.9349	56.54737
A.296.ASP.H	A.296.ASP.N	A.296.ASP.CA	8.378911	121.1574	53.29505
A.297.LYS.H	A.297.LYS.N	A.297.LYS.CA	7.547766	117.5865	51.77262
A.298.ARG.H	A.298.ARG.N	A.298.ARG.CA	6.980189	122.7278	54.2791
A.299.ILE.H	A.299.ILE.N	A.299.ILE.CA	6.975611	125.2685	59.2033
A.300.THR.H	A.300.THR.N	A.300.THR.CA	7.302046	109.3539	57.13917
A.301.ALA.H	A.301.ALA.N	A.301.ALA.CA	9.439607	122.137	53.19437
A.302.ALA.H	A.302.ALA.N	A.302.ALA.CA	8.535994	116.3033	52.12255
A.303.GLN.H	A.303.GLN.N	A.303.GLN.CA	7.342033	116.1017	55.24422
A.304.ALA.H	A.304.ALA.N	A.304.ALA.CA	8.610991	123.9154	51.85565
A.305.LEU.H	A.305.LEU.N	A.305.LEU.CA	7.581618	116.3925	54.53498
A.306.ALA.H	A.306.ALA.N	A.306.ALA.CA	6.534342	115.2006	47.89851
A.307.HIS.H	A.307.HIS.N	A.307.HIS.CA	7.878606	122.6786	55.69256
A.308.ALA.H	A.308.ALA.N	A.308.ALA.CA	8.268339	132.7913	52.12034
A.309.TYR.H	A.309.TYR.N	A.309.TYR.CA	11.63658	124.903	57.68306

A.310.PHE.H	A.310.PHE.N	A.310.PHE.CA	7.571573	110.4552	52.98242
A.311.ALA.H	A.311.ALA.N	A.311.ALA.CA	7.446389	123.6093	52.77031
A.312.GLN.H	A.312.GLN.N	A.312.GLN.CA	8.584807	113.9957	54.12899
A.313.TYR.H	A.313.TYR.N	A.313.TYR.CA	7.374053	116.0736	54.88391
A.314.HIS.H	A.314.HIS.N	A.314.HIS.CA	7.74173	115.728	53.07327
A.315.ASP.H	A.315.ASP.N	A.315.ASP.CA	7.376901	125.1399	47.84424
A.317.ASP.H	A.317.ASP.N	A.317.ASP.CA	7.873475	117.3866	52.2283
A.318.ASP.H	A.318.ASP.N	A.318.ASP.CA	7.924737	121.2124	49.62059
A.319.GLU.H	A.319.GLU.N	A.319.GLU.CA	7.720413	121.4992	50.50775
A.321.VAL.H	A.321.VAL.N	A.321.VAL.CA	7.777764	109.0199	56.4058
A.322.ALA.H	A.322.ALA.N	A.322.ALA.CA	8.36354	123.3899	47.76458
A.323.ASP.H	A.323.ASP.N	A.323.ASP.CA	8.000268	121.1268	50.05589
A.326.ASP.H	A.326.ASP.N	A.326.ASP.CA	6.871856	122.9427	51.17668
A.330.GLU.H	A.330.GLU.N	A.330.GLU.CA	9.850526	114.8671	56.74283
A.331.SER.H	A.331.SER.N	A.331.SER.CA	7.430816	112.7157	54.81225
A.332.ARG.H	A.332.ARG.N	A.332.ARG.CA	7.539417	121.9719	53.10521
A.333.ASP.H	A.333.ASP.N	A.333.ASP.CA	8.493904	124.7622	50.26376
A.334.LEU.H	A.334.LEU.N	A.334.LEU.CA	7.734526	123.0058	49.71843
A.335.LEU.H	A.335.LEU.N	A.335.LEU.CA	8.670089	119.8234	50.8565
A.336.ILE.H	A.336.ILE.N	A.336.ILE.CA	8.872362	121.7153	63.8981
A.337.ASP.H	A.337.ASP.N	A.337.ASP.CA	8.312884	115.7826	54.06829
A.338.GLU.H	A.338.GLU.N	A.338.GLU.CA	7.001996	120.5143	55.49933
A.339.TRP.H	A.339.TRP.N	A.339.TRP.CA	7.605311	119.5392	56.93152
A.340.LYS.H	A.340.LYS.N	A.340.LYS.CA	8.681154	121.4359	57.21774
A.341.SER.H	A.341.SER.N	A.341.SER.CA	7.519175	114.5242	57.55322
A.342.LEU.H	A.342.LEU.N	A.342.LEU.CA	7.905451	120.4177	54.51646
A.345.ASP.H	A.345.ASP.N	A.345.ASP.CA	8.023764	117.377	54.19063
A.346.GLU.H	A.346.GLU.N	A.346.GLU.CA	7.456572	118.1311	54.70541
A.347.VAL.H	A.347.VAL.N	A.347.VAL.CA	7.985177	121.7365	63.17012
A.348.ILE.H	A.348.ILE.N	A.348.ILE.CA	7.948196	115.3949	60.06711
A.349.SER.H	A.349.SER.N	A.349.SER.CA	7.356833	111.9942	55.05659
A.350.PHE.H	A.350.PHE.N	A.350.PHE.CA	7.028993	124.1832	56.51935
A.351.VAL.H	A.351.VAL.N	A.351.VAL.CA	7.749784	131.3826	55.91983
A.355.LEU.H	A.355.LEU.N	A.355.LEU.CA	8.203582	123.5862	51.60736
A.356.ASP.H	A.356.ASP.N	A.356.ASP.CA	8.213855	121.4369	51.41935
A.357.GLN.H	A.357.GLN.N	A.357.GLN.CA	8.156141	120.2248	52.53472
A.358.GLU.H	A.358.GLU.N	A.358.GLU.CA	8.249356	122.9346	52.93629
A.359.GLU.H	A.359.GLU.N	A.359.GLU.CA	8.284951	122.3393	53.38389
A.360.MET.H	A.360.MET.N	A.360.MET.CA	8.23057	122.0971	52.1978
A.361.GLU.H	A.361.GLU.N	A.361.GLU.CA	8.305122	122.8653	53.38101
A.362.SER.H	A.362.SER.N	A.362.SER.CA	7.857474	123.0026	56.80716

Table 10.7 Chemical shifts of D168A (BMRB nomenclature is i+2)

Assign F1	Assign F2	Assign F3	Pos F1	Pos F2	Pos F3
A.7.ARG.H	A.7.ARG.N	A.7.ARG.CA	8.382194	125.6941	50.94346
A.9.THR.H	A.9.THR.N	A.10.PHE.CA	8.755229	127.3672	53.77962
A.9.THR.H	A.9.THR.N	A.9.THR.CA	8.39836	117.3876	59.89082
A.11.TYR.H	A.11.TYR.N	A.11.TYR.CA	9.043745	120.1395	52.72015
A.12.ARG.H	A.12.ARG.N	A.12.ARG.CA	8.377512	120.2617	51.27168
A.13.GLN.H	A.13.GLN.N	A.13.GLN.CA	8.900282	122.6624	51.59914
A.14.GLU.H	A.14.GLU.N	A.14.GLU.CA	8.771361	125.4849	52.15125
A.15.LEU.H	A.15.LEU.N	A.15.LEU.CA	8.927726	128.5485	50.79236
A.17.LYS.H	A.17.LYS.N	A.17.LYS.CA	8.802871	110.1412	54.62527
A.18.THR.H	A.18.THR.N	A.18.THR.CA	7.774155	116.1119	58.2974
A.19.ILE.H	A.19.ILE.N	A.19.ILE.CA	8.533085	125.7946	56.97223
A.20.TRP.H	A.20.TRP.N	A.20.TRP.CA	9.164086	131.0261	53.68233
A.21.GLU.H	A.21.GLU.N	A.21.GLU.CA	8.27196	128.6323	51.42904
A.22.VAL.H	A.22.VAL.N	A.22.VAL.CA	7.556146	112.0578	53.1108
A.24.GLU.H	A.24.GLU.N	A.24.GLU.CA	8.071668	119.1912	55.442
A.25.ARG.H	A.25.ARG.N	A.25.ARG.CA	7.434078	117.2092	54.49868
A.26.TYR.H	A.26.TYR.N	A.26.TYR.CA	7.692674	118.5401	54.04088
A.27.GLN.H	A.27.GLN.N	A.27.GLN.CA	9.110385	122.7447	50.51747
A.28.ASN.H	A.28.ASN.N	A.28.ASN.CA	8.721094	117.3906	50.46776
A.29.LEU.H	A.29.LEU.N	A.29.LEU.CA	8.440734	120.1769	36.90891
A.29.LEU.H	A.29.LEU.N	A.29.LEU.CA	8.455803	120.4287	53.84966
A.30.SER.H	A.30.SER.N	A.30.SER.CA	8.674098	116.3435	51.6336
A.32.VAL.H	A.32.VAL.N	A.32.VAL.CA	8.547136	122.3486	60.77285
A.33.GLY.H	A.33.GLY.N	A.33.GLY.CA	7.697071	108.6244	42.41967
A.34.SER.H	A.34.SER.N	A.34.SER.CA	8.35208	116.4854	53.67077
A.35.GLY.H	A.35.GLY.N	A.35.GLY.CA	8.117868	110.7997	41.10138
A.37.TYR.H	A.37.TYR.N	A.37.TYR.CA	8.008457	113.8845	54.13456
A.38.GLY.H	A.38.GLY.N	A.38.GLY.CA	7.239462	108.6029	42.59977
A.39.SER.H	A.39.SER.N	A.39.SER.CA	8.108128	116.032	55.0106
A.40.VAL.H	A.40.VAL.N	A.40.VAL.CA	8.639207	122.6612	58.20246
A.41.CYS.H	A.41.CYS.N	A.41.CYS.CA	9.191366	125.4775	54.69288
A.42.ALA.H	A.42.ALA.N	A.42.ALA.CA	8.719962	125.919	47.42016
A.43.ALA.H	A.43.ALA.N	A.43.ALA.CA	8.98733	120.8205	47.60424
A.44.PHE.H	A.44.PHE.N	A.44.PHE.CA	9.140636	122.8933	53.91544
A.45.ASP.H	A.45.ASP.N	A.45.ASP.CA	8.195738	125.9016	48.65707
A.46.THR.H	A.46.THR.N	A.46.THR.CA	9.02915	117.6543	60.61997
A.47.LYS.H	A.47.LYS.N	A.47.LYS.CA	7.730708	121.3809	55.27264
A.48.THR.H	A.48.THR.N	A.48.THR.CA	6.447468	104.7819	58.5342
A.49.GLY.H	A.49.GLY.N	A.49.GLY.CA	8.25098	112.0773	42.77149
A.50.LEU.H	A.50.LEU.N	A.50.LEU.CA	7.029845	119.5495	50.56121
A.51.ARG.H	A.51.ARG.N	A.51.ARG.CA	8.185991	119.7336	53.603
A.52.VAL.H	A.52.VAL.N	A.52.VAL.CA	8.731109	116.7603	56.05327

A.53.ALA.H	A.53.ALA.N	A.53.ALA.CA	8.736823	123.0528	47.14801
A.55.LYS.H	A.55.LYS.N	A.55.LYS.CA	9.535482	129.7692	51.01812
A.56.LYS.H	A.56.LYS.N	A.56.LYS.CA	8.500006	128.6795	51.2077
A.57.LEU.H	A.57.LEU.N	A.57.LEU.CA	7.938929	128.9777	51.8398
A.58.SER.H	A.58.SER.N	A.58.SER.CA	7.950689	117.6111	54.16719
A.59.ARG.H	A.59.ARG.N	A.59.ARG.CA	8.663114	123.1804	53.04531
A.62.GLN.H	A.62.GLN.N	A.62.GLN.CA	7.038014	115.785	54.63584
A.63.SER.H	A.63.SER.N	A.63.SER.CA	7.373045	110.7213	53.5252
A.64.ILE.H	A.64.ILE.N	A.64.ILE.CA	9.146387	123.2678	63.1057
A.65.ILE.H	A.65.ILE.N	A.65.ILE.CA	7.48249	118.8525	61.06634
A.67.ALA.H	A.67.ALA.N	A.67.ALA.CA	8.513589	124.3988	52.10812
A.68.LYS.H	A.68.LYS.N	A.68.LYS.CA	7.737216	118.5456	56.27128
A.69.ARG.H	A.69.ARG.N	A.69.ARG.CA	7.328226	119.1526	56.31743
A.70.THR.H	A.70.THR.N	A.70.THR.CA	8.373776	119.7321	63.70133
A.71.TYR.H	A.71.TYR.N	A.71.TYR.CA	7.519567	122.6944	59.62831
A.81.LYS.H	A.81.LYS.N	A.81.LYS.CA	8.429407	128.4956	51.8269
A.82.HIS.H	A.82.HIS.N	A.82.HIS.CA	8.587809	123.7915	53.96767
A.83.GLU.H	A.83.GLU.N	A.83.GLU.CA	7.923062	126.671	56.10972
A.85.VAL.H	A.85.VAL.N	A.85.VAL.CA	7.584825	119.8409	57.73335
A.87.GLY.H	A.87.GLY.N	A.87.GLY.CA	7.52211	109.5564	40.78504
A.88.LEU.H	A.88.LEU.N	A.88.LEU.CA	8.262353	120.9682	51.54309
A.89.LEU.H	A.89.LEU.N	A.89.LEU.CA	8.874026	126.4229	52.26087
A.91.VAL.H	A.91.VAL.N	A.91.VAL.CA	7.749452	120.7831	56.37986
A.93.THR.H	A.93.THR.N	A.93.THR.CA	8.909443	113.8232	54.08623
A.95.ALA.H	A.95.ALA.N	A.95.ALA.CA	7.649621	122.0425	49.58186
A.96.ARG.H	A.96.ARG.N	A.96.ARG.CA	9.213039	121.0913	53.0985
A.97.SER.H	A.97.SER.N	A.97.SER.CA	7.301601	111.1344	53.29597
A.98.LEU.H	A.98.LEU.N	A.98.LEU.CA	8.414619	122.352	53.77106
A.99.GLU.H	A.99.GLU.N	A.99.GLU.CA	8.241738	117.451	56.23485
A.100.GLU.H	A.100.GLU.N	A.100.GLU.CA	6.922609	115.1929	51.62793
A.101.PHE.H	A.101.PHE.N	A.101.PHE.CA	7.244782	122.2164	53.91619
A.102.ASN.H	A.102.ASN.N	A.102.ASN.CA	8.49516	125.7826	50.69787
A.103.ASP.H	A.103.ASP.N	A.103.ASP.CA	7.568991	115.7644	50.1169
A.104.VAL.H	A.104.VAL.N	A.104.VAL.CA	8.378426	120.9916	58.48014
A.106.LEU.H	A.106.LEU.N	A.106.LEU.CA	8.65678	119.7923	49.70394
A.108.THR.H	A.108.THR.N	A.108.THR.CA	8.902564	117.8536	56.71715
A.109.HIS.H	A.109.HIS.N	A.109.HIS.CA	8.862684	119.2038	56.54702
A.110.LEU.H	A.110.LEU.N	A.110.LEU.CA	8.090979	125.5533	51.48306
A.112.GLY.H	A.112.GLY.N	A.112.GLY.CA	8.068921	108.6029	42.41967
A.113.ALA.H	A.113.ALA.N	A.113.ALA.CA	7.788954	123.5977	48.5544
A.114.ASP.H	A.114.ASP.N	A.114.ASP.CA	7.930362	118.2795	49.21584
A.116.ASN.H	A.116.ASN.N	A.116.ASN.CA	7.57655	117.7319	53.23716
A.117.ASN.H	A.117.ASN.N	A.117.ASN.CA	7.809686	118.2444	54.85491
A.120.LYS.H	A.120.LYS.N	A.120.LYS.CA	7.301961	117.3909	53.82429
A.121.CYS.H	A.121.CYS.N	A.121.CYS.CA	7.530798	113.6859	55.11785
A.122.GLN.H	A.122.GLN.N	A.122.GLN.CA	7.868998	119.8751	50.84363

A.124.LEU.H	A.124.LEU.N	A.124.LEU.CA	8.605042	127.285	51.06059
A.127.ASP.H	A.127.ASP.N	A.127.ASP.CA	7.776586	116.11	54.58855
A.129.VAL.H	A.129.VAL.N	A.129.VAL.CA	8.070462	120.7741	64.85479
A.130.GLN.H	A.130.GLN.N	A.130.GLN.CA	8.347867	118.318	56.15207
A.132.LEU.H	A.132.LEU.N	A.132.LEU.CA	8.819068	120.4896	55.23342
A.134.TYR.H	A.134.TYR.N	A.134.TYR.CA	8.865002	120.2032	54.73973
A.139.GLY.H	A.139.GLY.N	A.139.GLY.CA	8.064953	107.3377	44.11256
A.140.LEU.H	A.140.LEU.N	A.140.LEU.CA	8.574292	121.7234	53.78756
A.141.LYS.H	A.141.LYS.N	A.141.LYS.CA	8.652343	119.5267	56.63782
A.142.TYR.H	A.142.TYR.N	A.142.TYR.CA	6.707236	118.3129	58.59433
A.143.ILE.H	A.143.ILE.N	A.143.ILE.CA	8.355354	120.1948	64.12189
A.144.HIS.H	A.144.HIS.N	A.144.HIS.CA	9.436924	119.8082	54.02754
A.145.SER.H	A.145.SER.N	A.145.SER.CA	7.777825	117.4391	58.20246
A.146.ALA.H	A.146.ALA.N	A.146.ALA.CA	7.327692	126.7785	48.45241
A.147.ASP.H	A.147.ASP.N	A.147.ASP.CA	8.127762	115.2223	52.4206
A.148.ILE.H	A.148.ILE.N	A.148.ILE.CA	7.168803	117.9175	56.38371
A.149.ILE.H	A.149.ILE.N	A.149.ILE.CA	7.787866	124.1541	57.12101
A.150.HIS.H	A.150.HIS.N	A.150.HIS.CA	7.277826	121.1055	59.64484
A.156.SER.H	A.156.SER.N	A.156.SER.CA	7.788527	106.1026	58.66778
A.157.ASN.H	A.157.ASN.N	A.157.ASN.CA	7.720716	118.9119	49.63275
A.158.LEU.H	A.158.LEU.N	A.158.LEU.CA	6.971548	119.6262	49.9204
A.159.ALA.H	A.159.ALA.N	A.159.ALA.CA	8.443955	125.4834	47.52474
A.160.VAL.H	A.160.VAL.N	A.160.VAL.CA	8.181598	117.3894	56.20403
A.162.GLU.H	A.162.GLU.N	A.162.GLU.CA	8.499753	116.3912	55.99583
A.165.GLU.H	A.165.GLU.N	A.165.GLU.CA	7.445751	118.6563	51.19597
A.166.LEU.H	A.166.LEU.N	A.166.LEU.CA	7.910623	126.124	49.72548
A.167.LYS.H	A.167.LYS.N	A.167.LYS.CA	8.900282	122.6624	51.59914
A.168.ILE.H	A.168.ILE.N	A.168.ILE.CA	8.126163	121.9874	59.43014
A.174.ALA.H	A.174.ALA.N	A.174.ALA.CA	8.000441	119.5208	56.91216
A.175.ARG.H	A.175.ARG.N	A.175.ARG.CA	8.344035	117.079	52.5564
A.179.ASP.H	A.179.ASP.N	A.179.ASP.CA	7.975225	120.4207	51.80728
A.180.GLU.H	A.180.GLU.N	A.180.GLU.CA	8.030873	120.7557	54.19707
A.181.MET.H	A.181.MET.N	A.181.MET.CA	8.06343	120.0509	51.77744
A.182.THR.H	A.182.THR.N	A.182.THR.CA	7.847863	114.2478	59.46658
A.183.GLY.H	A.183.GLY.N	A.183.GLY.CA	8.177641	111.1451	42.00717
A.184.TYR.H	A.184.TYR.N	A.184.TYR.CA	7.78306	121.2224	54.76463
A.185.VAL.H	A.185.VAL.N	A.185.VAL.CA	7.747624	123.1984	59.72487
A.191.ARG.H	A.191.ARG.N	A.191.ARG.CA	7.278902	122.6694	52.40861
A.192.ALA.H	A.192.ALA.N	A.192.ALA.CA	8.809382	126.051	47.38961
A.197.LEU.H	A.197.LEU.N	A.197.LEU.CA	9.078871	125.2104	55.33204
A.198.ASN.H	A.198.ASN.N	A.198.ASN.CA	7.808644	115.4142	50.58777
A.199.TRP.H	A.199.TRP.N	A.199.TRP.CA	8.4333	125.5221	51.18153
A.200.MET.H	A.200.MET.N	A.200.MET.CA	8.639207	120.3889	58.86949
A.202.TYR.H	A.202.TYR.N	A.202.TYR.CA	10.07177	126.9642	49.40537
A.203.ASN.H	A.203.ASN.N	A.203.ASN.CA	8.727351	124.8747	53.3475
A.205.THR.H	A.205.THR.N	A.205.THR.CA	8.273253	115.4647	56.16085

A.208.ILE.H	A.208.ILE.N	A.208.ILE.CA	7.13424	119.3593	57.8019
A.209.TRP.H	A.209.TRP.N	A.209.TRP.CA	7.448994	121.1051	57.9956
A.210.SER.H	A.210.SER.N	A.210.SER.CA	7.514591	112.4017	59.15369
A.211.VAL.H	A.211.VAL.N	A.211.VAL.CA	7.889169	120.1426	64.31878
A.212.GLY.H	A.212.GLY.N	A.212.GLY.CA	8.468622	110.4566	44.74456
A.213.CYS.H	A.213.CYS.N	A.213.CYS.CA	7.788827	119.2556	61.01815
A.214.ILE.H	A.214.ILE.N	A.214.ILE.CA	8.334913	124.5576	62.74339
A.215.MET.H	A.215.MET.N	A.215.MET.CA	9.264032	120.8189	57.29343
A.216.ALA.H	A.216.ALA.N	A.216.ALA.CA	8.036041	118.5827	52.52815
A.217.GLU.H	A.217.GLU.N	A.217.GLU.CA	7.033739	120.5014	55.60367
A.218.LEU.H	A.218.LEU.N	A.218.LEU.CA	7.197304	116.4311	54.28825
A.219.LEU.H	A.219.LEU.N	A.219.LEU.CA	8.440678	118.2391	53.82738
A.220.THR.H	A.220.THR.N	A.220.THR.CA	7.840155	105.8445	59.03996
A.221.GLY.H	A.221.GLY.N	A.221.GLY.CA	8.357991	113.2438	42.44411
A.222.ARG.H	A.222.ARG.N	A.222.ARG.CA	7.924092	119.1205	50.79805
A.223.THR.H	A.223.THR.N	A.223.THR.CA	7.870914	119.8868	60.42784
A.224.LEU.H	A.224.LEU.N	A.224.LEU.CA	7.765597	117.8983	49.88324
A.227.GLY.H	A.227.GLY.N	A.227.GLY.CA	8.272928	113.7014	42.40053
A.230.HIS.H	A.230.HIS.N	A.230.HIS.CA	8.520996	114.5205	49.06145
A.239.ARG.H	A.239.ARG.N	A.239.ARG.CA	8.141051	116.7543	56.03793
A.240.LEU.H	A.240.LEU.N	A.240.LEU.CA	7.527502	117.8842	54.50022
A.241.VAL.H	A.241.VAL.N	A.241.VAL.CA	8.357854	122.4012	55.31718
A.245.GLY.H	A.245.GLY.N	A.245.GLY.CA	8.220647	108.9655	40.61303
A.246.ALA.H	A.246.ALA.N	A.246.ALA.CA	8.294029	121.3943	52.14556
A.248.LEU.H	A.248.LEU.N	A.248.LEU.CA	7.387673	120.4764	53.69953
A.249.LEU.H	A.249.LEU.N	A.249.LEU.CA	7.802009	118.1375	53.65178
A.250.LYS.H	A.250.LYS.N	A.250.LYS.CA	7.538045	120.814	52.89548
A.256.SER.H	A.256.SER.N	A.256.SER.CA	8.299482	113.941	57.86334
A.257.ALA.H	A.257.ALA.N	A.257.ALA.CA	7.615316	125.8188	51.67539
A.262.GLN.H	A.262.GLN.N	A.262.GLN.CA	7.992558	118.2829	54.95788
A.263.SER.H	A.263.SER.N	A.263.SER.CA	7.348042	113.9529	56.17919
A.264.LEU.H	A.264.LEU.N		6.864781	122.9785	51.20028
A.267.MET.H	A.267.MET.N	A.267.MET.CA	8.647165	124.0258	54.22087
A.269.LYS.H	A.269.LYS.N	A.269.LYS.CA	8.193557	120.4975	53.60515
A.270.MET.H	A.270.MET.N	A.270.MET.CA	8.33032	126.0992	52.86691
A.271.ASN.H	A.271.ASN.N	A.271.ASN.CA	8.497471	120.4607	49.69291
A.272.PHE.H	A.272.PHE.N	A.272.PHE.CA	9.330086	129.9638	56.75727
A.273.ALA.H	A.273.ALA.N	A.273.ALA.CA	8.473004	122.3852	51.54053
A.274.ASN.H	A.274.ASN.N	A.274.ASN.CA	7.374421	113.1215	50.57138
A.275.VAL.H	A.275.VAL.N	A.275.VAL.CA	7.118189	120.1499	61.11621
A.276.PHE.H	A.276.PHE.N	A.276.PHE.CA	7.538045	120.814	52.89548
A.277.ILE.H	A.277.ILE.N	A.277.ILE.CA	6.793282	120.9247	59.20548
A.278.GLY.H	A.278.GLY.N	A.278.GLY.CA	8.940064	116.421	41.91809
A.279.ALA.H	A.279.ALA.N	A.279.ALA.CA	7.311943	122.0354	48.0093
A.280.ASN.H	A.280.ASN.N	A.280.ASN.CA	9.047409	122.6611	48.21327
A.282.LEU.H	A.282.LEU.N	A.282.LEU.CA	8.340457	117.0549	54.00097

A.283.ALA.H	A.283.ALA.N	A.283.ALA.CA	7.024513	121.1588	50.83162
A.284.VAL.H	A.284.VAL.N	A.284.VAL.CA	7.006171	116.3853	63.83141
A.285.ASP.H	A.285.ASP.N	A.285.ASP.CA	7.40877	117.9441	54.62872
A.286.LEU.H	A.286.LEU.N	A.286.LEU.CA	7.028738	117.6947	54.4599
A.287.LEU.H	A.287.LEU.N	A.287.LEU.CA	8.014164	119.0276	55.18808
A.288.GLU.H	A.288.GLU.N	A.288.GLU.CA	7.930362	116.9427	55.9293
A.289.LYS.H	A.289.LYS.N	A.289.LYS.CA	7.256361	116.032	54.33495
A.290.MET.H	A.290.MET.N	A.290.MET.CA	7.545933	117.6434	56.373
A.291.LEU.H	A.291.LEU.N	A.291.LEU.CA	7.758969	119.2073	56.38742
A.296.ASP.H	A.296.ASP.N	A.296.ASP.CA	8.384441	121.0999	53.28701
A.297.LYS.H	A.297.LYS.N	A.297.LYS.CA	7.578156	117.3939	51.64878
A.298.ARG.H	A.298.ARG.N	A.298.ARG.CA	6.956223	122.6676	54.20405
A.299.ILE.H	A.299.ILE.N	A.299.ILE.CA	6.931785	125.5074	59.32245
A.300.THR.H	A.300.THR.N	A.300.THR.CA	7.289363	109.4842	57.14682
A.301.ALA.H	A.301.ALA.N	A.301.ALA.CA	9.51006	122.2987	53.15373
A.302.ALA.H	A.302.ALA.N	A.302.ALA.CA	8.500971	116.3843	52.23031
A.303.GLN.H	A.303.GLN.N	A.303.GLN.CA	7.348214	116.0885	54.9552
A.304.ALA.H	A.304.ALA.N	A.304.ALA.CA	8.640162	124.2832	51.81116
A.305.LEU.H	A.305.LEU.N	A.305.LEU.CA	7.573952	116.4961	54.60836
A.306.ALA.H	A.306.ALA.N	A.306.ALA.CA	6.609207	115.567	47.64134
A.307.HIS.H	A.307.HIS.N	A.307.HIS.CA	7.871478	122.633	55.67881
A.308.ALA.H	A.308.ALA.N	A.308.ALA.CA	8.284125	132.8583	52.15791
A.309.TYR.H	A.309.TYR.N	A.309.TYR.CA	11.59742	125.6561	57.52295
A.310.PHE.H	A.310.PHE.N	A.310.PHE.CA	7.571453	110.3186	53.09138
A.311.ALA.H	A.311.ALA.N	A.311.ALA.CA	7.452403	123.6071	52.80057
A.312.GLN.H	A.312.GLN.N	A.312.GLN.CA	8.580543	113.9995	54.16361
A.313.TYR.H	A.313.TYR.N	A.313.TYR.CA	7.377854	115.479	55.70222
A.314.HIS.H	A.314.HIS.N	A.314.HIS.CA	7.741212	115.5858	52.9714
A.315.ASP.H	A.315.ASP.N	A.315.ASP.CA	7.382319	125.1197	47.87921
A.317.ASP.H	A.317.ASP.N	A.317.ASP.CA	7.868393	117.3668	52.21815
A.318.ASP.H	A.318.ASP.N	A.318.ASP.CA	7.92237	121.3744	49.56787
A.319.GLU.H	A.319.GLU.N	A.319.GLU.CA	7.723924	121.4957	50.57454
A.321.VAL.H	A.321.VAL.N	A.321.VAL.CA	7.807444	108.9285	56.36022
A.322.ALA.H	A.322.ALA.N	A.322.ALA.CA	8.361053	123.2974	48.51402
A.323.ASP.H	A.323.ASP.N	A.323.ASP.CA	8.035189	121.0812	50.09404
A.326.ASP.H	A.326.ASP.N	A.326.ASP.CA	6.864781	122.9785	51.20028
A.330.GLU.H	A.330.GLU.N	A.330.GLU.CA	9.812592	115.1867	56.48903
A.331.SER.H	A.331.SER.N	A.331.SER.CA	7.463467	112.6631	54.8184
A.332.ARG.H	A.332.ARG.N	A.332.ARG.CA	7.608383	121.53	53.06054
A.333.ASP.H	A.333.ASP.N	A.333.ASP.CA	8.461526	124.5429	50.47449
A.334.LEU.H	A.334.LEU.N	A.334.LEU.CA	7.666963	122.9579	49.77113
A.335.LEU.H	A.335.LEU.N	A.335.LEU.CA	8.653997	119.7797	50.88331
A.336.ILE.H	A.336.ILE.N	A.336.ILE.CA	8.857145	121.6152	64.04819
A.337.ASP.H	A.337.ASP.N	A.337.ASP.CA	8.282851	116.0061	54.10948
A.338.GLU.H	A.338.GLU.N	A.338.GLU.CA	7.00778	120.5318	55.52556
A.339.TRP.H	A.339.TRP.N	A.339.TRP.CA	7.549758	119.4908	56.84682

A.340.LYS.H	A.340.LYS.N	A.340.LYS.CA	8.638369	121.2282	57.40303
A.341.SER.H	A.341.SER.N	A.341.SER.CA	7.532457	114.5377	57.8303
A.342.LEU.H	A.342.LEU.N	A.342.LEU.CA	7.913493	120.4818	54.51662
A.345.ASP.H	A.345.ASP.N	A.345.ASP.CA	8.036447	117.6815	54.01744
A.346.GLU.H	A.346.GLU.N	A.346.GLU.CA	7.469343	118.4017	54.67892
A.347.VAL.H	A.347.VAL.N	A.347.VAL.CA	7.987584	122.0457	62.32069
A.348.ILE.H	A.348.ILE.N	A.348.ILE.CA	7.977749	115.5256	60.07533
A.349.SER.H	A.349.SER.N	A.349.SER.CA	7.400003	112.1889	55.14144
A.350.PHE.H	A.350.PHE.N	A.350.PHE.CA	7.060691	124.2224	56.67707
A.351.VAL.H	A.351.VAL.N	A.351.VAL.CA	7.77964	131.4123	55.48002
A.355.LEU.H	A.355.LEU.N	A.355.LEU.CA	8.213511	123.6194	51.64276
A.356.ASP.H	A.356.ASP.N	A.356.ASP.CA	8.220674	121.458	51.43564
A.357.GLN.H	A.357.GLN.N	A.357.GLN.CA	8.162145	120.3215	52.55648
A.358.GLU.H	A.358.GLU.N	A.358.GLU.CA	8.249664	122.8927	52.975
A.359.GLU.H	A.359.GLU.N	A.359.GLU.CA	8.288973	122.3348	53.41829
A.360.MET.H	A.360.MET.N	A.360.MET.CA	8.231035	122.0857	52.57691
A.361.GLU.H	A.361.GLU.N	A.361.GLU.CA	8.340258	121.5843	52.54444
A.362.SER.H	A.362.SER.N	A.362.SER.CA	7.859258	123.0087	56.79436

Table 10.8 : Chemical Shifts of V38A (BMRB nomenclature is i+2)

Assign F1	**Assign F2**	**Pos F1**	**Pos F2**
A.7.ARG.H	A.7.ARG.N	8.374642	125.7232
A.9.THR.H	A.9.THR.N	8.394463	117.4655
A.10.PHE.H	A.10.PHE.N	8.735953	127.3486
A.11.TYR.H	A.11.TYR.N	9.066962	120.293
A.12.ARG.H	A.12.ARG.N	8.385508	120.1767
A.13.GLN.H	A.13.GLN.N	8.848642	122.4096
A.14.GLU.H	A.14.GLU.N	8.777955	125.687
A.15.LEU.H	A.15.LEU.N	8.911758	128.6697
A.17.LYS.H	A.17.LYS.N	8.797272	109.9947
A.18.THR.H	A.18.THR.N	7.770941	115.7584
A.19.ILE.H	A.19.ILE.N	8.509843	125.7092
A.20.TRP.H	A.20.TRP.N	9.197329	131.3129
A.21.GLU.H	A.21.GLU.N	8.183469	128.2859
A.22.VAL.H	A.22.VAL.N	7.58152	112.3615
A.24.GLU.H	A.24.GLU.N	8.041948	119.1821
A.25.ARG.H	A.25.ARG.N	7.419648	117.311
A.26.TYR.H	A.26.TYR.N	7.782172	118.1913
A.27.GLN.H	A.27.GLN.N	9.110532	122.6081
A.28.ASN.H	A.28.ASN.N	8.732635	117.5134
A.29.LEU.H	A.29.LEU.N	8.484276	120.332
A.30.SER.H	A.30.SER.N	8.654339	116.2594
A.35.GLY.H	A.35.GLY.N	8.177089	110.5761
A.37.TYR.H	A.37.TYR.N	8.053538	113.2625
A.39.SER.H	A.39.SER.N	8.077963	115.9145

A.43.ALA.H	A.43.ALA.N	8.886858	120.8942
A.44.PHE.H	A.44.PHE.N	9.109761	122.6209
A.45.ASP.H	A.45.ASP.N	8.222772	125.9984
A.46.THR.H	A.46.THR.N	8.926824	117.4655
A.47.LYS.H	A.47.LYS.N	7.735898	121.395
A.48.THR.H	A.48.THR.N	6.460622	104.803
A.49.GLY.H	A.49.GLY.N	8.247506	112.139
A.50.LEU.H	A.50.LEU.N	7.023296	119.7055
A.51.ARG.H	A.51.ARG.N	8.163234	119.6915
A.57.LEU.H	A.57.LEU.N	8.069016	128.7321
A.58.SER.H	A.58.SER.N	7.960434	117.9888
A.59.ARG.H	A.59.ARG.N	8.648808	123.1955
A.61.PHE.H	A.61.PHE.N	7.797435	112.7983
A.62.GLN.H	A.62.GLN.N	6.978518	115.5469
A.63.SER.H	A.63.SER.N	7.353283	110.7542
A.64.ILE.H	A.64.ILE.N	9.094275	123.3229
A.65.ILE.H	A.65.ILE.N	7.508179	118.9136
A.67.ALA.H	A.67.ALA.N	8.525768	123.6751
A.68.LYS.H	A.68.LYS.N	7.719798	118.4206
A.69.ARG.H	A.69.ARG.N	7.41107	119.2911
A.70.THR.H	A.70.THR.N	8.380888	120.0175
A.81.LYS.H	A.81.LYS.N	8.438132	128.701
A.82.HIS.H	A.82.HIS.N	8.592971	124.0316
A.83.GLU.H	A.83.GLU.N	7.958547	125.5822
A.84.ASN.H	A.84.ASN.N	11.25358	118.0967
A.85.VAL.H	A.85.VAL.N	7.608687	119.846
A.86.ILE.H	A.86.ILE.N	8.256068	129.279
A.88.LEU.H	A.88.LEU.N	8.222248	121.2539
A.89.LEU.H	A.89.LEU.N	8.873468	126.128
A.93.THR.H	A.93.THR.N	8.876289	113.8169
A.95.ALA.H	A.95.ALA.N	7.652773	122.4178
A.96.ARG.H	A.96.ARG.N	9.178015	121.2699
A.97.SER.H	A.97.SER.N	7.288769	111.353
A.98.LEU.H	A.98.LEU.N	8.364345	122.4579
A.99.GLU.H	A.99.GLU.N	8.206755	117.3823
A.100.GLU.H	A.100.GLU.N	6.936166	115.4164
A.101.PHE.H	A.101.PHE.N	7.206226	122.2853
A.102.ASN.H	A.102.ASN.N	8.504267	125.4313
A.103.ASP.H	A.103.ASP.N	7.50645	115.6381
A.104.VAL.H	A.104.VAL.N	8.369475	121.0638
A.105.TYR.H	A.105.TYR.N	8.144209	125.4515
A.106.LEU.H	A.106.LEU.N	8.667846	119.8351
A.108.THR.H	A.108.THR.N	8.935706	118.1185
A.109.HIS.H	A.109.HIS.N	8.798585	119.3855
A.112.GLY.H	A.112.GLY.N	8.058221	108.7186
A.113.ALA.H	A.113.ALA.N	7.798058	123.7573

A.114.ASP.H	A.114.ASP.N	7.910078	118.5437
A.116.ASN.H	A.116.ASN.N	7.568573	117.7754
A.117.ASN.H	A.117.ASN.N	7.866955	118.2985
A.120.LYS.H	A.120.LYS.N	7.296366	117.4509
A.121.CYS.H	A.121.CYS.N	7.537245	113.7914
A.122.GLN.H	A.122.GLN.N	7.865586	119.82
A.124.LEU.H	A.124.LEU.N	8.467214	126.8571
A.127.ASP.H	A.127.ASP.N	7.767861	115.8571
A.129.VAL.H	A.129.VAL.N	8.053728	119.9691
A.130.GLN.H	A.130.GLN.N	8.322822	118.321
A.134.TYR.H	A.134.TYR.N	8.842477	119.8822
A.140.LEU.H	A.140.LEU.N	8.609688	121.681
A.141.LYS.H	A.141.LYS.N	8.603174	119.4164
A.142.TYR.H	A.142.TYR.N	6.731599	118.1756
A.143.ILE.H	A.143.ILE.N	8.381658	120.0876
A.144.HIS.H	A.144.HIS.N	9.432981	119.839
A.145.SER.H	A.145.SER.N	7.766512	116.4419
A.146.ALA.H	A.146.ALA.N	7.322915	126.5075
A.147.ASP.H	A.147.ASP.N	8.105765	115.2755
A.148.ILE.H	A.148.ILE.N	7.164697	119.2332
A.149.ILE.H	A.149.ILE.N	7.784404	123.5363
A.150.HIS.H	A.150.HIS.N	7.279625	120.9156
A.157.ASN.H	A.157.ASN.N	7.696542	119.0097
A.158.LEU.H	A.158.LEU.N	6.965064	119.3606
A.159.ALA.H	A.159.ALA.N	8.299326	124.9882
A.160.VAL.H	A.160.VAL.N	8.199824	117.3059
A.162.GLU.H	A.162.GLU.N	8.533336	116.374
A.165.GLU.H	A.165.GLU.N	7.39644	119.0205
A.167.LYS.H	A.167.LYS.N	8.857699	122.5577
A.168.ILE.H	A.168.ILE.N	8.147475	121.9156
A.174.ALA.H	A.174.ALA.N	7.916468	119.5563
A.175.ARG.H	A.175.ARG.N	8.337247	117.1147
A.179.ASP.H	A.179.ASP.N	8.003619	119.9732
A.180.GLU.H	A.180.GLU.N	8.035383	120.5567
A.181.MET.H	A.181.MET.N	8.062197	120.1187
A.182.THR.H	A.182.THR.N	7.83958	114.0922
A.183.GLY.H	A.183.GLY.N	8.190319	111.343
A.184.TYR.H	A.184.TYR.N	7.771348	120.9922
A.185.VAL.H	A.185.VAL.N	7.719391	123.0849
A.191.ARG.H	A.191.ARG.N	7.231714	122.4892
A.192.ALA.H	A.192.ALA.N	8.791744	126.3432
A.197.LEU.H	A.197.LEU.N	9.117388	126.5298
A.198.ASN.H	A.198.ASN.N	7.806757	115.3055
A.199.TRP.H	A.199.TRP.N	8.506576	125.323
A.200.MET.H	A.200.MET.N	8.595627	120.1292
A.202.TYR.H	A.202.TYR.N	10.04575	127.1286

A.203.ASN.H	A.203.ASN.N	8.698559	124.8992
A.205.THR.H	A.205.THR.N	8.26677	115.588
A.208.ILE.H	A.208.ILE.N	7.164307	119.3041
A.209.TRP.H	A.209.TRP.N	7.42958	120.8755
A.210.SER.H	A.210.SER.N	7.434437	112.8184
A.211.VAL.H	A.211.VAL.N	7.890037	120.0157
A.212.GLY.H	A.212.GLY.N	8.300592	110.1476
A.213.CYS.H	A.213.CYS.N	7.78815	119.4198
A.214.ILE.H	A.214.ILE.N	8.351109	124.0322
A.218.LEU.H	A.218.LEU.N	7.188194	116.4198
A.219.LEU.H	A.219.LEU.N	8.38807	118.4777
A.220.THR.H	A.220.THR.N	7.870174	106.1009
A.222.ARG.H	A.222.ARG.N	7.93668	119.2625
A.223.THR.H	A.223.THR.N	7.837099	120.5993
A.224.LEU.H	A.224.LEU.N	7.773042	117.9608
A.227.GLY.H	A.227.GLY.N	8.263294	113.7214
A.228.THR.H	A.228.THR.N	10.03219	116.7275
A.229.ASP.H	A.229.ASP.N	8.556417	130.7801
A.230.HIS.H	A.230.HIS.N	8.487277	114.3777
A.239.ARG.H	A.239.ARG.N	8.148322	116.7413
A.240.LEU.H	A.240.LEU.N	7.513822	117.7728
A.241.VAL.H	A.241.VAL.N	8.373364	122.4592
A.245.GLY.H	A.245.GLY.N	8.221046	108.8822
A.246.ALA.H	A.246.ALA.N	8.298482	121.1934
A.248.LEU.H	A.248.LEU.N	7.396924	120.5527
A.249.LEU.H	A.249.LEU.N	7.8001	118.1448
A.250.LYS.H	A.250.LYS.N	7.525513	120.834
A.256.SER.H	A.256.SER.N	8.270136	113.8436
A.257.ALA.H	A.257.ALA.N	7.628568	125.7499
A.262.GLN.H	A.262.GLN.N	8.013617	118.246
A.263.SER.H	A.263.SER.N	7.414787	113.7733
A.267.MET.H	A.267.MET.N	8.606848	124.4184
A.270.MET.H	A.270.MET.N	8.321882	126.1283
A.271.ASN.H	A.271.ASN.N	8.486586	120.4021
A.272.PHE.H	A.272.PHE.N	9.31881	129.9871
A.273.ALA.H	A.273.ALA.N	8.452474	122.3791
A.274.ASN.H	A.274.ASN.N	7.369462	112.9455
A.275.VAL.H	A.275.VAL.N	7.113173	120.1374
A.276.PHE.H	A.276.PHE.N	7.52458	120.7954
A.277.ILE.H	A.277.ILE.N	6.786628	120.9515
A.278.GLY.H	A.278.GLY.N	8.927486	116.4054
A.279.ALA.H	A.279.ALA.N	7.313375	122.0288
A.280.ASN.H	A.280.ASN.N	9.023996	122.6068
A.282.LEU.H	A.282.LEU.N	8.336936	117.1572
A.285.ASP.H	A.285.ASP.N	7.394061	117.9052
A.287.LEU.H	A.287.LEU.N	8.034585	120.5878

A.288.GLU.H	A.288.GLU.N	7.872818	117.4602
A.289.LYS.H	A.289.LYS.N	7.231113	116.286
A.290.MET.H	A.290.MET.N	7.57167	117.8422
A.291.LEU.H	A.291.LEU.N	7.776643	119.16
A.296.ASP.H	A.296.ASP.N	8.473182	121.3291
A.297.LYS.H	A.297.LYS.N	7.553942	117.7754
A.298.ARG.H	A.298.ARG.N	6.957261	122.558
A.299.ILE.H	A.299.ILE.N	6.998936	125.093
A.300.THR.H	A.300.THR.N	7.306837	109.4137
A.301.ALA.H	A.301.ALA.N	9.431125	122.1896
A.302.ALA.H	A.302.ALA.N	8.533336	116.2497
A.303.GLN.H	A.303.GLN.N	7.350122	116.0214
A.304.ALA.H	A.304.ALA.N	8.609336	123.9194
A.306.ALA.H	A.306.ALA.N	6.529299	115.1779
A.307.HIS.H	A.307.HIS.N	7.913524	122.6353
A.308.ALA.H	A.308.ALA.N	8.264078	132.814
A.309.TYR.H	A.309.TYR.N	11.56429	125.1365
A.310.PHE.H	A.310.PHE.N	7.576224	110.3723
A.311.ALA.H	A.311.ALA.N	7.440887	123.6434
A.312.GLN.H	A.312.GLN.N	8.576514	114.0701
A.313.TYR.H	A.313.TYR.N	7.342969	116.0998
A.314.HIS.H	A.314.HIS.N	7.768631	115.7393
A.315.ASP.H	A.315.ASP.N	7.355586	124.9963
A.317.ASP.H	A.317.ASP.N	7.87375	117.5078
A.318.ASP.H	A.318.ASP.N	7.909436	121.2529
A.319.GLU.H	A.319.GLU.N	7.730508	121.5097
A.321.VAL.H	A.321.VAL.N	7.770102	109.1181
A.322.ALA.H	A.322.ALA.N	8.364682	123.5903
A.323.ASP.H	A.323.ASP.N	8.009811	121.2264
A.326.ASP.H	A.326.ASP.N	6.875356	122.9702
A.330.GLU.H	A.330.GLU.N	9.824488	114.7977
A.331.SER.H	A.331.SER.N	7.435992	112.776
A.332.ARG.H	A.332.ARG.N	7.536804	121.9392
A.333.ASP.H	A.333.ASP.N	8.479027	124.6158
A.334.LEU.H	A.334.LEU.N	7.717835	123.1197
A.335.LEU.H	A.335.LEU.N	8.667075	119.8128
A.336.ILE.H	A.336.ILE.N	8.86544	121.7159
A.337.ASP.H	A.337.ASP.N	8.287608	115.7539
A.338.GLU.H	A.338.GLU.N	7.003005	120.5698
A.339.TRP.H	A.339.TRP.N	7.604837	119.7154
A.340.LYS.H	A.340.LYS.N	8.645879	121.4709
A.341.SER.H	A.341.SER.N	7.521739	114.4942
A.342.LEU.H	A.342.LEU.N	7.861736	119.9951
A.344.TYR.H	A.344.TYR.N	8.69576	124.9468
A.345.ASP.H	A.345.ASP.N	8.040392	117.5008
A.346.GLU.H	A.346.GLU.N	7.468324	118.3967

A.347.VAL.H	A.347.VAL.N	7.954348	121.8604
A.348.ILE.H	A.348.ILE.N	7.940534	115.4283
A.349.SER.H	A.349.SER.N	7.350725	111.9484
A.350.PHE.H	A.350.PHE.N	7.02583	124.1533
A.351.VAL.H	A.351.VAL.N	7.741588	131.2811
A.355.LEU.H	A.355.LEU.N	8.199155	123.5593
A.356.ASP.H	A.356.ASP.N	8.20764	121.4962
A.357.GLN.H	A.357.GLN.N	8.152548	120.2883
A.358.GLU.H	A.358.GLU.N	8.238812	122.8539
A.359.GLU.H	A.359.GLU.N	8.279452	122.3226
A.360.MET.H	A.360.MET.N	8.274787	122.3547
A.361.GLU.H	A.361.GLU.N	8.306207	123.1894
A.362.SER.H	A.362.SER.N	7.856029	123.0949

Table 10.9: Significant Correlation differences between WT and D168A after heating

residue_i	**residue_j**	**delta_corr**	**FDR**
109	113	0.914165	3.18E-03
41	45	0.889143	4.27E-04
110	114	0.885435	2.52E-02
111	115	0.87829	2.22E-02
88	100	0.777941	3.55E-02
234	239	0.745823	2.76E-03
40	46	0.713531	2.42E-03
62	100	-0.684771	3.10E-02
82	166	0.651825	1.12E-02
82	164	0.643482	3.00E-02
82	165	0.635438	8.56E-03
81	164	0.634502	1.75E-03
30	37	-0.596271	6.47E-06
87	102	0.583042	2.30E-02
86	103	0.550122	1.03E-02
86	102	0.547967	1.80E-02
234	238	0.547555	2.93E-02
70	346	0.491729	6.08E-07
71	342	0.447615	2.53E-03
70	343	0.357219	2.34E-02
70	342	0.251656	9.14E-03
66	339	0.234275	2.80E-02
132	207	0.205591	2.42E-05
138	142	0.202303	3.18E-03

233	237	0.179818	4.27E-04
137	141	0.17887	2.52E-02
229	233	0.173236	2.22E-02
231	235	0.157959	3.55E-02
228	232	0.157435	2.76E-03
124	128	0.157222	2.42E-03
230	234	0.148146	3.10E-02
136	140	0.144919	1.12E-02
125	129	0.143649	3.00E-02
335	339	0.116431	8.56E-03
232	236	0.114245	1.75E-03
337	341	0.113691	6.47E-06
67	71	0.100361	2.30E-02
336	340	0.094251	1.34E-06
339	343	0.086496	1.37E-03
338	342	0.07956	9.13E-04
66	70	0.063979	1.68E-02
334	338	0.06117	9.11E-04

Table 10.10 : Significant correlation differences before and after heating for WT

Residue_i	Residue_j	DeltaCorr	p-value
282	286	0.878181	0.00E+00
221	228	-0.83802	0.00E+00
188	206	-0.83727	0.00E+00
188	202	-0.76596	0.00E+00
109	154	-0.76397	0.00E+00
109	156	-0.75314	0.00E+00
212	220	-0.74402	0.00E+00
139	146	0.705087	0.00E+00
220	269	-0.69381	0.00E+00
65	169	-0.68616	0.00E+00
62	100	0.684771	0.00E+00
232	268	-0.68193	0.00E+00
235	268	-0.65601	0.00E+00
220	283	-0.64963	0.00E+00
222	269	-0.6402	0.00E+00
108	156	-0.63188	0.00E+00
108	155	-0.62096	0.00E+00
60	64	-0.61905	3.81E-03
11	15	-0.61728	5.41E-03
220	232	-0.61222	9.16E-05

Table 10.11 : Significant correlation differences before and after heating for D168A

Residue_i	Residue_j	DeltaCorr	p-value
341	345	0.921956	5.60E-04
342	346	0.870852	9.80E-03
87	101	0.79024	5.64E-03
87	102	0.785966	7.80E-04
39	50	-0.77281	9.87E-04
86	102	0.748851	2.35E-03
234	239	0.745823	7.85E-04
70	346	0.562235	8.96E-04
130	303	-0.5031	3.10E-04
134	297	-0.48583	5.12E-04
66	339	0.469651	4.56E-04
70	343	0.453491	1.25E-04
70	342	0.451025	2.38E-04
67	330	-0.39019	2.73E-11